Measurement of the top quark pole mass using double differential ttbar cross sections in the ATLAS experiment at the LHC and improvement of the modelling uncertainties in top quark mass analyses

Tetiana Moskalets

Thèse de doctorat

NNT: 2020UPASP008

université PARIS-SACLAY

Measurement of the top quark pole mass using double differential $t\bar{t}$ cross sections in the ATLAS experiment at the LHC and improvement of the modelling uncertainties in top quark mass analyses

Thèse de doctorat de l'université Paris-Saclay

École doctorale n° 576,
Particules, Hadrons, Énergie et Noyau:
Instrumentation, Image, Cosmos et Simulation (PHENIICS)
Spécialité de doctorat: Physique des particules
Unité de recherche: Université Paris-Saclay,
Commissariat à l'Energie Atomique et aux Energies Alternatives (CEA),
Institut de Recherche sur les lois Fondamentales de l'Univers (IRFU),
Département de Physique des Particules (DPhP),
91191, Gif-sur-Yvette, France.
Référent: Faculté des sciences d'Orsay

**Thèse présentée et soutenue à Gif-sur-Yvette,
le 24 septembre 2020, par**

Tetiana MOSKALETS

Composition du jury:

Laurent Serin Directeur de recherche, IJCLab Orsay	Président
Matteo Maria Cacciari Professeur, LPTHE Paris	Rapporteur & Examinateur
Marcel Andre Vos Chercheur associé (HDR), IFIC Valencia	Rapporteur & Examinateur
Veronique Boisvert Professeur, RHUL London	Examinatrice
Maria Aldaya Martin Chercheuse, DESY Hamburg	Examinatrice
Frédéric Déliot Chercheur sénior, CEA Saclay	Directeur

Contents

List of Figures

List of Tables

Introduction

The current understanding of the particle physics is based on the Standard Model (SM), which describes all the elementary particles and all their interactions, except gravity. The predictions of the SM have been successfully confirmed in many high-energy experiments. The recent and most famous verification of the SM is the observation of the Higgs boson by the two general-puprose experiments, ATLAS and CMS, at the CERN Large Hadron Collider (LHC) in 2012.

The top quark, which is the heaviest elementary particle of the SM, has a special place in it. Having the largest coupling to the Higgs boson, the top quark gives one of the main contributions in many perturbative calculations. For example, the top quark largely contributes to the Higgs self-coupling loop corrections, which determine the stability of the SM vacuum and hence allow to estimate the Universe lifetime. Also, the top quark mass appears in the consistency tests of the electroweak theory. For all these reasons, a precise determination of the top quark mass is important.

The measurements of the top quark mass using various methods are actively ongoing in ATLAS. Indirect methods to measure the top quark mass, which allow to measure a theoretically well-defined pole or $\overline{\text{MS}}$ mass, until recently gave much larger uncertainty (1-1.5%) then the direct methods (0.5%), in which the top mass or an observable highly sensitive to it is directly reconstructed. The large uncertainty in the indirect measurements was usually related to uncertainties on the theoretical predictions, which are compared to the measured total or differential $t\bar{t}$ cross sections. Currently, more and more precise theoretical calculations become available, in particular for the differential $t\bar{t}$ cross sections, allowing to improve the top quark mass uncertainty in the indirect methods and make it comparable or even smaller than the uncertainty given by the direct methods. Further reduction of the top quark mass uncertainty is possible by extracting it from multidimensional differential $t\bar{t}$ cross section measured using a large enough dataset and this thesis describes such an analysis.

Chapter 5 of this thesis presents the top quark pole mass determination from single and double differential $t\bar{t}$ cross sections in the lepton+jets channel at $\sqrt{s} = 13$ TeV with the ATLAS detector. Studies presented in this chapter focus on consistency tests of the mass extraction procedure, performed using simulated samples. The preliminary estimate of the experimental and theoretical uncertainties is also discussed. After the analysis procedure is fully settled, the top quark mass will be extracted from the double differential cross section measured using the data collected by the ATLAS detector during 2015 and 2016 and corresponding to an integrated luminosity of 36 fb^{-1}.

As top quark mass measurements become more precise, some of the experimental systematic uncertainties, which were not dominant before, become more important. Chapters 6 to 8 of this thesis are devoted to improvement of such systematic uncertainties.

Chapter 6 presents a study of parton shower uncertainties using the Herwig 7 generator in the context of $t\bar{t}$ production. An alternative approach to define a parton shower and hadronisation uncertainties is

discussed. We study the variations of the parton shower type, matching and various scale variations and analyse their impact on the observables commonly used in the top quark analyses. This work has been conducted as a qualification task in order to become an ATLAS author.

Chapter 7 shows the measurement of observables sensitive to colour reconnection (CR) in $t\bar{t}$ dilepton events. The main observables that have the largest dependence on the choice of the CR model are related to the number of the charged particle tracks and their transverse momenta. This analysis aims at improving the CR uncertainty in the top quark mass measurements by constraining some of the PYTHIA 8 CR models using data. The full Run 2 data set, collected during 2015–2018 and corresponding to a total integrated luminosity of 139 fb $^{-1}$ at $\sqrt{s}$ = 13 TeV, is used. The chapter focuses on particular studies, related to unfolding of the two-dimensional observables.

Chapter 8 describes another study aiming at improving the hadronisation uncertainty of the top quark mass. The goal is to factorise out the jet energy scale effects present within the hadronisation uncertainty in its current definition. The method used in this study is the recalibration of jets, which are defined in one Monte-Carlo generator, to match the jets in another Monte-Carlo generator.

The rest of this thesis is structured as follows. An overview of the Standard Model of particle physics is presented in Chapter 1. The basic principles of the hadron collision event simulation in the Monte-Carlo generators are given in Chapter 2. The LHC and the ATLAS detector are described in Chapter 3. An introduction about top quark physics and an overview of the top quark mass measurement methods are given in Chapter 4.

1 Theoretical background: the Standard Model

The Standard Model (SM) of particle physics is a quantum field theory of the strong, electromagnetic (EM) and weak interactions of elementary particles. Its modern formulation has been completed in the 1970s [1, 2] and since then its predictions have been successfully confirmed in many high-energy experiments. The mostly known verification of the SM is the recent observation of the Higgs boson by the ATLAS and CMS Collaborations at the CERN Large Hadron Collider (LHC) in 2012 [3, 4].

According to the SM [5, 6] all matter consists of the spin-$\frac{1}{2}$ particles, *fermions*, which obey the Fermi–Dirac statistics and the Pauli principle. Fermions can be divided into quarks (u, d, s, c, b, t), which interact via all three forces, and leptons ($e, \nu_e, \mu, \nu_\mu, \tau, \nu_\tau$), which couple to the electromagnetic (only e, μ, τ) and weak interaction. All fermions are divided into three generations, based on their mass. They can also be classified by the weak isospin (one of the charges in the electroweak theory, see Section 1.3). All the SM fermions and their properties are presented in Table 1.1.

Particle	Generation	Mass	Electric charge (e)	Weak isospin
up quark (u)	I	$2.16^{+0.49}_{-0.26}$ MeV	+2/3	+1/2
down quark (d)	I	$4.67^{+0.48}_{-0.17}$ MeV	-1/3	-1/2
charm quark (c)	II	1.27 ± 0.02 GeV	+2/3	+1/2
strange quark (s)	II	93^{+11}_{-5} MeV	-1/3	-1/2
top quark (t)	III	172.9 ± 0.4 GeV	+2/3	+1/2
bottom quark (b)	III	$4.18^{+0.03}_{-0.02}$ GeV	-1/3	-1/2
electron neutrino (ν_e)	I	< 2 eV	0	+1/2
electron (e)	I	0.511 MeV	-1	-1/2
muon neutrino (ν_μ)	II	< 0.19 MeV	0	+1/2
muon (μ)	II	105.658 MeV	-1	-1/2
tau neutrino (ν_τ)	III	< 18.2 MeV	0	+1/2
tau (τ)	III	1776.86 ± 0.12 MeV	-1	-1/2

Table 1.1: Overview of the properties of the Standard Model particles [7]. Electron and muon mass uncertainties are not given since they are $\lesssim$ eV.

In the Standard Model, each fermion has its antifermion counterpart with the same mass and spin and opposite *charges* (electrical charge, colour charge for quarks, weak isospin, see Sections 1.2 and 1.3).

The SM interactions are mediated by spin-1 gauge bosons, which obey the Bose–Einstein statistics: the gluons (g) are responsible for the strong interaction, the photon (γ) and the W- and Z- bosons are transmitting the electromagnetic and the weak interactions, respectively. The properties of the gauge bosons as well as the ranges of the interaction which they mediate are given in Table 1.2.

Boson	Mass	Electric charge (e)	Interaction	Interaction range (m)
gluon (g)	0	0	strong	10^{-15}
photon (γ)	0	0	EM	∞
$W^{\pm}$-boson	80.379 ± 0.012 GeV	± 1	weak	10^{-18}
Z^0-boson	91.1876 ± 0.0021 GeV	0	weak	10^{-18}

Table 1.2: Properties of the Standard Model gauge bosons [7].

There is one more boson included in the SM, the Higgs boson (H), which is not an interaction mediator but it is responsible for the spontaneous symmetry breaking (SSB) of the electroweak interaction and for giving masses to the particles (see Section 1.4). The Higgs boson has a zero spin, a zero electric charge and a mass $m_H = 125.10 \pm 0.14$ GeV [7].

Standard Model as a Quantum Field Theory

The Standard Model is described by a *Lagrangian*[1] which is invariant under the local gauge transformations of the $SU(3)_C \otimes SU(2)_L \otimes U(1)_Y$ group and under the global transformations of the Poincaré group [5, 6, 8]. Global transformations include translations, rotations and Lorentz boosts. Local gauge transformations correspond to the fundamental interactions:

- The $SU(3)_C$ group where "C" means *colour* is the symmetry group of Quantum Chromodynamics (QCD) describing the strong interaction of coloured particles. Any particle (strictly speaking, its *quantum field*) which transforms under $SU(3)_C$ is "coloured" and is subjected to the strong interaction. The gauge bosons of QCD, the gluons, which also carry colour charges, are massless as any gauge bosons of a non-broken gauge symmetry. More information on QCD is given in Section 1.2.

- The $SU(2)_L \otimes U(1)_Y$ group (where "L" stands for *left* and "Y" stands for a *weak hypercharge*) is the symmetry group of the electroweak interaction (EW). The EW gauge bosons are also predicted to be massless. However, they have been observed to be massive. This can be explained be the fact that the EW symmetry is spontaneously broken due to the Higgs mechanism, see Section 1.4.

  After spontaneous symmetry breaking, the $SU(2)_L \otimes U(1)_Y$ group is reduced to $U(1)_Q$ (with Q being the electric charge) which is the symmetry of Quantum Electrodynamics (QED) describing the EM interaction. The EM charge Q is related to the EW charges through the Gell-Mann–Nishijima formula:

$$Q = \frac{1}{2}Y + T_3. \tag{1.1}$$

  where T_3 is the third component of the *weak isospin* (see Section 1.3).

  The gauge boson of QED, the photon, is naturally massless, whereas the leftover weak bosons, the $W^{\pm}$ and Z^0, gain mass through the Higgs mechanism [9–11]. More details about the EW interaction and the SSB is presented in Section 1.3 and Section 1.4.

[1] Here and afterwards by Lagrangian we mean Lagrangian density

1.1 Quantum electrodynamics

Interactions between electrically charged particles can be described by a separate theory: Quantum Electrodynamics (QED). QED is an abelian gauge theory based on the $U(1)_Q$ symmetry and the following Lagrangian:

$$\mathcal{L}_{\text{QED}} = \bar{\psi}(i\gamma^\mu D_\mu - m)\psi - \frac{1}{4}F_{\mu\nu}F^{\mu\nu}, \tag{1.2}$$

where

- γ^μ are the Dirac matrices,
- m is a charged particle mass,
- ψ is a Dirac 4-component spinor in the coordinate space and $\bar{\psi} = \psi^\dagger\gamma^0$ is its adjoint spinor.
- $D_\mu = \partial_\mu - ieQA_\mu$ is a covariant derivative,
- e is the electromagnetic coupling constant and Q is the electric charge of the considered fermion ψ in units of the electron charge. The coupling is also often written in terms of the *fine structure constant* $\alpha = e^2/4\pi$.
- A_μ is the photon gauge field which is introduced in order to achieve Lagrangian invariance under the local $U(1)$ transformations: $U(x) = \exp(i\alpha(x))$.
- $F_{\mu\nu}$ is the photon field strength tensor, which is equal to $F_{\mu\nu} = \partial_\mu A_\nu - \partial_\nu A_\mu$.

The pictorial representation of the QED interaction is given in Fig. 1.1: it shows a Feynman diagram of a fermion–photon vertex.

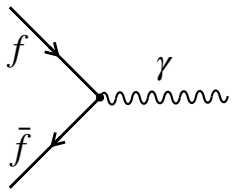

Figure 1.1: The basic vertex of QED: interaction between a charged fermion and a photon.

The electromagnetic coupling constant is energy dependent, i.e. it depends on the momentum transfer in a given process. For example, at asymptotically low energies $\alpha \approx 1/137$ and at the scale of the Z boson mass (~90 GeV) $\alpha \approx 1/127$. The α energy evolution, like for any gauge coupling, is described by the renormalisation group equation (RGE):

$$\mu_R^2 \frac{d\alpha}{d\mu_R^2} = \beta(\alpha) = b_0\alpha^2 + b_1\alpha^3 + b_2\alpha^4 + ..., \tag{1.3}$$

where μ_R is the scale at which the renormalisation is done (*renormalisation scale*) and the coefficients $b_{0,1,2,...}$ are called the β-function coefficients.

1.2 Quantum chromodynamics

Before that quantum chromodynamics has been formulated as a theory of strong interactions of quarks and gluons, there have been different attempts to build up a theory which would explain and classify a large number of new hadrons detected in experiments in the middle of the 20th century. The first quark model containing 3 quarks (u, d, s) has been proposed by Gell-Mann [12] and Zweig [13, 14] in 1964 after several discoveries of strange hadrons (hadrons containing s-quarks) in 1950-60s. The existence of a fourth quark was predicted by Glashow, Iliopoulos and Maiani in 1970 [15] and shortly after, in 1974 the J/ψ meson consisting of a c-quark-antiquark pair has been discovered at SLAC [16] and BNL [17]. The prediction of existence of a third quark generation has been done by Makoto Kobayashi and Toshihide Maskawa in 1973 [18] in order to explain the observed CP violations in kaon decay. Four years after, in 1977, the Υ meson ($b\bar{b}$) and the b-quark were discovered at Fermilab [19]. Since the top quark appears to be much heavier than other quarks and requires much more energy to be produced in hadron collisions, it took almost twenty years before the existence of the top quark was confirmed. The top quark was discovered by the CDF [20] and D0 [21] collaborations at the Tevatron in 1995. The evidence of the remaining ingredient of the QCD theory, gluons, was made in three-jet events at DESY in 1979 [22].

The QCD in its current form starting from a concept of "color" (as an additional quantum number of quarks) was initially developed by Harald Fritzsch Heinrich Leutwyler, and Murray Gell-Mann in the middle of the 70s [23]. The QCD describing the strong interaction is a particular case of a Yang–Mills theory[2]: it is a gauge theory based on the $SU(3)$ symmetry [5, 6, 8]. The QCD Lagrangian reads

$$\mathcal{L}_{\text{QCD}} = \bar{\psi}(i\gamma^\mu D_\mu - m)\psi - \frac{1}{4}G^a_{\mu\nu}G^{\mu\nu\,a}, \tag{1.4}$$

where

- m is a quark mass,
- ψ is a Dirac 4-component spinor in the coordinate space and also a quark triplet of the "red" (ψ_r), "green" (ψ_g) and "blue" (ψ_b) quark fields: $\psi = (\psi_r, \psi_g, \psi_b)^{\mathrm{T}}$. Its adjoint spinor $\bar{\psi} = \psi^\dagger\gamma^0$ also carries a colour index, therefore, any expression with $\bar{\psi}\psi$ implies a summation over the colour indices.
- $D_\mu = \partial_\mu - ig_S A^a_\mu \frac{\lambda^a}{2}$ is a covariant derivative,
- g_S is the coupling constant of strong interaction,
- A^a_μ are spin-1 gauge fields (gluons),
- λ^a are the Gell-Mann matrices ($a = 0, \ldots, 7$). The traceless and Hermitian matrices $\lambda^a/2$ are the *generators* of the $SU(3)$ group, which means that any local $SU(3)$-rotation can be expressed as $U(x) = \exp[i\omega_\alpha(x)\lambda_\alpha/2]$ where ω_α are numerical coefficients. The direct consequence of

[2] A Yang–Mills theory is a non-abelian gauge theory based on the $SU(N)$ symmetry group, i.e. it is a quantum field theory described by a Lagrangian which is invariant under local $SU(N)$ transformations. Here, $SU(N)$ stands for the *special unitary group* of degree N and it is a Lie group of $N \times N$ unitary matrices with determinant 1. Non-abelian means that the elements of the group do not commute.

requiring the invariance of the Lagrangian under these $SU(3)$ transformations is the need to include the gluon fields to the Lagrangian.

- $G^a_{\mu\nu} = \partial_\mu A^a_\nu - \partial_\nu A^a_\mu + g_S f^{abc} A^b_\mu A^c_\nu$ is the gluon field strength tensor, where f^{abc} are the *structure constants* of $SU(3)$ which enter the algebra of the group generators: $[\frac{1}{2}\lambda^a, \frac{1}{2}\lambda^b] = \frac{1}{2} i f^{abc} \lambda^c$.

There are two more remarks to make here. First, although in QCD the mass term for the quarks is allowed, we will see later that the electroweak theory requires all fermions to be massless, and in the final version of the SM Lagrangian there is no mass term for quarks before symmetry breaking. Second, as it was mentioned before, there are six types ("*flavours*") of quarks in the Standard Model, u, d, s, c, b, t. From the point of view of QCD there is no difference between them and if one wanted to write a Lagrangian including all six quarks, one would need just to do a summation over the flavours: $\bar{\psi}\gamma^\mu D_\mu \psi \rightsquigarrow \sum_{i=u}^{t} \bar{\psi}_i \gamma^\mu D_\mu \psi_i$.

The interaction between quarks and gluons in QCD can be illustrated using the Feynman diagrams in Fig. 1.2: the left diagram shows a quark emitting a gluon and the middle and right diagrams represent the interaction between three and four gluons, respectively.

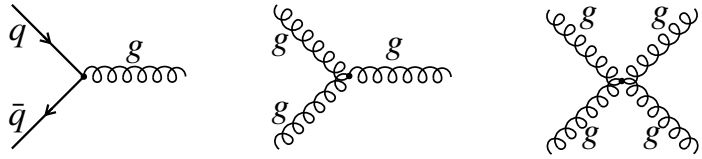

Figure 1.2: Feynman diagrams for the quark–gluon vertex (left), three-gluon interaction (middle) and four-gluon interaction (right).

The QCD coupling constant depends on the energy of the process, but unlike the QED coupling constant in the previous section, the QCD coupling has a negative one-loop beta function:

$$\beta(\alpha_S)^{\text{1-loop}} = -b_0 \alpha_S^2 = -\frac{7}{4\pi}\alpha_S^2, \tag{1.5}$$

where $\alpha_S = g_S^2/(4\pi)$. If one keeps only the first term of the β-function expansion in the RGE for the strong coupling constant, the analytic solution of Eq. (1.3) is:

$$\alpha_S(\mu_R^2) = \frac{1}{b_0 \ln(\mu_R^2/\Lambda^2)}, \tag{1.6}$$

where the constant of integration Λ corresponds to the scale at which the perturbatively-defined coupling would diverge. The world average of Λ is [7] $\Lambda = 332 \pm 17$ MeV. The scale Λ is called the QCD hadronisation scale, since at energies approaching $\Lambda \sim 1$ GeV QCD becomes a strongly-coupled theory and the non-perturbative dynamic (hadronisation) dominates. When the scale Λ is reached there are no free quarks and gluons any more, they are *confined* inside hadrons (this is called *confinement*). Another phenomenon which follows from Eq. (1.6) is the *asymptotic freedom* of quarks at the very large energies: when $\mu_R \to \infty$ the coupling α_S tends to zero and the quarks behave as free particles.

At energies typical for hard scattering processes at the LHC ~TeV the strong coupling constant is around $\alpha_S \sim 0.1$, therefore perturbative QCD is successfully applied in this energy range.

1.3 Electroweak theory

It appears that the weak interaction cannot be consistently described on its own. In the Standard Model the electromagnetic and the weak interactions are considered within a single theory called the EW theory, which is a gauge theory based on the $SU(2)_L \otimes U(1)_Y$ symmetry.

The gauge bosons of $SU(2)_L$ and $U(1)_Y$ are A^a_μ, $a = 1, 2, 3$ and B_μ and the corresponding gauge coupling constants are denoted as g and g', respectively. The linear combinations of the fields A^a_μ and B_μ after SSB (see the next section) correspond to the fields of the $W^\pm$, Z^0 bosons and the photon γ which are observed experimentally. The existence of the W and Z bosons was first established by UA1 and UA2 collaborations at the CERN SPS collider in 1983 [24–27].

The $U(1)_Y$ describes a gauge theory analogous to QED and the index Y denotes the *hypercharge* associated with it, an analogue of the EM charge. The value of the hypercharge can be found from the Gell-Mann–Nishijima formula Eq. (1.1).

Similarly to the spin of the particle related to the $SU(2)$ rotational symmetry, in $SU(2)_L$ a *weak isospin* is assigned to each interacting particle. Like in the case of the spin, the observables for the weak isospin are its absolute value T and its third component T_3. The values of T_3 for the different fermions are given in Table 1.1 in the column "weak isospin". The index L in $SU(2)_L$ means that the $SU(2)$ symmetry concerns only the "left-handed" components of the fields. The spinor of any fermion can be split into a "left-handed" (ψ_L) and a "right-handed" (ψ_R) component as follows:

$$\psi = \psi_L + \psi_R, \quad \psi_L = \frac{1-\gamma^5}{2}\psi, \quad \psi_R = \frac{1+\gamma^5}{2}\psi, \quad \gamma^5 = i\gamma^0\gamma^1\gamma^2\gamma^3, \tag{1.7}$$

where $\gamma^{0,1,2,3}$ are the Dirac matrices. Under the $SU(2)_L$ rotations, the left-handed fermions transform as doublets and the right-handed ones transform as singlets. The lepton doublet of the i^{th} generation (see Table 1.1) is defined as

$$L_{L,i} = \begin{pmatrix} \nu_i \\ l_i^- \end{pmatrix}, \tag{1.8}$$

where l_i^- stands for the electron, muon or τ and the ν_i is the corresponding neutrino.

The quark doublet is defined as

$$Q_{L,i} = \begin{pmatrix} u_i \\ d_i' \end{pmatrix}, \tag{1.9}$$

where the up quarks u_i are u, c, t and the down quarks (which are weak interaction eigenstates) are mixed: $d_i' = \sum_J V_{ij} d_j$. The d_j here stand for the physical d, s, b quarks with defined mass ("mass eigenstates") and V is the Cabibbo–Kobayashi–Maskawa mixing matrix [18, 28]. The up and down quark right-handed singlets are denoted as $u_{R,i}$ and $d_{R,i}$, respectively, and the right-handed leptons are named as $e_{R,i}$.

The EW Lagrangian is constructed as follows:

$$\begin{aligned} \mathcal{L}_{\text{EW}} = {} & \bar{Q}_L i\gamma^\mu D_\mu Q_L + \bar{u}_R i\gamma^\mu D_\mu u_R + \bar{d}_R i\gamma^\mu D_\mu d_R \\ & + \bar{L}_L i\gamma^\mu D_\mu L_L + \bar{e}_R i\gamma^\mu D_\mu e_R \\ & - \frac{1}{4} A^a_{\mu\nu} A^{\mu\nu\, a} - \frac{1}{4} B_{\mu\nu} B^{\mu\nu}, \end{aligned} \tag{1.10}$$

where

- the indices for the fermion generations are dropped,
- a bar above the symbol means that it is an adjoint spinor,
- the covariance derivatives are defined as,

$$
\begin{aligned}
D_\mu Q_L &= (\partial_\mu - igA^a_\mu \frac{\sigma^a}{2} - \frac{i}{6}g'B_\mu)Q_L, \\
D_\mu u_R &= (\partial_\mu - i\frac{2}{3}g'B_\mu)u_R, \\
D_\mu d_R &= (\partial_\mu + \frac{i}{3}g'B_\mu)u_R, \\
D_\mu L_L &= (\partial_\mu - igA^a_\mu \frac{\sigma^a}{2} + \frac{i}{2}g'B_\mu)L_L, \\
D_\mu e_R &= (\partial_\mu + g'B_\mu)u_R,
\end{aligned}
\tag{1.11}
$$

- σ^a are the Pauli matrices,
- $B_{\mu\nu}$ is the strength tensor of the field B_μ: $B_{\mu\nu} = \partial_\mu B_\nu - \partial_\nu B_\mu$,
- $A^a_{\mu\nu}$ is the strength tensor of the field A^a_μ: $A^a_{\mu\nu} = \partial_\mu A^a_\nu - \partial_\nu A^a_\mu + g'\epsilon^{abc}A^b_\mu A^c_\nu$, where ϵ^{abc} is the Levi-Civita symbol which defines the *structure constants* of $SU(2)$ and enters the algebra of the group generators: $[\frac{1}{2}\sigma^a, \frac{1}{2}\sigma^b] = \frac{1}{2}i\epsilon^{abc}\sigma^c$.

One can see from Eq. (1.11) that all the left-handed particles interact with all four gauge bosons, while the right-handed electron/muon/τ and quarks interact only with B_μ.

The basic EW interaction vertices are shown in Fig. 1.3. Note that the W, Z, γ bosons are linear combinations of the gauge A^a_μ, B_μ bosons, the relation between them will be discussed in the next section in the context of the EW boson masses.

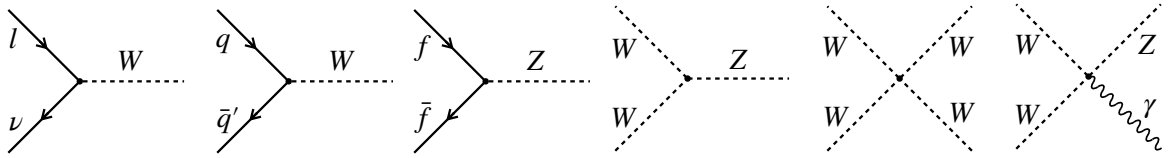

Figure 1.3: A variety of EW interaction vertices. From left to right: W boson coupling to leptons, W boson coupling to quarks, Z boson interacting with an arbitrary EW fermion, interaction vertices of the EW gauge bosons (not all of them).

Although the Standard Model assumes massless neutrinos, numerous observations of neutrino oscillations [29–31] imply that the neutrinos have small non-zero masses. The physical neutrinos are the particles with defined mass ("mass eigenstates"), but the EW Lagrangian describes neutrinos with well-defined flavour (electron, muon or τ neutrino — "flavour eigenstates"), hence, the mass eigenstates are linear combinations of the flavour eigenstates. The mixing between them is described by the Pontecorvo–Maki–Nakagawa–Sakata matrix [32, 33].

1.4 EW spontaneous symmetry breaking and the Higgs mechanism

The electroweak theory in its original form described in the previous section does not answer one fundamental question: why almost all observed particles have mass if it is not allowed by the EW theory. This inconsistency can be fixed by the Higgs mechanism [9–11], which we briefly describe below.

We start by introducing a Higgs field: a complex $SU(2)$ doublet Φ of scalar fields ϕ^+ and ϕ^0 (four components in total):

$$\Phi = \begin{pmatrix} \phi^+ \\ \phi^0 \end{pmatrix}, \tag{1.12}$$

with hypercharge $Y = 1$, coupled to itself and to the electroweak sector. If one chooses the Higgs field potential in the form

$$V(\phi) = \mu^2 \Phi^\dagger \Phi + \lambda (\Phi^\dagger \Phi)^2, \quad \lambda > 0, \tag{1.13}$$

in the case of $\mu^2 < 0$, which corresponds to a potential illustrated in Fig. 1.4, the Higgs field acquires a non-zero vacuum expectation value (VEV):

$$\langle \Phi \rangle = \frac{1}{\sqrt{2}} \begin{pmatrix} 0 \\ \upsilon \end{pmatrix}, \quad \upsilon = \sqrt{-\mu^2/\lambda}, \tag{1.14}$$

inducing the spontaneous breaking of the EW $SU(2)_L \times U(1)_Y$ gauge symmetry into the QED $U(1)_Q$ symmetry. The expression for υ in Eq. (1.14) is found through the minimisation of the potential in

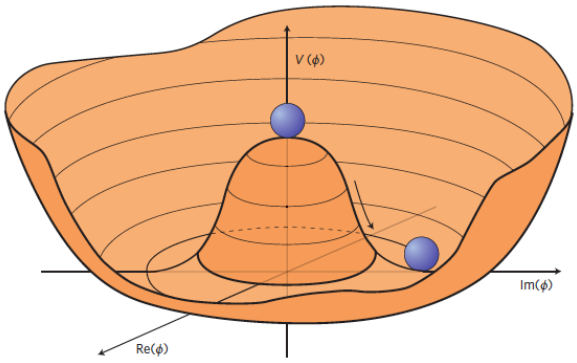

Figure 1.4: The schematic drawing of the Higgs potential in the case of $\mu^2 < 0$ and how the field (blue circle) "falls" into the minimum of the potential. Strictly speaking, this picture represents a simpler case than the one described in the text: a case of a *complex scalar* Higgs field ϕ. However, since it is problematic to depict a potential depending on all four components of a considered complex doublet Φ, this simplified illustration serves well enough for our purposes. The picture is taken from [34]

Eq. (1.13). The numerical value of υ is around 246 GeV [7].

Near the minimum of the potential the Higgs field can be expressed in a following way:

$$\Phi = \frac{1}{\sqrt{2}} \begin{pmatrix} 0 \\ \upsilon + H(x) \end{pmatrix}, \tag{1.15}$$

which means that after SSB only one component of the Higgs field $H(x)$ is left and will take part in the kinematics. In order to trace where did the other three components go, let us look at the EW Lagrangian for the Higgs field:

$$\mathcal{L} = (D_\mu \Phi)^\dagger (D^\mu \Phi) - \mu^2 \Phi^\dagger \Phi - \lambda (\Phi^\dagger \Phi)^2, \tag{1.16}$$

where the covariant derivative includes the coupling of the Higgs field to the EW gauge bosons A^a_μ and B_μ:

$$D_\mu \Phi = (\partial_\mu + i g A^a_\mu \frac{\sigma^a}{2} + \frac{i}{2} g' B_\mu)\phi. \tag{1.17}$$

One can show [5] that the SSB which allowed us to present the Higgs field in the form of Eq. (1.15) leads to appearance of three mass terms being a linear combinations of the EW gauge bosons masses and a mass term for the Higgs field itself, if we substitute Eq. (1.15) into Eq. (1.16). It is said that the EW gauge bosons "absorbed" the three components of the Higgs field and acquired masses in that way.

From the mathematical point of view, the mass terms for the EW gauge bosons come from the square of the covariant derivative. The relevant terms in the Lagrangian are:

$$\Delta\mathcal{L} = \frac{1}{2}(0\ v)\left(g A^a_\mu \frac{\sigma^a}{2} + \frac{1}{2} g' B_\mu\right)\left(g A^{b\mu} \frac{\sigma^a}{2} + \frac{1}{2} g' B^\mu\right)\begin{pmatrix}0\\ v\end{pmatrix}, \tag{1.18}$$

where one can notice the pattern $(const \cdot A \cdot A)$ or $(const \cdot B \cdot B)$ which corresponds to mass terms.

After some tensor algebra we get three massive vector fields, which correspond to the observed W and Z bosons:

$$W^\pm_\mu = \frac{1}{\sqrt{2}}(A^1_\mu \mp i A^2_\mu) \quad \text{with mass} \quad m_W = g\frac{v}{2}, \tag{1.19}$$

$$Z^0_\mu = \frac{1}{\sqrt{g^2 + g'^2}}(g A^3_\mu - g' B_\mu) \quad \text{with mass} \quad m_Z = \sqrt{g^2 + g'^2}\frac{v}{2}, \tag{1.20}$$

and one massless vector field, which corresponds to the photon

$$A_\mu = \frac{1}{\sqrt{g^2 + g'^2}}\left(g' A^3_\mu + g B_\mu\right). \tag{1.21}$$

The full covariant derivative term now looks like

$$\mathcal{L}_{\text{derivative}} = \frac{1}{2}(\partial_\mu H)(\partial^\mu H) + \left(m_W^2 W^+_\mu W^{\mu-} + \frac{1}{2} m_Z^2 Z_\mu Z^\mu\right)\left(1 + \frac{H}{v}\right), \tag{1.22}$$

and includes EW bosons mass terms, the kinematic term $\sim (\partial H)^2$ for the remaining component of the Higgs field H, which in fact corresponds to the observed Higgs boson, and the Higgs field interaction with the W and Z bosons $\sim W^2 H$, $\sim Z^2 H$.

The mass term of the Higgs boson and its self-coupling follow from the potential term in the Lagrangian Eq. (1.16):

$$\mathcal{L}_{\text{potential}} = -\frac{1}{2}(-2\mu^2)H^2 - \lambda v H^3 - \frac{\lambda}{4}H^4, \tag{1.23}$$

where the first term is the mass term of a scalar Higgs field with mass $m_H = -2\mu^2 = 2\lambda v^2$, and the second and third terms represent the three-Higgs and four-Higgs coupling. The experimental value for the Higgs boson mass $m_H = 125.10 \pm 0.14$ GeV (current average [7]) has been measured for the first time by the ATLAS and CMS Collaborations at the LHC in 2012 [3, 4].

Finally, the fermion masses can be added to the SM by introducing the Yukawa interaction of the fermions with the Higgs field (the procedure is explained in details for example here [34]). We will consider as example an arbitrary SM fermion with left- and right-handed components ψ_L and ψ_R, which couples to the Higgs field according to the following Yukawa Lagrangian:

$$\mathcal{L}_{\text{Yukawa}} = -\lambda_f\,(\bar{\psi}_L \Phi\, \psi_R + \psi_L \Phi^{\dagger} \bar{\psi}_R), \tag{1.24}$$

where λ_f is the fermion coupling to the Higgs field.

By substituting Eq. (1.15) into Eq. (1.24) we get a fermion mass term plus a remaining fermion–Higgs interaction term:

$$\mathcal{L}_{\text{Yukawa}} = -\frac{\lambda_f}{\sqrt{2}}(v+h)(\bar{\psi}_L\psi_R + \psi_L\bar{\psi}_R) = -\frac{\lambda_f v}{\sqrt{2}}\bar{\psi}\psi - \frac{\lambda_f}{\sqrt{2}}h\bar{\psi}\psi, \quad \psi \equiv \begin{pmatrix}\psi_L \\ \psi_R\end{pmatrix}, \tag{1.25}$$

with the mass of the fermion being $\lambda_f v/\sqrt{2}$.

The diagram view of all the interaction vertices for the Higgs boson couplings that we mentioned above is given in Fig. 1.5.

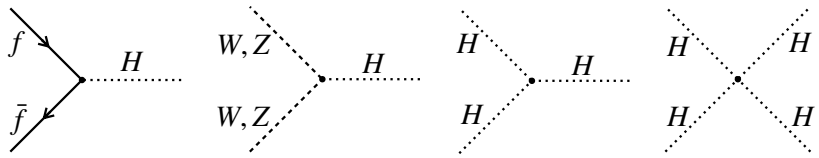

Figure 1.5: From left to right: Feynman diagrams of the fermion–Higgs coupling, the Higgs boson interaction with a W or a Z boson and three- and four-Higgs self-interaction.

2 Hadron collision event simulation

Hadron collisions which occur at the LHC involve a large number of particles. The simulations of such processes with many degrees of freedom often rely on integration in a large number of dimensions. The most common approach for these simulations is to use Monte Carlo methods: computational algorithms which use random sampling. For example, matrix element calculations involve integration in $(3n-4)$-dimensional phase space for a n-particle final state [35]. For a process producing more than two final state particles (i.e. for > 2 dimensions), numerical integration using Monte Carlo techniques converges faster than in any other calculation.

Monte Carlo event generators were designed to perform various calculations e.g. matrix elements and cross sections. The aim is to generate "events", which contain information about the properties (momenta, spins etc) of the final state particles and for which the production rate follows the probability to produce such final state according to the Standard Model.

In any general-purpose event generator, in order to simulate a high-energy-physics (HEP) proton–proton collision event one should perform several calculations: [35]

- Given initial momenta of incoming partons, determine the probability to find these partons in the two colliding protons using the *parton distribution functions* (PDFs),
- Compute the *matrix element* which describes a single interaction between two partons up to a certain order in perturbation theory, that can be computed from first principles,
- Perform the *parton showering*: add QCD emission off initial and final partons, which can be estimated using different approximations based on first principles,
- Using non-perturbative models take into account the *hadronisation* and *colour reconnection* (transition from QCD deconfinement to confinement) which cannot be derived within perturbation theory,
- Using soft-QCD models estimate effects of *multiple parton interactions* (MPI) and *underlying event* (all interactions of low-energy partons which do not take part in the hard scattering).

The cross section of $ab \to n$ scattering at a hadron collider can be factorised as follows [35]:

$$\sigma = \sum_{a,b} \int_0^1 dx_a dx_b \int d\Phi_n f_a^{h_1}(x_a, \mu_\mathrm{F}) f_b^{h_2}(x_b, \mu_\mathrm{F}) \frac{1}{2x_a x_b s} |\mathcal{M}_{ab\to n}|^2(\Phi_n; \mu_\mathrm{F}, \mu_\mathrm{R}), \tag{2.1}$$

where

- $f^h_{a(b)}(x_{a(b)}, \mu_F)$ is the PDF, it depends on the momentum fraction $x_{a(b)}$ of parton $a(b)$ with respect to its parent hadron of type h, and on the factorisation scale μ_F [1],

- s is the hadronic centre-of-mass energy squared,

- $\mathcal{M}_{ab\to n}$ is the matrix element of the hard scattering, which depends in particular on a phase space, Φ_n, and on the renormalisation[2] and factorisation scales $\mu_{R,F}$.

- $d\Phi_n$ is the differential phase space element of n final-state particles:

$$d\Phi_n = \prod_{i=1}^{n} \frac{d^3 p_i}{(2\pi)^3 2E_i} \cdot (2\pi)^4 \delta^{(4)}(p_a + p_b - \sum_{i=1}^{n} p_i), \tag{2.2}$$

  where E_i and p_i are the energy and momentum of the i-th particle and $p_{a,b}$ are the momenta of the initial-state particles.

In the following sections, each step of the HEP event simulation will be described in more details.

2.1 Parton distribution functions

Parton distribution functions play a central role in event generators for simulation of the hadron collision events, since they define the internal parton content of the proton and hence directly influence the event rate. The PDF $f_i(x, \mu_F)$ defines a probability to find a parton i with a momentum fraction x when a proton is probed at a factorisation scale μ_F. The underlying physics describing a proton wave function is non-perturbative, therefore the PDFs cannot be found from first principles. However, the evolution of PDFs (from a low scale μ_{F0} towards larger scales) is described by the DGLAP[3] [36–38] equations.

Several collaborations (ABKM [39], CTEQ [40], GJR [41], HERA [42], MSTW [43], NNPDF [44]) elaborate various tunes by comparing the predictions from the DGLAP equations with data from deeply inelastic electron–proton, proton–proton and proton–antiproton scatterings. Their results are presented in a form of PDF sets in the LHAPDF library [45] accessed now by all Monte–Carlo generators.

[1] The factorisation scale μ_F is an energy scale at which the QCD interaction is factorised into low-energy effects (at energies below μ_F) described by the evolution of PDFs and high-energy effects (at energies above μ_F) described by perturbative QCD.

[2] The renormalisation scale μ_R is an energy scale at which the renormalisation of QCD is done and the strong coupling constant α_S is evaluated.

[3] DGLAP = Dokshitzer–Gribov–Lipatov–Altarelli–Parisi

2.2 Matrix element

The hard scattering between the partons occurs at the strong coupling constant $\alpha_S < 1$[4] which allows to use perturbation theory and expand the scattering amplitude $\mathcal{M}_{ab\to n}$ in powers of α_S. By cutting the expansion at a certain order one gets a certain *fixed order calculation* of the matrix element:

- *Leading-order* (LO) calculation contains tree-level amplitudes,
- *Next-to-leading order* (NLO) calculation includes tree-level and one-loop amplitudes (plus possibly an extra emission)
- By adding an extra loop to the corresponding Feynman diagram one goes to the next order of calculation (NNLO, that is *next-to-next-to-leading order*).

Modern event generators are able to compute a majority of the processes at NLO and some selected processes at NNLO.

Although for the hard (large-angle) scattering perturbation theory allows to cut the expansion at a fixed order, there are regions of phase space in which higher-order terms are enhanced and should be taken into account. These include soft region, when a low-energy gluon is emitted, and collinear region, when a parton splits into two almost collinear ones. In a soft or collinear region one is confronted with large logarithmic terms: logarithms of ratios of terms that include the interaction scale over the cut-off scale. The computation of such logarithmic terms in the soft and collinear regions, where these terms are large and cannot be neglected, is only possible within the parton shower approximation, which is defined in the next section.

2.3 Parton shower modelling

A parton shower represents an approximate perturbative treatment of QCD dynamics at momentum scales greater than some infra-red cut-off value, typically taken to be of the order of 1 GeV^2, under which the hadronisation (hadron formation due to QCD confinement) happens [46]. The shower evolves in a cascade-like manner (until the momenta of the partons in the shower reach the cut-off), with generation of a large number of partons due to soft/collinear QCD emission.

In order to understand the parton shower approach let us consider a final state of n partons produced in a certain hard (LO) process. A shower formation starts when one of the partons (parton i) emits almost collinearly a parton j. The calculation of the parton shower is based on a factorisation property of the resulting n+1-particle state: the n+1-particle cross section can be expressed as a product of the n-particle cross section, one-particle phase space and a splitting function. Knowing the total

[4] The reasoning can be repeated in the same way for an electroweak process, occurring at electromagnetic and weak coupling constants $\alpha_{EM}, \alpha_W < 1$.

cross section of a LO process σ_n one can find the corresponding differential NLO cross section in the collinear limit as follows:

$$d\sigma^j_{n+1} \approx \sigma_n \sum_{\text{emitter } i} \frac{\alpha_S}{2\pi} \frac{d\theta_{ji}}{\theta_{ji}} dz_{ji} P_{ji}(z_{ji}, \phi_{ji}) \tag{2.3}$$

where

- j is a collinear parton with energy fraction z_{ji} w.r.t the emitter i; z is also called a *splitting variable*.
- ϕ_{ji} is the azimuth of j around the i-axis.
- θ_{ji} is emission angle between i and j, it serves also as an *evolution variable*: a variable which we use to parametrise the phase space.

  Instead of the emission angle θ a different evolution variable can be chosen: $q^2 = z(1-z)E^2\theta^2$ (the virtuality[5] of the off-shell emitter with energy E), $k_\perp^2 = z^2(1-z)^2E^2\theta^2$ (the emitted parton's transverse momentum w.r.t. the emitter) or $\tilde{q}^2 = E^2\theta^2$ (another angular variable, corresponding to the so-called $\tilde{q}$ shower). For all these variables the calculation in the collinear limit is the same, whereas the extrapolation beyond this limit depends on the choice of the variable.
- $P_{ji}(z_{ji}, \phi_{ji})$ is a spin-dependent *splitting function* (kernel), which describes the distribution of the energy fraction z_{ji} and which is enhanced for $z_{ji} = 0$ or $z_{ji} = 1$ depending on the type of splitting.

  By neglecting spin correlations one can introduce spin-averaged splitting functions $P_{ji}(z_{ji})$, which are also the ones appearing in the DGLAP equations for PDF and which explicit form at the lowest order can be computed directly from QCD [36]:

$$P_{qg}(z) = \frac{4}{3}\frac{1+z^2}{1-z}, \tag{2.4}$$

$$P_{gg}(z) = \frac{6(1-z(1-z))^2}{z(1-z)}, \tag{2.5}$$

$$P_{gq}(z) = \frac{1}{2}(z^2 + (1-z)^2). \tag{2.6}$$

Given the factorisation formula for the n+1-particle cross section Eq. (2.3), by iterating one can generate multiple emissions off the n-particle state, n+1-particle state and so on.

Up to now, we have focused only on the collinear-enhanced real parton emissions, but there are also other effects of the same order in perturbation theory, virtual loop corrections, which can be

[5] The virtuality q^2 of the particle equals $q^2 = -p^2$ where p is 4-momentum of the particle

also included in the parton shower approximation. To estimate these corrections, let us introduce a probability $\Delta_i(Q^2, q^2)$ that parton i does not split between two scales, Q^2 and $q^2 < Q^2$:

$$\Delta_i(Q^2, q^2) = \exp\left[-\int_{q^2}^{Q^2} \frac{\alpha_S}{2\pi}\frac{dk^2}{k^2} \int_{1-Q_0^2/k^2}^{Q_0^2/k^2} dz P_{ji}(z)\right], \tag{2.7}$$

where, k is some evolution variable, Q_0^2 is a shower cut-off and z is the splitting variable. The emission corresponding to $k > Q_0$ is finite and *resolvable* (meaning, it is included in the parton shower) and the one with $k < Q_0$ is either too soft or at too small angle (*non-resolvable*, not included in the shower). Then, the total contribution of the non-resolvable emission (a probability that no splittings at all will occur from the initial scale Q^2 until the shower cut-off scale Q_0) is given by $\Delta_i(Q^2, Q_0^2)$, which is called a *Sudakov form factor* and which represents a divergent loop correction of the hard process:

$$\Delta_i(Q^2, Q_0^2) = \exp\left[-\int_{Q_0^2}^{Q^2} \frac{\alpha_S}{2\pi}\frac{dk^2}{k^2} \int_{1-Q_0^2/k^2}^{Q_0^2/k^2} dz P_{ji}(z)\right] \sim \exp\left[-\frac{4}{3}\frac{\alpha_S}{2\pi}\log^2\frac{Q^2}{Q_0^2}\right]. \tag{2.8}$$

Now, let us turn back to the parton shower. In order to construct a shower model, one needs to define:

- an *evolution variable*,
- a *splitting variable* z
- a shower starting scale Q, which is the momentum transferred from the hard process.

The main requirement imposed on all the parton shower algorithms is the ability to take into account the colour coherence of soft gluons. This property can be seen from the following example [35]: we want to calculate an amplitude of a process in which a quark emits a hard gluon (at high-energy and small angle) and a soft gluon (at low-energy and wide-angle). The amplitude is calculated as a coherent sum of the amplitudes in which the soft gluon is attached to each of the external partons (see Fig. 2.1).

Figure 2.1: Soft gluon coherence: the sum of the diagrams in which the soft gluon (waved line) is emitted from any of the external partons (left diagram) is equivalent to the diagram where the soft gluon is emitted strictly before the hard gluon (right diagram). The figure is taken from [35].

Due to the destructive interference between such diagrams the resulting amplitude is identical to the amplitude of a process in which the softer emission happened *before* the harder one.

This effect is called colour coherence because a soft gluon is not able to resolve the details of the colour line that emits it, in this situation there is no difference between emission by a single parton or by a bundle of collinear partons, they act as a coherent coloured object.

By generalising the last example to several emissions we can see that the colour coherence enforces the harder gluons to be emitted at successively smaller opening angles, since from Fig. 2.1, effectively, any softer emission (at wider angle) always happens before any harder emission (at smaller angle). From the Monte–Carlo point of view, one of the solutions to achieve this is to introduce explicit *angular ordering* (first time done in [47]) of the shower. In this approach, the emissions are ordered by the angle θ between the emitter and the emitted collinear parton. Later, this formalism was updated by introducing an angular variable related to the transverse momentum [48–51]. The new formalism allows to improve the Lorentz invariance of the evolution, to simplify the coverage of the phase space while the direct angular ordering is kept and to achieve a better treatment of heavy quark fragmentation. Such a shower with $\tilde{q}^2 = E^2\theta^2$ (where E is the energy of the emitter) as an evolution variable is called a $\tilde{q}$-shower.

One of the drawbacks of angular-ordered showers is the impossibility to have a transverse momentum or virtuality as ordering variable, since in this case one would have to manually veto any emission that is larger in angle than the previous one. However, the transverse momentum or virtuality is a better choice for the matching of the shower to the matrix element. Indeed, in this case the hardest emission is generated first and as a result the matrix element corrections are simpler to implement, whereas for the angular-ordered showers where the first emission is not the hardest one would need to manually truncate the shower (see the next section).

However, the *dipole shower* [52] based on so-called Catani–Seymour colour dipoles and subtraction kernels [53] overcomes this restriction and allows to have a transverse momentum as ordering variable. The Catani–Seymour approach assumes 2→3 splittings: the emission originates from a colour dipole instead of a single parton. Because of an additional colour-connected parton as momentum-balancing third party, colour coherence enters naturally and one does not have to enforce it through explicit angular ordering.

2.4 Matching a matrix element to a parton shower

As it was shown before, fixed-order matrix elements are good in describing hard parton scattering, but not soft and collinear emission; on the other hand, the parton shower approximation allows to make calculations in the soft/collinear region but gives a poor approximation at wide scattering angles. Clearly, to have a good description of an arbitrary partonic state, one needs to combine these two approaches.

However, there is no factorisation theorem that would allow to unambiguously separate the cross section of the event into a matrix element of the hard process and the subsequent parton shower. For a multi-jet event it becomes difficult to determine, which component of the event belongs to the hard process and which to the parton shower. For example, a $(n+1)$-jet event can be produced in two ways: from the $(n+1)$-parton state which was emitting soft/collinear radiation or from a n-parton state which has emitted a hard, wide-angle emission which evolved into an extra jet.

Therefore, when one invents a factorisation prescription (how to separate a matrix element from a parton shower), which is also called a *matching scheme*, one should define which of the two paths holds for each event. The main risk which a matching scheme should avoid is the double counting in some regions of phase space since the same logarithmic terms get included in both, a matrix element and a parton shower. An illustrative example of such double counting for e^+e^- process is shown in Fig. 2.2: if one blindly sums the terms given by the parton shower (filled circles in the subfigure (a)) to the ones from the matrix element (filled circles in the subfigure (b)), some of the largest logarithms are added twice.

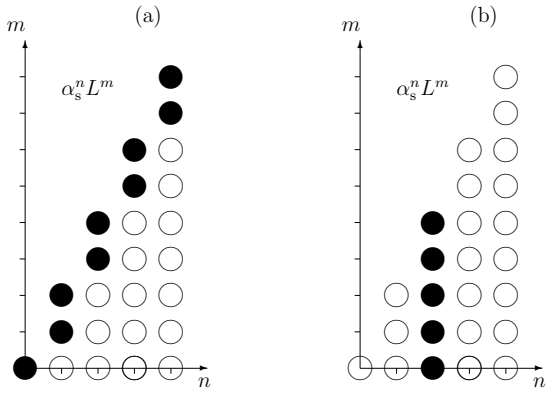

Figure 2.2: Pictorial view of the α_S-expansion terms of the $e^+e^- \to jets$ cross section. Each circle represents a term of the expansion $\alpha_S^n L^m$, with a logarithmic term $L^m = \log(Q_{cm}/Q_{jet})^m$ depending on the jet resolution scale Q_{jet} and the scale Q_{cm} of the order of the invariant mass of the system. The terms included in a next-to-leading-log parton shower are shown as filled circles in (a); the terms included in the tree-level matrix element are shown as filled circles in (b). Figure taken from [35].

There are several matching procedures developed during the past several decades:

- Tree-level matching [54]: including the $\alpha_S^1 L_0$ term (see Fig. 2.2) but only in the real emission
- NLO matching: taking into account the full effect of $\alpha_S^1 L_0$ in the real and virtual contributions [55–57]
- Multi-jet merging at LO and NLO: various ways of including the higher logarithmic terms in the parton shower and the higher order terms in the real emission [58–60].

Now, we will concentrate on the NLO matching (that also includes tree-level matching as first step), which is currently used in Monte-Carlo generators like Herwig 7.

We start from an inclusive NLO cross section which can be written in the following general form: [35]:

$$\begin{aligned} d\sigma^{NLO} = d\Phi_0 \left[B(\Phi_0) + \alpha_S V_1(\Phi_0) + \alpha_S \int d\Phi_{1|0} S_1(\Phi_1) \right] \\ + d\Phi_1 \left[\alpha_S R_1(\Phi_1) - \alpha_S S_1(\Phi_1) \right], \end{aligned} \tag{2.9}$$

where

- Φ_0 and $B(\Phi_0)$ are the Born-level phase space and tree-level matrix element,
- Φ_1 and $\alpha_S R_1(\Phi_1)$ are the real-emission phase space and tree-level matrix element,
- The $\alpha_S V_1(\Phi_0)$ term contains the loop contribution,
- $\alpha_S S_1(\Phi_1)$ is the subtraction term, which is integrated over the one-particle phase-space element $\Phi_{1|0}$ and is introduced to regularise the loop correction and real-emission terms and make the whole expression finite.

By splitting the real-emission term in the singular and non-singular parts $R_1(\Phi_1) = R_1^s(\Phi_1) + R_1^{ns}(\Phi_1)$ [6] and by adding the singular part to the Born-level part we get

$$d\sigma^{NLO} = d\Phi_0 \bar{B}(\Phi_0) + d\Phi_1 \alpha_S R_1^{ns}(\Phi_1), \tag{2.10}$$

where $\bar{B}(\Phi_0)$ is the NLO-weighted Born-level term with the singular terms integrated out:

$$\begin{aligned}\bar{B}(\Phi_0) = B(\Phi_0) + \alpha_S V_1(\Phi_0) + \alpha_S \int d\Phi_{1|0} S_1(\Phi_1) \\ + \alpha_S \int d\Phi_{1|0} \left[R_1^s(\Phi_1) - S_1(\Phi_1)\right].\end{aligned} \tag{2.11}$$

The inclusive cross section with first parton shower emission included can be represented as follows:

$$d\sigma^{PS} = d\Phi_0 B(\Phi_0) \left[\Delta(Q^2, Q_0^2) + \int_{Q_0^2} \frac{dq^2}{q^2} \int dz \frac{\alpha_S}{2\pi} P(z) \Delta(Q^2, q^2)\right], \tag{2.12}$$

where q^2 is chosen as an ordering/evolution variable of the shower, Δ is a Sudakov form-factor and Q^2 and Q_0^2 are the starting and the cut-off scales, respectively.

Then, the first matching procedure consists in substituting the singular part of the real-emission correction for the splitting function into Eq. (2.12):

$$\frac{dq^2}{q^2} dz \frac{\alpha_S}{2\pi} P(z) \rightsquigarrow d\Phi_{1|0} \frac{R_1^s(\Phi_1)}{B(\Phi_0)}. \tag{2.13}$$

Note that this substitution takes place also in the expression of the Sudakov form factor Eq. (2.8) (let us denote it as $\bar{\Delta}$ after the replacement has been applied).

The inclusive cross section now takes the form

$$\begin{aligned}d\sigma^{PScorr} = d\Phi_0 B(\Phi_0) \left[\bar{\Delta}(Q^2, Q_0^2) + \int d\Phi_{1|0(>Q_0^2)} \alpha_S \frac{R_1^s(\Phi_1)}{B(\Phi_0)} \bar{\Delta}(Q^2, q^2)\right] \\ + d\Phi_1 \alpha_S R_1^{ns}(\Phi_1),\end{aligned} \tag{2.14}$$

where the real emission term weighted by the Sudakov form factor gives higher-order $\alpha_S^n L^{2n}$ and $\alpha_S^n L^{2n-1}$ terms (see their illustration in Fig. 2.2). Then, the rest of the parton shower emission will be represented as all the higher-logarithmic terms.

[6] The splitting into R_1^s and R_1^{ns} is in principle arbitrary as long as the divergent terms are fully contained in R_1^s. We will use this possibility of arbitrary splitting later.

The second step consists in getting $O(\alpha_S)$ accuracy in the cross section. There are two approaches here: the subtractive (based on MC@NLO[7] [55, 56]) and the multiplicative (based on POWHEG[8] [57]) schemes.

The POWHEG approach works as a reweighting procedure (that is why it is called multiplicative): the Born-level matrix element is replaced by the NLO weighted Born-level term in Eq. (2.14) and also the whole real-emission term is taken as its singular part, so that $R_1^{\text{ns}} = 0$: [6]

$$d\sigma^{\text{POWHEG}} = d\Phi_0 \bar{B}(\Phi_0) \left[\bar{\Delta}(Q^2, Q_0^2) + \int d\Phi_{1|0(>Q_0^2)} \alpha_S \frac{R_1(\Phi_1)}{B(\Phi_0)} \bar{\Delta}(Q^2, q^2) \right]. \tag{2.15}$$

The first POWHEG emission included in Eq. (2.15) and being calculated with full NLO accuracy is supposed to be the hardest one. Then, in order to make sure that all the following shower emissions will be softer than the first one, ideally, we need a shower which is ordered in hardness, that is a dipole shower (remember, it has a transverse momentum as ordering variable). On the contrary, if the parton shower is an angular-ordered one (e.g. $\tilde{q}$-shower), not ordered in hardness, one cannot just start it after the POWHEG emission, but one needs to rearrange the whole structure. First, we determine the angular shower variables (q_1^2, z_1) corresponding to the POWHEG emission. Then, we evolve the shower starting from the Born state at the scale Q^2 down to q_1^2 while vetoing all the emissions which are harder than the POWHEG emission. After that we put in the POWHEG emission at the scale q_1^2 and then let the shower evolve further down to the cut-off scale Q_0^2, continuing to veto all the emission harder than the first one. By such a procedure we get a so-called truncated, vetoed shower.

The main idea of the second scheme, MC@NLO is to take the singular terms R_1^s to be identical to the subtraction terms S_1 [6] (that is why this matching is called subtractive) in Eq. (2.11). Because of the replacement Eq. (2.13), Eq. (2.11) can be now expressed as a convolution of the Born term and the splitting function $S_1 = B \otimes P$[10]:

$$\begin{aligned} d\sigma^{\text{MC@NLO}} = d\Phi_0 &\left[B(\Phi_0) + \alpha_S V_1(\Phi_0) + \alpha_S B(\Phi_0) \otimes \int d\Phi_{1|0} P(\Phi_{1|0}) \right] \\ &\times \left[\Delta(Q^2, Q_0^2) + \int_{Q_0^2} \frac{dq^2}{q^2} \int dz \frac{\alpha_S}{2\pi} P(z) \Delta(Q^2, q^2) \right] \\ &+ d\Phi_1 \alpha_S \left[R_1(\Phi_1) - B(\Phi_0) \otimes P(\Phi_{1|0}) \right]. \end{aligned} \tag{2.16}$$

In this case, there are two sets of events to which the parton shower is added afterwards: $\mathbb{S}$-events which contain Born-level states (the first term $d\Phi_0[\dots] \times [\dots]$ in Eq. (2.16)) and $\mathbb{H}$-events containing one extra parton (the second term $d\Phi_1 \alpha_S [\dots]$ in Eq. (2.16)). In this approach a $O(\alpha_S)$ contribution of the parton shower is replaced by an exact NLO result. The MC@NLO scheme is equivalent to the POWHEG one at $O(\alpha_S)$ level, although for MC@NLO the weights of the generated $\mathbb{H}$-event states are not guaranteed to be positive (the bracket in the second term of Eq. (2.16) can turn negative).

[7] MC@NLO = Monte Carlo at NLO accuracy

[8] POWHEG = POsitive Weight Hardest Emission Generator

[10] The convolution of functions f and g is defined as $(f \otimes g)(x) = \int f(y) g(x - y) dy$

2.5 Hadronisation

The hadronisation process is a non-perturbative transition from a partonic final state to a hadronic final state. Two common phenomenological hadronisation models exist: the string [61, 62] and the cluster [63, 64] models. The main difference between them is that in the string model partons transform directly into hadrons and in the cluster model there is an intermediate stage when the partons form cluster objects with a few GeV mass.

The most complex and well-known string fragmentation model is the Lund one [62] and it is mainly used by PYTHIA. An example of hadron production from a $q\overline{q}$ pair is illustrated on Fig. 2.3 [35].

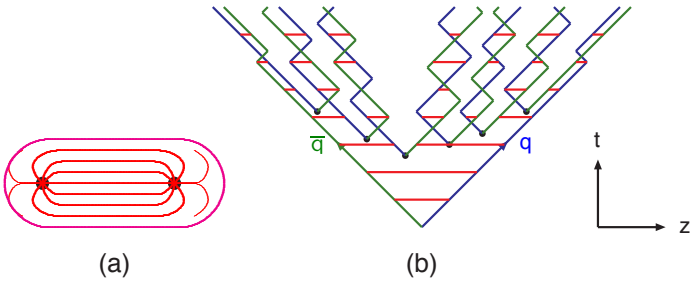

Figure 2.3: (a) A colour flux tube between a quark and an antiquark. (b) The motion and breakup of a string system along the z coordinate with time t; diagonal lines represent quarks/antiquarks, horizontal lines show the composition of the string system at a certain moment of time. Figure taken from [35].

With time, as partons move apart, a colour tube between the two partons (representing the gluons) gets stretched and the confinement potential rises linearly until the string breaks with a new $q'\overline{q}'$ pair created in the middle. If the energy of the string allows, more $q\overline{q}$ pairs will be created in a same manner. In the end, one gets a set of hadrons, each formed by a quark from one break and an antiquark from an adjacent break.

The advantage of the string model is its collinear and infrared safety: the effect on the string motion caused by emitted soft/collinear gluon is so small that it can be neglected. This makes the hadronisation process also less dependent on the parton shower cut-off.

The main issue of the string model is that a lot of the parameters describing the flavour properties cannot be determined from anywhere but from the data. Another drawback is that the string model is based on fragmentation of a single isolated string, that is, several simultaneously produced strings will evolve and break independently. Then, the collective phenomena such as rescattering between hadrons are not taken into account.

The cluster hadronisation model, used by HERWIG, is based on a preconfinement property of perturbative QCD [65] which predicts a formation of the colour-singlet parton clusters with a universal invariant mass distribution (depending only on the shower evolution and QCD scales). Since clusters are formed at low scales, the heavy flavour production is suppressed. The hadronisation starts with a $g \to q\overline{q}$ splitting and then the clusters are created from the colour-connected $q\overline{q}$ pairs. The subsequent cluster-hadrons transition mostly happens through the quasi-two-body sequential phase-space decay:

cluster decays into two less excited states (which decay further into two even less excited states and so on) with three-body and rescattering effects neglected.

The basic cluster model has the same weakness as the string model, namely, it does not take into account interaction between clusters. This issue can be partially solved by including a scheme of colour reconnection between the clusters. The main advantage of the cluster model over the string model is a smaller number of parameters, although in some cases (e.g. when combined with angular-ordered shower) the string model describes data slightly better.

2.6 Soft QCD and underlying event

Let us settle the terminology used for describing the various soft QCD sub-processes taking place simultaneously with the hard scattering during the HEP event:

- **Elastic and inelastic scattering.** Elastic scattering includes all reactions of the type: $A(p_A)B(p_B) \to A(p'_A)B(p'_B)$. Inelastic scattering covers everything else ($AB \to X \neq AB$) and can be further divided into diffractive (single-, double- and central) and non-diffractive topologies.

- **Minimum bias events:** class of the events that are selected with the minimum possible selection bias, so that they are as inclusive as possible.

- **Underlying event:** all additional low-energy interactions accompanying the hard scattering. Underlying event is defined after all bremsstrahlung off the hard interaction has already been taken into account.

  For many generators, such as Herwig, Pythia and Sherpa [66] the simulation of the underlying event physics is based on phenomenological models for hard and soft multiple partonic interaction (MPI) [67]. For example, in [68] it is described how the free parameters of the Herwig++ MPI model are tuned to describe the underlying event data. The main underlying event observables which are used to tune the MPI model are the number of the charged particles and the sum of the particle transverse momenta.

- **Multiple parton interactions (MPI):** effect of more than one pair of parton interacting in a hadron–hadron collision.

  The main observable consequence of inclusion MPI into Monte–Carlo is the possibility of having several hard parton–parton interactions in the same hadron–hadron event. The corresponding jets mostly form back-to-back pairs, contrary to the bremsstrahlung jets collinear to the partons from which they were produced. The current models of MPI (for example, the eikonal model [69] used by Herwig) mostly evolve from the perturbative model proposed in [70], based on a single parton–parton scattering process and its variations. The hard interactions are modelled as hard QCD $2 \to 2$ scatterings with a transverse momentum above the minimum cut-off value $p_\perp^{\min}$. In the low-momentum region $0 < p_\perp < p_\perp^{\min}$, soft scatterings occur with a transverse momentum distributed as a Gaussian, which should be matched at $p_\perp = p_\perp^{\min}$ with the $p_\perp$ distribution in the hard region.

The number of multiple interactions is regulated by colour screening and saturation effects.

In order to be more realistic, the MPI models should be extended in order to include perturbative rescattering effects, showering and decorrelation of MPI jets, and colour correlations and reconnections, but not all of the effects are available in the current models.

The main parameters of the majority of eikonal models are the $p_{\perp}^{\min}$ perturbative cut-off, the collision energy dependence of this cut-off (the parameters of the corresponding function), the distribution of the hadronic matter and the parameters of the models describing the colour reconnection of strings or clusters (depending on the chosen hadronisation model) [71].

The MPI models are tuned using minimum bias and underlying event data from hadron colliders at different collider energies.

- **Colour reconnection** is a mechanism that describes non-trivial and non-linear interactions/correlations of colour charges which occur during hadronisation [72] in the regions with parton high density (formed in multi-parton interactions, parton showers and coming from beam remnants). These non-linear interactions, especially between different MPI systems, are the most poorly understood part of the MPI-based models and they are giving significant uncertainties.

  First study on colour reconnections was done by Gustafson, Pettersson and Zerwas (GPZ) [73] using hadronic WW LEP events. In their model, the effects of the colour interference and gluon exchange taking place between two W systems at the perturbative level lead to significant uncertainty in the W mass determination. Next attempts were made by Sjöstrand and Khoze (SK) [74, 75] who considered that the colour reconnection happens non-perturbatively during QCD string interaction. This model predicted much smaller W mass uncertainty (~40 MeV).

  Then, several other models have been developed, the most known are the Lund model, based on QCD dipoles [76], and the Webber model, based on clusters [77].

  Further processing of the LEP data allowed to exclude the first most crude models (such as GPZ and SK) but still it was not enough. For example, the presence of the colour fields with wavelengths ~1 GeV (confinement scale), which affect the colour neutralisation process (formation of neutrally coloured objects i.e. hadrons) [78], could not be constrained by using only the LEP data.

  The inclusion of the minimum-bias and underlying event data from LHC and Tevatron triggered the emergence of a new generation of the colour reconnection models [79, 80] and tunes [81]. They are now able to describe much better, for example, the distributions of the mean transverse momentum of charged particles as a function of the number of charged particles.

- **The diffractive processes** are also not usually covered by MPI models but they can be separately described by non-perturbative models. These include, for example, the *pomeron model* [82] which postulates that the total cross section is derived from the exchange of "reggeons" and "pomerons": colour-singlet fluctuations consisting mostly of quarks/antiquarks and gluons, respectively. In this description, the diffractive processes are modelled as partonic collisions between pomeron fluctuations.

3 The ATLAS experiment at the Large Hadron Collider

The Large Hadron Collider[83] and its detectors are built at the CERN[1] laboratory complex which is now referred to as the European Laboratory for Particle Physics. CERN, located on the Franco-Swiss border near Geneva, was founded in 1954 by 12 member states and currently includes 23 member states from all over the Europe and beyond. CERN's main area of research is particle physics and it includes a large accelerator complex and many particle detectors.

3.1 The Large Hadron Collider

The Large Hadron Collider is a circular particle accelerator with a circumference of 26.7 km located about a hundred metres underground. It was designed to collide proton beams with a centre-of-mass energy of 14 TeV and heavy ion (Pb) beams with an energy of 2.8 TeV per nucleon. However, up to now, the maximum centre-of-mass energy achieved was 13 TeV in proton collisions and 2.56 TeV per nucleon in heavy ion collision.

The protons which collide in the LHC are obtained by stripping electrons from hydrogen atoms. First, protons are accelerated to 50 MeV (which corresponds to $\beta \approx 5\%$[2]) in a linear accelerator called the LINAC 2. After the LINAC 2, in the Proton Synchrotron Booster (PSB) protons are accelerated to 1.4 GeV ($\beta \approx 83\%$) and then to 25 GeV ($\beta \approx 99.9\%$) in the Proton Synchrotron (PS). The PSB has a radius of 25 meters and it became operational in 1972. The PS with 628 metres in circumference is the CERN's first synchrotron, which began its operation in 1959. After the PS, protons are sent to the 7-km-long Super Proton Synchrotron (SPS), where they are accelerated to 450 GeV ($\beta \approx 99.9998\%$).

The SPS, commissioned in 1976, has a long history. From 1981 to 1991, the SPS was called S$p\bar{p}$S since it served as a proton-antiproton collider and in 1983, the UA1 and UA2 experiments which analysed data delivered by the S$p\bar{p}$S have discovered the W and Z bosons. Between 1989 and 2000, the SPS has been injecting electrons and positrons to the Large Electron–Positron Collider (LEP). Now, as the LHC is using the LEP tunnel, the SPS continues to be the final injector of the acceleration complex. The last acceleration stage happens in the LHC where two beams, one in clockwise and a second in anticlockwise direction, are accelerated for 20 minutes to 6.5 TeV ($\beta \approx 99.999999\%$).

An overview of the CERN accelerator complex is shown in Fig. 3.1.

[1] CERN stands for the "Centre Européen pour la Recherche Nucléaire" in French

[2] β is a speed expressed as a fraction of the speed of light

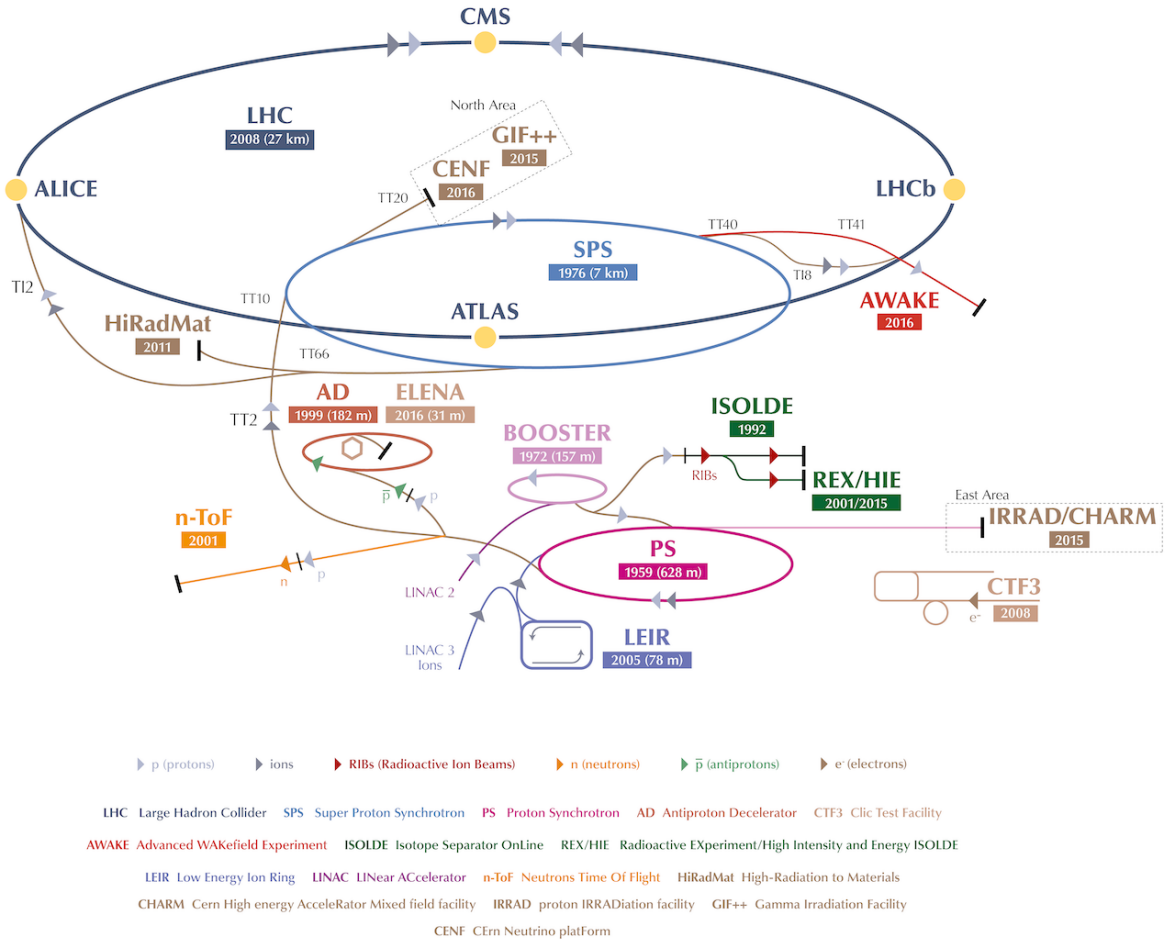

Figure 3.1: The CERN accelerator complex [84].

The collisions of bunches with 10^{11} protons at the LHC happen every 25 ns which corresponds to a rate of 40 MHz. The bunch spacing of 25 ns is the design value, although in the first two years of operation it was 50 ns.

The event rate of the LHC collisions for a particular process with a cross section σ is given by

$$\frac{dN}{dt} = \mathcal{L}\sigma, \tag{3.1}$$

where $\mathcal{L}$ is the machine *instantaneous luminosity*, which can be expressed in terms of the beam parameters:

$$L = \frac{N_b^2 n_b f_{rev} \gamma_r}{4\pi\epsilon_n \beta^*} F, \tag{3.2}$$

with the number of particles per bunch N_b, the number of bunches per beam n_b, the revolution frequency f_{rev}, the relativistic gamma factor γ_r, the normalised transverse beam emittance ϵ_n, the beta function at the collision point β^*, and the geometric luminosity reduction factor F due to the crossing angle at the interaction point.

Two general purpose detectors, ATLAS and CMS are located around the LHC. In 2018, LHC has set a record for the instantaneous luminosity delivered to ATLAS in proton-proton collisions (2.1×10^{34} cm^{-2}s^{-1}) which is even higher than the design value of 10^{34} cm^{-2}s^{-1}.

The integral of the instantaneous luminosity over time T is called the integrated luminosity:

$$L = \int_0^T \mathcal{L}(t)dt. \tag{3.3}$$

The integrated luminosity as a function of time is shown in Fig. 3.2. ATLAS records not all the data delivered by LHC (see the different labels in the plot) because of the detector inefficiencies and dead times.

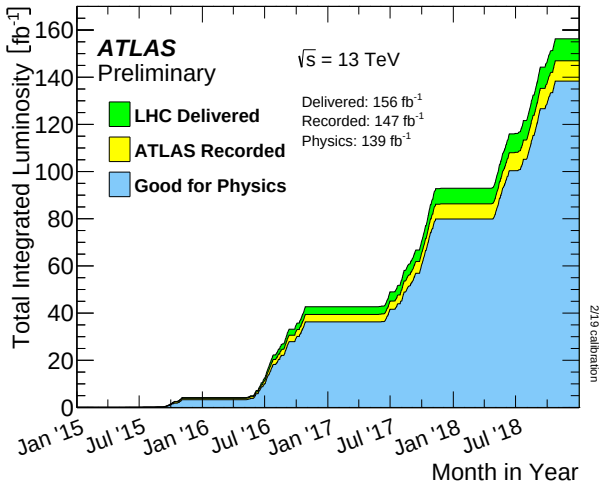

Figure 3.2: Cumulative luminosity versus time delivered to ATLAS (green), recorded by ATLAS (yellow), and certified to be good quality data (blue) during stable beams for pp collisions at 13 TeV centre-of-mass energy in 2015–2018 [85].

Until now, there have been two operational runs at the LHC: Run 1 in 2009–2013 (during which the Higgs boson was discovered) and Run 2 in 2015–2018. The centre-of-mass energy of the beams was 7–8 TeV in Run 1 and 13 TeV in Run 2. In the next running period, Run 3, which is scheduled to start around in 2021, the operational energy may finally reach the design energy 14 TeV.

3.2 The ATLAS detector

A Toroidal **L**HC **A**pparatu**S** (ATLAS) is one of the two general purpose detectors at the LHC (the other one is CMS) built to probe proton-proton and ion-ion collisions [86].

The ATLAS detector is designed to perform precise measurements of the Standard Model parameters, top quark physics, Higgs boson physics (initially, the search for the Higgs boson) and also searches for New Physics.

The ATLAS detector has a forward-backward symmetric cylindrical geometry and it covers almost 4π in solid angle.

An overall schematic picture of the detector is given in Fig. 3.3 and its main performance goals are listed in Table 3.1.

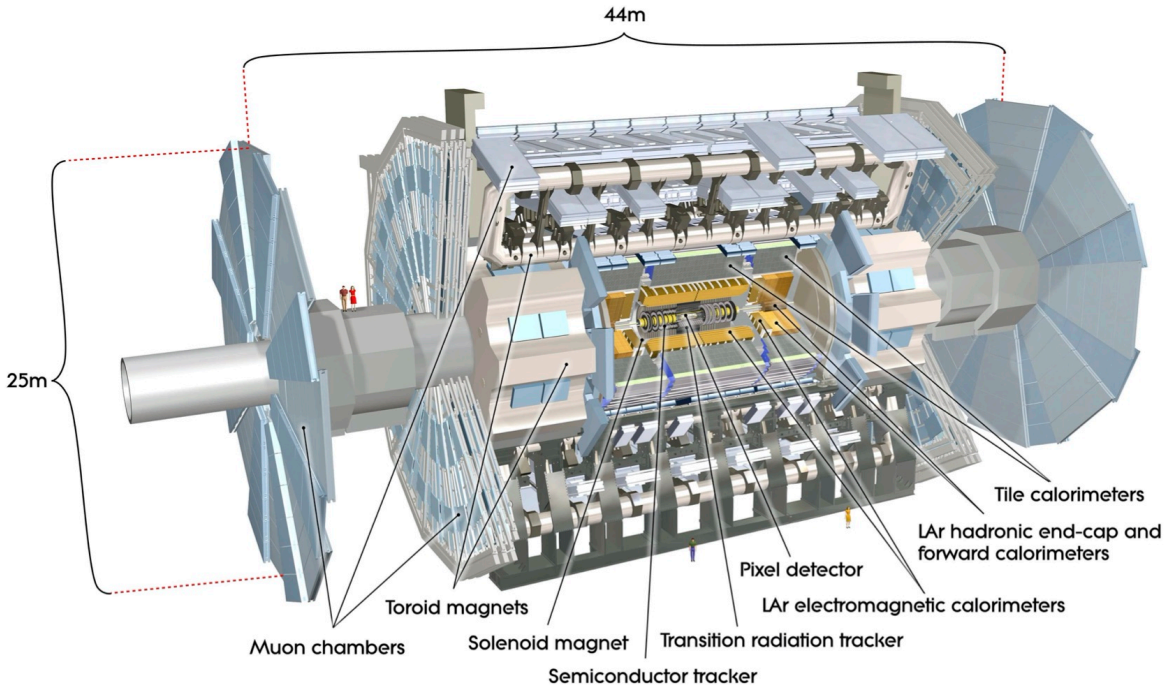

Figure 3.3: Cut-away view of the ATLAS detector [87], which is 25 m in height, 44 m in length and weights ~7000 tonnes.

Detector component	Required resolution	η coverage	
		Measurement	Trigger
Tracking	$\sigma_{p_T}/p_T = 0.05\% p_T \oplus 1\%$	± 2.5	
Electromagnetic calorimeter	$\sigma_E/E = 10\%/\sqrt{E} \oplus 0.7\%$	± 3.2	± 2.5
Hadronic calorimetry (jets)			
barrel and end-cap	$\sigma_E/E = 50\%/\sqrt{E} \oplus 3\%$	± 3.2	± 3.2
forward	$\sigma_E/E = 100\%/\sqrt{E} \oplus 10\%$	$3.1 < \lvert\eta\rvert < 4.9$	$3.1 < \lvert\eta\rvert < 4.9$
Muon spectrometer	$\sigma_{p_T} = 10\%$ at $p_T = 1$ TeV	± 2.7	± 2.4

Table 3.1: General performance goals of the ATLAS detector, the units for E and p_T are in GeV. The table is taken from [86].

3.2.1 Coordinate system

ATLAS uses a coordinate system with the origin at the *nominal interaction point (IP)* at the centre of the detector. The x axis is chosen to point towards the centre of the LHC ring, the y axis points upwards and the the z axis is along the beam line. The direction of z axis is chosen in such a way that the coordinate system is right-handed. Because of the cylindrical detector shape, the spherical

coordinates are often convenient: the radial distance r, the azimuthal angle ϕ measured in the xy plane and the polar angle θ measured from the beam axis. Along with θ the pseudorapidity is defined as $\eta = -\ln[\tan(\theta/2)]$ which is approximately equal to the rapidity in the relativistic limit $\eta \approx \frac{1}{2}\ln[(E + p_{\mathrm{L}})/(E - p_{\mathrm{L}})]$. The rapidity (and pseudorapidity in the relativistic/massless limit) is widely used since it is Lorentz-invariant as well as the angular separation $\Delta R_y = \sqrt{(\Delta y)^2 + (\Delta\phi)^2}$. As for the physical observables, their transverse projections on the xy plane are often used when the z-component is not known and denoted with a subscript T, such as the transverse momentum $p_{\mathrm{T}} = \sqrt{p_x^2 + p_y^2}$ and transverse energy $E_T = E \sin\phi$.

3.2.2 Magnets

The magnetic system of ATLAS consists of four superconducting magnets (illustrated in Fig. 3.4): a solenoid, a barrel toroid and two end-cap todoids. The magnets are needed to bend the trajectories of

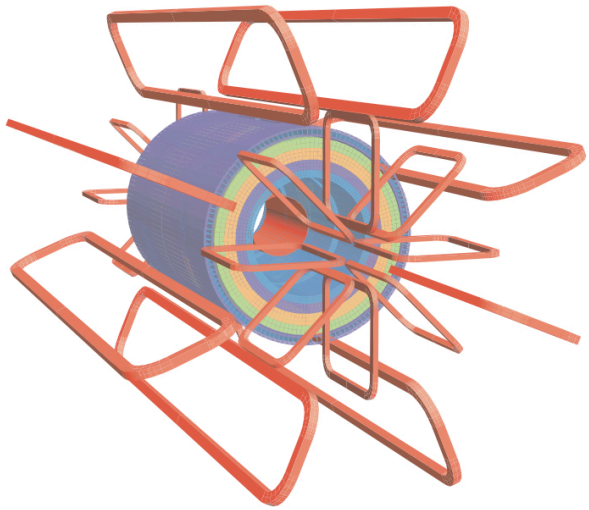

Figure 3.4: The spatial arrangement of the three toroid coils and the solenoid winding (in red) [86]. Concentric to the solenoid, the four layers of the tile calorimeter plus an outside return yoke are also shown.

the charged particles which is required to measure their transverse momentum p_{T}:

$$p_{\mathrm{T}} = \sqrt{4\pi\alpha}|q|BR \approx 0.3|q|\left(\frac{B}{\mathrm{Tesla}}\right)\left(\frac{R}{\mathrm{meter}}\right)\ \mathrm{GeV}, \tag{3.4}$$

where B is the magnetic field, R is the curvature radius of the particle trajectory with charge q and α is the fine-structure constant.

The central solenoid is located around the inner detector, for which it provides a 2 T axial magnetic field, and is aligned on the beam axis. It is built relatively thin (~0.66 radiation length[3]) in order to absorb as less as possible energy of the incoming particles, otherwise the performance of the electromagnetic calorimeter which surrounds the solenoid would be reduced. For the coil, the Al-stabilised Nb/Ti conductor is used. It operates at a nominal current of 7.73 kA and a nominal temperature of 4.5 K

[3] The radiation length is the mean distance over which a high-energy electron loses all but $1/e$ of its energy.

which is achieved with liquid helium cooling. The solenoid is 2.5 m in diameter and 5.8 m in length and the coil mass is 5.4 tons.

The system of air-core toroids surrounding the calorimeter generates a toroidal magnetic field of up to 2.5 T in the barrel and 4 T in the end-caps which bends the muon trajectories in the ϕ direction in the muon spectrometer. As it is shown in Fig. 3.4 the barrel toroid contains eight coils, each of them is enclosed in a separate racetrack-shaped, stainless-steel vacuum vessel and further in a cryostat. The total cold mass of the barrel is 360 tons. The toroidal magnetic field propagates in both, barrel and end-cap regions. Each end-cap toroid contains eight square coil units inserted in a single vacuum vessel and a cryostat. The cold mass of each end-cap weights 140 tons. The barrel and end-caps are constructed using the same technology and conductor as the solenoid magnet. The magnet nominal current is 20.5 kA achieved at a temperature of 4.6 K.

3.2.3 The Inner Detector

The ATLAS Inner Detector (ID) [88, 89] immersed into the solenoid magnetic field of 2 T provides high resolution measurements of momentum and of primary and secondary vertices for charged tracks with $|\eta| < 2.5$. A detailed schematic view of the inner detector is shown in Fig. 3.5

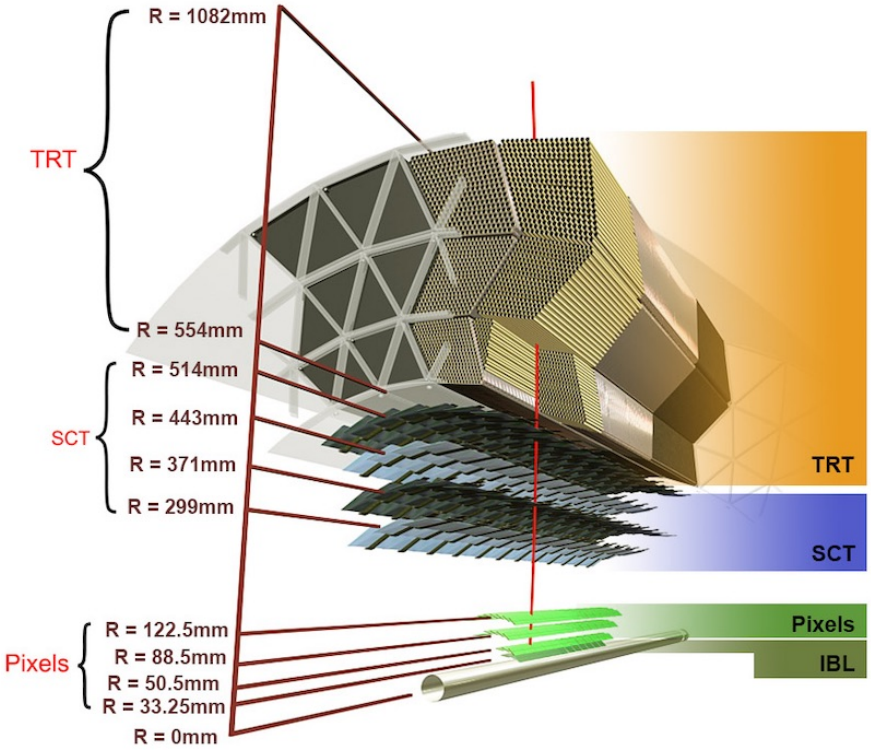

Figure 3.5: The Inner Detector layout including the new Insertable B-Layer (IBL) [90].

The ID has cylindrical geometry and consists of three nested sub-detectors shown in Fig. 3.6: a pixel detector, a silicon micro-strip tracker (SCT) and a transition radiation tracker (TRT). Each of the

sub-detectors has a barrel part and two end-caps.

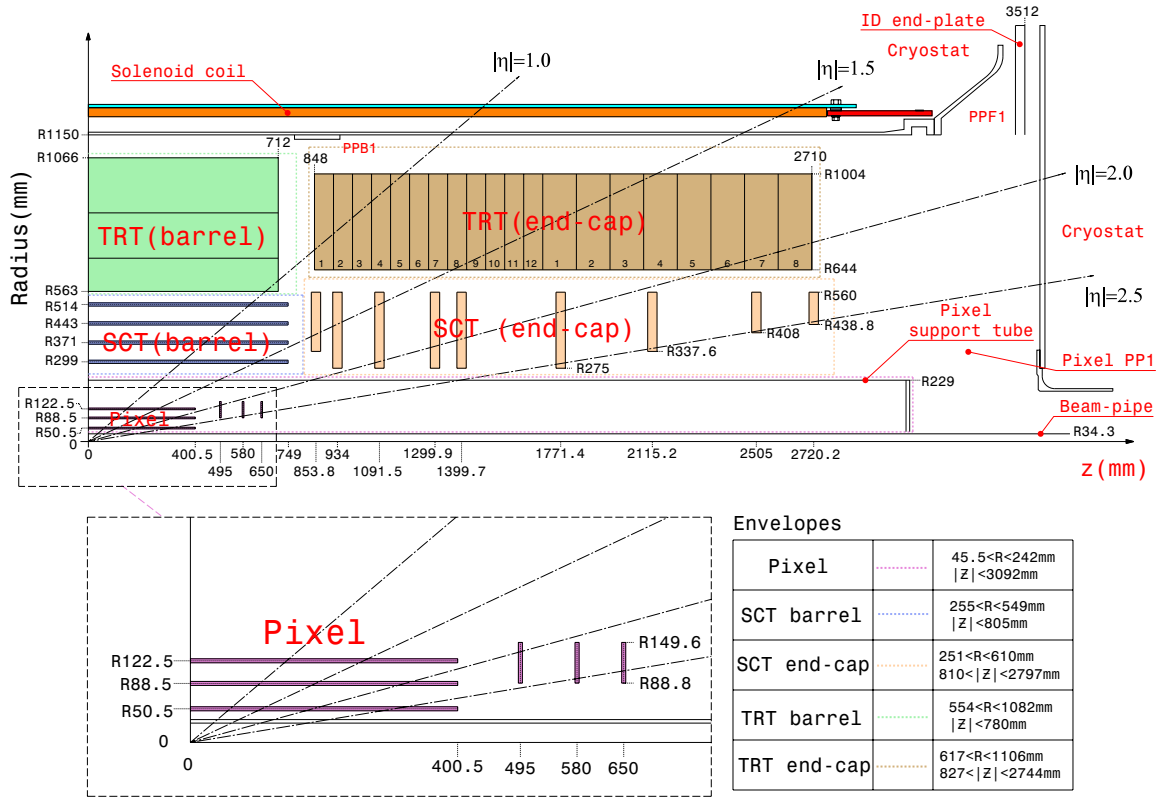

Figure 3.6: A schematic view of a quarter-section of the ATLAS ID in the (r, z) plane showing locations and dimensions of the pixel detector, the SCT and the TRT, as well as a magnified view of the pixel detector in the bottom. The figure is taken from [86].

The pixel detector barrel consists of four concentric cylindrical silicon-pixel layers at radii 33.5, 50.5, 88.5 and 122.5 mm. The three end-cap layers are located at $|z| = 495, 580$ and 650 mm on each side of the interaction point. The innermost barrel layer is called the *insertable B-layer* (IBL) [91] and it extends up to $|\eta| = 3.0$. The IBL was installed in 2014 in order to improve the tracks impact parameter, the vertex reconstruction and the b-tagging performance (see Section 3.3). The IBL consists of silicon pixels with individual sensors elements of 50×250 μm^2 (in the $\phi \times z$ direction), while the rest of the pixel detector uses pixels with dimensions 50×400 μm^2. Such pixels allow to achieve a resolution of 10 μm and 115 μm in the ϕ and z directions. The total number of the pixels in the ID is about 100 millions. A charged particle passing through a silicon pixel, which is a semiconductor, creates electron-hole pairs. This charge signal recorded as time over threshold (ToT) is called a pixel hit. These hits are used to reconstruct the particle tracks.

The SCT barrel contains four layers of 80 μm × 6 cm silicon strips located at radii 299, 371, 443 and 514 mm. Each silicon module is double: it is made of a back-to-back pair of sensors with 40 mrad angle between them, which allow to distinguish between several particles passing through a strip. Each SCT end-cap consists of nine double layers of strips situated from 848 to 2720.2 mm in the z direction. The SCT provides spatial resolution of 17 μm and 580 μm in ϕ and z directions, respectively. In total,

the SCT carries more than 3000 modules and 6 million channels.

For the transition radiation tracker polyimide drift (straw) tubes are used. The straws have diameters of 4 mm and length of 144 cm in the barrel and 37 cm in the end-caps. There are 73 layers of straws (52 544 straws in total) interleaved with carbon fibres in the TRT barrel and 160 straw planes (122 800 straws in total) interleaved with foils in the end-caps. The straws in the barrel are parallel to the beam pipe and the ones in the end-caps are arranged radially. The charged particles with $p_{\mathrm{T}} > 0.5$ GeV and $|\eta| < 2.0$ will cross at least 36 straws in the barrel, whereas the particles with $0.8 < |\eta| < 1.0$ crossing the end-caps will pass through at least 22 straws. The anodes of the barrel and the end-cap straws are made of tungsten wires plated with gold. The straw tubes are filled with a gas mixture: 70% Xe, 27% CO_2 and 3% O_2, which is ionised when a charged particle passes through it. The resolution achieved in the r-ϕ direction is 130 μm. Although the TRT lacks information in the z direction and has lower resolution in r-ϕ direction than the SCT, it provides extra hits and hence improves the track reconstruction efficiency (see Section 3.3.1).

3.2.4 Calorimeters

Calorimeters measure the energy and the position of a passing particle by absorbing its energy. The electromagnetic (EM) and the hadronic calorimeters are adapted to detect the energy from electromagnetically and strongly interacting particles, respectively. Therefore, electrons, positrons and photons are detected by the EM calorimeter and the energy of hadrons is measured in the hadronic calorimeter. However, muons and hadrons also leave small energy deposits in the EM calorimeter, which helps in the determination of their direction and in matching them to the tracks.

The ATLAS calorimeter system contains several sampling detectors with cylindrical symmetry and coverage up to $|\eta| < 4.9$. Any sampling calorimeter is composed of alternating layers of active and absorbing material. An incoming particle creates an electromagnetic or a hadronic shower by interacting with the dense material of the absorber, the secondary particles composing a shower ionise the active material and eventually get stopped by the absorber. The ionisation radiation which is read out from the active medium constitutes only a part of the particle energy, therefore its total energy should be computed from the reconstructed one using some subsequent calibration.

A schematic image of the ATLAS calorimeter is given in Fig. 3.7.

In the electromagnetic liquid argon (LAr) calorimeter:

- The barrel contains one presampler layer ($|\eta| < 1.52$) and 5 layers covering $|\eta| < 1.475$.
- Each of the two end-caps (EMEC) contains one presampler layer ($1.5 < |\eta| < 1.8$) and 7 layers covering $1.375 < |\eta| < 3.2$.

In the hadronic calorimeter:

- The scintillator tile calorimeter contains 3 layers in the barrel ($|\eta| < 1.0$) and 3 layers in the extended barrel ($0.8 < |\eta| < 1.7$).
- The LAr hadronic end-caps (HEC) consisting of 4 layers and covering $3.1 < |\eta| < 4.9$.
- The LAr forward calorimeter (FCal) consisting of 3 layers and covering $3.1 < |\eta| < 4.9$.

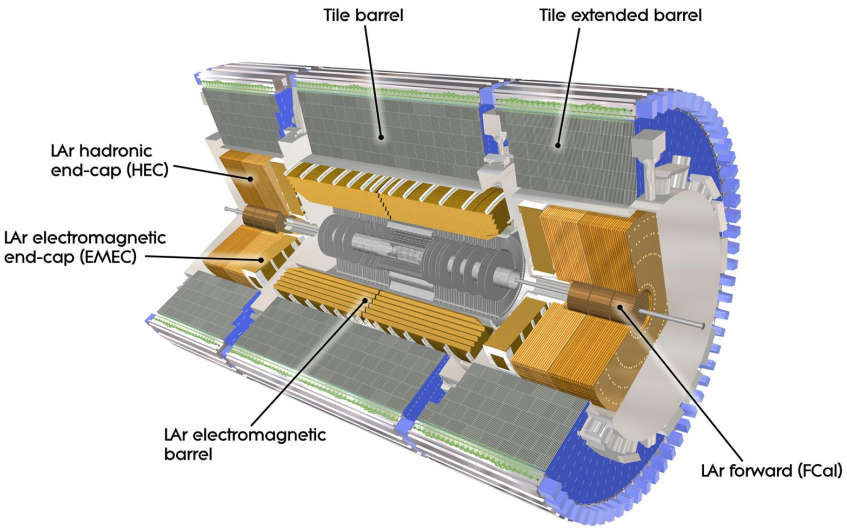

Figure 3.7: Computer Generated image of the ATLAS calorimeter [92].

The electromagnetic calorimeters (barrel and end-caps) use liquid argon as active material and lead as absorber. The accordion shape of kapton electrodes of the calorimeter allows to fit several active layers in depth (while having the absorber flat with respect to $|\eta|$) and provides complete ϕ symmetry without azimuthal breaks. The arrangement of the different layers can be seen on a sketch of a part of the LAr calorimeter in Fig. 3.8.

The scintillator tile calorimeter located outside the EM calorimeter is a sampling detector with steel as absorber and scintillating tiles as active material. The read-out from the scintillating tiles into the photomultiplier tubes is done using wavelength shifting fibers.

The hadronic end-cap calorimeter, placed behind the electromagnetic end-caps, is built from copper plates interleaved with LAr gaps.

The LAr forward calorimeter (FCal) integrated into the end-cap cryostats consists of three modules in each end-cap. The first module is made of copper and serves as an electromagnetic calorimeter. The other two modules are made of tungsten and are optimised for energy measurements of the hadronic interactions. The electrode structure of the FCal modules consists of rods and tubes, whereas the liquid argon is placed between them.

The amount of material in the different parts of the calorimeters in units of interaction length is shown in Fig. 3.9. The interaction length for hadrons passing through the hadronic calorimeter is called *nuclear interaction length* and it is defined as the mean distance over which a high-energy hadron loses all but $1/e$ of its energy. The interaction length for electrons in the electromagnetic calorimeter is called the *radiation length* and it is the mean distance over which a high-energy electron loses all but $1/e$ of its energy. The radiation length approximately equals to:

$$X_0[\mathrm{g}\cdot\mathrm{cm}^{-2}] \simeq \frac{716\mathrm{g}\cdot\mathrm{cm}^{-2}A}{Z(Z+1)\ln(287/\sqrt{Z})}, \tag{3.5}$$

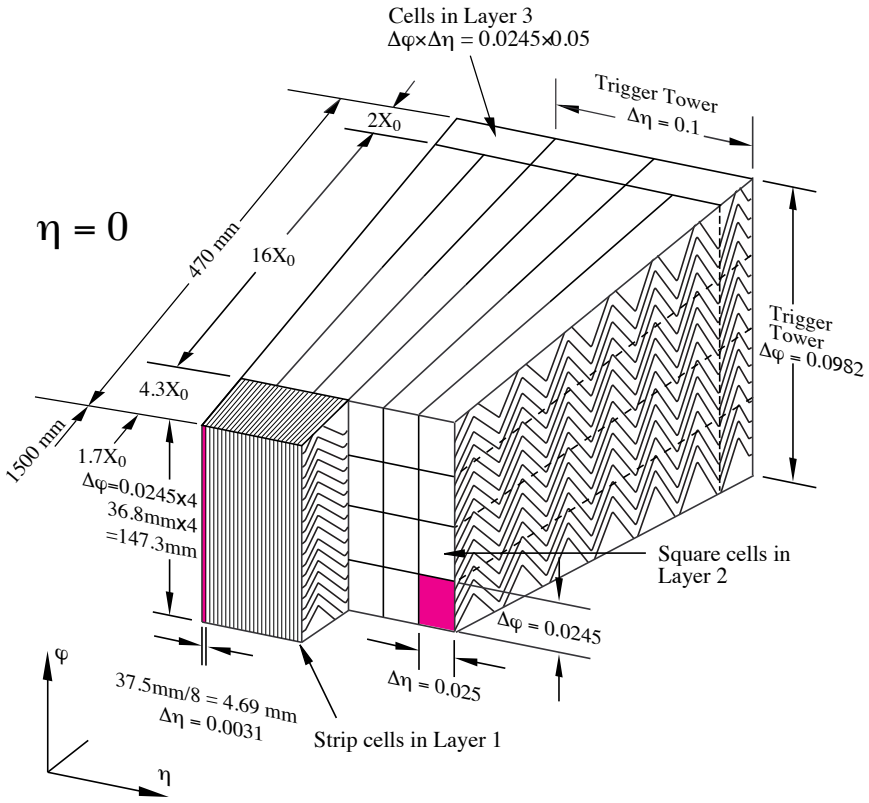

Figure 3.8: Schematic drawing of an EM barrel module with different layers visible. The granularity in η and ϕ of the cells is also indicated [86].

where Z is the atomic number and A is the mass number of the nucleus in the detector material [93].

3.2.5 The muon spectrometer

The outermost part of the ATLAS detector, the muon spectrometer [86, 94], is able to detect, to identify the charge and to measure the momentum of the muons passing the barrel and end-cap calorimeters with pseudorapidity $|\eta| < 2.7$. The target transverse momentum resolution is 10% for 1 TeV tracks which corresponds to the measurements of the 500 μm sagitta of the track along the beam axis with a precision of 50 μm. The measurement of the muon momentum is based on bending their trajectories in the magnetic field of the three superconducting air-core toroid magnets:

- The tracks of the muons with $|\eta| < 1.4$ are bent with the large barrel toroid.
- The tracks with $1.6 < |\eta| < 2.7$ are bent with either of the two smaller end-cap toroids which are placed at both ends of the barrel.
- The tracks in the transition region $1.4 < |\eta| < 1.6$ get deflected by a combination of the barrel and the end-cap magnetic fields.

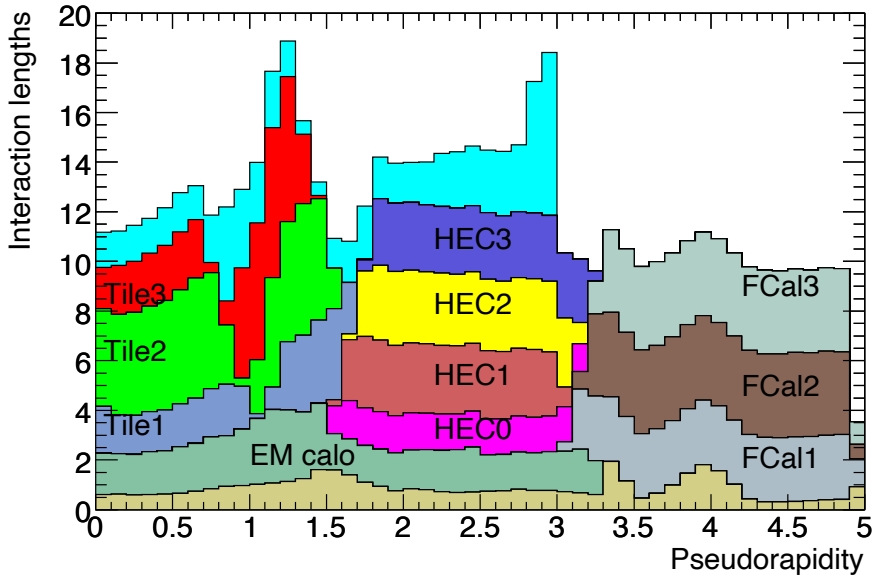

Figure 3.9: The total amount of material, in units of interaction length and as a function of $|\eta|$, in front of the EM calorimeter (the lowest band without the label), in different sub-detectors/layers of the calorimeter (bands with labels on them) and in front of the first active layer of the muon spectrometer (upper cyan band). The figure is taken from [86].

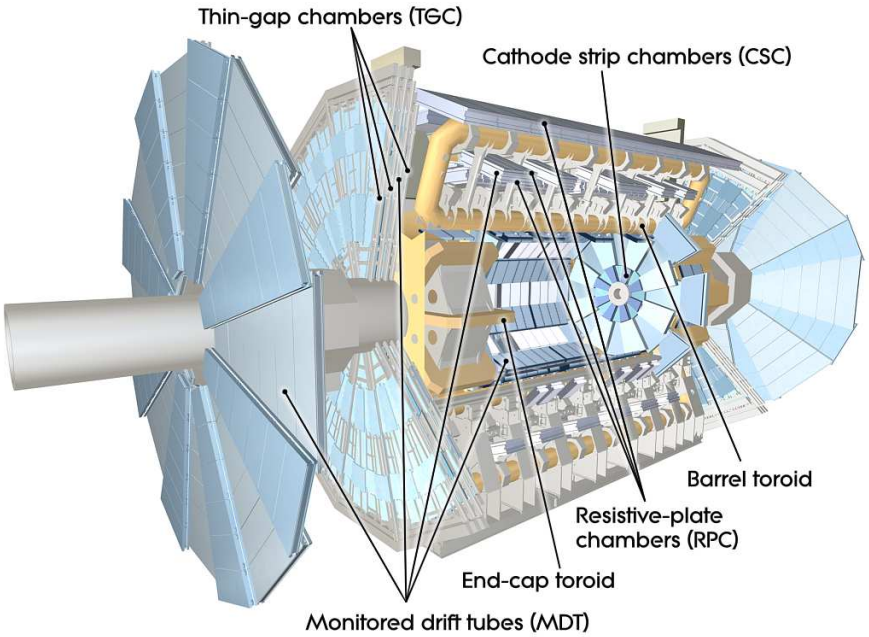

Figure 3.10: Cut-away view of the ATLAS detector with sub-detectors of the muon system indicated [86].

The layout of the muon system is shown in Fig. 3.10.

In the pseudorapidity region $|\eta| < 2$, the muon coordinates in the bending plane are measured by the Monitored Drift Tubes (MDT). The MDT chambers consist of 372 000 aluminium pressurised drift tubes with a diameter of ~ 30 mm, oriented in the ϕ direction. The tube length varies from 70 cm to 630 cm, depending of the location. Each tube is filled with Ar/CO_2 (93%/7%) as gas mixture under a pressure of 3 bar. The operating gas was chosen mainly due to its good ageing properties. The particles passing through the tube ionise the gas and release the electrons which are collected at the tungsten–rhenium wire anode of 50 μm. The average resolution per drift tube is about 80 μm.

In the first layer of the end-cap, which corresponds to $2 < |\eta| < 2.7$, the counting rates of the incoming particles exceed the limit of safe operation of the MDT's which is about 150 Hz/cm^2. Therefore, in this $|\eta|$ region the Cathode Strip Chambers (CSC) are used instead, which combine high spatial and time resolution with low neutron sensitivity and capability to operate under rates until 1000 Hz/cm^2, which is sufficient for the muon system. The CSC system in each end-cap consists of two disks with eight chambers each. Each chamber contains four CSC planes providing four independent measurements in η and ϕ for a track. A CSC's are multiwire proportional chambers operating using Ar/CO_2 (80%/20%) as gas mixture. The tungsten–rhenium anode wires have a diameter of 30 μm and are radially oriented. Both copper cathodes are segmented into strips, which are perpendicular to the wires on one side and parallel on another side, hence providing two coordinates transverse to each other. The resolution of CSC is 60 μm per CSC plane.

The trigger chambers are inserted into the muon system to provide fast information on muon tracks to the L1 trigger which can recognise the muon multiplicity and the approximate energy range. In particular, the trigger chambers provide bunch-crossing information, thresholds for the muon p_{T} measurements and measure the muon coordinate in the direction orthogonal to the one provided by MDT's. For the barrel region ($|\eta| < 1.05$), the Resistive Plate Chambers (RPC's) have been selected: two RPC stations sandwich the MDT's of the middle layer and the third one is positioned close to the outer MDT layer. In the end-cap region ($1.05 < |\eta| < 2.4$), four layers of the Thin Gap Chambers (TGC's) are used: three layers in front and behind the second MDT wheel and the fourth layer in front of the innermost tracking layer.

The RPC is an avalanche gaseous detector made of two parallel resistive Bakelite plates at 2 mm distance between each other, filled with $C_2H_2F_4$/Iso-C_4H_{10}/SF_6 (94.7/5/0.3) as gas mixture. Each RPC station consists of two independent detector layers, each measuring η and ϕ, so three RPC stations deliver six measurements of η and ϕ for each track. Such redundancy of the coordinate measurements allows to use coincidence scheme to reject fake tracks and improve the trigger efficiency in the presence of inefficiencies.

The TGC are multi-wire proportional chambers with a gas gap of 2.8 mm between graphite cathodes and 50 μm wires distributed inside at 1.4 mm from the cathodes and 1.8 mm between each other. TGC's operate in a quasi-saturated mode using a gas mixture of CO_2 and n-C_5H_{12}. They provide the muon trigger information and the second (azimuthal) coordinate to complement the measurement of the MDT's in the radial direction.

The arrangement of the different layers of the muon system sub-detectors is pictured in Fig. 3.11.

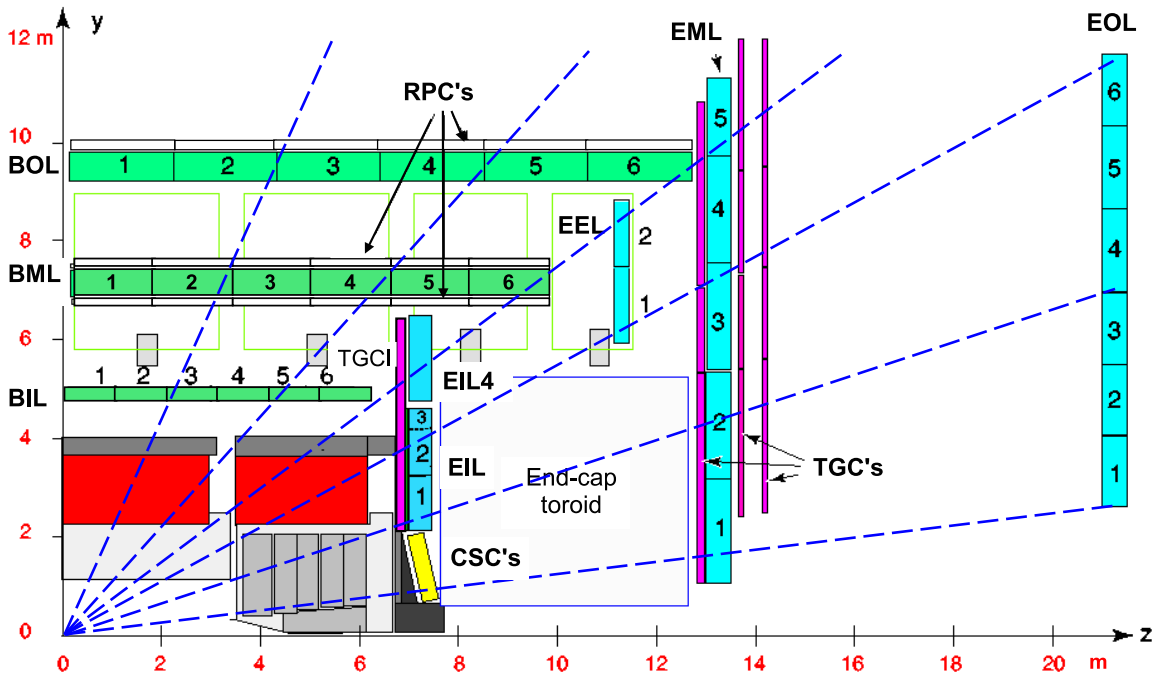

Figure 3.11: The schematic view of the muon spectrometer components in the (y,z) plane [86]. The placement of the RPC's, TGC's and CSC's are shown with arrows. The different layers of MDT's are denoted with labels BIL, BML, BOL, EIL, EML, EOL, in which the first letter stands for "**B**arrel" or "**E**nd-cap", the second letter refers to the layer (**I**nner, **M**iddle or **O**uter) and the last "L" means "**L**arge sector". The dashed blue straight lines represent the trajectories of the passing infinite-momentum muons.

3.2.6 The LUCID detector

The LUminosity Cherenkov Integrating Detector (LUCID) [95] is a luminosity monitor which consists of two modules mounted at $z = \pm 17$ m on both sides from the ATLAS IP. LUCID provides precise bunch-to-bunch measurement of the instantaneous luminosity by detecting particles produced by inelastic pp scattering in the forward region, the number of which is proportional to the mean number of interactions per bunch crossing $\langle\mu\rangle$.

Each module contains 16 photomultiplier tubes (PMT's) arranged in four groups around the beampipe, four fiber bundles and four additional PMT's placed at 1.5 m from the beampipe. When incoming charged particles pass through the quartz windows of the PMT's around the beampipe and the fiber bundles, they produce Cherenkov light, which is detected afterwards by the PMT's.

The luminosity measurements provided by LUCID are given in luminosity blocks (LB) of 60 seconds and the average luminosity in a LB is defined as:

$$L_{\mathrm{LB}} = \frac{f_{\mathrm{LHC}}}{\sigma^{\mathrm{vis}}} \sum_{j=1}^{n_{\mathrm{b}}} \mu_j^{\mathrm{vis}}, \tag{3.6}$$

where $f_{\text{LHC}} = 11245$ Hz is the LHC revolution frequency, σ^{vis} is the visible cross section[4], n_{b} is the number of bunch pairs colliding in ATLAS and μ^{vis} is the visible number of interactions[5].

The absolute calibration of σ^{vis} is done using special *van der Meer* scans [96], during which the beams are separated in the horizontal and vertical direction and for each value of separation a measurement of the interaction rate of the beams is done.

3.2.7 Trigger and data acquisition

The Trigger and Data Acquisition (TDAQ) system shown in Fig. 3.12 is used to filter and record the data from the LHC collisions. The choice of the trigger thresholds should allow, on one hand, to maximise the physics output of the experiment and, on the other hand, to fit within the rate and bandwidth limits of the ATLAS detector and offline computing.

During Run 2, the bunch crossing rate at LHC reached 40 MHz which translated into a data rate of 6 TB/s flowing from the detector. The trigger system was able to reduce the event rate from 40 MHz to 1 kHz, corresponding to ~1 GB/s, a data rate which is manageable for the computational resources.

The collision events are selected at two levels: the hardware-based Level-1 (L1) and the software-based High-Level Trigger (HLT) [97].

The L1 trigger allows to reduce the event rate to ~75 kHz and the HLT trigger decreases the output rate to 1 kHz (it was 400 Hz in Run 1). At L1, the decision to accept an event is done by the central trigger processor (CTP), which uses information from the Level-1 calorimeter trigger (L1 Calo), the Level-1 muon trigger (L1 Muon) and from several other subsystems such as the Minimum Bias Trigger Scintillators (MBTS), the LUCID Cherenkov counter and the Zero-Degree Calorimeter (ZDC)[6].

Before reaching the CTP, the L1 Calo input, formed in several identification subsystems (the Cluster Processor CP and the Jet/Energy-sum Processor JEP) and merged in the cluster merger modules (CMX), is transferred to the intermediate topological trigger (L1 Topo) consisting of the two FPGA[7]-based processor modules for preselection. The information from L1 Muon is transmitted to L1 Topo and the CTP through a specific Muon-to-CTP interface (MUCPTI). An extra L1 component, a FPGA-based Fast TracKer (FTK), provides the global ID track reconstruction information to the HLT by performing a fast linear fit of the tracks.

The events accepted by the L1 trigger are buffered in the Read-Out System (ROS) and then passed to the HLT as well as the Region-of-Interest (RoI) information from the L1, which can be used for regional reconstruction in the HLT algorithms. The events which are accepted by the HLT are then transferred to some local storage at the experimental site and exported to the Tier-0 facility at the

[4] The visible cross section is defined as a product of the inelastic pp cross section, of the efficiency and of the acceptance of the luminosity detector.

[5] The visible number of interactions is the number of pp interactions in a given colliding bunch pair times the efficiency and acceptance of the luminosity detector.

[6] Zero-Degree Calorimeter is a forward detector located at ±140 m from the interaction point. Its primary purpose is to detect forward neutrons from heavy-ion collisions [86].

[7] Field-Programmable Gate Array

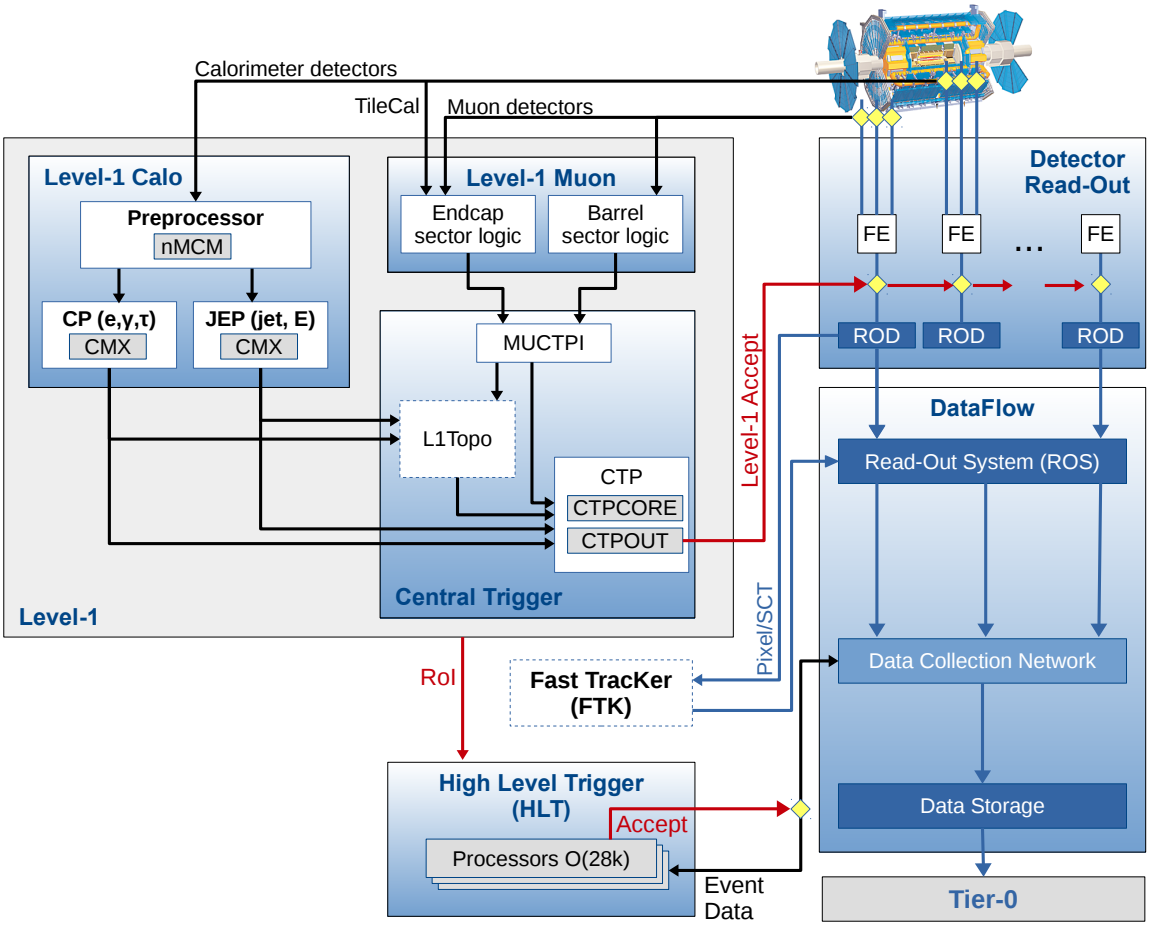

Figure 3.12: The trigger components of the ATLAS TDAQ system in Run 2 [97]. The Level-1 Topological Trigger (L1 Topo) and Fast Tracker (FTK) were commissioned in 2015. The abbreviations used in the block-scheme are: TileCal = tile calorimeter, nMCM = new multi-chip module, CP = cluster processor, JEP = jet energy/sum processor, CMX = cluster merger modules, MUCTPI = muon-to-CTP interface, FE = front-end electronic, ROD = readout driver, RoI = region of interest.

CERN computing centre for offline reconstruction. Events accepted by the HLT are written into several data streams:

- The *main stream* includes all events for physics analyses.
- A small fraction of events from the main stream are also written to the *express stream* at a rate of 10–20 Hz. The fast offline reconstruction of the express stream events provides calibration and data quality information prior to the reconstruction of the full main stream.
- About twenty additional streams are used for calibration, monitoring and detector performance studies.
- The *debug* streams are used for events which cannot be properly processed at the HLT or have other DAQ-related problems. These events are reprocessed offline.

For a given LHC run, ATLAS chooses a list of L1 and HLT triggers which is called a *trigger menu* and which consists of

- primary triggers needed for physics analyses,
- support triggers needed for efficiency/performance measurements and monitoring,
- alternative triggers that work using alternative reconstruction algorithms,
- backup triggers with tighter selections,
- calibration triggers needed for detector calibration.

All triggers are identified by their level, their particle type, their p_{T} threshold value and various further selection criteria. For example, `L1_2MU4` is a L1 trigger which requires at least two muons (`2MU`) with $p_{\mathrm{T}} > 4$ GeV and `HLT_g120_loose` is a HLT trigger accepting photons (`g`) with $p_{\mathrm{T}} > 120$ GeV and "loose" isolation. Some of the triggers, usually the low-p_{T} ones, run with a "prescaling" in order to fit into the bandwidth of the detector: prescale N means that only 1 of N events accepted by the L1 trigger will be passed to HLT.

The effect of switching the prescaling can be seen on Fig. 3.13(a) and Fig. 3.13(b) showing the L1 and HLT trigger rates grouped by signatures: the removal of the prescaling of some triggers results in a "step" in the trigger rates.

3.3 Object reconstruction

The event reconstruction is the transformation of the detector hits into physics objects and the main goal of the reconstruction algorithms is to identify prompt particles (final particles of the hard process).

The first stage of the reconstruction (*prompt* reconstruction) of such objects as electrons and jets is done at the CERN computing centre (called Tier-0), where the "raw" data accepted by the trigger system is transmitted. After that, the raw data together with some partially reconstructed objects are sent to 13 computer centres (called Tier-1), where the data is prepared for analysis, namely where the particle identification and calibration is done. The different steps of reconstruction, identification and calibration for each particle are described in the following sections.

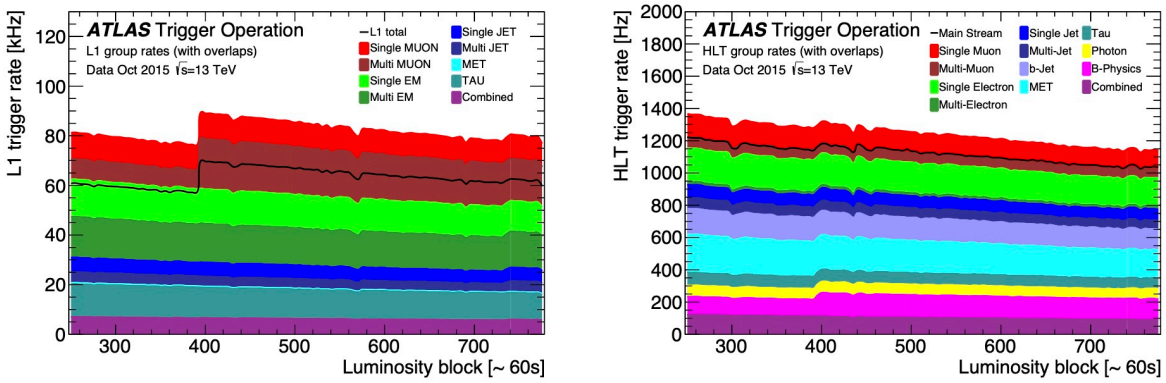

(a) (b)

Figure 3.13: L1 and HLT trigger rates grouped by trigger signature during an LHC fill in October 2015 with a peak luminosity of 4.5×10^{33} cm^{-2} s^{-1} [97]. Some of the trigger groups (Tau, *b*-Jet, B-Physics, Combined) include multiple triggers combining different trigger signatures.

In order to calibrate the reconstructed objects and to determine the efficiency [8] of the reconstruction one often needs to simulate the detector response. The simulation of the particle interaction with the ATLAS detector is done using the Geant4 toolkit [98].

During the simulation of the detector effects most of the computing time is spent on the simulation of the calorimeters. For many purposes it is sufficient to parametrise the calorimeter response and to get an approximate simulation which it called the ATLAS fast calorimeter simulation (AtlFastII or AFII) [99]. AFII simulation is ~20 times faster than the full Geant4 simulation (called FullSim).

3.3.1 Tracks

The trajectories (*tracks*) of charged particles are reconstructed using the information from the ID: the pixel detector, the SCT and TRT [86, 100].

Track reconstruction can be divided in three stages: pre-processing (pattern finding), track finding and post-processing (vertex finding). However, the modern track reconstruction does not clearly distinguish the first two steps since sometimes the track fitters incorporate an intrinsic pattern recognition in the fitting process. The New Tracking (NEWT) in the Inner Detector [101] exploits two reconstruction sequences: the main *inside-out* reconstruction and a consecutive *outside-in* reconstruction.

The *inside-out* scheme starts with a **pre-processing** stage when the raw data from the pixel and SCT detectors are assembled into clusters using a connected component analysis (CCA) algorithm [102]. The obtained clusters are transformed into three-dimensional measurements (*space-points*), which are the points where a charged particle has passed through the active material of the ID. The possible *merged clusters* in the pixel detector, created by charge deposits from multiple particles, are identified and split using a novel technique based on artificial neural networks [103]. Also, at the preprocessing stage the TRT raw timing information is translated into calibrated drift circles.

[8] The efficiency ϵ is the probability to pass the selection for an object: $\epsilon = \frac{\text{number of objects per event passing selection}}{\text{total number of objects per event}}$.

During the second **track-finding** stage the prompt tracks originating from the vicinity of the interaction region are identified using the information from the pixel and SCT detectors [104]. First, from a combination of three space-points in adjacent detector layers (among the pixel layers and the first SCT layer) the track seeds are formed. Then, the seeds are extrapolated through the rest of the pixel and SCT detectors and the track candidates are built using a combinational Kalman filter algorithm [105]. After that, "outlier" clusters are removed, ambiguities in the cluster-to-track association are resolved, and fake tracks are rejected. The next step is to add the information from the TRT: the selected tracks are extended into the TRT and they are associated to the TRT drift-circles reconstructed at the previous stage. Extended tracks are then refitted using the information from all three detectors.

The inside-out scheme which relies on a track seed found in the silicon tracker does not allow to find all the tracks since e.g. the tracks from the secondary[9] decay vertices and from photon conversions may not have a sufficient number of silicon hits. To improve the reconstruction of these kinds kinds of tracks, the reverse *outside-in* scheme is employed. First, the track segments in the TRT are identified using a Hough transform mechanism [106]. Then they are extended back into the SCT and pixel detectors (this is called *backtracking*). The backtracking allows to find small track segments which have been missed during the inside-out scheme.

At the last **post-processing** stage the reconstructed tracks are used to find the primary[10] and secondary vertices.

The reconstruction of a primary vertex consists in vertex finding (matching of the reconstructed tracks to the vertex candidates) and vertex fitting (actual reconstruction of a vertex and its covariance matrix) [107]. The vertex candidates are found using an iterative procedure starting from a vertex seed, which is based on the position of the beam spot in the transverse plane. The third, z coordinate of the seed is calculated using the Half-Sample Mode algorithm [108] from the z-coordinates of tracks at their points of closest approach to the beam spot. Then, using a vertex seed as starting point and the parameters of the reconstructed tracks, the vertex-finding algorithm performs an iterative χ^2 minimisation to find an optimal vertex position. All vertices with at least two associated tracks are counted as primary vertex candidates. Including the reconstructed position and the width of the beam spot in the primary vertex fit allows to distinguish the secondary vertices (outside the beam spot) and to remove them from the fit.

Performance

The quality of the track and vertex reconstruction is defined by the corresponding efficiencies which are determined from a data to Monte-Carlo comparison.

The **track reconstruction efficiency** is evaluated by matching the reconstructed tracks to particles in the MC simulation [109]. The association is done between the *primary tracks* and the *primary charged particles* which are defined as follows:

- Primary charged particles are charged particles with a mean lifetime of $\tau > 300$ ps.

[9] The secondary vertex is the place of a decay of heavy-flavour or long-lived particle.
[10] Primary vertex is a place of an individual proton-proton collision.

- A primary track is a reconstructed track with a weighted matching probability $P_{\text{match}} > 0.5$, where P_{match} is defined in terms of the number of hits in the inner detectors common to a given track and the corresponding truth particle ($N^{\text{common}}_{\text{Pixel, SCT, TRT}}$) and the number of hits which compose the track ($N^{\text{track}}_{\text{Pixel, SCT, TRT}}$):

$$P_{\text{match}} = \frac{10 \cdot N^{\text{common}}_{\text{Pixel}} + 5 \cdot N^{\text{common}}_{\text{SCT}} + 1 \cdot N^{\text{common}}_{\text{TRT}}}{10 \cdot N^{\text{track}}_{\text{Pixel}} + 5 \cdot N^{\text{track}}_{\text{SCT}} + 1 \cdot N^{\text{track}}_{\text{TRT}}}. \tag{3.7}$$

Then, the tracking efficiency as a function of the truth particle p_{T} and η is equal to:

$$\epsilon(p_{\text{T}}, \eta) = \frac{N^{\text{matched}}_{\text{rec}}(p_{\text{T}}, \eta)}{N_{\text{gen}}(p_{\text{T}}, \eta)}, \tag{3.8}$$

where $N^{\text{matched}}_{\text{rec}}(p_{\text{T}}, \eta)$ is the number of primary tracks matched to charged particles as described above and $N_{\text{gen}}(p_{\text{T}}, \eta)$ is the number of primary charged particles.

The track reconstruction efficiency evaluated from PYTHIA8 simulation is shown in Fig. 3.14. The Tight

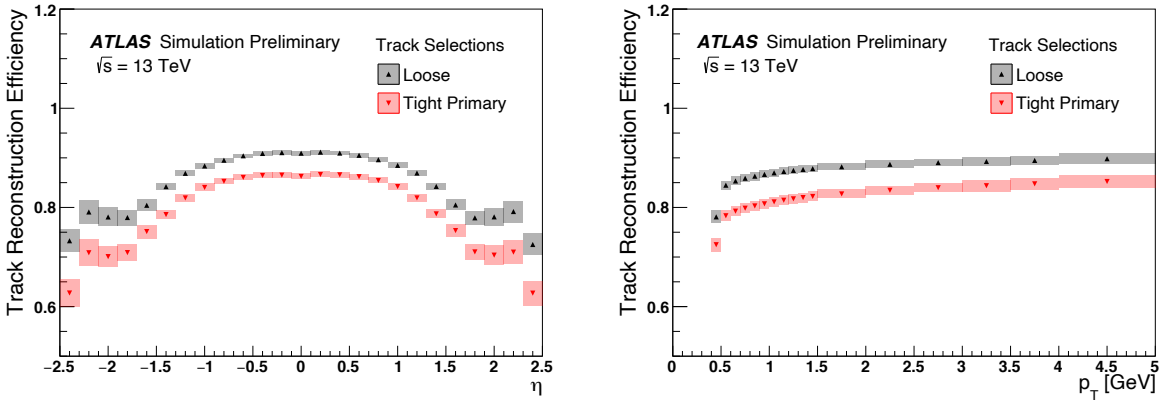

(a) (b)

Figure 3.14: Track reconstruction efficiency calculated using minimum bias MC events (accepted by a trigger with very loose requirements) as a function of η (a) and p_{T} (b) of the truth charged particle for tight and loose track selections. The bands represent the total systematic uncertainty. The figure is taken from [109].

Primary track reconstruction efficiency is overall lower by 5-10% than the Loose track reconstruction efficiency because the Tight Primary selection has stricter requirements (larger number of required silicon hits).

The vertex reconstruction efficiency is measured from data by taking the ratio between events with a reconstructed vertex and events with at least two reconstructed tracks. The vertex efficiency determined from the first two weeks of Run 2 data is shown in Fig. 3.15.

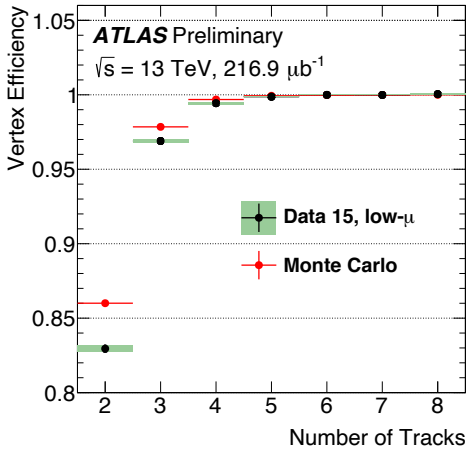

Figure 3.15: Vertex reconstruction efficiency as a function of the number of tracks in data with a low average number of interactions per bunch crossing (μ). The figure is taken from [110].

3.3.2 Calorimeter clustering algorithms

Calorimeters play a crucial role in particle reconstruction, providing precise measurements of the energies and positions of electrons, photons, jets and allowing to distinguish between them. An incoming particle produces a shower and leaves its energy in a number of calorimeter cells. An electron or a photon initiates an electromagnetic shower (see Section 3.3.3) and a hadron leaves a hadronic shower (see Section 3.3.5). In order to group all the relevant cells and to read out the total deposited energy, several clustering algorithms has been developed. There are two clustering algorithms which are used in ATLAS: the "sliding-window" and the topological clustering algorithm.

- In the "sliding-window" algorithm [111] the calorimeter cells are summed within a fixed-size rectangular window, which is adjusted in position such that it contains a local maximum of the transverse energy. The calorimeter is divided in η and ϕ directions into a grid of elements of size $\Delta\eta \times \Delta\phi$ and to each element a "tower" of the corresponding cells in all longitudinal layers is assigned. The energy of each "tower" is calculated as a sum of all its cells in the longitudinal direction. The seed of a cluster is found by moving a window of size $N_\eta^{\text{window}} \times N_\phi^{\text{window}}$ (in units of $\Delta\eta \times \Delta\phi$) through a grid and computing the total energy (sum of the tower energies) contained in a window. When the energy within a window reaches its local maximum and is above a predefined threshold, a seed (precluster) is formed. The size of the window and the energy threshold depend on the calorimeter in which the algorithm is applied (the electromagnetic calorimeter or a combination of the electromagnetic and hadronic calorimeters). Then, all cells within a rectangle of size $N_\eta^{\text{cluster}} \times N_\phi^{\text{cluster}}$ centered on the seed position are assigned to a cluster. The cluster size is chosen depending on the hypothesized particle type and the location of the cluster in the calorimeter.

  During Run 1, this algorithm has been successfully used for the reconstruction of the electromagnetic showers and jets from tau-lepton decays. Currently, for most of the analyses the topological clustering algorithm is used since it allows to implement the particle flow reconstruction algorithm [112] which combines the information from the tracker and the calorimeter. Originally, the particle flow algorithm has been introduced for jet reconstruction, but starting from 2017 it is also used for electrons and photons.

- The topological clustering [113] is an iterative algorithm which forms a topo-cluster from a seed cell by adding the neighbouring cells with significant signals compared to the expected noise. The significance of the cell signal $\zeta^{\mathrm{EM}}_{\mathrm{cell}}$ is defined as a ratio of the cell signal $E^{\mathrm{EM}}_{\mathrm{cell}}$ to the expected noise $\sigma^{\mathrm{EM}}_{\mathrm{noise,cell}}$

$$\zeta^{\mathrm{EM}}_{\mathrm{cell}} = E^{\mathrm{EM}}_{\mathrm{cell}} / \sigma^{\mathrm{EM}}_{\mathrm{noise,cell}}. \tag{3.9}$$

  The clustering starts from a calorimeter cell with a significance larger then the primary seed threshold S (the default is $S = 4$). The neighboured cells having a significance above the threshold for growth control N (the default is $N = 2$) are collected together with the seed into a protocluster and this procedure is repeated iteratively. If a particular neighbour appears to be another seed (passing the threshold S) it is added to the considered proto-cluster together with its own proto-cluster. The resulting proto-cluster represents a seed (or a set of seeds) surrounded by a set of connected cells passing the threshold N and further surrounded by an envelope of cells with less significant signals, i.e. with significance above the principal cell threshold P which is set to zero by default.

  In general, the proto-cluster can contain signals from two or more particles closely passing through the calorimeter. In order to separate the signals of these particles the cluster splitting algorithm is employed. The splitting starts from a search for local maxima in a proto-cluster, where the local maximum is defined as a cell having $E^{\mathrm{EM}}_{\mathrm{cell}} > 500$ MeV and having at least four neighbours without a larger signal. Then, the rest of the cells in the proto-cluster are distributed between the found local maxima forming several topo-clusters. The cell which is a neighbour to two or more local maxima is assigned to the two topo-clusters with highest energies and its signal is shared between them according to the geometrical weights $w^{\mathrm{geo}}_{\mathrm{cell},1}$ and $w^{\mathrm{geo}}_{\mathrm{cell},2}$ which depend on the topo-clusters energies $E^{\mathrm{EM}}_{\mathrm{clus},1}$ and $E^{\mathrm{EM}}_{\mathrm{clus},2}$ and the cell distances to these topo-clusters d_1 and d_2:

$$w^{\mathrm{geo}}_{\mathrm{cell},1} = \frac{E^{\mathrm{EM}}_{\mathrm{clus},1}}{E^{\mathrm{EM}}_{\mathrm{clus},1} + r E^{\mathrm{EM}}_{\mathrm{clus},2}}, \quad w^{\mathrm{geo}}_{\mathrm{cell},2} = 1 - w^{\mathrm{geo}}_{\mathrm{cell},1}, \quad r = \exp(d_1 - d_2). \tag{3.10}$$

  A proto-cluster with one or no local maxima forms itself a single topo-cluster.

3.3.3 Electrons and photons

An electron produced in a collision while traversing the detector interacts with the detector material and loses energy via bremsstrahlung. The radiated photons can convert into electron-positron pairs which in their turn will interact with the detector material. As a result, the passing electron induces the generation of a collection of (usually collimated) photons, electrons and positrons which is called an electromagnetic shower and which is detected by the inner detector and the electromagnetic calorimeter. The scheme of an electron path through the different parts of the detector is illustrated in the Fig. 3.16.

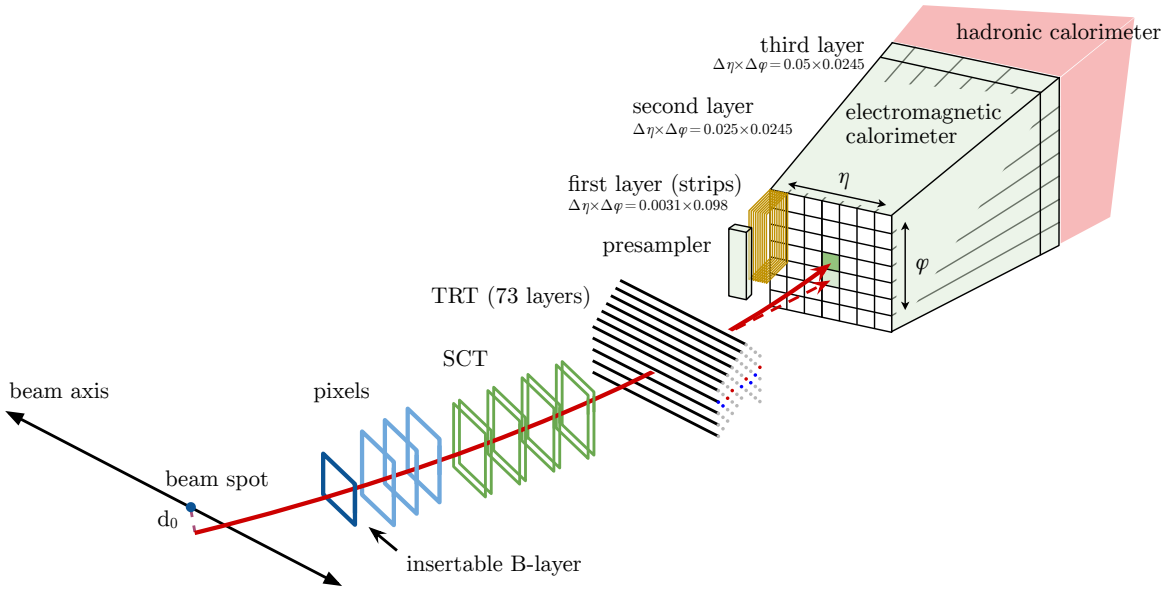

Figure 3.16: A schematic picture of the electron trajectory (in red) through the subdetectors of the tracking system and the calorimeter. The red dashed line is the trajectory of a photon emitted by the electron after interaction with the material of the tracking system. The figure is taken from [114].

Reconstruction

The electron reconstruction[11] [114] is based on the following signatures observed in the detector components: localised clusters in the electromagnetic calorimeter, tracks in the inner detector and close proximity (in $\eta \times \phi$ plane) of these tracks to the clusters matched to them.

The photon reconstruction is done in a similar way since a photon also produces an electromagnetic shower and leaves a cluster of deposits in the calorimeter, but no track in the inner detector.

As it was mentioned in the Section 3.3.2, in the past, the fixed-size clustering (sliding-window) algorithm was used for the electron reconstruction because the calibration methodology did not allow to apply it to the dynamically-sized clusters. Currently, due to the development of multivariate calibration techniques, the calibration of the dynamically-sized clusters became possible and now the topological clusters (topo-clusters) are used to reconstruct the electromagnetic showers from electrons and photons [115]. A primary advantage of using topo-clusters is that we can recover a soft photon emitted by an electron in the inner detector and connect this photon to the associated electron (in this case, the combination of an electron cluster and a photon cluster is called a supercluster). There are also other advantages:

- Topo-clusters collect more energy on average than sliding window clusters (hence, one needs to apply smaller corrections for energy losses)
- Topo-clusters result in a linear energy response and very good energy resolution in a wide range of energies (better than for sliding window algorithms)

[11] In this section, by "electron reconstruction" we mean the same reconstruction procedure for both, electron and positron.

The electron and photon topo-cluster reconstruction is done as explained in Section 3.3.2 with the default set of thresholds ($S = 4$, $N = 2$, $P = 0$) commonly called a "4-2-0" topo-cluster reconstruction.

The track reconstruction is done as described in Section 3.3.1. The track candidates are fitted using a global χ^2 fitter [116] and the tracks loosely matched [12] to the topo-clusters are refitted using a Gaussian Sum Filter fitter [118], a non-linear generalisation of the Kalman filter. Then, the refitted tracks are matched to the topo-clusters with tighter requirements in η and ϕ.

Identification

Electron identification means to distinguish the "signal" electrons (prompt electrons) from the "background" electrons: jets that mimic the signature of prompt electrons, electrons from photon conversions in the detector material, and non-prompt electrons from the decay of heavy flavour hadrons.

The prompt electrons are identified using a likelihood-based method. The likelihood (LH) for signal (or background) $L_{\mathrm{S(B)}}$ is built using measurements from the tracker, the calorimeter and quantities related to both systems:

$$L_{\mathrm{S(B)}}(\mathbf{x}) = \prod_{i=1}^{n} P_{\mathrm{S(B)},i}(x_i), \tag{3.11}$$

where $\mathbf{x}$ is a vector of quantities and $P_{\mathrm{S(B)},i}(x_i)$ is the value of the signal (background) probability density function (pdf) for the quantity i at the value x_i. The pdfs of the electrons with transverse energies 4.5 GeV $< E_{\mathrm{T}} <$ 15 GeV are found using $J/\psi \rightarrow ee$ simulated events and the pdfs for $E_{\mathrm{T}} <$ 15 GeV are found using $Z \rightarrow ee$ Monte Carlo simulation.

In order to achieve various required efficiencies for the reconstructed electrons there are four fixed values of the LH discriminant defined and four respective operating points: VeryLoose, Loose, Medium, and Tight. For example, the identification efficiencies of prompt electrons with $E_{\mathrm{T}} = 40$ GeV are 93%, 88%, and 80% for the Loose, Medium, and Tight operating points, respectively, see Fig. 3.17.

3.3.4 Muons

The muon reconstruction is done using mainly the information from the inner detector (ID) and the muon system (MS), but the information from the calorimeter is also sometimes used [119]. In the inner detector, the muon tracks are reconstructed as any other charged particle tracks, as described in Section 3.3.1.

The reconstruction in the muon system starts with the determination of the hit patterns. A Hough transform [120] is used to find the hits forming a trajectory in the bending plane of the detector in each MDT chamber and the neighbouring trigger chamber, afterwards the hits are fitted using a straight

[12] Loose matching refers to a weak requirement imposed on the distance in the $\eta \times \phi$ plane between the cluster barycentre and a track extrapolated to the EM calorimeter: roughly, 0.2 in ϕ and 0.05 in η, more details are given in [117].

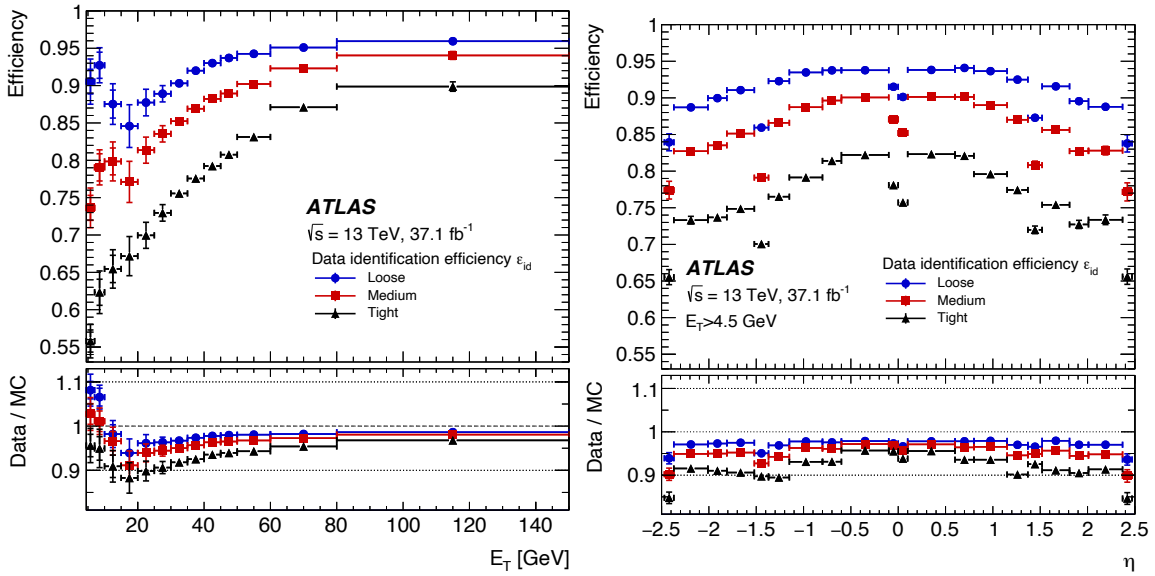

Figure 3.17: Measured efficiency for electrons in $Z \to ee$ events for Loose, Medium, Tight operating points as a function of the electron E_{T} (left) and η (right). The data efficiency is obtained by applying to the $Z \to ee$ simulation the data-to-simulation efficiency ratios, measured in $J/\psi \to ee$ and $Z \to ee$ events. The data-to-simulation ratios are plotted in the bottom pads. The figure is taken from [114].

line. The RPC or TGC hits give a muon coordinate orthogonal to the bending plane and the CSC detectors are used to build segments using a separate search in the η and ϕ planes.

Then, by fitting together hits from different segments the muon track candidates are formed. A track candidate is accepted if the χ^2 from a global χ^2 fit of the hits associated with a track satisfies some selection criteria. Finally, a search for additional hits consistent with the track candidate trajectory is performed. If extra hits are found, the track candidate is refit.

After the track reconstruction in the tracker and in the muon system is done, a combined reconstruction is performed using various algorithms. Four muon types are distinguished depending of the subdetectors used in the reconstruction:

- Combined muon: after track reconstruction in the ID and MS, a combined track is built by performing a global refit of all the hits from both ID and MS. Most muons are reconstructed using an *outside-in* approach: the tracks reconstructed in MS are extrapolated to the ID.

- Segment-tagged muons: a track in the ID is identified as a muon if its extrapolation to the MS is matched to at least one local track segment in the MDT or CSC. The segment tagging is used for muons which cross only one muon chamber layer because they have a low p_{T} or because they pass through MS regions with reduced acceptance.

- Calorimeter-tagged muons: a track in the ID is classified as a muon if it is matched to a signal in the calorimeter compatible with a minimum-ionizing particle. This type of tagging is used only in the region $|\eta| < 0.1$ where no MS hits are expected because the muon spectrometer is not fully instrumented there (due to the space left for cabling).

- Extrapolated muons: the muon reconstruction is only done in the muon system and the spectrometer track is compatible with originating from the interaction point. The extrapolated muons are used in the $2.5 < |\eta| < 2.7$ region, not covered by the ID.

After the combined reconstruction, the overlaps between different muon types are resolved. From the two muons sharing the same ID track the preferable one is the combined muon, then the segment-tagged, then the calorimeter-tagged one.

The identification of prompt muons is done by applying quality requirements which allow to reject the muons from pion and kaon decays. There are four muon identification selections (*Medium*, *Loose*, *Tight* and *High-*p_{T}) which differ by the reconstruction muon types which are allowed, the number of required hits in the MDT and CSC layers, the η cuts and the cuts on the ρ' and q/p variables (for the combined muons only) where:

- The q/p *significance* is the absolute value of the difference between the charge/momentum ratio of the muons measured in the ID ($(q/p)_{\mathrm{ID}}$) and MS ($(q/p)_{\mathrm{MS}}$) divided by the sum in quadrature of the respective uncertainties (σ):

$$q/p \text{ significance} = \left| \frac{(q/p)_{\mathrm{ID}} - (q/p)_{\mathrm{MS}}}{\sqrt{\sigma(q/p)^2_{\mathrm{ID}} + \sigma(q/p)^2_{\mathrm{MS}}}} \right|. \tag{3.12}$$

- ρ' is the absolute value of the difference between the transverse momentum measured in the ID ($p_{\mathrm{T}}^{\mathrm{ID}}$) and MS ($p_{\mathrm{T}}^{\mathrm{MS}}$) divided by the transverse momentum of the combined track $p_{\mathrm{T}}^{\mathrm{CB}}$:

$$\rho' = \left| \frac{p_{\mathrm{T}}^{\mathrm{ID}} - p_{\mathrm{T}}^{\mathrm{MS}}}{p_{\mathrm{T}}^{\mathrm{CB}}} \right|. \tag{3.13}$$

The selection requirements for the ID track are the same for all muon types: ≥ 1 Pixel hit, ≥ 5 SCT hits, < 3 Pixel or SCT holes[13] and $\geq 10\%$ of the TRT hits (originally forming a track) included in the final fit.

As an example, the reconstruction efficiency for the different muon selections in $Z \to \mu\mu$ events is presented in Fig. 3.18.

3.3.5 Jets

A jet is a collimated bundle of hadrons which is formed during the hadronisation of a quark or a gluon produced in hadron collisions. It is reconstructed as a single object in the detector.

Depending on which subdetector is providing the information for the reconstruction, one distinguishes three types of reconstructed jets: *calorimeter jets*, *track jets* and *particle flow jets*.

[13] A hole is an absence of a hit in the active sensor traversed by the track.

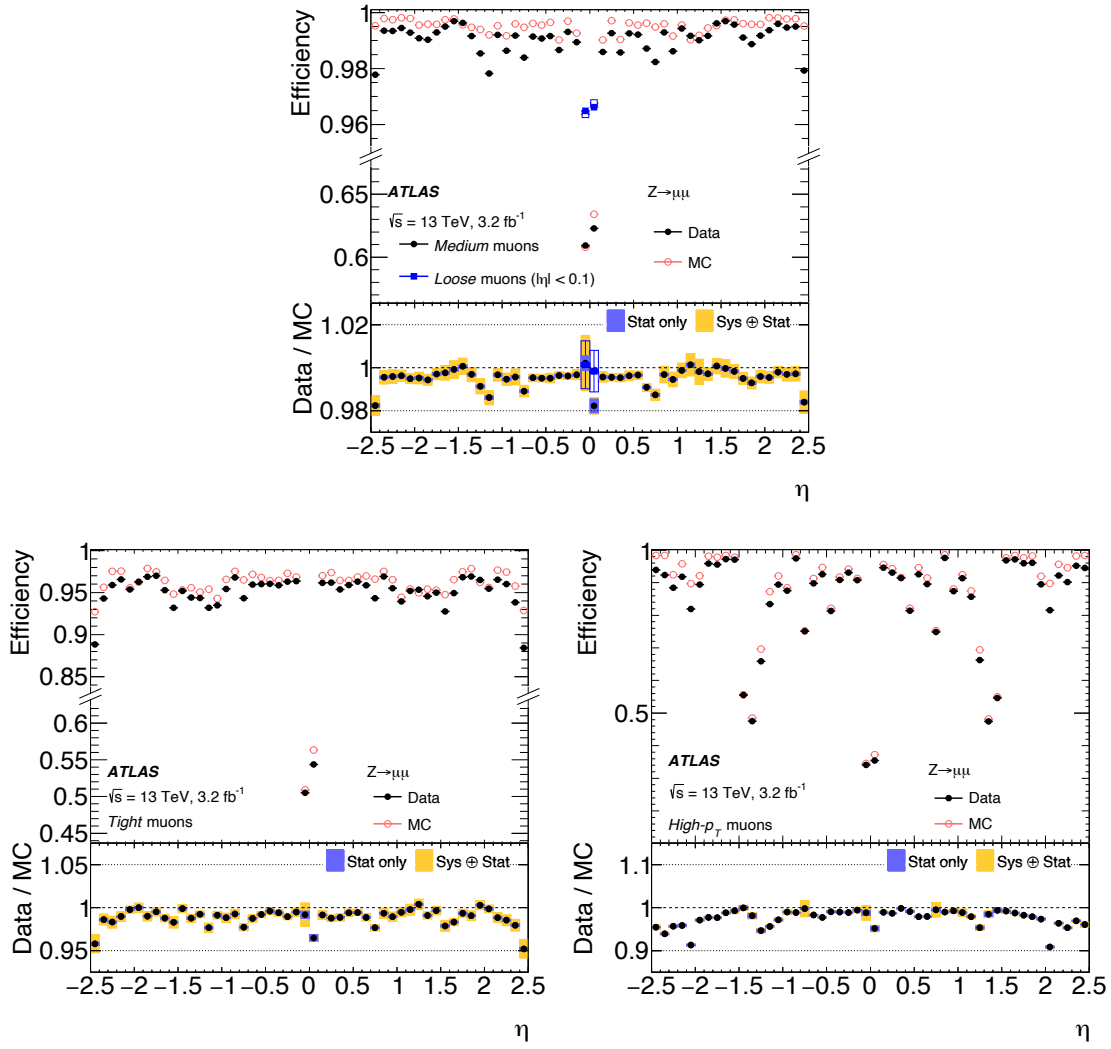

Figure 3.18: Reconstruction efficiency of the muons with $p_{\mathrm{T}} > 10$ GeV as a function of η in $Z \to \mu\mu$ events is shown for *Loose* and *Medium* (top), *Tight* (bottom left), and *High-*p_{T} (bottom right) muon selections. The data-to-simulation ratios are plotted in the bottom pads. The figure is taken from [119].

Calorimeter jets are reconstructed from topological clusters (see Section 3.3.2) in the calorimeter with the anti-k_t algorithm [121] and a radius parameter[14] $R = 0.4$ (by default) using the FastJet software package [122]. Before reconstruction, the clusters are calibrated to the electromagnetic energy scale and after reconstruction the jets are calibrated to the jet energy scale (JES) using *in situ* corrections based on data and corrections based on simulation.

The overall scheme of the calorimeter jets calibration is shown in Fig. 3.19.

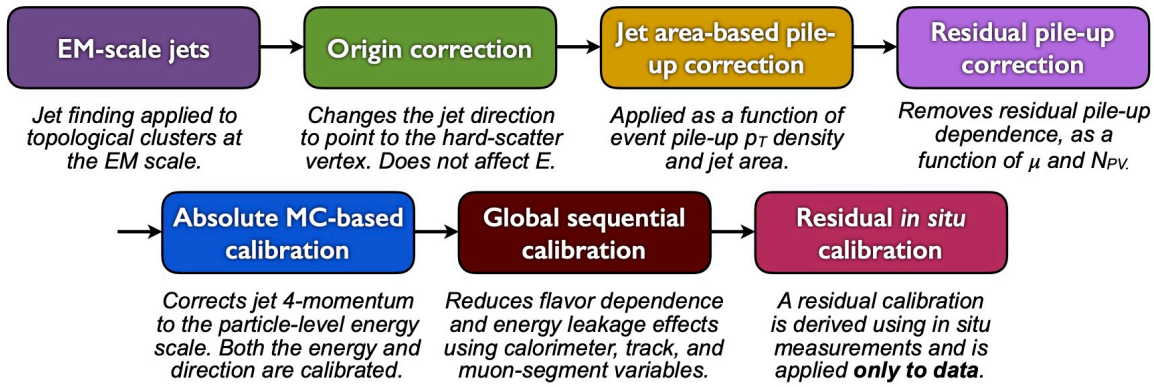

Figure 3.19: The algorithm for the jet calibration. Each stage of the calibration (except of the origin correction which does not affect the jet energy) is applied to the jet four-momentum. The figure is taken from [123].

Each step of the calibration [123] applies a correction to the jet four-momentum, except the origin correction which does not affect the jet energy.

- The first correction is applied to the jet origin to improve the jet η resolution. It is done by recalculating the jet four-momentum to point to the primary vertex rather than to the centre of the detector.

- The pile-up correction, which removes the effects of pile-up from the jet momentum measurement, is done in two steps: an area-based p_{T} density subtraction [124] and a residual correction using MC simulation.

  The pile-up contribution is calculated from the MC simulation using the median p_{T} density ρ of jets in the $\eta \times \phi$ plane: $\rho = p_{\mathrm{T}}/A$, where A is the area of a jet calculated using *ghost association*. "Ghost particles" are fictitious simulated particles of infinitesimal momentum added uniformly in solid angle to the event before the jet reconstruction. The relative number of ghost particles associated with a jet after clustering defines the jet area A. The ratio of the ρ-subtracted jet p_{T} to the uncorrected jet p_{T} is taken as a correction factor applied to the jet four-momentum.

  In addition to a global correction procedure, variables like the jet vertex fraction (JVF) and the jet vertex tagger JVT [125] are also used to reject jets that result from fluctuations in the pile-up p_{T} density [126].

[14] Radius of a conical jet in $\eta \times \phi$ plane.

- The absolute JES calibration using dijet MC events corrects the jet four-momentum to the particle-level energy scale. First, the reconstructed jet energy is corrected to the truth jet [15] energy. Jets are geometrically matched to the truth jets (they should match within $\Delta R = 0.3$[16]) and are required to be isolated, i.e. not to have other jets of $p_{\mathrm{T}} > 7$ GeV within $\Delta R = 0.6$. The jet calibration factor is taken as the inverse of the average *energy response*, which is defined as the mean of a Gaussian fit of the $E_{\mathrm{reco}}/E_{\mathrm{truth}}$ distribution (ratio of the reconstructed to the truth jet energy). An example of the jet response for dijet events simulated with Pythia is shown in Fig. 3.20.

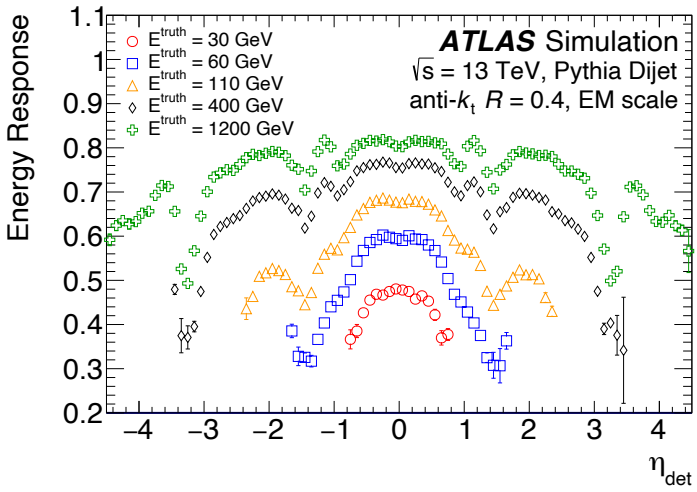

Figure 3.20: The average energy response of jets after origin and pile-up correction, corresponding to truth jets with different energies. The figure is taken from [123].

- The global sequential calibration [127] of the jet energy is done using the information from the tracker, calorimeter and the muon system. It consists in sequential application of five jet four-momentum corrections, calculated by inverting the reconstructed jet response in MC events, which account for the jet response dependence on:

  1. The fraction of jet energy measured in the first layer of the Tile calorimeter,
  2. The fraction of jet energy measured in the third layer of the LAr calorimeter,
  3. The number of tracks with $p_{\mathrm{T}} > 1$ GeV ghost-associated with the jet,
  4. The average transverse distance in the $\eta \times \phi$ plane between the jet axis and all tracks of $p_{\mathrm{T}} > 1$ GeV ghost-associated to the jet,
  5. The number of muon track segments ghost-associated with the jet.

  After each correction, a constant factor is applied to ensure that the average energy is unchanged at each stage.

[15] Truth jets are reconstructed using stable, final-state particles from MC generators as input and are defined at the particle-level energy scale.

[16] The angular distance ΔR is defined as $\Delta R = \sqrt{(\Delta\phi)^2 + (\Delta\eta)^2}$.

- The residual *in situ* calibration of the jets in the data accounts for differences in the jet response between the data and MC simulation and is done using well-measured reference objects: photons, Z bosons and well-calibrated low-p_{T} jets, where the latter are used to calibrate the high-p_{T} jets.

  For each calibration the correction factor to the jet four-momentum is defined as the ratio of the response $\mathcal{R}_{in\ situ}$ in the MC simulation and data: $\mathcal{R}^{\mathrm{MC}}_{in\ situ}/\mathcal{R}^{\mathrm{data}}_{in\ situ}$, where the response $\mathcal{R}_{in\ situ}$ is defined as the average ratio of jet p_{T} to the reference object p_{T},

Track jets (used in some Run 1 data analyses) are reconstructed from inner detector tracks using the anti-k_t algorithm with a radius parameter $R = 0.2$ or $R = 0.4$ [128]. The tracks used in the jet clustering (at least two tracks are needed for a track jet) are required to be matched to the primary vertex and have $p_{\mathrm{T}} > 0.5$ GeV and $|\eta| < 2.5$. For the track jets the pile-up, jet origin and jet energy corrections are also done (as for the calorimeter jets), as well as the global sequential calibration and the *in situ* calibration using dijet events.

Particle flow [112] is an approach introduced for Run 2, in which the jet reconstruction is done using information from both the tracker and calorimeters. The procedure is to take advantages of the best performances of both subdetectors, since low-energy particles are better reconstructed in the tracker and at high energies, the calorimeter has a better energy resolution. In the calorimeter, the topological clustering is used (see Section 3.3.2), as for calorimeter jets, and the resulting topo-clusters are calibrated at the electromagnetic scale. The tracks used in the particle flow algorithm are required to pass the "tight selection" (at least nine silicon hits with no missing pixel hits), to be within $|\eta| < 2.5$ and to have $0.5 < p_{\mathrm{T}} < 40$ GeV. Then, the particle flow algorithm attempts to match the selected tracks to the topo-clusters. Additional optimisation is done by calculating the expected energy in the calorimeter and comparing it to the actual deposit, recovering the split showers (corresponding to several topo-clusters coming from a single jet). The procedure of the track-to-cluster association is schematically illustrated in the Fig. 3.21.

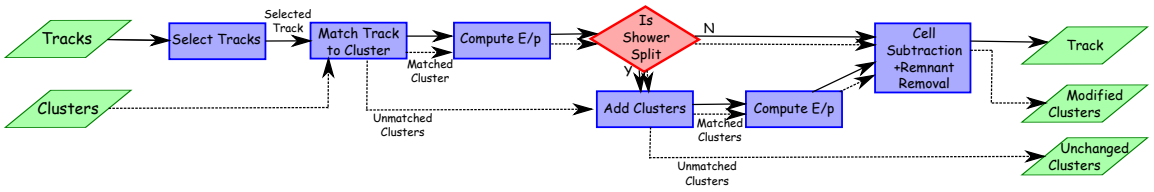

Figure 3.21: A flow-chart illustrating the particle flow algorithm. The figure is taken from [112].

The calibration of the particle flow jets is similar to the one for the calorimeter jets:

- The pile-up correction is done using the jet ghost-area subtraction method [124].
- The jet response is corrected to match the average particle level response using numerical inversion based on Monte Carlo events [129] and the global sequential correction process [127].
- The full *in situ* calibration to data is not performed, but data and MC are compared for $Z \to \mu\mu$ events in order to validate the calibration procedure.

b-tagging

The identification of jets containing b-hadrons (b-jets) is called b-tagging and is extremely important to analyse the processes involving b-quarks in the hard scattering or particle decay.

A number of b-tagging algorithms of different complexity was developed for Run 1 and Run 2 [130]:

- The impact parameter based algorithms IP2D and IP3D determine the impact parameter significance of the tracks matched to the jet and use a log likelihood ratio method to discriminate between the b-, c- and light hadrons [131].
- The secondary vertex based algorithm is explicitly reconstructing the displaced secondary vertex within a jet by building two-track vertices and then removing the ones identified with long-lived particle decay (K_S or Λ), photon conversions or hadronic interactions with the detector material [131].
- The decay chain multi-vertex algorithm, JetFitter aims at reconstructing the full decay chain: Primary Vertex $\rightarrow b \rightarrow c$-hadron. A Kalman filter is used to find the connection between the primary, secondary and tertiary (charm decay) vertices [104].
- A new multivariate b-tagging algorithm MV2c10 [132], based on a boosted decision tree, has been developed specifically for Run 2 and its main difference from the previous ones is its optimisation to use the insertable B-layer (IBL) which has been installed between Run 1 and Run 2.

  The inputs to MV2c10 are provided by the algorithms described above: a log likelihood ratio method as in IP2D/IP3D and a Kalman filter as in JetFitter. In addition, the jet p_{T} and η are included in the training to take advantage of correlations with other variables [132].

  The BDT training is performed by assigning b-jets as signal, and other jets as background. By changing the fraction of c-jets in the background one can enhance the c-jet rejection performance. The percentage of c-jets in the background is reflected in the name of the MV2 taggers (there are three of them in total, MV2c00, MV2c10 and MV2c20): MV2c10 uses 7% of c-jets, while MV2c20 uses 15% of c-jets and MV2c00 does not use any c-jets in the training [133].

  The BDT output for different jets is given in Fig. 3.22(a).

  By cutting at different values on the BDT output distribution one can achieve a different level of the c- and light jets rejection while keeping a certain fraction of the b-jets (b-jet efficiency). In such a way, the BDT cut defines a so-called *working point* (WP), for example the 70% WP will provide a 70% b-jet efficiency for a given $t\bar{t}$ sample. The dependency between the b-jet efficiency and the background rejection is shown in Fig. 3.22(b).

3.3.6 Missing transverse momentum

Neutrinos cannot be detected directly because they interact very weakly with matter. The only observable related to neutrinos which we are able to reconstruct is the missing transverse momentum vector $\vec{E}_{\mathrm{T}}^{\mathrm{miss}}$ which is the momentum of the neutrino (or a sum of momenta if several neutrinos have been produced) in the plane transverse to the beam direction. The magnitude of $\vec{E}_{\mathrm{T}}^{\mathrm{miss}}$ is usually

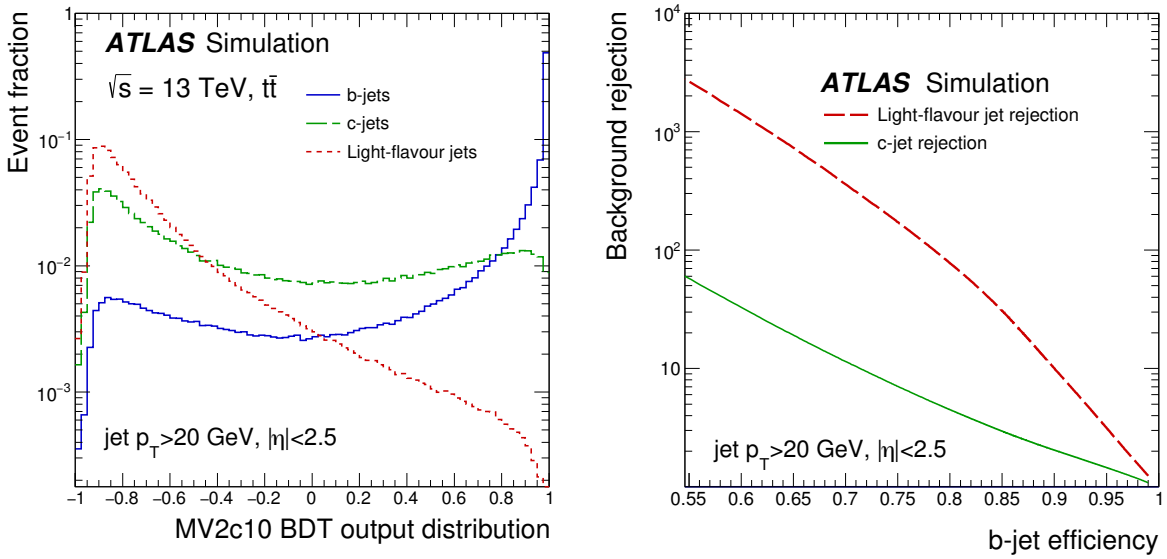

(a) (b)

Figure 3.22: (a) The MV2c10 BDT output for b-jets (blue), c-jets (green) and light-flavour jets (red) in a $t\bar{t}$ sample simulated using POWHEG+PYTHIA6. (b) The background rejection factors for c-jets (green) and light-flavour jets (red) as a function of the b-tagging efficiency of the MV2c10 algorithm. The figure is taken from [132].

denoted as $E_{\mathrm{T}}^{\mathrm{miss}}$. Since the total transverse momentum of all produced particles is expected to be zero, $\vec{E}_{\mathrm{T}}^{\mathrm{miss}}$ is a vector opposite to the sum of the transverse momenta of all other produced particles.

The reconstructed $E_{\mathrm{T}}^{\mathrm{miss}}$ includes two types of contributions [134]:

- The *hard-event signals* from fully reconstructed and calibrated particles (electrons, photons, τ-leptons, muons) and jets, which are called *hard objects*. Hard objects are selected using a standard reconstruction and identification procedures described in the above sections. The potential double counting between them is resolved.
- The *soft-event signals* which leave hits or energy deposits in the detector but cannot be reconstructed as prompt particles. The soft term of the $E_{\mathrm{T}}^{\mathrm{miss}}$ can be reconstructed in two ways. The first one is to take all the inner detector tracks coming from a primary vertex and not corresponding to the hard objects. The second way, more inclusive, is based on including the calorimeter topo-clusters which correspond to low-energy particles and do not contribute to the hard objects. However, due to larger dependence on pile-up, the calorimeter-based reconstruction has worse performance than the track-based one.

4 Top quark mass measurements

The top quark was discovered by the CDF [20] and D0 [21] collaborations at the Tevatron in 1995. Even earlier, in 1973 the existence of the third generation of quarks could be postulated [18] to explain the observed CP violations in kaon decays. After the discovery of the bottom quark in 1977 [19] it was highly expected that the sixth quark must also exist.

The top quark has a special place in the Standard Model. It is the heaviest particle of the Standard model with a mass $m_t = 172.9 \pm 0.4$ GeV [7] corresponding to a Yukawa coupling $y_t = \sqrt{2}m_t/v \approx 1$. As a result, the top quark also has a large decay width [1] $\Gamma_t \approx 1.35$ GeV and hence a short lifetime $\sim 5 \times 10^{-25}$ s, which is smaller than the time needed for the hadronisation, that is why the top quark is the only quark which does not form hadrons. Since the top quark decays before hadronisation and before spin decorrelation[2], one can measure directly its mass (see how the quarks acquire masses through the Higgs mechanism in Section 1.4).

Due to the large top quark mass, which corresponds to a value of the couplings to the Higgs boson very close to unity, loop corrections involving the top quark are often dominant in perturbative calculations. The one-loop Feynman diagrams corresponding to such corrections in some SM precision observables are shown in Fig. 4.1.

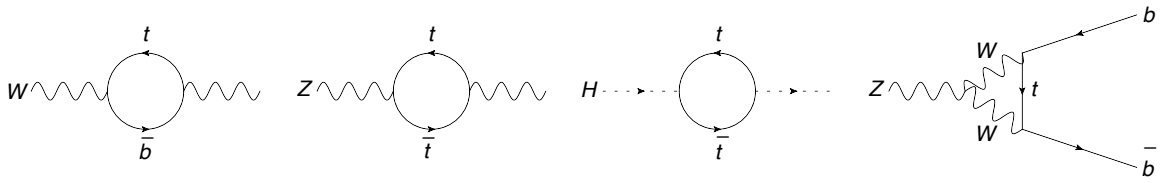

Figure 4.1: Some of the Feynman diagrams for first-order corrections to precision observables, which involve the top quark. From left to right: W, Z and Higgs boson self-energies, effective coupling of bottom quarks to the Z boson. The figure is taken from [136].

[1] The top width predicted in the SM at NLO can be expressed in terms of the top quark mass m_t, W boson mass M_W, the QCD coupling α_S and Fermi constant G_F, see [135]:

$$\Gamma_t = \frac{G_F m_t^3}{8\pi\sqrt{2}} \left(1 - \frac{M_W^2}{m_t^2}\right) \left(1 + 2\frac{M_W^2}{m_t^2}\right) \left[1 - \frac{2\alpha_S}{3\pi} \left(\frac{2\pi^2}{3} - \frac{5}{2}\right)\right] \tag{4.1}$$

[2] Top quark-antiquark pairs are produced with correlated spins and since their spins do not have enough time to decorrelate before top quark decays one can access their spin information via the top quark decay products.

Electroweak consistency tests

In particular, the top quark mass appears in the consistency tests of the electroweak sector, called *global electroweak fits*. One of the observables considered in the global electroweak fit is the W boson mass, which can be expressed in terms of well-measured electroweak quantities [137]:

$$m_W^2 = \frac{\pi\alpha}{\sqrt{2}G_{\mathrm{F}}\sin^2\theta_W(1-\Delta r)} \tag{4.2}$$

where α is the EM coupling constant, G_{F} is the Fermi constant, $\theta_W = 1 - m_W^2/m_Z^2$ is the electroweak mixing angle and Δr contains the one-loop corrections. The main contribution to the one-loop corrections comes from the top quark:

$$(\Delta r)_{\mathrm{top}} \simeq -\frac{3G_{\mathrm{F}}}{8\sqrt{2}\pi^2\tan^2\theta_W}m_t^2, \tag{4.3}$$

which corresponds to first two diagrams in Fig. 4.1. Another important contribution comes from the Higgs boson:

$$(\Delta r)_{\mathrm{Higgs}} \simeq \frac{3G_{\mathrm{F}}m_W^2}{8\sqrt{2}\pi^2}\left(\ln\frac{m_H^2}{m_Z^2} - \frac{5}{6}\right), \tag{4.4}$$

If we substitute Eqs. (4.3) and (4.4) into Eq. (4.2) and put the measured values of the top quark and Higgs boson masses, one can compare the estimation of m_W with its directly measured value, which is a consistency test of the SM. The only thing which one should keep in mind is that the constraints on m_H will be much weaker than those on m_t because the m_H dependence in Eq. (4.4) is logarithmic, which is weaker than the quadratic dependence on m_t of the top quark correction in Eq. (4.3).

The result of a global electroweak fit in Fig. 4.2 shows a comparison between the directly measured W boson and top quark masses, their estimation using the measured Higgs boson mass and various SM fits in which some of m_t, m_W, m_H are included and some are excluded (indirect measurements). The indirect measurements (blue and grey contours in the figure) agree with the direct m_t and m_W measurements, which shows the consistency of the SM. However, the large uncertainty of the indirect measurements, especially of m_t, prevents this test from being stringent enough. Therefore, new developments on more precise indirect determination of m_t and m_W are needed.

Electroweak vacuum stability

The top quark is also one of the two main contributions to the Higgs self-coupling loop corrections. There are two most important sources driving the renormalisation of λ [34],[139]:

1. The Higgs self-coupling, which alone would lead to the following solution of the RGE for λ:

$$\lambda(\mu_{\mathrm{R}}) = \frac{\lambda(v)}{1 - \frac{3}{4\pi^2}\lambda(v)\ln\frac{\mu_{\mathrm{R}}^2}{v^2}} \qquad (\text{ + subleading terms}), \tag{4.5}$$

   where $\mu_R > v$ is some renormalisation scale.

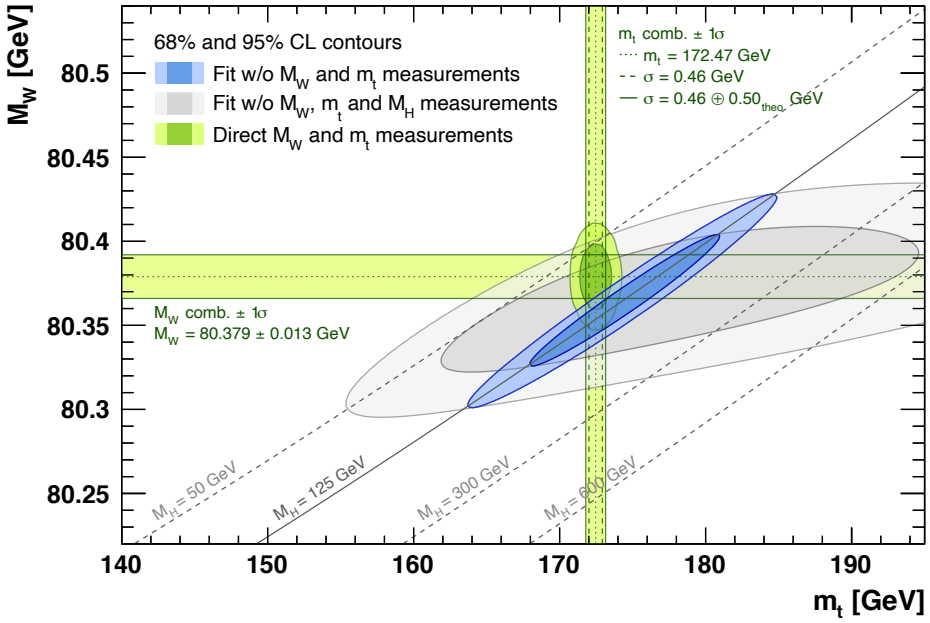

Figure 4.2: Contours at 68% and 95% confidence level of W boson mass versus top quark mass coming from SM fits including (blue) and excluding (grey) the Higgs mass measurements, compared to their direct measurements (green bands and ellipses). The figure is taken from [138].

2. The Higgs coupling to the top quark, which alone would give another RGE solution:

$$\lambda(\mu_R) = \lambda(v) - \frac{2m_t^4}{4\pi^2 v^4} \ln \frac{\mu_R^2}{v^2} \qquad (\text{ + subleading terms}), \tag{4.6}$$

The self-renormalisation (case 1) makes λ larger with increasing energy Q which may lead to a singularity similar to the Landau pole. The renormalisation by the top quark, on the other hand, reduces λ with increasing Q and may drive it to negative values at some high scale above v.

If λ turns negative, the sides of the Higgs potential will bend and go down to minus infinity instead of plus infinity as before. Then, the VEV won't be at the true minimum of the potential anymore, which would lead to a possible tunnelling of the Higgs field from the original VEV to the lower (maybe, an infinitely low) value of the potential and would destabilise the Universe. The probability of the tunnelling in this case defines the lifetime of the Universe.

Therefore, the masses of the Higgs boson and of the top quark are the key parameters influencing the stability of the SM vacuum. The phase diagram of the stability for the different values of m_H^{pole} and m_t^{pole} is shown in Fig. 4.3, where m_H^{pole} and m_t^{pole} refer to the masses in *pole renormalisation scheme*[3].

The experimentally measured values of the Higgs and top quark masses ($m_t \sim 173$ GeV, $m_H \sim 125$ GeV) correspond in Fig. 4.3 to a metastable vacuum, that is with a very long lifetime. The Higgs self-coupling

[3] The different mass definitions will be discussed in Section 4.1 for the example of the top quark

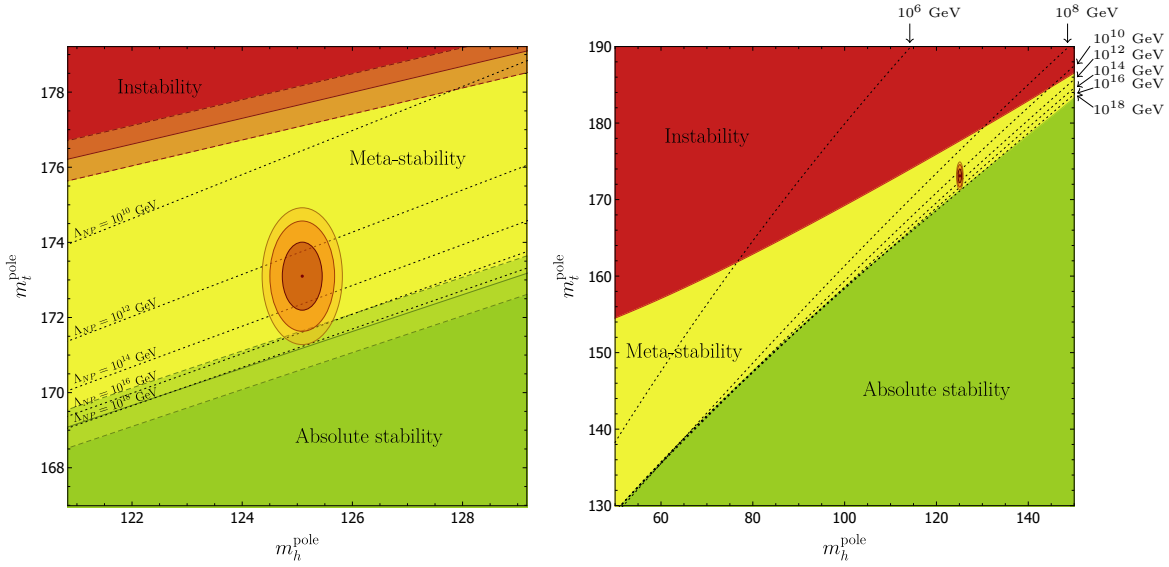

Figure 4.3: Phase diagram for stability in the m_t^{pole}/m_H^{pole} plane. The Higgs and top quarks masses are defined in pole renormalisation scheme. The figure is taken from [140].

λ will turn negative at a scale $\sim 10^{10}$–10^{14} GeV if no physics beyond the Standard Model is present at a lower energy scale. However, the lifetime of the vacuum which can be estimated [140] appears to be 10^{161} years, which is much larger than the current lifetime of the Universe.

For all the reasons outlined above, a precise determination of the top quark mass is important.

4.1 Theoretical definition of the top quark mass

The top quark mass, as all other quark masses, is subjected to QCD loop corrections and its value depends on a choice of the renormalisation scheme. In the context of the global electroweak fit, where the top quark mass is used, the conventional choice is the *pole mass*. In this definition, the top quark is considered as a "free" fermion, for which the pole mass is defined as the real part of the pole of the renormalised top quark propagator [4] [141].

In the pole mass scheme the divergent mass corrections are subtracted in such a way that the pole in the quark propagator remains fixed at any order in perturbation theory [142].

[4] The propagator is a function that specifies the probability amplitude for a particle to travel between two spacetime points. A propagator in momentum space represents a particle travelling with a certain momentum and is denoted in Feynman diagrams as a line. For example, a momentum-space propagator of a free spin-1/2 particle with a mass m and a 4-momentum p is written as

$$S(p) = \frac{\gamma^\mu p_\mu + m}{p^2 - m^2 + i\epsilon}, \tag{4.7}$$

where γ^μ are Dirac gamma matrices and $i\epsilon$ with $\epsilon \to 0$ is a prescription for how to handle the poles in the complex p_0-plane.

The advantage of the pole mass scheme is that the pole mass is gauge invariant at each order of the perturbation theory and finite in the infrared limit (at asymptotically low energies).

However, the top quark mass parameter that is introduced in the QCD Lagrangian coincides with the position of the pole in the quark propagator only at zeroth order in perturbation theory. At higher orders the top mass requires renormalisation. It can be shown that the sum of the infrared QCD radiative corrections at all orders lead to some irreducible intrinsic uncertainties of the pole mass definition [141, 142]. This full QCD correction to the pole mass is of the order of the QCD scale Λ_{QCD} and is called a *renormalon ambiguity* or an *infrared renormalon* [143]. The theoretical calculations predict a value for the renormalon ambiguity equal to 110 [144] or 250 [145] MeV[5].Therefore, any measurement of the top quark pole mass cannot be more precise than these values.

Alternatively, the top quark mass can be defined in the *minimal subtraction renormalisation scheme* ("MS mass"), or as other "short-distance mass" [141]. The class of "short-distance masses" include scale-dependent mass definitions, which do not contain any non-perturbative ambiguities and can be converted to the pole mass at a given order of perturbation theory in a unique way [141] (still, within an uncertainty). The characteristic feature of the MS scheme is the subtraction of a pure $1/\epsilon$ pole in the divergent mass correction. Also, in the MS scheme the position of the pole in the top quark propagator receives corrections at all orders in perturbation theory [142]. The MS scheme defines a mass at a given energy scale and its energy dependence is defined by the RGE, which can be solved at the four-loop order in perturbation theory [146]. The general relation of the top quark masses defined in the pole and MS schemes is expressed as follows:

$$m_t^{\mathrm{pole}} = m_t^{\mathrm{MSr}}(R,\mu) + \delta m_t(R,\mu), \tag{4.8}$$

where m_t^{pole} is the pole mass, R and μ are energy scale parameters [147] of the so-called "MSr" mass m_t^{MSr} and the difference δm_t contains corrections known to four-loops in QCD [148]. At $R = 0$ the MSr mass equals to the pole mass and at $R = m$, where m is defined to be as $m_t^{\mathrm{MSr}}(m) = m$, it turns into the "$\overline{\mathrm{MS}}$" mass, which corresponds to the *modified minimal subtraction renormalisation scheme* [142]. Therefore, the MSr mass can be considered as a formal interpolation between the $\overline{\mathrm{MS}}$ mass and the pole mass.

The difference between the pole mass m_t^{pole} and the $\overline{\mathrm{MS}}$ mass m for $m = 163.643$ GeV is about 10 GeV [148]:

$$m_t^{\mathrm{pole}} = m + \underbrace{7.557}_{\mathrm{NLO}} + \underbrace{1.617}_{\mathrm{NNLO}} + \underbrace{0.501}_{\mathrm{N^3LO}} + \underbrace{0.195 \pm 0.005}_{\mathrm{N^4LO}} \text{ GeV}, \quad m = 163.643 \text{ GeV}, \ \alpha(6)_{\mathrm{S}}(m) = 0.1088. \tag{4.9}$$

Which top mass definition should be used to describe the experimentally measured mass, is still an open question. In [147] it is argued that the "Monte-Carlo" mass obtained in direct top quark measurements (see section Section 4.3) is close to the MSr mass evaluated at small scale. In [149] an approximate relation between the Monte-Carlo mass and the MSr mass at $R = 1$ GeV is found, which gives a difference of 200 MeV between those masses. On the other hand, the pole mass, which is claimed to be determined in indirect measurements (see section Section 4.4) differs from the MSr

[5] Such discrepancy comes from different orders at which the two calculations of the top quark mass ambiguity are truncated.

mass by the similar amount [142]. Given that, one could speculate that the Monte-Carlo mass and the pole mass values are very close, at least within the current top quark mass measurement uncertainty which is about 0.5 GeV, but the discussion is still ongoing among theorists. For example, in [147] it is suggested to include two additional components in the MC mass uncertainty if one identifies it with the pole mass: 0.5 GeV which accounts for the problem of MC mass interpretation plus 250 MeV for the pole mass renormalon ambiguity. Another possibility, recommended by the author of [147] is to identify the MC mass with the MSr mass at $R = 1.3$ GeV by adding an uncertainty of 0.5 GeV due the interpretation problem.

4.2 Top-quark pair production at the LHC

Since the top quark interacts via all SM forces, there are many possible ways to create top quarks. At hadron colliders, such as LHC and Tevatron, the most probable production channels are through strong interaction. At Tevatron, protons were collided at 1.96 TeV centre-of-mass energy against antiprotons and hence the antiquarks were present as *valence quarks*[6]. The main production channel was $q\bar{q} \rightarrow t\bar{t}$ (85%). The corresponding Feynman diagram is shown in Fig. 4.4 (a).

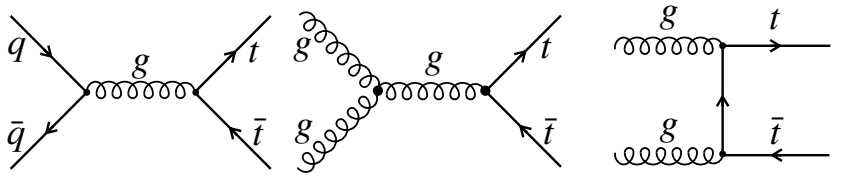

(a) $q\bar{q}$ annihilation (b) gluon fusion, s-channel (c) gluon fusion, t-channel

Figure 4.4: Feynman diagrams of the $t\bar{t}$ production.

At LHC, which is a proton-proton collider, the top quark pairs are mainly produced through gluon fusion (80-90%). During Run 1, protons were collided at the centre-of-mass energies 7 and 8 TeV and during Run 2, the centre-of-mass energy reached 13 TeV. The corresponding Feynman diagrams are shown in Fig. 4.4 (b) and Fig. 4.4 (c).

The centre-of-mass energy ($\sqrt{s}$) dependence of the $t\bar{t}$ production cross section is shown in Fig. 4.5 [150]. The production cross section measured at the Tevatron and the LHC is compared to the NNLO+NNLL theoretical prediction [151, 152].

The top quark reconstruction methods and the overall analysis strategy largely depend on the top quark decay mode which is chosen for the event selection. The top quark itself decays in almost 100% of the cases into a W boson and a b quark, since the corresponding V_{tb} element of the CKM matrix is about 0.999. Then, the b quark creates a b-jet and the W-boson can decay either leptonically (into a lepton and a neutrino) or hadronically (into two quarks), see Fig. 4.6.

[6] The quarks determining the quantum numbers of an hadron are called valence quarks. For example, two u quarks and a d quark are the valence quarks of the proton.

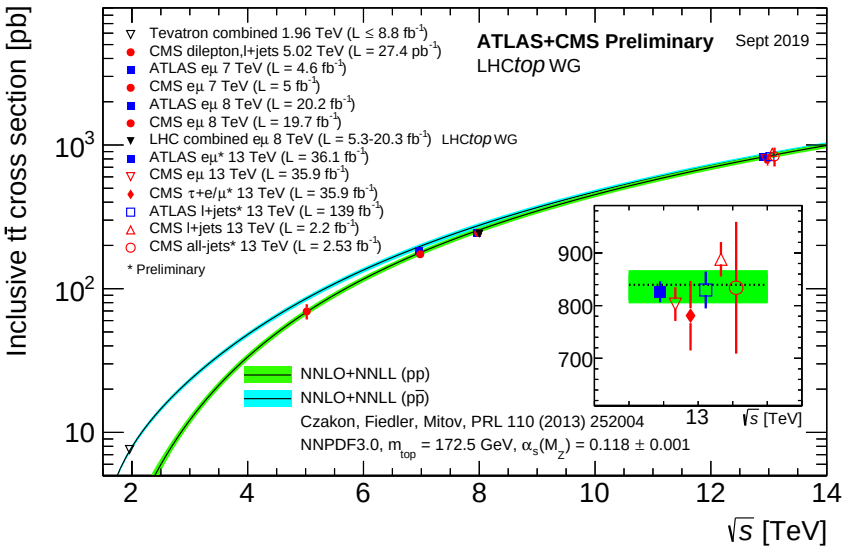

Figure 4.5: Summary of the ATLAS, CMS and combined Tevatron measurements of the top-pair production cross-section as a function of the centre-of-mass energy [150] compared to the NNLO QCD calculation complemented with NNLL soft-gluon resummation (calculated using the Top++2.0 program [151, 152]).

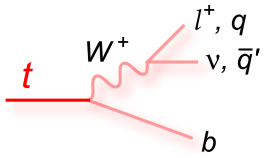

Figure 4.6: The Feynman diagram of the top quark decay [153].

Depending on the decay channels of two W bosons coming from the decay of a $t\bar{t}$ pair, either two leptons and two jets can be produced, or one lepton and four jets, or six jets, which are called the *dilepton*, *lepton+jets* and *all-hadronic* (or *all-jets*) $t\bar{t}$ decay channels, respectively. Fig. 4.7 shows a scheme with all top pair decay channels and a pie chart illustrating the sizes of the top pair branching fractions. One can notice that the all-hadronic decay channel benefits from high data statistics (and small statistical uncertainty), since it is the most populated one. However, it suffers from high background contamination since there are a lot of processes with only jets in final state. On the other hand, the dilepton channel has an opposite problem: while having a "clean", easily reconstructable final state with smaller background it has lower probability.

4.3 Standard top quark mass measurements

Currently, the most precise top quark mass measurements are done using the direct or "standard" methods, leading to an uncertainty around 0.5%. In these methods, mainly, the top quark mass distribution is directly reconstructed from the measured top quark decay products. When a full

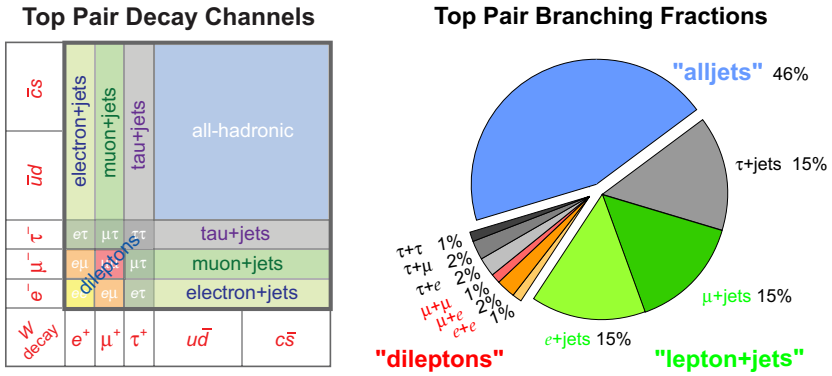

Figure 4.7: Overview of top quark pair decay channels (left) and relative size of top quark pair branching fractions (right). The pictures are taken from [153].

reconstruction of the top quark mass is impossible, a distribution of a variable that is highly sensitive to m_t is used.

There are three main types of standard measurements:

- In the **"template method"**, the top quark decay kinematics is fully or partially reconstructed and then probability density functions are built from templates constructed with MC simulation for the chosen observables sensitive to m_t. The measured distribution of a chosen variable is compared to the templates generated for different values of m_t and then a likelihood or a χ^2 fit is used to determine the top quark mass. If the top quark is fully reconstructed (in the lepton+jets or the all-hadronic top quark decay channels), the distribution of the reconstructed top quark masses itself can be used to build the templates. In the dileptonic channel with partial reconstruction the distribution of the invariant mass of a lepton and a b-jet (M_{lb}) is often used. A multi-dimensional template fit built from several input distributions can be used to determine the top quark mass together with other parameters, e.g. a global jet energy scale factor (JSF).

  The template method has been exploited by all experiments which measure the top quark mass: CDF and D0 at the Tevatron and ATLAS and CMS at the LHC. Currently it is used in most of the ATLAS direct measurements.

- The **"matrix element method"** uses all kinematic information to calculate the probability of each event to be compatible with the $t\bar{t}$ process. This probability depends on m_t and possible other parameters. The probability is calculated using leading-order matrix elements describing the signal and background processes relevant for the analysis. The measured ("detector-level") four-vectors are linked to parton-level four vectors used in the matrix element throught the probabilistic transfer functions [154].

  At CDF and D0 which had rather small data sets compared to the ones provided by the LHC, the matrix element method was widely used, because it maximises the statistical power of the considered data sample. However, this comes at the cost of a high computational demand.

- The **"ideogram method"**, invented at the Tevatron and now mostly used by CMS, combines the above two approaches and can be considered as an effective approximation of the matrix element

method. In this approach, the kinematic fit of the top quark decay products to a $t\bar{t}$ hypothesis is compared to the MC-based likelihood functions (ideograms) for each event. The ideograms can be one- or multi-dimensional depending on additional parameters to be determined from data along with the top quark mass.

The most precise top quark mass measurements using the Tevatron $p\bar{p}$ collision data at a centre-of-mass energy $\sqrt{s} = 1.96$ TeV are done in the lepton+jets decay channel and yield a total uncertainty below 1 GeV. The best D0 measurement giving $m_t = 174.98 \pm 0.76$ GeV [155] is done with 9.7 fb^{-1} of integrated luminosity using the matrix element technique. The best measurement done by the CDF collaboration uses 5.6 fb^{-1} of integrated luminosity and gives $m_t = 172.1 \pm 1.1(\text{stat.}) \pm 0.9(\text{syst.})$ GeV [156]. The measurement is performed by constructing templates of three kinematic variables in the lepton+jets channel and of two kinematic variables in the dilepton channel.

The combination of all published results from the Tevatron Run I (1992–1996) and the most precise published and preliminary results from Run II (2001–2011), performed using the best linear unbiased estimator (BLUE) method [157], yields $m_t = 174.30 \pm 0.65$ GeV [158].

The ATLAS and CMS collaborations performed a variety of direct m_t measurements using pp collision data collected at the LHC at $\sqrt{s} = 7, 8$ and 13 TeV.

The latest m_t measurements in the all-hadronic decay channel are described below:

- The ATLAS measurement is using 20.2 fb^{-1} of data at $\sqrt{s} = 8$ TeV [159]. The top-quark mass is obtained from template fits to the ratio of a three-jet mass to a dijet mass. The three-jet mass corresponds to three jets coming from the top quark decay and the dijet mass is obtained from two jets assigned to the W boson decay. The measured top quark mass is:

$$m_t = 173.72 \pm 0.55(\text{stat.}) \pm 1.01(\text{syst.}) \text{ GeV}. \tag{4.10}$$

- The CMS measurement at $\sqrt{s} = 13$ TeV is using 35.9 fb^{-1} of pp collision data [160]. The decay of the $t\bar{t}$ system is reconstructed using a kinematic fit and the top quark mass is determined together with a jet energy scale factor (JSF). The resulting top quark mass is:

$$m_t = 172.34 \pm 0.20(\text{stat.} + \text{JSF}) \pm 0.76(\text{syst.}) \text{ GeV}. \tag{4.11}$$

The latest m_t measurements in the lepton+jets decay channel are described below:

- The ATLAS measurement is using 20.2 fb^{-1} of data at $\sqrt{s} = 8$ TeV [161]. The top quark mass is determined together with a JSF and a relative b-to-light jet energy scale factor exploiting a three-dimensional template technique. The top quark mass is measured to be:

$$m_t = 172.08 \pm 0.39(\text{stat.}) \pm 0.82(\text{syst.}) \text{ GeV}. \tag{4.12}$$

- The CMS measurement is using 19.7 fb^{-1} data set at $\sqrt{s} = 8$ TeV [162]. The measured top quark mass is:

$$m_t = 172.35 \pm 0.16(\text{stat.}) \pm 0.48(\text{syst.}) \text{ GeV}. \tag{4.13}$$

  The top quark mass is also studied as a function of the event kinematic properties.

- CMS has also performed a measurement using 35.9 fb^{-1} of data at $\sqrt{s}$ = 13 TeV [163]. The mass is reconstructed from a kinematic fit of the decay products to a $t\bar{t}$ hypothesis. Using the ideogram method, the top quark mass is determined simultaneously with an overall jet energy scale factor (JSF):

$$m_t = 172.25 \pm 0.08(\text{stat.} + \text{JSF}) \pm 0.62(\text{syst.}) \text{ GeV}. \tag{4.14}$$

The latest m_t measurements in the dilepton decay channel, both performed using $\sqrt{s}$ = 8 TeV data, are described below:

- The ATLAS measurement is using 20.2 fb^{-1} of data [164], in which the top quark mass is measured using the distributions of the invariant masses of lepton-b-jet pairs and yields:

$$m_t = 172.99 \pm 0.41(\text{stat.}) \pm 0.74(\text{syst.}) \text{ GeV}. \tag{4.15}$$

- The CMS measurement is using 19.7 fb^{-1} of data [165]. The top quark mass together with a JSF is determined using three kinematic observables sensitive to the value of m_t: an invariant lepton-b-jet mass in one approach or an invariant lepton-neutrino-b-jet[7] mass in another approach which is fit simultaneously with a "stransverse mass"[8]. The top quark mass is measured to be:

$$m_t = 172.22 \pm 0.18(\text{stat.})^{-0.93}_{+0.89}(\text{syst.}) \text{ GeV}. \tag{4.16}$$

The summary of all ATLAS and CMS direct m_t measurements is presented in Fig. 4.8 together with the 2018 ATLAS combination, the 2015 CMS combination and earlier LHC and LHC+Tevatron combinations [150].

The main weakness of the standard methods is that they largely rely on the Monte Carlo (MC) simulations, which are used for the calibration, and hence a top quark mass extracted using a standard method could be called a "MC mass". The MC mass is a parameter of a Monte Carlo generator which may differ by several hundreds of MeV from a well-defined top quark mass in the quantum field theory: pole mass or, for instance, $\overline{\text{MS}}$ mass. This difference comes from the fact that the MC generators use an energy cut in the parton shower and also model the hadronisation step and the colour reconnection, which cannot be computed with perturbative QCD [141]. An additional source of the difference could be also the modelling of the top quark width in the MC, which is not always implemented following rigorous QCD prescriptions.

4.4 Alternative top quark mass measurements

Indirect or "alternative" methods to measure the top quark mass are able to measure a pole or a $\overline{\text{MS}}$ mass because they measure observables which can be obtained from fixed order theoretical

[7] The neutrino momentum is estimated by the MAOS reconstruction technique which is explained in [166].

[8] The stransverse mass is constructed with the b and $\bar{b}$ daughters of the $t\bar{t}$ system. The nick-name "stransverse mass" arose as a shortened form of "supersymmetric transverse mass", since is was originally applied to supersymmetric events in cases where the transverse mass was no longer usable [167].

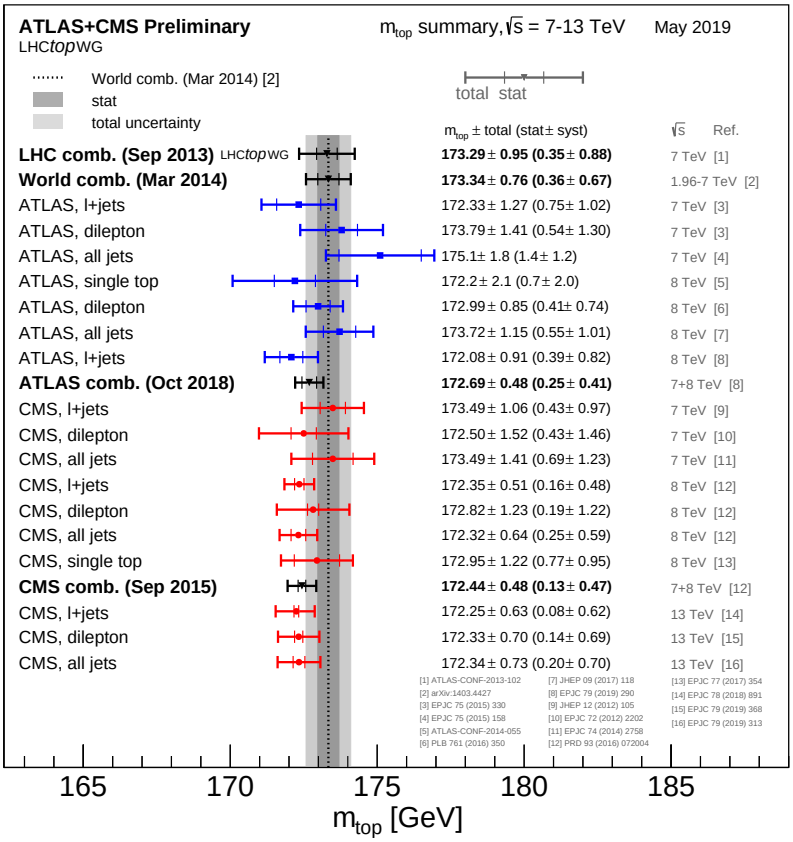

Figure 4.8: Summary of the ATLAS and CMS measurements performed using different top quark decay (direct) compared with the LHC and Tevatron+LHC combinations [150].

calculations at NLO or NNLO. Indirect measurements exploit the top quark mass dependence of inclusive or differential $t\bar{t}$ production cross sections.

The first analyses to extract the pole or the $\overline{\text{MS}}$ mass were performed by the D0 collaboration [168, 169]. The inclusive measured $t\bar{t}$ production cross section was compared to its NNLO and NLO+NNLL theoretical calculation and the pole mass was extracted using a likelihood method. The $\overline{\text{MS}}$ mass was calculated in [168] using a conversion formula at three-loop level (see Section 4.1).

Despite the fact that currently the total $t\bar{t}$ cross section is calculated rather precisely, at NNLO+NNLL [151], the top quark mass measurements which use solely an inclusive cross section give a top quark mass uncertainty not less than 2 GeV, see the latest ATLAS and CMS results:

- The ATLAS measurement is using the 13 TeV data set of 36.1 fb^{-1} [170]. The top quark pole mass is extracted by comparing the $t\bar{t}$ production cross section measured using $e\mu$ events to the theoretical calculations at NNLO+NNLL:

$$m_t^{\text{pole}} = 173.1^{+2.0}_{-2.1}\ \text{GeV}. \tag{4.17}$$

- The CMS measurement is using 35.9 fb^{-1} of 13 TeV data analysed in the dilepton top quark decay channel [171]. The top quark mass together with the strong coupling constant are extracted from the $t\bar{t}$ production cross section compared to the NNLO theoretical predictions. The top quark pole and $\overline{\text{MS}}$ masses are extracted using different PDF sets, for example, the result for the NNPDF3.1 set is:

$$\begin{aligned} m_t^{\text{pole}} &= 172.4 \pm 1.6(\text{fit} + \text{PDF}{+}\alpha_S)^{+1.3}_{-2.0}(\text{scale})\ \text{GeV}, \\ m_t^{\overline{\text{MS}}}(m_t) &= 164.5 \pm 1.5(\text{fit} + \text{PDF}{+}\alpha_S)^{+0.1}_{-1.0}(\text{scale})\ \text{GeV}. \end{aligned} \tag{4.18}$$

Differential cross sections $d\sigma_{t\bar{t}}/dX$ allow for more precise top quark mass measurements because they carry more information than the inclusive cross section and include the m_t dependence not only in the overall normalisation, but also in the shape of the distribution. From this point of view the absolute cross sections are more advantageous than the normalised ones, however, the normalised cross sections allow to reduce the experimental uncertainty components.

The latest m_t^{pole} and $m_t^{\overline{\text{MS}}}$ measurements using single differential cross sections are discussed below:

- The ATLAS measurement with 20.2 fb^{-1} of data at 8 TeV uses $t\bar{t}$ events in the dileptonic final state [172]. The single lepton and dilepton kinematic distributions are measured and are compared to the predictions from a variety of MC event generators, as well as fixed-order QCD calculations. A combined fit of NLO fixed-order predictions to all the measured distributions yields a top quark mass value of:

$$m_t^{\text{pole}} = 173.2 \pm 0.9(\text{stat.}) \pm 0.8(\text{syst.}) \pm 1.2(\text{theo.})\ \text{GeV}. \tag{4.19}$$

- The ATLAS measurement with 20.2 fb^{-1} of data at 8 TeV uses $t\bar{t}+1$ jet events in the lepton+jets final state [173]. The top quark pole and $\overline{\text{MS}}$ masses are obtained by comparing the normalised $t\bar{t}$+jet differential cross section to the NLO QCD predictions:

$$\begin{aligned} m_t^{\text{pole}} &= 171.1 \pm 0.4(\text{stat.}) \pm 0.9(\text{syst.})^{+0.7}_{-0.3}(\text{theo.})\ \text{GeV}, \\ m_t^{\overline{\text{MS}}}(m_t) &= 162.9 \pm 0.5(\text{stat.}) \pm 1.0(\text{syst.})^{+2.1}_{-1.2}(\text{theo.})\ \text{GeV}. \end{aligned} \tag{4.20}$$

- The CMS measurement with 19.7 fb^{-1} of data at 8 TeV uses top quark pair events produced in association with additional hard jets in the dilepton top quark decay channel [174]. The mass is extracted from the normalised invariant mass distribution of the $t\bar{t}$+jet system and the related normalised differential cross section and gives:

$$m_t = 169.9 \pm 1.1(\text{stat.})^{+2.5}_{-3.1}(\text{syst.})^{+3.6}_{-1.6}(\text{theo.})\ \text{GeV}. \tag{4.21}$$

- The CMS measurement with 35.9 fb^{-1} of data at 13 TeV uses $t\bar{t}$ events in the dilepton decay channel [175]. The mass of the top quark in the $\overline{\text{MS}}$ scheme as a function of the scale (equal to the $t\bar{t}$ invariant mass) is extracted from a comparison of the differential $t\bar{t}$ cross section as a function of the $t\bar{t}$ invariant mass to NLO theoretical predictions. The results are shown in Fig. 4.9.

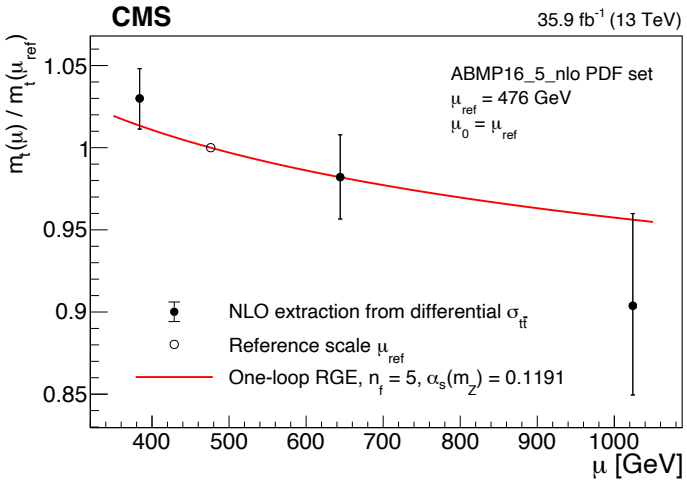

Figure 4.9: Extracted running of the top quark mass $m_t(\mu)/m_t(\mu_{\text{ref}})$ compared to the RGE NLO prediction [175].

- The CMS measurement with 35.9 fb^{-1} of data at 13 TeV uses $t\bar{t}$ events with boosted top quarks in the lepton+jets decay channel [176]. The $t\bar{t}$ cross section as a function of the jet mass is used to extract the top quark mass of:

$$m_t = 172.6 \pm 0.4(\text{stat.}) \pm 1.6(\text{exp.}) \pm 1.5(\text{model}) \pm 1.0(\text{theo.})\ \text{GeV}. \tag{4.22}$$

The analysis can be improved further by using several sensitive observables in order to build a multi-dimensional differential cross section, which could potentially result in an even more precise top quark mass measurement, if the statistical uncertainty would be small enough. Currently, there is only one such measurement which is published:

- The CMS measurement with 35.9 fb^{-1} of data at 13 TeV uses $t\bar{t}$ events in the dilepton decay channel [177]. The triple-differential $t\bar{t}$ cross section measurement as a function of the invariant mass and rapidity of the $t\bar{t}$ system and the multiplicity of additional jets compared to NLO predictions is used to extract values of the strong coupling strength α_S and the top quark pole mass:

$$m_t^{\text{pole}} = 170.5 \pm 0.7(\text{fit}) \pm 0.1(\text{model})^{+0.0}_{-0.1}(\text{param.}) \pm 0.3(\text{scale})\ \text{GeV}. \tag{4.23}$$

The analysis which will be described in this thesis in Chapter 5 uses double differential cross sections and is the first analysis, in which the measured differential $t\bar{t}$ cross sections are compared to the NNLO theoretical predictions.

The summary of the ATLAS and CMS indirect top quark mass measurements compared to the ATLAS and CMS combinations is shown in Fig. 4.10.

4.5 Systematic uncertainties

At Tevatron and during Run I at LHC the recorded data samples were relatively small and the statistical uncertainty was often a dominant one. Now, for the Run II analyses, as the analysed data samples

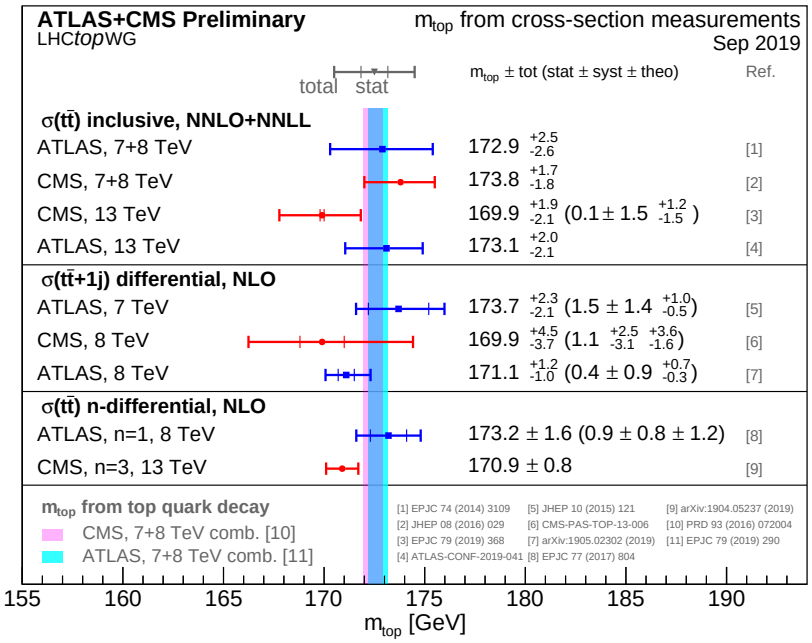

Figure 4.10: Summary of indirect m_t measurements at ATLAS and CMS compared to ATLAS and CMS combinations [150].

become larger and the respective statistical uncertainty become smaller, the systematic and theoretical components of the total uncertainty on top quark measurements becomes more and more important. The theoretical uncertainty is often not under our control since it depends on the availability of more precise theoretical calculations. However, one can elaborate new analysis methods and new observables which could be less influenced by the higher-order corrections and more sensitive to the top quark mass. On the other hand, many components of the systematic uncertainty are constrained from data and can be improved and reduced.

4.5.1 Uncertainties on the signal process ($t\bar{t}$) modelling

Usually, the following sources of $t\bar{t}$ modelling uncertainties are considered[9]:

- The uncertainty on the parton density functions describing the proton content,
- The uncertainty related to the modelling of the perturbatively calculated processes: matrix element (ME), parton showering (PS), ME/PS NLO matching, scale choices in these calculations,
- The uncertainty related to the modelling of the non-perturbative processes: hadronisation, colour reconnection (CR), underlying event (UE).

[9] For some of the uncertainties, it is difficult to unambiguously separate different effects, e.g. the matrix element and the parton shower. Here, we describe a common convention for the uncertainty breakdown, used in ATLAS and CMS.

In what follows, we will describe one by one how the different systematic uncertainty components are defined for the top quark mass measurements in ATLAS and CMS and how some of them can be possibly improved (in the context of ATLAS analyses).

- The uncertainty related to the choice of the **matrix element** generator is determined by comparing two setups where the ME is implemented either with POWHEG or with MC@NLO. This approach have been used for various analyses in both experiments. Currently, in many ATLAS analyses, the POWHEG–MC@NLO difference is said to cover also the uncertainty related to the choice of the NLO matching scheme. Sometimes, instead of MC@NLO, SHERPA is used as an alternative ME generator.

  Recently, CMS chose to define the NLO matching uncertainty by comparing PYTHIA setups with different values of the $h_{\text{damp}} = 1.58^{+0.66}_{-0.59}$ parameter[10] within its uncertainties.

- The uncertainties coming from the choice of the **renormalisation and factorisation scales** in the modelling of the ME, PS, initial and final state radiation (ISR/FSR) are estimated by varying the corresponding parameters in PYTHIA.

  In ATLAS, usually, a single *ISR/FSR* uncertainty is defined which accounts for all variations. It is found by comparing PYTHIA setups with different PERUGIA tunes [81]: PERUGIA 2012 RADLO and RADHI, which differ in several parameters: QCD scale Λ_{QCD}, h_{damp} (equal to m_t or $2m_t$), and the ME $\mu_{\text{R}}/\mu_{\text{F}}$ scales (which vary by a factor of 2 up and down). However, recent ATLAS recommendations describe separate ISR and FSR uncertainties. In these updates, the *ISR uncertainty* is obtained by comparing two PYTHIA setups where the h_{damp} parameter, the ME scales and tuned variations of the shower ISR are varied coherently. The *FSR uncertainty* is calculated by varying the $\mu_{\text{R}}/\mu_{\text{F}}$ parton shower scales by a factor 2 up and down.

  CMS estimates μ_R/μ_F scale uncertainties by varying μ_R/μ_F by a factor of two up and down in the matrix element, initial and final state radiation. For the FSR scales sometimes a factor of $\sqrt{2}$ is used instead of a factor of 2. Depending on the analysis, either a single μ_R/μ_F scale uncertainty is defined (in this case, the scales are varied simultaneously), or separate uncertainties for ME, ISR scales and FSR scales.

- To estimate the **hadronisation** modelling uncertainty, the parton showers modelled with HERWIG and PYTHIA are compared, since they use two different hadronisation schemes: in HERWIG the cluster hadronisation model is implemented and in PYTHIA it is the string model. In some ATLAS analyses (e.g. in [173]), the PYTHIA–HERWIG comparison also includes an uncertainty that covers parton shower effects. In this case, different types of parton showers are taken in the two generators: a p_{T}-ordered shower in PYTHIA and an angular-ordered shower in HERWIG. This is an alternative way to estimate the parton shower uncertainty, comparing to the one mentioned above, in which the $\mu_{\text{R,F}}$ scales are varied within a single type of parton shower in PYTHIA. In Chapter 6, another approach to the parton shower uncertainty estimation in discussed, in which both, the shower type variations and the scale variations are considered for the parton shower simulated with the HERWIG generator.

[10] The resummation damping factor h_{damp} is a parameter of the ME/PS matching which adjusts the radiation at high p_{T}.

In recent analyses the PYTHIA–HERWIG difference is referred to as an hadronisation uncertainty, however it is not a consistent estimate since apart from the different hadronisation schemes, PYTHIA and HERWIG have some mismatching parameters. For example, HERWIG does not have an h_{damp} parameter set (effectively, it is equal to infinity), whereas in PYTHIA h_{damp} is always set to a finite value. Because of that, discussions are on-going to define the hadronisation uncertainty within a single generator, in which different hadronisation models are available, like in SHERPA or HERWIG7.2.X.

There is also another issue with the given definition of the hadronisation uncertainty: it may overlap with the JES uncertainty since different parton shower and hadronisation models in PYTHIA and HERWIG also change the calibration of the jet energies. This was a motivation to perform the studies that are described in Chapter 8.

In CMS two uncertainties related to hadronisation effects are defined. First, the flavour-dependent hadronisation uncertainty called "flavour jet energy calibration uncertainty" or "JEC flavour" is defined as the difference in jet energy response between the PYTHIA and HERWIG showering. The "JEC flavour" is estimated as a part of the JES uncertainty. Second, the b-jet modelling uncertainty is calculated as a sum of three components: one is determined using variations of the Bowler–Lund fragmentation function; a second comes from the comparison of the Bowler–Lund and Peterson fragmentation functions; a third component is obtained using variations of the semileptonic b-hadron branching fraction.

- The **colour reconnection uncertainty** is estimated by comparing different tunes or models in PYTHIA. In the ATLAS analyses, two PYTHIA setups are compared: the PERUGIA tune and the PERUGIA LOCR, which differ by the value of the colour reconnection strength. However, currently there is no well-formulated "official" ATLAS recommendation of how to calculate the CR uncertainty. This is related to the fact that certain CR models in PYTHIA lead to large uncertainties on m_t (for example, in [160]) and the reason for that may be their bad agreement with the data. Therefore, there is a strong motivation to perform studies which could constrain these PYTHIA models using data and would allow to define the CR uncertainty through variation of the remaining models. One such study is described in Chapter 7.

  In CMS analyses, two uncertainties related to the CR modelling are defined: the CR uncertainty and the early resonant decay (ERD) uncertainty. The *CR uncertainty* is obtained by comparing the default PYTHIA model to the "QCD inspired" and "gluon move" models. In those three models the default "late resonant decays" option is implemented: only the top quark is involved in the CR but not its decay products. There is also an alternative model in PYTHIA, ERD model, in which CR involves also the decay products. The difference between the results given by the default and the ERD PYTHIA setups is taken into account by the *ERD uncertainty*.

- The **underlying event** uncertainty is estimated by varying MPI parameters in PYTHIA. In ATLAS, the number of MPI is varied by switching on/off the `mpiHi` parameter of the PERUGIA 2012 tune.

  In CMS, the results obtained with the PERUGIA 2011 tune are compared to results obtained using the PERUGIA 2011 MPIHI and PERUGIA 2011 TEVATRON tunes.

- The **PDF uncertainty** is estimated either computing the sum in quadrature of the differences in fitted m_t for the PDF eigenvectors or replicas variations or as half the envelope encompassing the predictions from chosen PDF sets.

  In ATLAS, the following PDF sets are used: CT10 NLO [178], MSTW2008 68% CL NLO [179] and NNPDF 2.3 NLO [180] sets. The old prescription consisted in computing the sum in quadrature of individual PDF uncertainty contributions:

  – The sum in quadrature of the differences in fitted m_t for the 26 eigenvector variations of CT10,

  – Two differences in m_t obtained from reweighting the central value of CT10 to MSTW2008 and NNPDF23

  In the new PDF4LHC prescription [181] the final uncertainty was calculated as half the envelope encompassing the predictions from the three PDF sets (CT10, MSTW2008, NNPDF23) along with their associated uncertainties.

  In the CMS analyses the PDF uncertainty is calculated using one of the following methods:

  – The variance of the results with 100 PDF replicas of the NNPDF3.0 NLO [182],

  – The PDF4LHC prescription,

  – The sum in quadrature of the CT10 or CT14 [183] PDF eigenvector variations.

4.5.2 Uncertainties on the modelling of the background processes

In ATLAS, the **background normalisation** and **background shape** uncertainties are calculated by varying the normalisation and shape for the MC-based and/or data-driven background estimates according to their uncertainties. The choice of which background contributions are varied depends on the $t\bar{t}$ decay channel of the analysis. Sometimes the two uncertainties are combined into a single uncertainty component. Also, in some analysis the uncertainties due to modelling of a specific background (e.g. Wt or diboson production) are singled out.

The CMS analyses estimate the uncertainties related to the background modelling in a similar way by varying the normalisation and shape of each background within its uncertainty.

4.5.3 Uncertainties on the detector response modelling

The uncertainty related to the modelling of the ATLAS detector response contains the following components:

- The **jet energy scale** (JES) uncertainty is calculated as a sum in quadrature of individual contributions. Each subcontribution is estimated as half of the absolute difference between results of up and down variations of the corresponding JES nuisance parameters, which were defined in in-situ calibration measurements of the jet energy (see, for example, [184]). Each variation corresponds to one standard deviation relative to the nominal JES. The b-jet energy

scale contribution is calculated separately. If the pile-up subtraction method based on jet area is used in the analysis, the terms to account for uncertainties in the pile-up estimation are added to the JES uncertainty.

- The ***b*-jet energy scale** (bJES) uncertainty is calculated similarly to the JES one, by performing up/down variations of parameters of the b-jet fragmentation modelling and then taking a quadratic sum of the subcontributions. The bJES parameters are taken from the b-jet energy measurements, for example [184].

Analyses which determine together with m_t the jet energy scale factors, JSF and bJSF, can significantly improve the corresponding systematic uncertainties, JES and bJES (see e.g. [160, 161, 163, 165]). In such measurements, most of the uncertainties induced by JES and bJES uncertainties are transformed into additional statistical components caused by the higher dimensionality of the fit (i.e. comparing to 1D fit to m_t). The sum in quadrature of the additional statistical uncertainty in m_t due to the JSF or bJSF fit and the residual JES-induced or bJES-induced systematic uncertainty is smaller than the original JES-induced or bJES-induced uncertainty.

- The **jet energy resolution** uncertainty is defined using the same strategy as the energy scale uncertainties using the respective parameters [129].

- The **jet reconstruction efficiency** uncertainty is introduced since the jet reconstruction efficiencies measured in data and simulation differ [128] and it reflect the precision with which the data-to-MC jet reconstruction efficiency ratio is known. To compute this uncertainty, a set of pseudo experiments is performed in which jets from MC simulated events are randomly removed. It is done in such a way that the modified jet reconstruction efficiency in simulation samples matches the values measured in data. The m_t difference with respect to the nominal sample is taken as systematic uncertainty.

- If the jet vertex fraction (JVF) requirement is used in the analysis to identify the jets originating from pile-up interactions, a respective **JVF** uncertainty is introduced. It is calculated by varying the requirement on the JVF within its uncertainty [185].

- The **flavour-tagging** uncertainties are related to the differences between b- and $c-$tagging efficiencies and mis-tag rates in data and simulation, which are removed by applying scale factors to simulated events (see, for example, [186]). The respective uncertainties are calculated by performing the up/down fluctuations of the scale factors and then summing them in quadrature.

- The **lepton** uncertainties which are measured in $J/\psi \to ll$ and $Z \to ll$ events (e.g. in [187, 188]) are related to the electron energy and muon momentum scales, lepton resolutions, trigger and identification efficiencies. For each component, the corresponding uncertainty is propagated to the analysis by variation of the respective quantity. If scale factors are applied to correct for the difference between the lepton efficiencies measured in data and in simulated events, the uncertainties in these correction factors are propagated to the measurement.

- The uncertainties on the energy scale of jets or leptons are also propagated to the uncertainty of the **missing transverse momentum** ($E_{\mathrm{T}}^{\mathrm{miss}}$). Other contributions to this uncertainty originate from the energy scale and resolution of the soft calorimeter energy deposits which are not

included in the reconstructed jets and leptons. They are evaluated by varying the uncertainty on the soft $E_{\mathrm{T}}^{\mathrm{miss}}$ components.

- The **pile-up** uncertainty (besides the component treated in the JES) accounts for the residual differences in average number of interactions per bunch crossing $\langle\mu\rangle$ between data and MC simulations. If a significant mismodelling of $\langle\mu\rangle$ is observed, simulated events are reweighted using a pile-up scale factor to match the $\langle\mu\rangle$ value measured in data. The uncertainty on these scale factors are propagated to the analysis.
- In some analyses, extra uncertainty components are included, for example related to the integrated luminosity, LHC beam energy and trigger efficiency.

In the CMS analyses, the strategy of constructing the detector systematic uncertainties is similar and many uncertainty components are similar: related to jet energy corrections, b-tagging and modelling, lepton scales and identification, $E_{\mathrm{T}}^{\mathrm{miss}}$ scale, pileup, trigger and integrated luminosity. Some of the individual components of the uncertainties and their estimation methods differ because of differences between ATLAS and CMS detectors.

5 Top quark pole mass determination from top-quark pair differential cross-sections in the lepton+jets channel at $\sqrt{s}$ = 13 TeV with the ATLAS detector

A precise measurement of the top quark mass compared with the value extracted from a global electroweak fit serves as one of the important consistency tests of the Standard Model, as it was described in Chapter 4. Various direct and indirect measurements of the top quark mass were performed by experiments at the Tevatron and LHC, they yield a spread of m_t values from 170 to 174 GeV with a total uncertainty around 1–2 GeV. The details on the most recent results and combinations have been given in Sections 4.3 and 4.4.

This chapter describes a new indirect measurement of m_t using pp collision data collected by ATLAS at the LHC at $\sqrt{s}$ = 13 TeV in the final state with one lepton and jets. For the first time the top quark mass is extracted by a fit of a double-differential $t\bar{t}$ production cross section to its NNLO predictions. Before, the only published ATLAS top quark mass measurement from $t\bar{t}$ (single) differential cross section [173] used $t\bar{t}$ +jet events. Since the NNLO predictions have a smaller theoretical uncertainty than the NLO ones, we expect that the theoretical uncertainty on the top quark mass in our measurement will be also reduced comparing to the m_t extracted in the previous analyses which used NLO calculations. The two-dimensional differential distribution is used since the m_t sensitivity is enhanced in that case comparing to a differential cross section as a function of a single variable. The considered double-differential cross section is a function of the invariant mass of the $t\bar{t}$ system ($m^{t\bar{t}}$) and of the transverse momentum of the top quark ($p_{\mathrm{T}}^{t,\mathrm{had}}$). The two corresponding one-dimensional cross sections are used in this study as well for consistency cross-checks.

5.1 Summary of the differential cross section measurements

The single and double differential cross sections used for the top quark mass extraction are described in [189].

The pp collision data collected at $\sqrt{s}$ = 13 TeV by the ATLAS detector during 2015 and 2016 and corresponding to an integrated luminosity of 36 fb^{-1} are used. The MC samples with full detector simulation included are used to estimate the $t\bar{t}$ signal and the background from W/Z+jets, diboson and single-top-quark production events. Backgrounds from events including a single non prompt or fake lepton are estimated using the data-driven matrix method [190].

Events are selected in the "resolved kinematic regime", which means that one requires the presence of exactly one electron or one muon and at least four jets, at least two of which have to be b-tagged.

The reconstruction procedure consists in associating four of the five p_{T}-ordered selected jets, the lepton and the missing transverse momentum to the top quarks and W boson by maximising a likelihood which describes the leading-order representation of the $t\bar{t}$ system decay as a function of the energies of the input particles and over the jet–parton assignment. The probabilities that the assignments correspond to a W boson and a top quark are included in the likelihood as Breit–Wigner distributions with the masses set to the world-average values of the measured m_W and m_t. The energies of the final state objects used to build the top and anti-top quark momenta are adjusted within the likelihood maximisation procedure. A requirement on the likelihood value is applied to enhance the presence of events which are consistent with the reconstruction hypothesis.

The reconstructed top quark four momenta are used afterwards to derive various kinematic distributions. Then, the corresponding differential cross sections at parton level are derived by using the iterative Bayesian unfolding procedure [191] as implemented in RooInfold package [192] (the detailed description of the unfolding is given in Section 7.3). First, the non-$t\bar{t}$ background contamination is subtracted. The $t\bar{t}$ events in the dilepton decay channel are also subtracted using a correction factor. Then, a multiplicative acceptance correction is applied, which is defined for each bin as the ratio of events passing both detector and parton level selections to the number of events that pass the detector level selection. The detector effects are corrected using the inverse of the migration matrix. Finally, an efficiency correction is applied which restores the contribution of the $t\bar{t}$ events that fulfil the parton level selection, but not the detector level.

Also, a covariance matrix $\mathrm{Cov}_{\mathrm{exp}}$ is obtained in the measurement, which is used afterwards in the mass extraction analysis. The matrix $\mathrm{Cov}_{\mathrm{exp}}$ includes the effects of all experimental systematic uncertainties and is derived as a sum of the "statistical+detector" and the "modelling" covariance matrices:

- The "statistical+detector" covariance matrix is obtained by performing 200 000 pseudo-experiments in which all detector and background uncertainties are propagated through the unfolding procedure by Gaussian-distributed shifts, and where all bin-to-bin correlations are taken into account. Each pseudo-experiment is obtained as a sum of the statistical and systematic variations to the original bin content of a given distribution. The variations of the statistical effects from data and MC simulations are derived by independent Poisson and Gaussian fluctuations, while for each systematic uncertainty coherent Gaussian fluctuations over all bins are used.

- The "modelling" covariance matrix is obtained by summing four separate covariance matrices corresponding to the effects of modelling the $t\bar{t}$ matrix element, parton shower and hadronisation, initial-/final-state radiation and PDF. The covariance matrix corresponding to each modelling uncertainty is built using the post-unfolding shifts. Each shift is found by scaling the measured cross section with the appropriate relative modelling uncertainty and the bin-to-bin correlations are set to unity.

The details of the calculation of the covariance matrix used in [189] is given in the internal documentation of [193] i.e. in Appendix J of [194].

The default binning schemes corresponding to the differential cross section distributions measured in [189] are the following:

- The bin edges of the $\frac{d^2\sigma}{dm^{t\bar{t}}\,dp_{\mathrm{T}}^{t,\mathrm{had}}}$ distribution are:
  - [0,90,180,1000] GeV for 325 GeV $< m^{t\bar{t}} <$ 500 GeV,
  - [0,80,170,280,1000] GeV for 500 GeV $< m^{t\bar{t}} <$ 700 GeV,
  - [0,90,170,270,370,1000] GeV for 700 GeV $< m^{t\bar{t}} <$ 1000 GeV,
  - [0,180,280,1000] GeV for 1000 GeV $< m^{t\bar{t}} <$ 2000 GeV.
- The bin edges of $\frac{d\sigma}{dm^{t\bar{t}}}$ are: [325,400,480,580,700,860,1020,1250,1500,2000] GeV.
- The bin edges of $\frac{d\sigma}{dp_{\mathrm{T}}^{t,\mathrm{had}}}$ are: [0,50,100,160,225,300,360,475,1000] GeV.

These binning schemes were obtained for the differential cross section measurement and are also used in the mass extraction analysis.

5.1.1 Binning optimisation studies based on sensitivity

Studies have been performed to optimise the binning of the differential distributions for the top quark mass extraction. These studies were performed based on the sensitivity of the corresponding distributions of the kinematic variables i.e. on the percentage variation of the distribution for a given variation in m_t.

The sensitivity S_i of a given bin i of a distribution with N_i events and its uncertainty σ_{S_i} are defined as:

$$S_i = \frac{1}{2}\sum_{k=1,2}\frac{1}{N_i(m_0)}\frac{|N_i(m_0)-N_i(m_k)|}{|m_0-m_k|} = \frac{1}{2\Delta m}\sum_{k=1,2}\left|1-\frac{N_i(m_k)}{N_i(m_0)}\right|,$$
$$\sigma_{S_i} = \frac{1}{2\Delta m N_i(m_0)}\sqrt{N_i(m_1)\left(1+\frac{N_i(m_1)}{N_i(m_0)}\right)+N_i(m_2)\left(1+\frac{N_i(m_2)}{N_i(m_0)}\right)}, \tag{5.1}$$

where $m_0 = 172.5$ GeV, $m_1 = 170.0$ GeV, $m_2 = 175.0$ GeV, $\Delta m = 2.5$ GeV. The value of S_i represents a relative change in the content of the ith bin per unit variation of the top quark mass i.e. a way to approximate the derivative of the ith bin content as a function of the top quark mass, divided by the ith bin content. The value of σ_{S_i} represents an uncertainty of the sensitivity S_i obtained by taking into account only the statistical fluctuations of the ith bin content.

We compute the average sensitivity $\bar{S}$ as a simple arithmetic mean, i.e. without taking into account the bin width:

$$\bar{S} = \sum_{i=1}^{n_{\mathrm{bins}}} S_i/n_{\mathrm{bins}}, \quad \sigma_{\bar{S}} = \sqrt{\sum_{i=1}^{n_{\mathrm{bins}}}\sigma_{S_i}^2}/n_{\mathrm{bins}}. \tag{5.2}$$

The average sensitivity is a figure of merit that amounts to how much on average, given a set of bins, the bin of this set will change, in relative value, when the top quark mass changes. Here, $\sigma_{\bar{S}}$ is the corresponding uncertainty. The binning scheme is considered to be optimal from the point of view of the sensitivity if the difference $(\bar{S} - \sigma_{\bar{S}})$ is maximal. Using this difference as a criterion is one of the ways to take into account the uncertainty $\sigma_{\bar{S}}$.

Example of binning optimisation

Let us find how the average sensitivity depends on the binning for the $m^{t\bar{t}}$ distribution. We start from the fine binning scheme[1] which corresponds to the sensitivity distribution represented in Fig. 5.1 on the left:

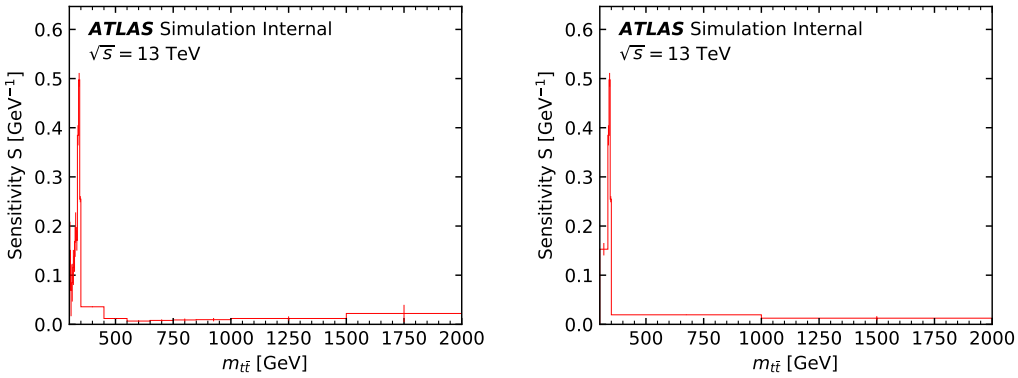

Figure 5.1: The sensitivity distributions of the $m^{t\bar{t}}$ distribution with fine binning (left) and with the binning which gives the highest sensitivity (right).

The average sensitivity of such distribution is equal to:

$$\bar{S}(m^{t\bar{t}}) = 0.115 \pm 0.006 \text{ GeV}^{-1}, \quad \bar{S} - \sigma_{\bar{S}} = 0.109 \text{ GeV}^{-1}. \tag{5.3}$$

By rebinning the histogram (see the right plot in Fig. 5.1), one can increase the average sensitivity:

$$\bar{S}(m^{t\bar{t}}) = 0.189 \pm 0.004 \text{ GeV}^{-1}, \quad \bar{S} - \sigma_{\bar{S}} = 0.185 \text{ GeV}^{-1}. \tag{5.4}$$

From the definition of the sensitivity it follows that to obtain a maximum average sensitivity one should keep the finest binning in the region with highest sensitivity and to merge the bins with lower sensitivity.

[1] The fine binning scheme for the $m^{t\bar{t}}$ distribution corresponds to the following bin edges: [250, 255, 260, 265, 270, 275, 280, 285, 290, 295, 300, 305, 310, 315, 320, 325, 330, 335, 340, 345, 350, 450, 550, 650, 750, 850, 1000, 1500, 2000] GeV.

Then, we consider the $p_{\mathrm{T}}^{t,\mathrm{had}}$ distribution. The fine binning scheme[2] (see left plot in Fig. 5.2) leads to the following average sensitivity value:

$$\bar{S}(p_{\mathrm{T}}^{t,\mathrm{had}}) = 0.025 \pm 0.002 \text{ GeV}^{-1}, \quad \bar{S} - \sigma_{\bar{S}} = 0.023 \text{ GeV}^{-1}. \tag{5.5}$$

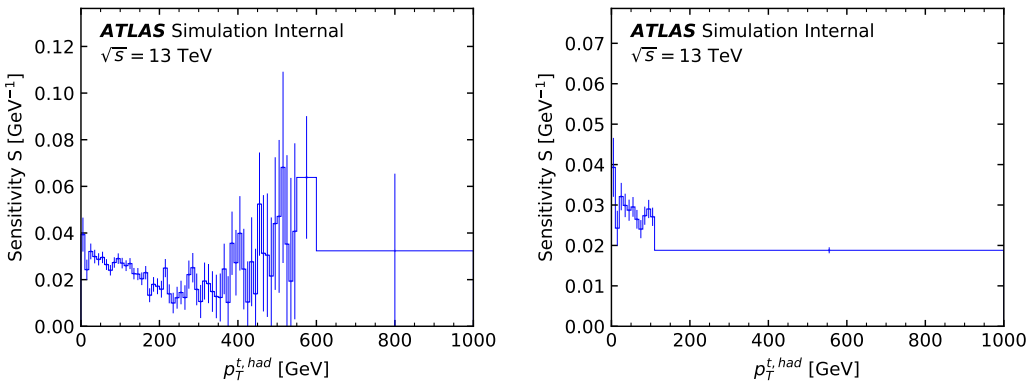

Figure 5.2: The sensitivity distributions of the $p_{\mathrm{T}}^{t,\mathrm{had}}$ distribution with fine binning (left) and with the binning which gives the highest sensitivity (right).

By merging the bins in the tail of the distribution as shown in the right plot of Fig. 5.2 the average sensitivity can be slightly increased:

$$\bar{S}(p_{\mathrm{T}}^{t,\mathrm{had}}) = 0.026 \pm 0.001 \text{ GeV}^{-1}, \quad \bar{S} - \sigma_{\bar{S}} = 0.025 \text{ GeV}^{-1}. \tag{5.6}$$

Let us see which sensitivity to m_t is provided by the binning schemes used in the differential cross section measurement, which were chosen by taking into account the detector resolution. The distributions of the sensitivity for the $m^{t\bar{t}}$ and $p_{\mathrm{T}}^{t,\mathrm{had}}$ distributions with such binning schemes are shown in Fig. 5.3.

The resulting average sensitivities are:

- For the $m^{t\bar{t}}$ distribution:

$$\bar{S}(p_{\mathrm{T}}^{t,\mathrm{had}}) = 0.047 \pm 0.002 \text{ GeV}^{-1}, \quad \bar{S} - \sigma_{\bar{S}} = 0.045 \text{ GeV}^{-1}. \tag{5.7}$$

- For the $p_{\mathrm{T}}^{t,\mathrm{had}}$ distribution:

$$\bar{S}(p_{\mathrm{T}}^{t,\mathrm{had}}) = 0.022 \pm 0.004 \text{ GeV}^{-1}, \quad \bar{S} - \sigma_{\bar{S}} = 0.018 \text{ GeV}^{-1}. \tag{5.8}$$

We can also try to construct a binning scheme which would be optimal in the two ways: it would give a sensitivity value as high as possible while taking into account the finite resolution, i.e. one would

[2] The fine binning scheme for the $p_{\mathrm{T}}^{t,\mathrm{had}}$ distribution corresponds to the following bin edges: [0,10,20,...,500,600,1000], where in [0,500] GeV range equidistant bins with 10 GeV width are used. The binning is chosen in such a way that the bin contents are not subjected to large statistical fluctuations.

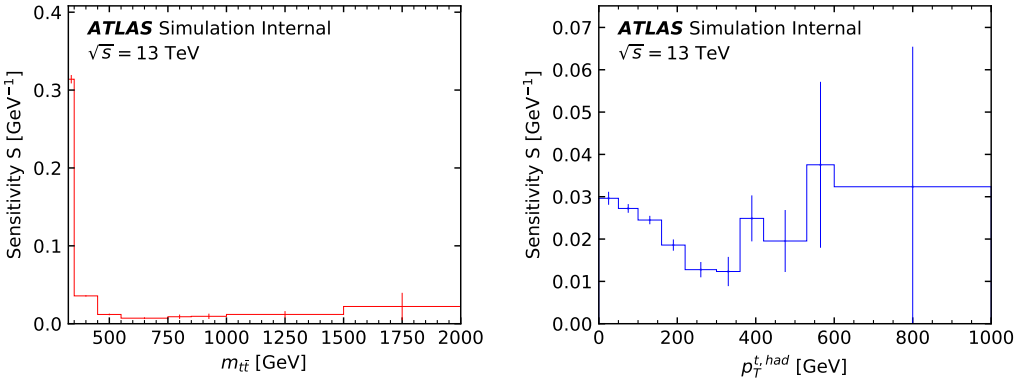

Figure 5.3: The sensitivity distributions of the $m^{t\bar{t}}$ (left) and $p_{\mathrm{T}}^{t,\mathrm{had}}$ (right) distributions with the binning schemes used in the differential cross section measurement. These binning schemes are optimised from the point of view of the resolution.

need to keep the bin widths larger than the resolution. We did a test optimisation starting from the fine binning and we obtained the improved binning schemes for the $m^{t\bar{t}}$ and the $p_{\mathrm{T}}^{t,\mathrm{had}}$ distributions which are presented in Fig. 5.4. In this test, the bin width is required to be larger than the 2×resolution, following the resolution criteria used in the differential cross section measurement [189].

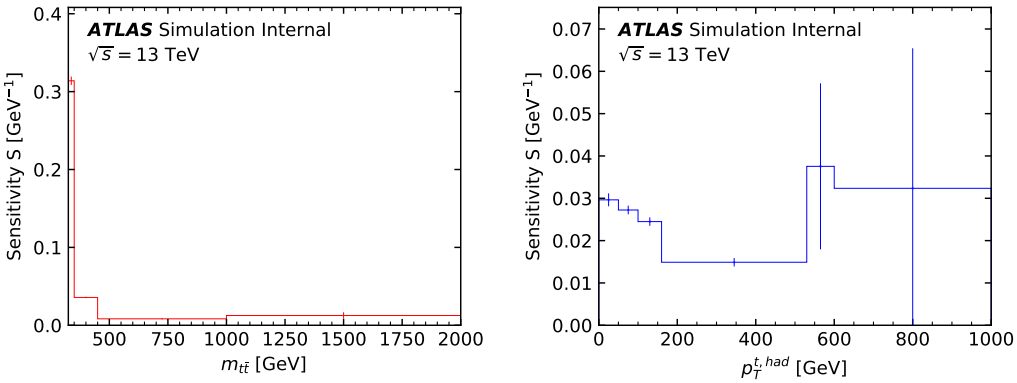

Figure 5.4: The sensitivity distributions of the $m^{t\bar{t}}$ (left) and $p_{\mathrm{T}}^{t,\mathrm{had}}$ (right) distributions with the binning schemes which are optimal from the sensitivity side and the resolution side.

The resulting average sensitivities are lower than in Eqs. (5.4) and (5.6), but the one for $m^{t\bar{t}}$ is visibly higher than for the binning scheme used in the differential cross section measurement:

$$\bar{S}(m^{t\bar{t}}) = 0.074 \pm 0.001 \text{ GeV}^{-1}, \quad \bar{S}(p_{\mathrm{T}}^{t,\mathrm{had}}) = 0.024 \pm 0.006 \text{ GeV}^{-1}. \tag{5.9}$$

We have seen that for $\frac{d\sigma}{dm^{t\bar{t}}}$ the first part of the distribution near the $t\bar{t}$ production threshold is by far more sensitive than all the rest of the distribution which has otherwise roughly constant sensitivity. For $\frac{d\sigma}{dp_{\mathrm{T}}^{t,\mathrm{had}}}$ the sensitivity decreases with increasing p_{T}. In general, these sensitivity studies present a

naive idealised starting point for a binning choice because they do not take into account the effect of the systematic uncertainties and their bin-to-bin correlations, which can change the impact of the different bins on the measurement and enhance or dilute their sensitivity, thus changing the initial picture. Also, changing the binning of the differential cross section is a time consuming process because of unfolding closure and stress tests which one needs to perform. Therefore, this small study serves mostly as a check of the presently used binning, while the binning from the $t\bar{t}$ differential cross section measurement [189] is input to the χ^2 calculation for the mass extraction.

5.2 Theoretical predictions for the differential cross section

The top quark mass extraction described in this chapter is done using the theoretical predictions for single and double differential cross sections for $t\bar{t}$ production at different values of m_t. Predictions are obtained at parton level and in the full phase space. For each m_t value, two separate double differential cross section predictions are calculated as a function of $m^{t\bar{t}}$ and of the average of the transverse momentum of the top quark and the antitop quark. The resulting double differential cross section is referred to as $\frac{d^2\sigma}{dm^{t\bar{t}}\,dp_{\mathrm{T,avt}}}$, where $p_{\mathrm{T,avt}}$ stands for the average of the p_{T} distributions of the top and antitop quarks.

Predictions for the single differential $t\bar{t}$ cross sections are also available as a function of $m^{t\bar{t}}$, of $p_{\mathrm{T,avt}}$ and of the momentum of the top quark that decays into hadrons ("hadronically decaying top"), $p_{\mathrm{T}}^{t,\mathrm{had}}$.

The single and double differential cross sections [189] are measured as function of $p_{\mathrm{T}}^{t,\mathrm{had}}$ and ($m^{t\bar{t}}$, $p_{\mathrm{T}}^{t,\mathrm{had}}$), respectively, instead of $p_{\mathrm{T,avt}}$ and ($m^{t\bar{t}}$, $p_{\mathrm{T,avt}}$). Studies using MC simulations at NLO with the parton shower and hadronisation included (NLO+PS) were performed to compare the predictions based on $p_{\mathrm{T,avt}}$ and $p_{\mathrm{T}}^{t,\mathrm{had}}$ (the details of the studies are given in Appendix A of [195]). The predictions are shown to be consistent within the statistical uncertainty resulting from the size of the MC sample ("MC statistical uncertainty").

The parton level phase space, to which the measurements are unfolded, is defined by the kinematic properties of the top and the antitop quarks at the parton level, that is independent of any decay. In addition to the NNLO fixed order calculations, for which no top quark decay is take into account, we also use predictions at NLO+PS. The NLO+PS predictions are obtained from MC simulations in which an approximate description of top quark decay is included, as well as the parton shower and hadronisation. The top quark four momenta are considered after final state radiation effects in the NLO+PS description.

The binning schemes corresponding to the theoretical predictions are the same as the ones reported for the measurements in Section 5.1. The NLO+PS predictions are available for seven top quark mass points: $m_t \in [170.0, 170.5, 171.5, 172.5, 173.5, 174.5, 175.0]$ GeV. The fixed order NNLO predictions are available for three mass points: $m_t \in [171.0, 172.5, 174.0]$ GeV.

5.2.1 NNLO predictions

NNLO fixed order predictions [151, 196, 197] for the $t\bar{t}$ differential cross sections are obtained with the FASTNLO [198–200] code convoluted with different PDF sets for various options of renormalisation and factorisation scales [201].

For a given m_t value seven parton level predictions are generated by assuming fixed values of the renormalisation μ_R and factorisation μ_F scales. The default value of μ_R and μ_F (let us call it μ_0) is chosen as follows:

- For the $m^{t\bar{t}}$ and the double-differential cross sections the default scale is:

$$\mu_0 = \frac{H_T}{4} \equiv \frac{1}{4}\left(\sqrt{m_t^2 + p_{T,t}^2} + \sqrt{m_t^2 + p_{T,\bar{t}}^2}\right), \tag{5.10}$$

  where $p_{T,t}$ and $p_{T,\bar{t}}$ are the transverse momenta of the top and the antitop quarks, respectively.

- For the $p_{T,avt}$ and for the double-differential cross section:

$$\mu_0 = \frac{M_T}{2} \equiv \frac{1}{2}\sqrt{m_t^2 + p_T^2}, \tag{5.11}$$

  where p_T refers to $p_{T,t}$ or $p_{T,\bar{t}}$ according to the distribution.

Seven pairs of scales are chosen: $(\mu_R, \mu_F) \in [(1,1), (2,1), (1,2), (0.5,1), (1.0,5), (0.5,0.5), (2,2)]$ in units of μ_0. The upper (lower) scale uncertainty in each bin of the differential cross section is calculated as an absolute difference between the value given by the (1,1) scale and the highest (lowest) value among those given by other scales. The relative values of the scale uncertainties are shown in Fig. 5.5: the lower scale uncertainty varies from 2% to 10% depending on the bin and the higher scale uncertainty varies between 1% to 6%. Each parton level prediction is convoluted with PDF4LHC NNLO PDF set [202]. Each sample is also normalised to the value of the NNLO+NNLL cross section for the considered value of the top quark mass, evaluated using the Top++2.0 program [151, 152].

The NNLO fixed order $\frac{d^2\sigma}{dm^{t\bar{t}}\,dp_T^{t,\mathrm{had}}}$, $\frac{d\sigma}{dm^{t\bar{t}}}$ and $\frac{d\sigma}{dp_T^{t,\mathrm{had}}}$ distributions corresponding to the three top quark masses and the central scale $(\mu_R, \mu_F) = (\mu_0, \mu_0)$ are shown in Fig. 5.6.

5.2.2 Width correction to the NNLO predictions

The NNLO predictions are produced in the narrow-width approximation, that is with top quark width of 10^{-5} GeV, whereas the SM prediction for the width of the top quark is equal to 1.33 GeV. In order to estimate the effect of this approximation on the final result, we performed a test where we applied LO correction scale factors to the NNLO differential cross sections in order to account for the effect of the non-zero top quark width.

To get the width correction we generated two kinds of LO samples, one with a "narrow" top quark width ($\Gamma_t = 10^{-5}$ GeV) and one with a nominal top quark width ($\Gamma_t = 1.33$ GeV), using the $t\bar{t}$dec version of the POWHEG generator [203]. Note that the calculation with a nominal top quark width does not include neither non-resonant nor off-shell effects. The LO samples are used because in POWHEG,

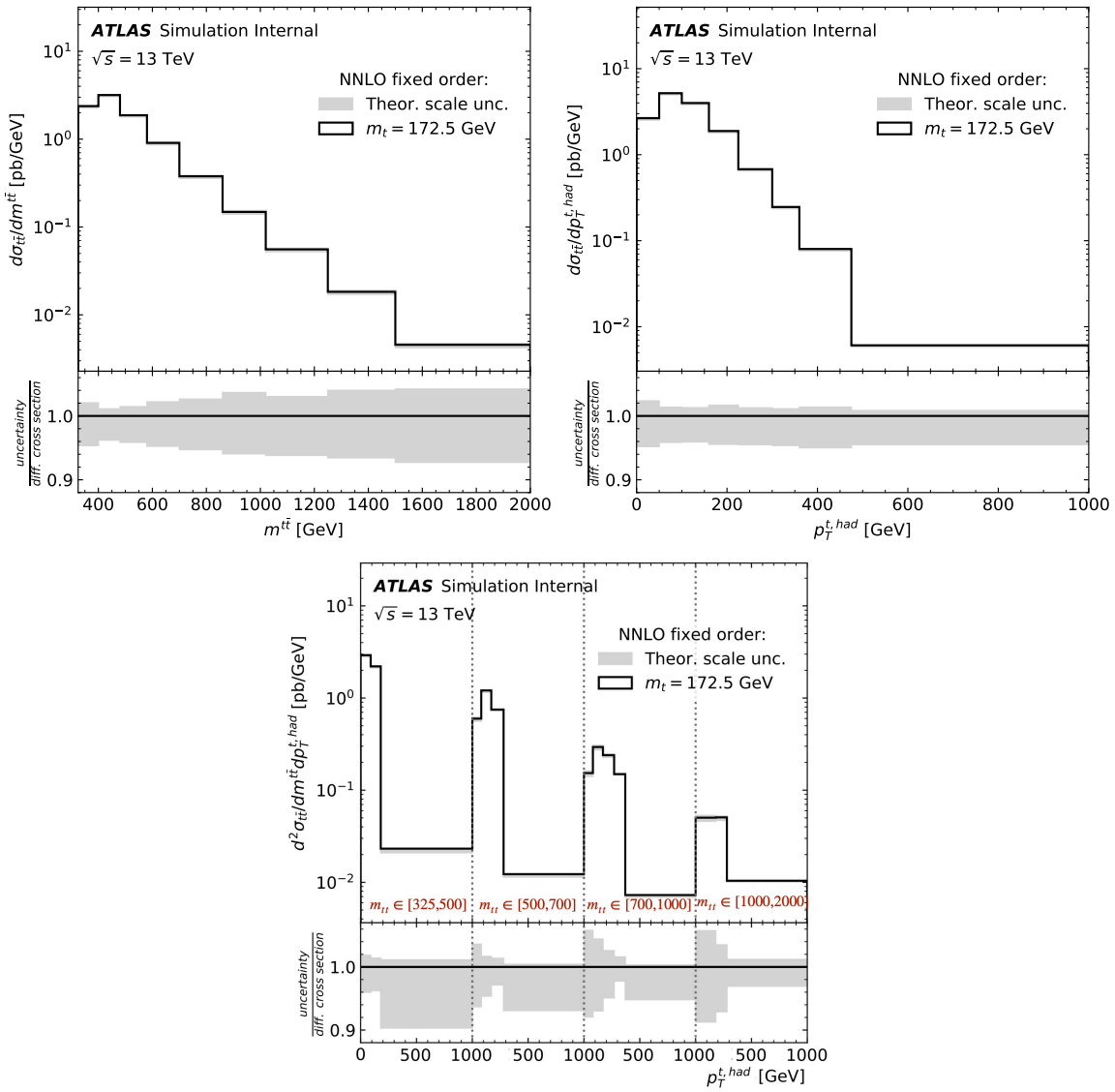

Figure 5.5: The differential cross sections $\frac{d\sigma}{dm^{t\bar{t}}}$ (upper left), $\frac{d\sigma}{dp_{\mathrm{T}}^{t,\mathrm{had}}}$ (upper right), $\frac{d^2\sigma}{dm^{t\bar{t}}\,dp_{\mathrm{T}}^{t,\mathrm{had}}}$ (bottom) for m_t = 172.5 GeV are shown together with the theoretical scale uncertainty (grey band). The relative value of the uncertainty is given in bottom pad.

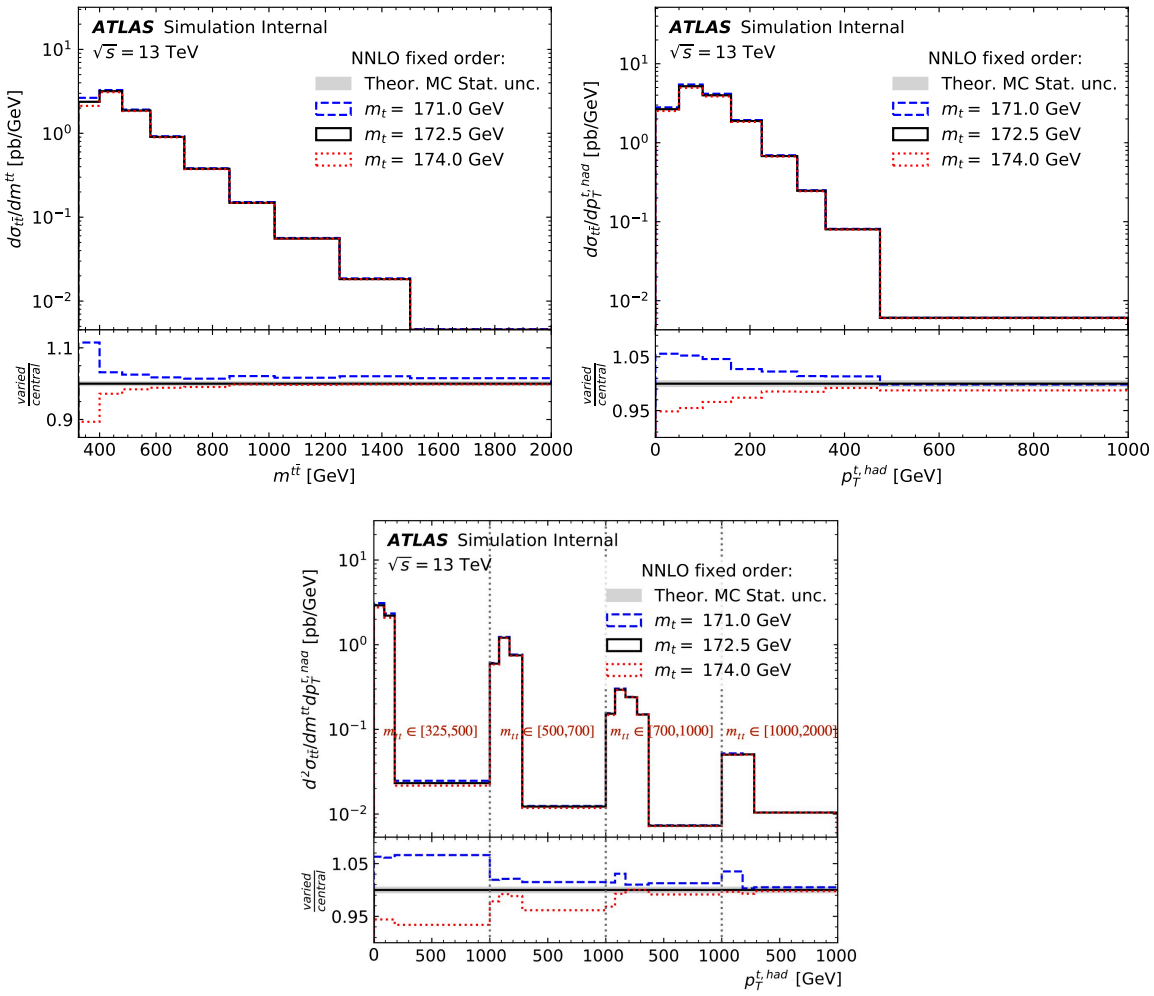

Figure 5.6: The differential cross sections $\frac{d\sigma}{dm^{t\bar{t}}}$ (upper left), $\frac{d\sigma}{dp_{\mathrm{T}}^{t,\mathrm{had}}}$ (upper right), $\frac{d^2\sigma}{dm^{t\bar{t}}\,dp_{\mathrm{T}}^{t,\mathrm{had}}}$ (bottom) for the three values of m_t = 171.0, 172.5, 174.0 GeV. The ratios w.r.t. the distribution for the nominal m_t = 172.5 GeV are given in bottom pads. The grey band (very thin on the plot) represents the 0.5% MC statistical uncertainty of the theoretical calculation.

for $t\bar{t}$ events in the lepton+jets decay channel, the top quark width effects are implemented only at LO. The correction factors are calculated for each bin as a ratio of the differential cross sections with a nominal and a narrow width in this bin.

The LO differential cross sections distributions for the nominal and the narrow top quark width as well as the width correction factors are given in Fig. 5.7 for a top quark mass $m_t = 172.5$ GeV.

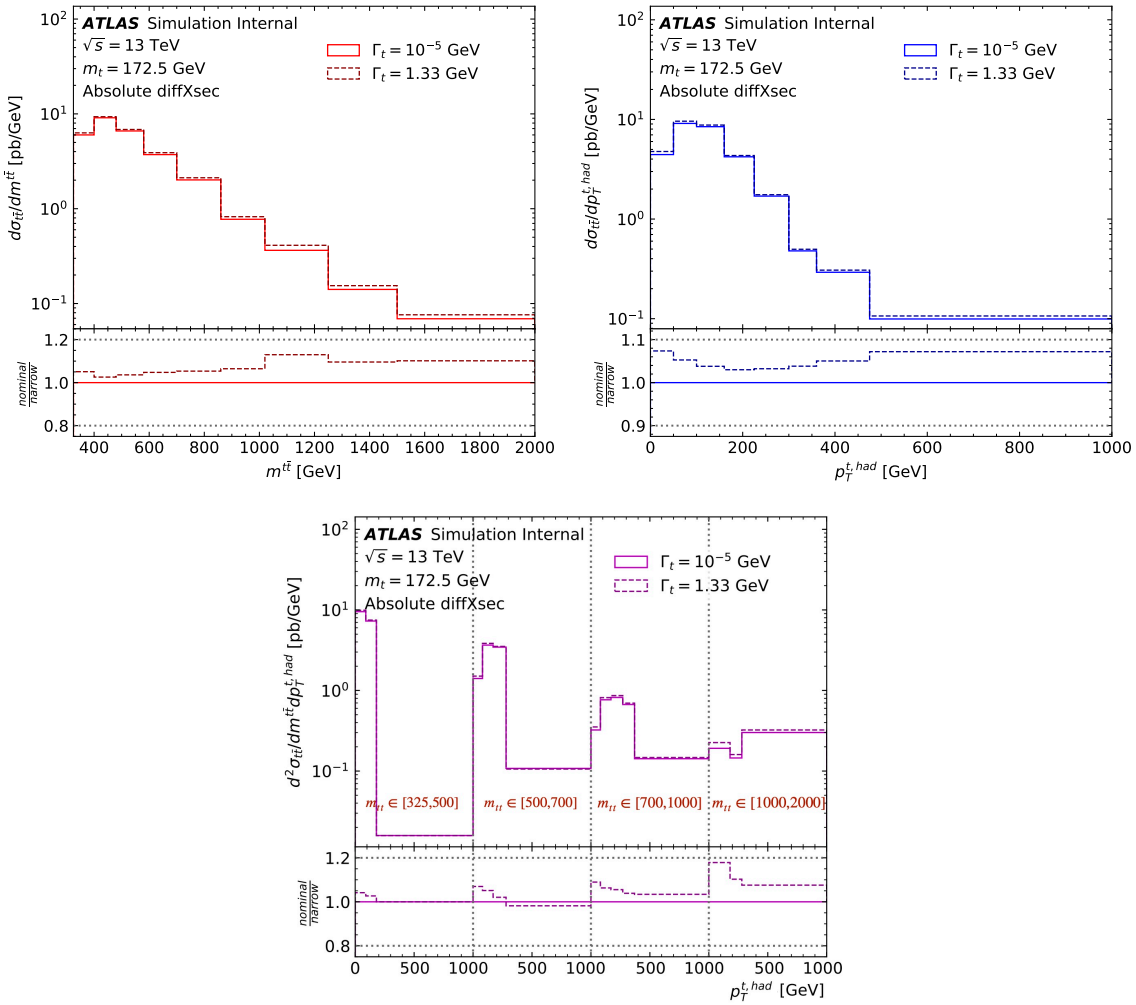

Figure 5.7: LO differential cross section distributions: $\frac{d\sigma}{dm^{t\bar{t}}}$ (upper left), $\frac{d\sigma}{dp_{\mathrm{T}}^{t,\mathrm{had}}}$ (upper right) and $\frac{d^2\sigma}{dm^{t\bar{t}}\,dp_{\mathrm{T}}^{t,\mathrm{had}}}$ (bottom), corresponding to the nominal top quark width ($\Gamma_t = 1.33$ GeV, dashed line) and the narrow top quark width ($\Gamma_t = 10^{-5}$ GeV, solid line). The bottom pad of each plot shows the ratio of the two curves, which is used as a width correction scale factor. The cross sections are scaled to an arbitrary integrated luminosity.

The correction factors are also obtained for $m_t = 170$ and 175 GeV and the rest of them, for the intermediate mass points, are obtained using an interpolation with a quadratic polynomial.

Table 5.1 shows how the result for the extracted top quark mass changes if one uses NNLO predictions with a width correction applied instead of original NNLO predictions. The mass extraction is

	narrow width	nominal width
$m^{t\bar{t}} \times p_{\mathrm{T}}^{t,\mathrm{had}}$	$170.85^{+0.55}_{-0.50}$	$171.81^{+0.18}_{-0.17}$
$m^{t\bar{t}}$	$172.28^{+0.64}_{-0.57}$	$173.10^{+0.94}_{-0.77}$
$p_{\mathrm{T}}^{t,\mathrm{had}}$	$174.30^{+1.20}_{-2.02}$	$174.79^{+1.01}_{-1.39}$

Table 5.1: Top quark mass (in GeV) extracted from a pseudo-data sample generated with m_t = 172.5 GeV and using the NNLO predictions with applied (right column) or not applied (middle column) width correction. The uncertainty to the mass includes experimental (statistical and systematic) and theoretical (PDF and α_{S}) components.

performed according to the procedure that will be described in Section 5.3.1. The results are showing that the extracted m_t value highly depends on whether the top quark width is taken into account and it shifts by 0.5-1 GeV.

We are still discussing the applicability of this width correction with theorists (in particular with a theory group providing us the NNLO predictions), since the interpretation of such width-corrected NNLO predictions and the corresponding width uncertainty is questionable. This is related to the fact that the NNLO predictions are calculated in the approximation which does not imply the decay of the top quarks, so adding a top quark width makes the whole calculation inconsistent. Therefore, we do not use yet the width correction as default in the analysis.

5.2.3 NLO+PS predictions

Predictions for the $t\bar{t}$ process at NLO+PS are obtained by MC simulation matching NLO matrix elements with parton shower and hadronisation. The matrix element is computed using the POWHEG-BOX v2 [204, 205] with the NNPDF3.0 NLO PDF set [182]. The top quark decay with all spin correlations preserved is modelled using MADSPIN [206]. The parton shower, hadronisation and underlying event are simulated using PYTHIA 8 (v8.186) [207] with the NNPDF2.3 LO PDF set and the A14 tune [208]. The renormalisation and factorisation scales in the matrix element are set to M_{T} (see Eq. (5.11) for definition). The samples are overlaid with multiple proton-proton collisions (pileup) simulated with the soft QCD processes of PYTHIA 8 using the A2 tune [209] and the MSTW2008 LO PDF set [179].

Each sample is normalised to the value of NNLO+NNLL cross section for the considered value of the top quark mass, evaluated using the Top++2.0 program.

5.3 Extraction of the top quark mass

The top quark mass is extracted as the value which minimises a χ^2 built using the theory predictions and the measured differential distributions as described below.

Three absolute differential cross sections derived at parton level are used to provide different estimates of m_t: $\frac{d\sigma}{dm^{t\bar{t}}}$, $\frac{d\sigma}{dp_{\mathrm{T}}^{t,\mathrm{had}}}$, $\frac{d^2\sigma}{dm^{t\bar{t}}\,dp_{\mathrm{T}}^{t,\mathrm{had}}}$. The final result for the top quark mass is obtained from the double differential cross section, whereas the mass extraction from the single differential cross sections is used as cross-check.

5.3.1 Mass fit

Given a measured $t\bar{t}$ differential cross section, the associated experimental and theoretical covariance matrices and a theoretical prediction, the m_t value is extracted by performing the following steps:

1. A χ^2 is computed as a function of the m_t value used in the prediction as:

$$\chi^2(m_t) = \sum_{i,j} \left(x_i^{\mathrm{meas}} - x_i^{\mathrm{pred}}(m_t)\right) \mathrm{Cov}_{i,j}^{-1}(m_t) \left(x_j^{\mathrm{meas}} - x_j^{\mathrm{pred}}(m_t)\right), \tag{5.12}$$

   where $x_i^{\mathrm{meas(pred)}}$ is the measured (predicted) $t\bar{t}$ differential cross section in bin i, Cov is the sum of the experimental covariance matrix $\mathrm{Cov}_{\mathrm{exp}}$ obtained as described in Section 5.1 and the theoretical covariance matrix $\mathrm{Cov}_{\mathrm{theo}}$ which will be described later in Section 5.5.2. The measurement x_i^{meas} as well as the experimental covariance matrix $\mathrm{Cov}_{\mathrm{exp}}$ have been derived using a NLO+PS MC sample with a fixed top quark mass of 172.5 GeV. After unblinding of the analysis, x_i^{meas} and $\mathrm{Cov}_{\mathrm{exp}}$ will be derived using data.

   The χ^2 (m_t) function is sampled by using predictions corresponding to different m_t values. The covariance matrix is kept constant in the χ^2 calculation. For the moment only MC simulation (where m_t = 172.5 GeV is set) is used for the covariance matrix computation. When the real data will be used, the modelling covariance will still be based on simulation with m_t = 172.5 GeV, but the uncertainties derived from data (e.g. the statistical uncertainty) will depend on the unknown m_t in data. A preliminary indication of the size of the effect obtained by including some dependence of the covariance matrix on m_t is given in Section 5.3.2.

   The predictions at an arbitrary value of m_t are obtained by assuming a quadratic dependence on m_t for each value of a given $t\bar{t}$ differential cross section is a given bin. Therefore, a second-order polynomial dependency is used for the prediction in the least-square fit in a given bin. For a given m_t interval $[m_{\mathrm{low}}, \ldots, m_{\mathrm{high}}]$, for which the predictions samples are available, the predictions for all m_t values in the range $[m_{\mathrm{low}} - 1\ \mathrm{GeV}, \ldots, m_{\mathrm{high}} + 1\ \mathrm{GeV}]$ with a step of 0.05 GeV are obtained. An example of m_t dependence of the double differential cross section is a given bin is given in Fig. 5.8.

   The full range of $[m_{\mathrm{low}}, \ldots, m_{\mathrm{high}}]$ if fixed for a given prediction (NLO+PS or NNLO). It has been checked that the error when extrapolating the ranges by 1 GeV is less than the statistical uncertainty of the theoretical predictions of 0.5% (see Section 5.3.3).

2. The m_t value for which the χ^2 function achieves its minimum $m_{t,\mathrm{min}}$, is found numerically among the set of predictions computed for different m_t values. The procedure of finding $m_{t,\mathrm{min}}$ is the following:

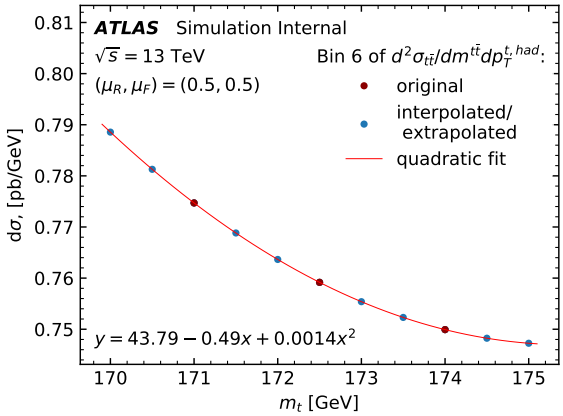

Figure 5.8: The double differential cross section in bin 6 at different m_t values. The dark red points represent the mass points available from NNLO theoretical calculations (see Section 5.2.1). The blue points represent the values obtained by inter-/extrapolation. The quadratic interpolation polynomial is shown as a red line and its formula is given a the bottom of the plot.

- First, a rough estimation of the top mass ($m_{t,\mathrm{min},0}$) is done: $m_{t,\mathrm{min},0}$ corresponds to the minimum of the χ^2 values, which are calculated for a set of m_t in the range $[m_{\mathrm{low}} - 1\ \mathrm{GeV}, m_{\mathrm{low}} - 0.05\ \mathrm{GeV}, \ldots, m_{\mathrm{high}} + 0.5\ \mathrm{GeV}, m_{\mathrm{high}} + 1\ \mathrm{GeV}]$, in which the interpolated predictions are obtained (see above).

- In the mass region $[m_{t,\mathrm{min},0} - 0.05\ \mathrm{GeV}, m_{t,\mathrm{min},0} + 0.05\ \mathrm{GeV}]$ further interpolation of the predictions is done, for all the intermediate mass points with a step of 0.001 GeV.

- The $m_{t,\mathrm{min}}$ value corresponding to the minimum χ^2 (χ^2_{min}) is found using the interpolated predictions obtained at the previous step. A minimum is picked among the χ^2 values for a set of m_t in the range $[m_{t,\mathrm{min},0} - 0.05\ \mathrm{GeV}, m_{t,\mathrm{min},0} + 0.05\ \mathrm{GeV}]$. The $m_{t,\mathrm{min}}$ value has a numerical precision of 1 MeV.

3. The values of m_t corresponding to $\chi^2_{\mathrm{min}} + 1$ are also determined numerically using the same technique adopted to find the minimum: a fine grid of mass varied predictions is produced close to the region where $\chi^2 = \chi^2_{\mathrm{min}} + 1$ [3]. The obtained values are named $m_{t,\mathrm{down}}$ and $m_{t,\mathrm{up}}$, depending if they are smaller or larger than $m_{t,\mathrm{min}}$. The differences from $m_{t,\mathrm{min}}$ provide an estimate of the 68% confidence level interval of the top quark mass as $[m_{t,\mathrm{min}} - |m_{t,\mathrm{down}} - m_{t,\mathrm{min}}|, m_{t,\mathrm{min}} + |m_{t,\mathrm{up}} - m_{t,\mathrm{min}}|]$. This interval is associated to the full statistical and systematic uncertainties, as well as the theoretical PDF and α_S uncertainties, which are all included in the covariance matrix Cov in Eq. (5.12).

   To get the total uncertainty of the top quark mass, an additional uncertainty needs to be addded because the scale uncertainty is not included in the theoretical covariance matrix. The propagation of uncertainties and their breakdown is described in Section 5.5.

[3] Compared to the alternative approach of fitting the χ^2 values for different m_t with a quadratic polynomial, the adopted approach makes full use of the shape of the χ^2 function without assuming a parabolic shape.

5.3.2 Top quark mass dependence of the covariance matrix

The uncertainties on the measured differential cross sections described in Section 5.1 and the theoretical uncertainties on the NNLO predictions described in Section 5.5 contain information on the input m_t value. For example, the MC samples used to estimate the experimental modelling uncertainties assume $m_t = 172.5$ GeV. However, the covariance matrix used in the mass extraction is potentially dependent on m_t and taking this dependence into account may influence the final uncertainty on the extracted m_t. Nevertheless, data information is used to determine some systematic uncertainties, thus superseding the simulation with the unknown top quark mass present in the data:

- The statistical uncertainty included in the covariance matrix is obtained by assuming the data yields as estimators of the mean for the independent Poisson fluctuations assumed in different bins,
- Most of the experimental systematic uncertainties are ultimately determined through data driven corrections.

No direct m_t dependence is expected in the uncertainties associated with nearly all of the backgrounds and in statistical uncertainties coming from the size of the simulated samples. However, these are not expected to be dominant effects in the measurement.

The theoretical covariance does include some m_t dependence, since the values of PDF and α_S uncertainties are available for three mass points from theory calculations. Also, in the mass determination the m_t dependence of the (dominant) scale uncertainty is kept, given that the values are also provided from theory.

Given that the samples used to calculate the modelling uncertainties are available only for a single m_t value of 172.5 GeV, we are able to get the covariance matrix with the modelling effects only for $m_t = 172.5$ GeV. Therefore, a fixed experimental covariance matrix (which contains detector and modelling systematic effects) is used for the calculation of the χ^2 at any m_t value.

In order to assess the impact of including some m_t dependence in the experimental covariance matrix, an (arbitrary) assumption about the mass variation is made. It is assumed that the total relative uncertainty of the $t\bar{t}$ differential cross section is a constant. The relative uncertainty is defined as the ratio of the total standard deviation to the central value of the $t\bar{t}$ differential cross section in a given bin. The top quark mass extraction is performed using both, mass-dependent and mass-independent experimental covariance matrices.

The experimental covariance matrix at a given m_t value is obtained by scaling the generic element of the nominal covariance matrix at $m_t = 172.5$ GeV by an element-dependent multiplicative factor derived from NLO+PS predictions at different m_t values. The multiplicative factor for element Cov(i,j) is the product of two ratios R(i,m)·R(j,m), where m is the value of the top quark mass and R is the ratio of the values of the differential cross sections (as functions of some variable X) corresponding to $m_t = m$ and to $m_t = 172.5$ GeV:

$$\mathrm{R(i},m) = \frac{\frac{d\sigma_{t\bar{t}}}{dX}(\mathrm{i},m)}{\frac{d\sigma_{t\bar{t}}}{dX}(\mathrm{i},\,172.5\ \mathrm{GeV})}. \tag{5.13}$$

The values of the extracted top quark mass and the uncertainties resulting from the χ^2 fits when using either constant or m_t-dependent experimental covariance matrix are shown in Table 5.2. Fits

	m_t-dependent covariance	constant covariance
$m^{t\bar{t}} \times p_{\mathrm{T}}^{t,\mathrm{had}}$	$172.50^{+0.51}_{-0.52}$	$172.50^{+0.50}_{-0.52}$
$m^{t\bar{t}}$	$172.50^{+0.66}_{-0.74}$	$172.50^{+0.71}_{-0.68}$
$p_{\mathrm{T}}^{t,\mathrm{had}}$	$172.50^{+2.83}_{-3.10}$	$172.50^{+3.18}_{-2.77}$

Table 5.2: The top quark mass results (in GeV) obtained using a m_t-dependent covariance matrix (middle column) and a constant one (right column). The NLO+PS pseudo-data and predictions are used. The m_t uncertainty includes experimental statistical and systematic effects.

of NLO+PS pseudo-data to NLO+PS predictions are considered. The results are consistent and the extracted total uncertainties are very close. Therefore, in the rest of the analysis we keep the experimental covariance constant.

5.3.3 Studies on extrapolation of theoretical predictions

In order to justify the possibility to extrapolate the predictions by 1 GeV (i.e. to get the predictions corresponding to m_t values that differ by 1 GeV from the highest and the lowest m_t available samples), an extrapolation test was performed using the predictions at NLO, for which the samples with $m_t \in [170.0, 171.5, 172.5, 173.5, 174.5, 175.0]$ GeV are available. The NLO fixed order samples are obtained in the same way as the NNLO ones as described in Section 5.2.1.

The extrapolation test consists in obtaining two differential cross section distributions corresponding to $m_t = 170.5, 174.5$ GeV by performing bin-by-bin extrapolation of the three available differential cross section distributions with $m_t = 171.5, 172.5, 173.5$ GeV and comparing the results to the original theoretically computed distributions with $m_t = 170.5, 174.5$ GeV. The extrapolation technique is described in Section 5.3.1. In Fig. 5.9 it is shown that the differential cross sections obtained by the extrapolation differ from the theoretically computed ones by less than the 0.5% MC statistical uncertainty of the theoretical NLO samples.

5.3.4 Mass extraction using the fully simulated sample and the NNLO predictions

The only fully simulated Powheg+Pythia 8 $t\bar{t}$ sample available in our study is the one with m_t = 172.5 GeV. It is used to build pseudo-data which are then fit to the NNLO predictions, using single or double differential $t\bar{t}$ cross sections. The pseudo-data sample is built by adding contributions of the $t\bar{t}$ signal and background samples, which underwent full simulation of the detector response. The background samples include contributions from simulated processes and data-driven contributions. The data-driven contribution takes into account the presence of non-prompt leptons or fake leptons (non-lepton particles identified as prompt leptons) passing the event selection. The following background processes have been simulated: single top quark production, W or Z bosons associated with jets, diboson production, $t\bar{t}$ in association with W or Z bosons, tZ, $t\bar{t}\,t\bar{t}$, $t\bar{t}\,WW$. In all samples that contain generated top quark the top quark mass is set to 172.5 GeV. The $t\bar{t}$ signal

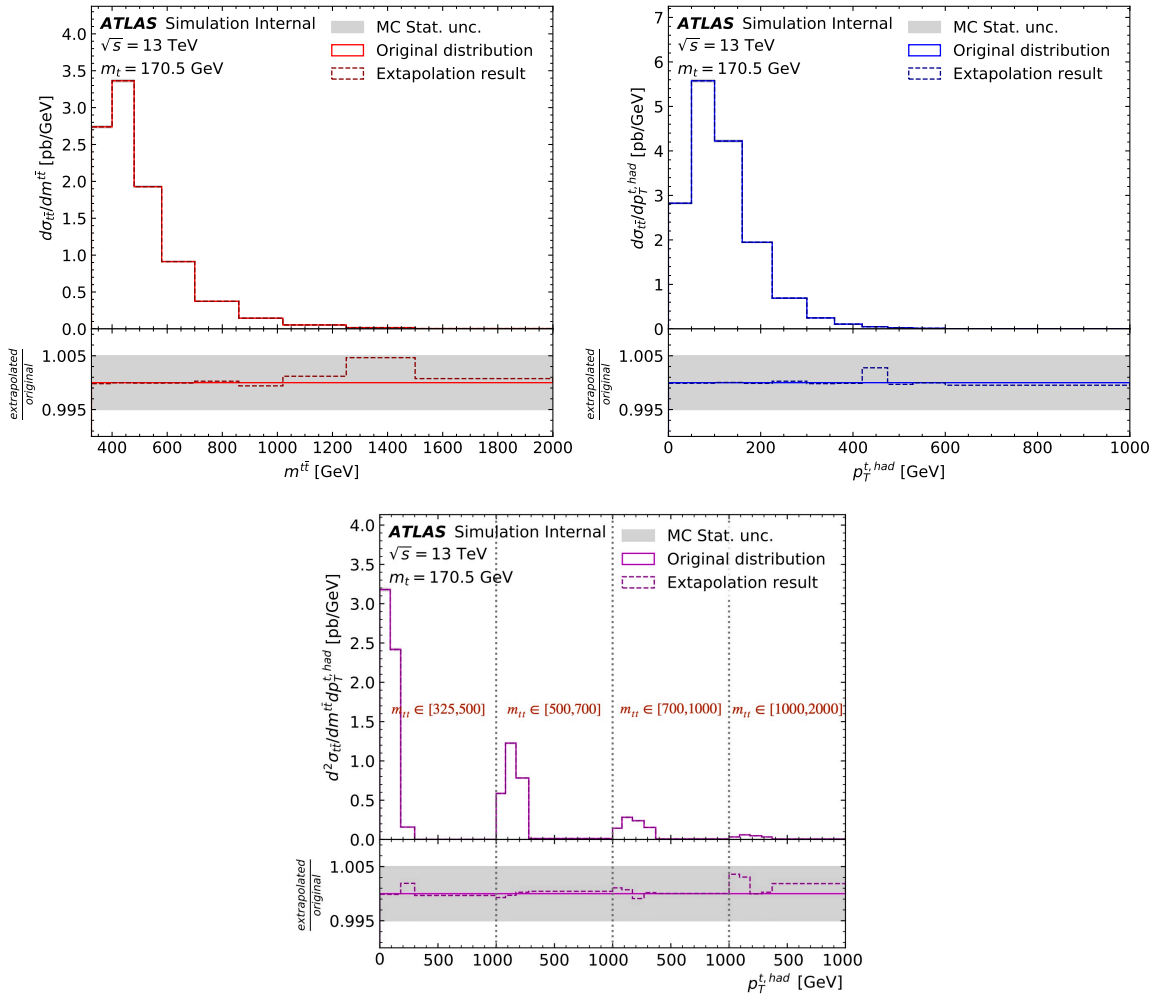

Figure 5.9: The ratio of the differential cross sections, $\frac{d\sigma}{dm^{t\bar{t}}}$ (upper left), $\frac{d\sigma}{dp_{\mathrm{T}}^{t,\mathrm{had}}}$ (upper right), $\frac{d^2\sigma}{dm^{t\bar{t}}\,dp_{\mathrm{T}}^{t,\mathrm{had}}}$ (bottom), from the original prediction samples and the ones obtained by extrapolation with $m_t = 170.5$ GeV.

contribution in the pseudo-data and the unfolding corrections are derived from the same simulated sample of $t\bar{t}$ events.

In this test, the pseudo-data sample is fit to the sets of NNLO predictions described in Section 5.2.1. The results of the mass extraction are summarised in Table 5.3. The variation of extracted top quark mass using different scale values in the NNLO predictions is shown in Table 5.4.

	extracted $m_t \pm \delta m_t$(stat.+syst.+PDF+α_S)$\pm\delta m_t$(scale) (GeV)
$m^{t\bar{t}} \times p_T^{t,\text{had}}$	$170.85^{+0.55\ +0.12}_{-0.50\ -0.35}$
$m^{t\bar{t}}$	$172.28^{+0.64\ +0.24}_{-0.57\ -0.23}$
$p_T^{t,\text{had}}$	$174.30^{+1.20\ +0.51}_{-2.02\ -0.49}$

Table 5.3: Top quark mass results (in GeV) from fitting pseudo-data fully-simulated sample generated using POWHEG+PYTHIA 8 with m_t = 172.5 GeV to NNLO predictions using single and double differential $t\bar{t}$ cross sections. The values of (μ_R, μ_F) are set to $(1, 1) \times \mu_0$ as defined in Section 5.2.1.

(μ_R, μ_F)	(0.5,0.5)	(0.5,1.0)	(1.0,0.5)	(1.0,1.0)	(1.0,2.0)	(2.0,2.0)	(2.0,2.0)
$m^{t\bar{t}} \times p_T^{t,\text{had}}$	170.83	170.79	170.97	170.85	170.88	170.70	170.50
$m^{t\bar{t}}$	172.48	172.52	172.19	172.28	172.33	172.05	172.12
$p_T^{t,\text{had}}$	174.09	174.33	173.81	174.30	174.66	174.23	174.81

Table 5.4: Top quark mass results (in GeV) from fitting pseudo-data generated with m_t = 172.5 GeV to the NNLO predictions for different values of (μ_R, μ_F) in units of μ_0, which are indicated in the header.

The extracted top quark mass typically differs from the input nominal value of 172.5 GeV by 1-2 GeV for the double differential cross section and the $p_T^{t,\text{had}}$ differential cross section, whereas for the $m^{t\bar{t}}$ differential cross section the extracted mass is consistent with the input mass within the uncertainty. The difference between the input and extracted m_t values is due to the different order between pseudo-data and predictions, namely, the pseudo-data are NLO, but include a parton shower and the predictions are of higher order but do not include parton shower effects. The possible implications of the presence/absence of the parton shower on the mass extraction results is going to be further investigated in the future. A possible way to do so is to compare the top quark mass extracted from the NLO+PS sample and from a NLO sample with only the first parton shower emission.

5.4 Linearity and calibration

The mass fit is required to be unbiased and with a validated uncertainty. The level of bias expected in the measurement is quantified by doing a linearity test. The linearity of the mass extraction procedure is tested by performing the mass extraction on simulated events generated at different known m_t (pseudo-data) and by comparing the fitted results to the input masses. For an unbiased measurement one expects a linear relation of the fitted mass to the input mass with unitary slope and zero intercept. The linearity test includes the impact of the assumption on the value of the top quark mass made in the kinematic fit reconstruction performed in the measurements on $t\bar{t}$ differential cross section (see Section 5.1).

The NLO+PS simulated samples that provide the input reconstructed events are generated for five top quark masses: 170.0, 171.5, 172.5, 173.5 and 175.0 GeV. The events are simulated with the same underlying generation parameters used for the NLO+PS theory predictions described in Section 5.2.3. All the samples used in the linearity tests are passed through the fast detector simulation and then unfolded to parton level.

Linearity studies are performed by fitting the NLO+PS pseudo-data to NLO+PS predictions using three options for the covariance matrix. One of the considered covariance matrices includes only Poisson statistical uncertainties due to the size of the pseudo-data sample. In the second case, the covariance matrix is derived by including only the statistical uncertainties on the pseudo-data sample normalised to the integrated luminosity of 36 fb^{-1} (corresponding to a real data sample). The third considered covariance matrix is Cov_{exp}, which includes all statistical and experimental systematic (i.e. detector and modelling) uncertainties. The first two covariance matrix options allows to quantify the possible biases due to the features of the mass extraction procedure, since one assumes that all systematic uncertainties are negligible. The third option aims at building confidence in the robustness of the extraction technique by showing if the inclusion of all experimental uncertainties and their correlations induces biases.

5.4.1 Closure test

The first linearity study is a technical closure test. It uses the NLO+PS predictions so that the predictions in the χ^2 are fully consistent with the pseudo-data and the corrections used in the unfolding. The fully simulated sample generated with $m_t = 172.5$ GeV and scaled to 36 fb^{-1} is used as pseudo-data. The pseudo-data is fit to the NLO+PS predictions to extract m_t according to the procedure outlined in Section 5.3.1. The difference between the extracted m_t and the input $m_t = 172.5$ GeV is called bias and represents the non-closure of the technique. The closure test is performed for the three options of the covariance matrix, described above. The χ^2 functions corresponding to the fit using a covariance matrix including the statistical and systematic effects are shown in Fig. 5.10.

The results of the mass extraction are summarised in Table 5.5[4], no sign of bias is observed.

5.4.2 Linearity test using fast simulated samples

The five fast-simulated $t\bar{t}$ NLO+PS pseudo-data samples generated with the top quark masses $m_t \in [170.0, 171.5, 172.5, 173.5, 175.0]$ GeV are used to perform the linearity studies described in this section. The unfolding corrections for each sample are obtained from one of these samples (we test different options). The background in all the samples is assumed to be subtracted with negligible uncertainty.

Two kinds of the linearity fits are performed:

[4] Here in the table and in some cases afterwards instead of naming the differential cross sections $\frac{d\sigma}{dm^{t\bar{t}}}$, $\frac{d\sigma}{dp_{\text{T}}^{t,\text{had}}}$, $\frac{d^2\sigma}{dm^{t\bar{t}}\,dp_{\text{T}}^{t,\text{had}}}$ we will refer to the corresponding variables, which the differential cross sections are the functions of: $t\bar{t}$, $p_{\text{T}}^{t,\text{had}}$ or $m^{t\bar{t}} \times p_{\text{T}}^{t,\text{had}}$ if one refers to the double-differential cross section.

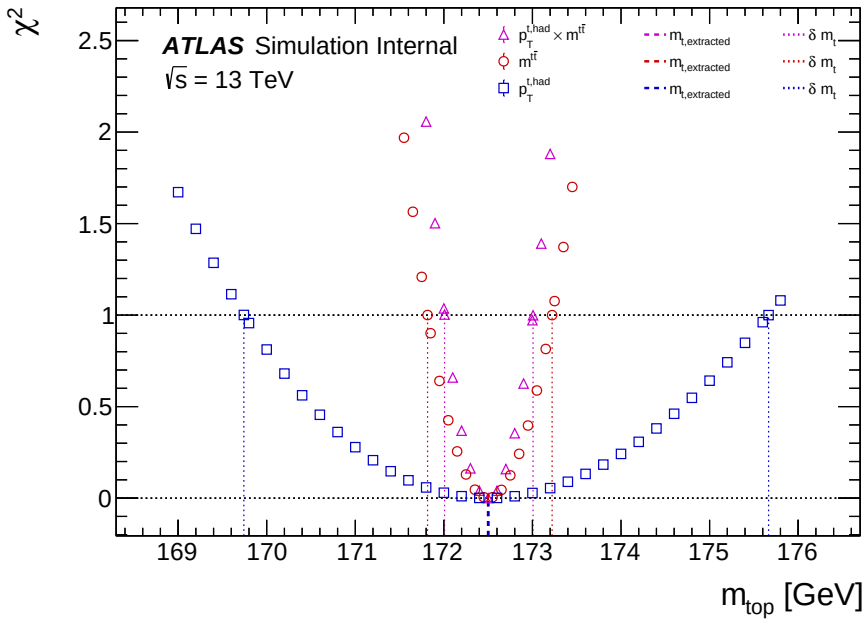

Figure 5.10: Top quark mass χ^2 distributions resulting from fitting NLO+PS pseudo-data generated with m_t = 172.5 GeV to NLO+PS predictions for three differential cross sections: $\frac{d\sigma}{dm^{t\bar{t}}}$ (red), $\frac{d\sigma}{dp_T^{t,had}}$ (blue), $\frac{d^2\sigma}{dm^{t\bar{t}}\,dp_T^{t,had}}$ (pink). The covariance matrix which includes all experimental statistical and systematic effects is used.

	extracted $m_t \pm \Delta m_t$ (GeV)		
	stat	MC stat	stat + exp syst
$m^{t\bar{t}} \times p_T^{t,had}$	$172.50^{+0.06}_{-0.06}$	$172.50^{+0.04}_{-0.04}$	$172.50^{+0.51}_{-0.49}$
$m^{t\bar{t}}$	$172.50^{+0.03}_{-0.03}$	$172.50^{+0.09}_{-0.09}$	$172.50^{+0.72}_{-0.68}$
$p_T^{t,had}$	$172.50^{+0.04}_{-0.04}$	$172.50^{+0.08}_{-0.08}$	$172.50^{+3.17}_{-2.76}$

Table 5.5: Top quark mass results from fitting NLO+PS pseudo-data generated with m_t = 172.5 GeV to NLO+PS predictions for three $t\bar{t}$ differential cross sections, $\frac{d^2\sigma}{dm^{t\bar{t}}\,dp_T^{t,had}}$, $\frac{d\sigma}{dm^{t\bar{t}}}$, $\frac{d\sigma}{dp_T^{t,had}}$, in three scenarios. Three options for the uncertanties included in the mass extraction are considered: data statistical effects only (stat), MC statistical effects only (MC stat) and all experimental statistical and systematic effects (stat+exp syst).

1. A closure test (a generalised version of the one described in Section 5.4.1) is obtained in the following way:
   - Each MC simulated sample with $m_t^{\text{true}} \in [170.0, 171.5, 172.5, 173.5, 175.0]$ GeV is used to build 5 different pseudo-data samples,
   - Each pseudo-data sample with a given m_t^{true} is unfolded using the unfolding corrections, which are obtained from itself, i.e. with the sample with $m_t = m_t^{\text{true}}$,
   - The mass extraction procedure is done for a given pseudo-data sample using the NLO+PS predictions and a covariance matrix which includes only MC statistical effects,
   - The extracted mass $m_t^{\text{extracted}}$ together with the corresponding input mass m_t^{true} is used in the linearity plot.

   The resulting five points $(m_t^{\text{extracted}} - 172.5, m_t^{\text{true}})$ of the linearity plot are fitted with a linear polynomial of the form $m_t^{\text{true}} = \alpha + \beta(m_t^{\text{extracted}} - 172.5)$ using a weighted least-squares fit. The parameters α and β are called "bias" and "slope", and in case of ideal linearity of the measurement they are equal to zero and unity, respectively.

   The three linearity plots corresponding to the three variables, $m^{t\bar{t}} \times p_{\text{T}}^{t,\text{had}}$, $m^{t\bar{t}}$ and $p_{\text{T}}^{t,\text{had}}$ are shown in Fig. 5.11. As in the first closure test in Section 5.4.1 no sign of bias or non-linearity is observed.

2. In a more realistic scenario one does not know the real value of m_t and one has to make an assumption about which m_t should be assumed in the unfolding corrections. Because of that, we perform a second linearity test obtained in the following way:
   - Each MC simulated sample with $m_t^{\text{true}} \in [170.0, 171.5, 172.5, 173.5, 175.0]$ GeV is used to build 5 different pseudo-data samples,
   - Each pseudo-data sample with a given m_t^{true} is unfolded using unfolding corrections, which are obtained from the sample with input mass $m_t = 172.5$ GeV,
   - The mass extraction is done for a given pseudo-data sample using NLO+PS predictions and a covariance matrix which includes only MC statistical effects,
   - The extracted mass $m_t^{\text{extracted}}$ is used in the linearity plot.

   The resulting five points $(m_t^{\text{extracted}} - 172.5, m_t^{\text{true}})$ of the linearity plot are fitted with a linear polynomial as in the previous case. The three linearity plots corresponding to the three variables, $m^{t\bar{t}} \times p_{\text{T}}^{t,\text{had}}$, $m^{t\bar{t}}$ and $p_{\text{T}}^{t,\text{had}}$ are shown in Fig. 5.12.

One observes a significant difference of the linearity curve slope from unity, which reflects the fact, that the difference between the input and the mass assumption used in the unfolding introduces a bias in the extracted mass. Regardless of the nature of such bias, one would need to develop a strategy to correct for it. Moreover, the linearity fit has a high χ^2 which reflects its non-linearity. The non-closure is related to the m_t dependence of the unfolding corrections, in particular of the efficiency and the migration matrix. Deeper understanding of the origin of this dependence is still on-going. Possible ways to deal with this issue are discussed in the following.

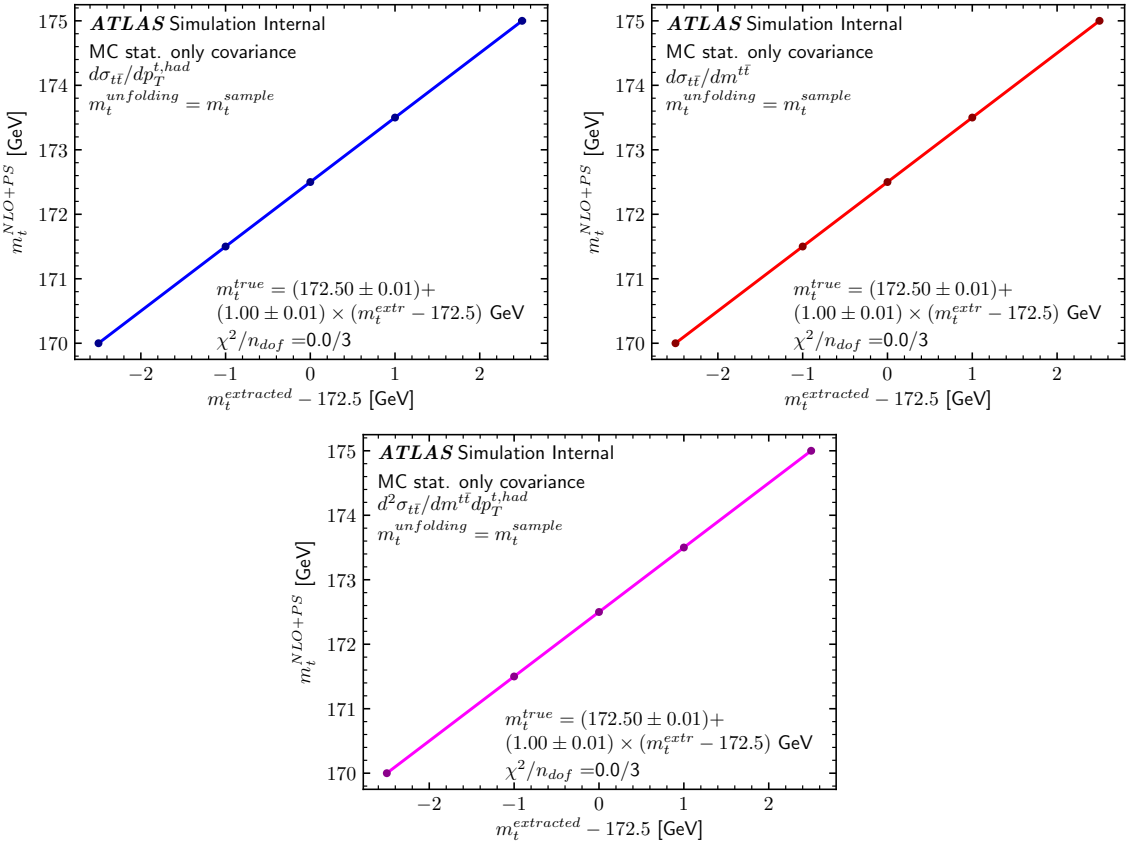

Figure 5.11: Linearity test performed using NLO+PS pseudo-data samples unfolded with the corrections from itself. Three differential cross sections, $\frac{d\sigma}{dm^{t\bar{t}}}$ (upper left), $\frac{d\sigma}{dp_{\mathrm{T}}^{t,\mathrm{had}}}$ (upper right), $\frac{d^2\sigma}{dm^{t\bar{t}}\,dp_{\mathrm{T}}^{t,\mathrm{had}}}$ (bottom), are used for the mass extraction. The covariance matrix which includes only MC statistical effects is used. The formula for the fitting linearity curve and the χ^2 of the fit are given at the bottom of the plot.

Calibration using the linearity curve

One of the possible ways to correct for the bias is to use the linearity curve as a calibration curve, i.e. in order to find the "true" top quark mass in the data or in a pseudo-data sample one needs to correct $m_t^{\mathrm{extracted}}$ extracted using the procedure described in Section 5.3.1 using the linearity curve formula: i.e. $m_t^{\mathrm{true}} = \alpha + \beta(m_t^{\mathrm{extracted}} - 172.5)$. Such a calibrated extracted mass m_t^{calib} would have an additional uncertainty, called the linearity uncertainty $\delta m_t^{\mathrm{lin}}$, which includes the propagated uncertainties from the linear fit, i.e. of the bias and the slope parameters of the linearity curve.

The calibrated masses using the linearity curve of the five top quark masses extracted from $\frac{d^2\sigma}{dm^{t\bar{t}}\,dp_{\mathrm{T}}^{t,\mathrm{had}}}$ are given in Table 5.6. Since a linear function is not enough for a linearity fit (it results in a fit with a high χ^2, see Fig. 5.12), the calibrated values of m_t are not consistent with the input m_t values. However, even if we use a higher-dimensional fit polynomial, this check is not enough to validate the calibration procedure. Several other tests are planned in which we will study how the linearity curve changes if one varies the pseudo-data distribution within the range of its systematic uncertainty.

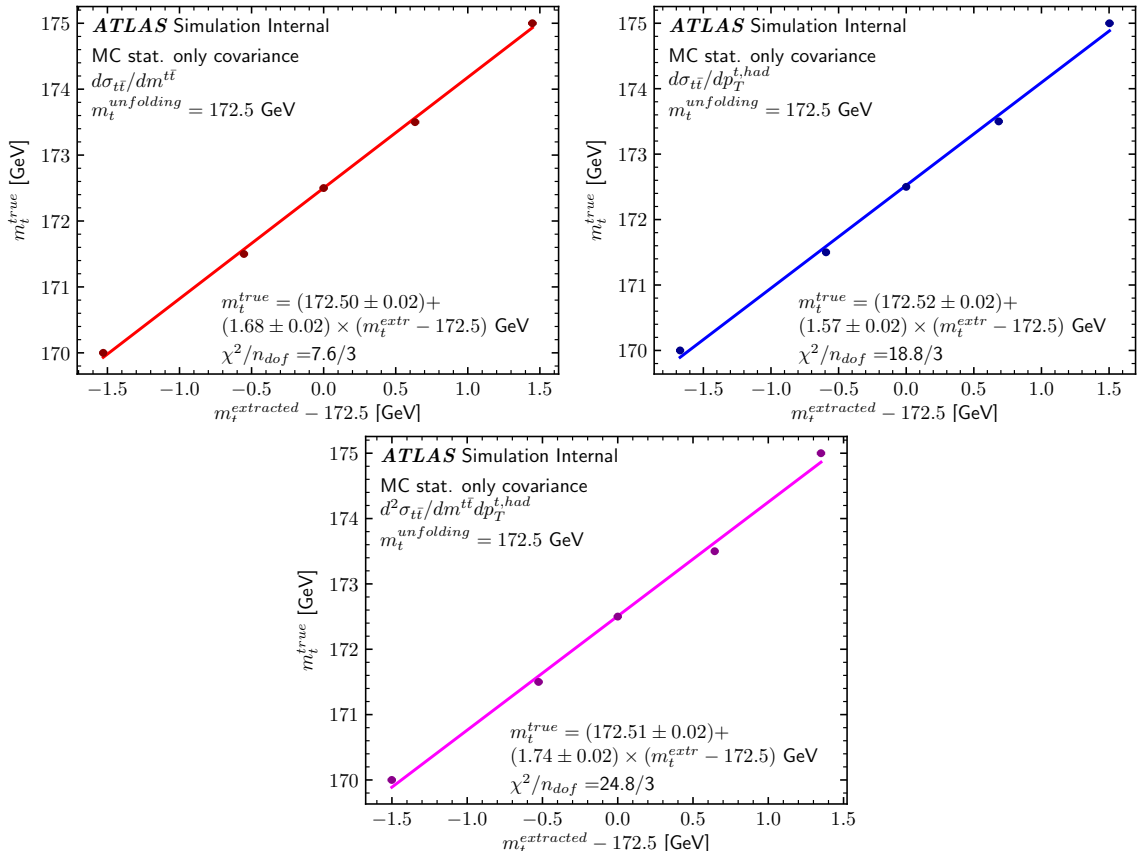

Figure 5.12: Linearity test performed using NLO+PS pseudo-data samples unfolded with the corrections from the sample with $m_t = 172.5$ GeV. Three differential cross sections, $\frac{d\sigma}{dm^{t\bar{t}}}$ (upper left), $\frac{d\sigma}{dp_{\mathrm{T}}^{t,\mathrm{had}}}$ (upper right), $\frac{d^2\sigma}{dm^{t\bar{t}}\,dp_{\mathrm{T}}^{t,\mathrm{had}}}$ (bottom), are used for the mass extraction. The covariance matrix which includes only MC statistical effects is used. The formula for the fitting linearity curve and the χ^2 of the fit are given at the bottom of the plot.

m_t^{true}	$m_t^{\mathrm{extracted}} \pm \delta m_t^{\mathrm{MCStat}}$	$m_t^{\mathrm{calib}} \pm \delta m_t^{\mathrm{lin}}$
170.0	171.00 ± 0.03	169.89 ± 0.04
171.5	171.97 ± 0.03	171.59 ± 0.02
172.5	172.50 ± 0.03	172.51 ± 0.02
173.5	173.14 ± 0.03	173.63 ± 0.03
175.0	173.85 ± 0.03	174.86 ± 0.04

Table 5.6: Example of calibration using the linearity curve of Fig. 5.12. The first column shows the generated m_t of the pseudo-data samples; the second column presents the extracted m_t values together with their MC statistical uncertainties; the calibrated m_t values and the linearity uncertaiinties are given in the third column. All values are in GeV.

Taking into account the m_t dependence in the unfolding

Instead of calibrating the extracted mass using the linearity curve, we are considering also a second strategy, which consists in including the m_t dependence of the unfolding in the χ^2 formula directly:

$$\chi^2(m_t) = \sum_{i,j} \left(x_i^{\text{meas}}(m_t) - x_i^{\text{pred}}(m_t)\right) \text{Cov}_{i,j}^{-1}(m_t) \left(x_j^{\text{meas}}(m_t) - x_j^{\text{pred}}(m_t)\right). \tag{5.14}$$

Here, instead of a fixed vector for the measured differential cross section values x_i^{meas} as in Eq. (5.12) we use a mass-dependent $x_i^{\text{meas}}(m_t)$, which means that for each considered mass point m_t^0 the differential cross section (from a sample with some input mass m_t^{in}) gets unfolded using unfolding corrections obtained from a sample with a consistent mass m_t^0.

However, the solution is not straightforward, since is it technically impossible to generate samples for all the mass points in the mass range considered for the χ^2 fit with a step of 1 MeV (see Section 5.3.1) to get the corresponding unfolding corrections. To get all needed unfolding corrections, we interpolate the reconstructed and the truth differential cross section distributions (used to find the unfolding corrections) between those available for the five mass points from the NLO+PS samples. The interpolation is done using a highest-degree polynomial (i.e. fourth-degree for five points) for each bin of the distribution. The corrections are then derived from these interpolated truth and reconstructed distributions. In this procedure, the corrections resulting from interpolation at each of the five original mass points are coinciding with the original ones (the ones before the interpolation), since the values of the corresponding differential cross section distributions are not shifted during the interpolation. Consequently, the top quark mass extracted from a sample with an input mass equal to either of these five does not have a bias, since the setup is the same as in the case of the linearity closure test.

The next step to validate this procedure is to generate several extra NLO+PS samples (with m_t = 169.0, 170.5, 174.5, 176.0 GeV) and to see if the interpolation using the five mass points provides consistent unfolding corrections (i.e. results with unbiased extracted m_t) for these new samples. As it was said before, the linearity test performed using the current MC samples gives unbiased results. If no new bias is observed in the linearity plot, we are going to employ this way of calculating the χ^2 for the default mass extraction. For the real data we would use the unfolding corrections obtained by interpolation of all available NLO+PS samples, in order to have even more precise parametrisation of the unfolding corrections.

Although this second strategy seems more coherent, the possible influence of the used MC information on the pole mass interpretation of the final results is still under discussion with theorists.

Also, for the second strategy we are investigating the possibility to apply a calibration which would account that the NNLO mass is used for the prediction while the NLO+PS mass is used to derive the unfolding corrections.

5.5 Uncertainties on the top quark mass

The sources of systematic uncertainties on the top quark mass are of experimental and theoretical origin. The experimental uncertainties result from the $t\bar{t}$ differential cross section measurements

used as inputs to the χ^2. The predictions carry additional theoretical uncertainties which are treated separately.

5.5.1 Experimental uncertainties

A number of experimental uncertainties are associated to each $t\bar{t}$ differential cross section measurement. A detailed description of the uncertainty sources are provided in the paper for the differential cross section measurements [189]. Their effects are included in the covariance matrix $\mathrm{Cov}_{\mathrm{exp}}$.

The breakdown of uncertainties is derived with "coarse granularity" (we merge some of the sources of uncertainties) to maximise robustness against statistical fluctuations in the estimate of the covariance matrix elements for the detector-related uncertainties.

The coarse grouping of the uncertainties is defined as follows:

- **Jets:** all the systematic uncertainties derived from the components of the jet energy scale, the jet energy resolution, the jet vertex fraction and the pile-up corrections.
- **Missing transverse momentum:** all the uncertainties due to the soft track component of the missing transverse momentum.
- ***b*-tagging:** all the components of the uncertainties related to b-tagging.
- **Leptons:** all the systematic uncertainties derived from the scale, resolution, trigger, isolation and reconstruction efficiencies associated with muons and electrons.
- **Backgrounds:** the uncertainties derived from the estimates of all the backgrounds (simulated and data-driven contributions).
- **PDF:** uncertainty due to the choice of the PDF set used in the modelling.
- **Generator:** uncertainty related to the MC generator used to calculate the matrix element.
- **ISR/FSR:** uncertainty related to the modelling of the initial- and final-state radiation.
- **Hadronisation:** uncertainty due to the choice of the MC generator for the parton shower and hadronisation.

5.5.2 Theoretical uncertainties

Theoretical uncertainties are related to the limited knowledge of the NNLO differential cross section predictions. These uncertainties include those from QCD scale variations that are used as proxy for the absence of higher order corrections, those resulting from the limited knowledge of the PDFs and from the uncertainty on the strong coupling constant α_S. The last two uncertainties are computed according to the PDF4LHC recommendations [202].

The PDF systematic uncertainty is computed using the FASTNLO code during the convolution of the theoretical NNLO fixed order predictions (at the central mass point $m_t = 172.5$ GeV) with a PDF4LHC15 NNLO PDF set, for which the MC representation with 100 replicas is provided. The

PDF4LHC15 NNLO PDF set is based on a statistical combination of the CT14, MMHT2014 and NNPDF3.0 PDF sets.

The α_S uncertainty of the differential cross section σ_i in bin i is computed as:

$$\delta_i^{\alpha_S} = \frac{1}{2}\left(\sigma_i(\alpha_S^{\text{down}}) - \sigma_i(\alpha_S^{\text{up}})\right), \tag{5.15}$$

where $\sigma_i(\alpha_S^{\text{down}})$ and $\sigma_i(\alpha_S^{\text{up}})$ are the values of the cross section at two different α_S points, $\alpha_S^{\text{down}} = 0.1165$ and $\alpha_S^{\text{down}} = 0.1195$, obtained by convolution of the theoretical NNLO fixed order prediction (at the central mass point $m_t = 172.5$ GeV) with two members of the PDF4LHC15 NNLO PDF set (averaged over the PDF values) in which α_S is set to α_S^{down} or α_S^{up}.

The PDF and α_S uncertainties are included in the theoretical covariance matrix Cov_{theo} which is used for the top quark mass extraction as described in Section 5.3.1. The Cov_{theo} covariance matrix is build assuming 100% correlation amongst the bins. The remaining theoretical uncertainty, the scale uncertainty, is added to the total uncertainty afterwards by performing the mass extraction with scale-varied predictions and looking at the differences in the extracted masses. This approach is chosen since the exact value of the bin-to-bin correlation coefficient of the scale uncertainty is unknown. The scale uncertainty is defined by the amplitude of the change of the extracted m_t when the NNLO predictions are computed with (μ_R, μ_F) scales varied up and down by a factor of two. Seven values of the top quark mass are extracted, each of them corresponding to the minimum of the χ^2 shape built using the theoretical predictions with one of the seven combinations of the (μ_R, μ_F) scales mentioned in Section 5.2.1: [(1,1),(2,1),(1,2),(0.5,1),(1.0,5),(0.5,0.5),(2,2)] in units of μ_0. Then, the upper (lower) scale uncertainty is taken to be the absolute value of the difference between the maximum (minimum) of the seven extracted masses and the one corresponding to the $(1, 1)$ scale.

The asymmetry of the scale uncertainty is taken into account, when adding it to the rest of the uncertainties by using the uncertainty addition technique proposed in [210]

5.5.3 Study on the bin-to-bin correlations of the scale uncertainty

In order to understand how the choice of the correlations in the theoretical covariance matrix affect the mass extraction results an additional test has been done. Different correlation factors between the bins of the covariance matrix are considered. For this particular test not only the PDF and α_S uncertainties, but also the scale uncertainty is included in the theoretical covariance matrix. The mass extraction is performed using the NLO+PS fully-simulated pseudo-data sample and the NNLO predictions at central (μ_R, μ_F) scales.

The results of the mass extraction when one assumes 100% correlated bins for the theoretical covariance matrix are shown in Table 5.7.

As discussed in Section 5.3.4, a perfect closure of the extracted mass compared to the input mass is not expected due to the different orders used for the pseudo-data and the predictions.

The results of the m_t extraction when the theoretical covariance matrix has 50% correlation between the bins are given in Table 5.8.

	extracted $m_t \pm \delta m_t$(stat.+syst.+PDF+α_S +scale) (GeV)
$m^{t\bar{t}} \times p_T^{t,\text{had}}$	$170.66^{+0.53}_{-0.55}$
$m^{t\bar{t}}$	$171.82^{+0.76}_{-0.62}$
$p_T^{t,\text{had}}$	$174.28^{+1.20}_{-2.00}$

Table 5.7: Top quark mass results (in GeV) obtained using NNLO predictions using fully correlated Cov_{theo}.

	extracted $m_t \pm \delta m_t$(stat.+syst.+PDF+α_S +scale) (GeV)
$m^{t\bar{t}} \times p_T^{t,\text{had}}$	$170.62^{+1.12}_{-1.01}$
$m^{t\bar{t}}$	$171.22^{+1.50}_{-1.33}$
$p_T^{t,\text{had}}$	$174.52^{+2.07}_{-3.77}$

Table 5.8: Top quark mass results (in GeV) obtained using NNLO predictions using partially correlated Cov_{theo}.

A noticeable increase of the total uncertainty is observed for all the variables, hence, the choice of the bin-to-bin correlation factor has a significant impact on the theoretical m_t uncertainty. Since the true value of the correlation cannot be easily estimated, the chosen procedure is to consider the theoretical scale uncertainty, which is the dominant one, separately from the other uncertainty components.

5.5.4 Uncertainty validation

A study of the difference of the m_t uncertainty (and of its breakdown in different components) when changing from single to double differential cross sections is performed. This allows to check the consistency of the m_t measurements when using different input $t\bar{t}$ differential cross sections and to investigate the origin of eventual decrease of the uncertainty sources between variables.

The study is performed by using a unique pseudo-data sample that underwent full detector simulation generated at NLO+PS accuracy with $m_t = 172.5$ GeV, by using the unfolding corrections from the same sample and the NNLO predictions.

In order to quantify the contribution of a given uncertainty source to the final uncertainty, m_t is extracted in two scenarios: the first scenario uses the full covariance matrix including all the effects and the second scenario uses the covariance matrix that includes all effects except the effect of interest. Then, the uncertainty corresponding to a given (group of) systematic component (components) $\delta m_{t,\text{sys}}$ is defined by the difference in quadrature between the uncertainties on the top quark mass obtained in the two scenarios, $\delta m_{t,\text{total}}$ and $\delta m_{t,\text{total-sys}}$:

$$\delta m_{t,\text{sys}} = \sqrt{\delta m^2_{t,\text{total}} - \delta m^2_{t,\text{total-sys}}}. \tag{5.16}$$

The results for the m_t uncertainty and its breakdown are summarised in Table 5.9 using the double differential cross section and in Tables 5.10 and 5.11 using the single differential cross sections.

The total expected uncertainty is at the level of 600 MeV for the double differential cross section. The $m^{t\bar{t}}$ differential cross section alone results into uncertainty at the level of 700 MeV and the top

Source of uncertainty	δm_t (GeV)
Backgrounds	+0.27 -0.21
b-tagging	+0.19 -0.10
Jets	+0.33 -0.29
Leptons	+0.09 -0.02
Missing transverse momentum	+0.03 -0.07
PDF	+0.12 -0.05
Generator	+0.27 -0.20
ISR/FSR	+0.13 -0.13
Hadronisation	+0.01 -0.01
Total experimental systematic uncertainty	+0.47 -0.44
Total experimental statistical uncertainty	+0.04 -0.04
Theoretical PDF and α_S uncertainties	+0.30 -0.20
Theoretical scale uncertainty	+0.12 -0.35
Total uncertainty	+0.59 -0.60

Table 5.9: Summary of expected statistical and systematic uncertainties in m_t extracted from a fit of $\frac{d^2\sigma}{dm^{t\bar{t}}\,dp_T^{t,\mathrm{had}}}$ to NNLO predictions. The pseudo-data are built using NLO+PS simulated events.

Source of uncertainty	Δm_t (GeV)
Backgrounds	+0.30 -0.19
b-tagging	+0.21 -0.09
Jets	+0.32 -0.24
Leptons	+0.07 -0.01
Missing transverse momentum	+0.03 -0.03
PDF	+0.05 -0.05
Generator	+0.12 -0.12
ISR/FSR	+0.24 -0.17
Hadronisation	+0.22 -0.11
Total experimental systematic uncertainty	+0.56 -0.51
Total experimental statistical uncertainty	+0.03 -0.04
Theoretical PDF and α_S uncertainties	+0.33 -0.20
Theoretical scale uncertainty	+0.24 -0.23
Total uncertainty	+0.68 -0.62

Table 5.10: Summary of expected statistical and systematic uncertainties in m_t extracted from a fit of $\frac{d\sigma}{dm^{t\bar{t}}}$ to NNLO predictions. The pseudo-data are built using NLO+PS simulated events.

Source of uncertainty	Δm_t (GeV)
Backgrounds	+1.07 -1.07
b-tagging	+0.71 -0.71
Jets	+0.74 -0.74
Leptons	+0.23 -0.23
Missing transverse momentum	+0.20 -0.20
PDF	+0.01 -0.01
Generator	+0.42 -0.42
ISR/FSR	+0.25 -0.25
Hadronisation	+0.39 -0.39
Total experimental systematic uncertainty	+1.18 -2.01
Total experimental statistical uncertainty	+0.04 -0.04
Theoretical PDF and α_S uncertainties	+0.22 -0.04
Theoretical scale uncertainty	+0.51 -0.49
Total uncertainty	+1.33 -2.07

Table 5.11: Summary of expected statistical and systematic uncertainties in m_t extracted from a fit of $\frac{d\sigma}{dp_T^{t,\text{had}}}$ to NNLO predictions. The pseudo-data are built using NLO+PS simulated events.

quark momentum, which is less constraining, results in total uncertainty of the order of 2 GeV. The combination of the two variables reduces the total experimental uncertainty.

The dominant experimental uncertainties for $\frac{d^2\sigma}{dm^{t\bar{t}}\,dp_T^{t,\text{had}}}$ and $\frac{d\sigma}{dm^{t\bar{t}}}$ are those from backgrounds and jet properties (the jet energy scale uncertainty is implemented in the differential cross section measurement using a set of 29 nuisance parameters). The generator uncertainty is also large for $\frac{d^2\sigma}{dm^{t\bar{t}}\,dp_T^{t,\text{had}}}$. The experimental uncertainties for $\frac{d\sigma}{dp_T^{t,\text{had}}}$ are dominated by those resulting from background, b-tagging effects and the jets. The theoretical scale uncertainty is about 0.5 GeV for $\frac{d\sigma}{dp_T^{t,\text{had}}}$ and twice smaller for $\frac{d^2\sigma}{dm^{t\bar{t}}\,dp_T^{t,\text{had}}}$ and $\frac{d\sigma}{dm^{t\bar{t}}}$. The expected scale m_t uncertainty (related to the NNLO calculations) for the double differential cross section is $^{+0.12}_{-0.35}$ which is smaller than in the previous top quark pole mass measurements which use NLO theoretical predictions. Indeed, m_t measured by ATLAS using single-differential $t\bar{t}$ +jet cross section [173] has $^{+0.6}_{-0.2}$ GeV scale uncertainty and m_t measured by CMS using triple-differential $t\bar{t}$ cross section [177] has $^{+0.3}_{-0.3}$ GeV scale uncertainty.

The total experimental systematic uncertainty in Tables 5.9 to 5.11 is calculated as $\delta m_{t,\text{total exp syst}} = \sqrt{\delta m^2_{t,\text{total exp.}} - \delta m^2_{t,\text{exp. stat.}}}$, where $\delta m_{t,\text{total exp}}$ is estimated using the covariance matrix which contains statistical, detector and modelling uncertainties and $\delta m_{t,\text{exp stat}}$ is estimated using the covariance matrix which contains the statistical uncertainty only. If one adds up all the individual uncertainties given in Tables 5.9 to 5.11 the resulting sum differs from the total experimental systematic uncertainty. For the $\frac{d^2\sigma}{dm^{t\bar{t}}\,dp_T^{t,\text{had}}}$ this difference is about ~100 MeV. For the $\frac{d\sigma}{dp_T^{t,\text{had}}}$ all the individual uncertainties and their sum are symmetric, whereas the total experimental systematic uncertainty is asymmetric. These differences are expected to be connected with the assumption of

100% bin-to-bin correlations in the modelling uncertainties. Since the individual uncertainties are computed using Eq. (5.16), where $\delta m^2_{t,\text{total}}$ is obtained using the covariance which has all effects including modelling, these assumptions on the correlation may influence the values of the individual uncertainties. A possible workaround under investigation would be to extract the mass using an alternative computation of the covariance, in which both, detector and modelling components are calculated using pseudo-experiments, i.e. no assumption on the correlation is done and the whole calculation is more coherent.

5.6 Conclusions

This chapter presented a measurement of the top quark pole mass extracted by a least squares fit of a parton level $t\bar{t}$ double differential cross section as a function of $m^{t\bar{t}}$ and $p_{\text{T}}^{t,\text{had}}$ to the NNLO theoretical prediction obtained as a function of the top quark mass in the pole mass scheme. At the moment, the analysis is "blinded", i.e. simulated NLO+PS pseudo-data are used instead of real data. In the future, the data sample of 36 fb^{-1} recorded at the centre-of-mass energy $\sqrt{s}$ = 13 TeV by the ATLAS detector at the LHC in 2015 and 2016 will be used. Events with exactly one electron or muon and at least two jets in the final state are used to measure the parton level differential cross sections of $t\bar{t}$ production as a function of top quark transverse momentum and of the invariant mass of the $t\bar{t}$ system, extrapolated to the full phase space.

With this method the total uncertainty on the top quark mass is expected to be of the order of 600 MeV, which is smaller than the previous ATLAS top quark pole mass measurements.

6 Parton shower uncertainties in HERWIG 7 for $t\bar{t}$ production

The study of parton shower uncertainties using the HERWIG 7 generator in the context of $t\bar{t}$ production is presented in this chapter.

This work has been conducted as a qualification task in order to become an ATLAS author.

6.1 Introduction

One of the sources of systematic uncertainties in the ATLAS measurements at the LHC is the ambiguities in modelling the low-p_{T} QCD phenomena: in particular, parton shower (PS), hadronisation, underlying event.

In ATLAS, the systematic uncertainty associated to the parton shower and hadronisation is currently estimated by comparing samples obtained using two Monte–Carlo (MC) generators namely PYTHIA 8 [207, 211] and HERWIG 7 [212, 213] (potentially interfaced with other programs to model the matrix element generation). The main difference between PYTHIA and HERWIG is the choice of the hadronisation model: the PYTHIA shower is modelled according to the string model [61, 62], while HERWIG exploits the cluster model [63, 64] (see Section 2.5).

This approach has been critisised recently, since it may be overestimating the uncertainty. The main argument is that some of the tuning parameters which are present in one generator are absent or impossible to change in another. Consequently, the comparison may be performed between not truly consistent setups which can result in a too conservative estimate.

An alternative approach may be to choose one of the two generators and to vary its available hadronisation/PS parameters in a certain range to derive uncertainties. The present study is oriented towards this alternative approach: we study the parton shower uncertainty in the HERWIG 7 generator using parameter shifts.

HERWIG 7[1] is a multi-purpose particle physics event generator, successor of the HERWIG 6 and Herwig++ series [214]. It allows the calculation of the matrix elements (ME) of one-loop QCD processes, supports two parton shower types and two ME/PS matching approaches. As well as other generators used by the ATLAS experiment, HERWIG 7 is integrated into the Athena software framework. The studies presented in this chapter has been performed using HERWIG 7.1.3, which was the newest version at that time included in Athena. Until the present studies, there was no proper way

[1] HERWIG = Hadron Emission Reactions With Interfering Gluons

to define a parton shower uncertainty for HERWIG 7 mainly due to the inability to access the variation of all needed parameters (scales) of the parton shower in HERWIG versions up to version 7.0 [215]. In the current HERWIG 7.1 series [213] this feature is available, however, the proper way to combine the individual components of the uncertainty is not obvious: one should carefully disentangle the different variations to prevent double counting.

In this chapter, we propose a recipe for the parton shower uncertainty calculation (Section 6.5) and discuss the implementation of the parameter variations. To quantify the effect of the variations we generate the corresponding MC samples with HERWIG 7.1.3 and compare to several unfolded data distributions measured by the ATLAS experiment using several available RIVET analyses, described in Section 6.4. The principles of the event simulation in the Monte-Carlo generators in general and in HERWIG 7 in particular are given in the Chapter 2 and Section 6.2, respectively. The common HERWIG 7 setup is described in Section 6.3. The results are discussed in Section 6.7 as well as the general conclusion and outlook.

6.2 Event simulation in HERWIG 7

In Chapter 2 it was described in detail which steps are performed for the simulation of a high-energy-physics proton–proton collision. In this section, we will focus on the models and parameters which are available in HERWIG 7.

- **Parton distribution functions:** in HERWIG 7 there is a possibility to choose which PDF sets from the LHAPDF library is used in the matrix element, parton shower and multiple parton interaction model.
- **Matrix element:** one can either calculate it directly in HERWIG 7 or take a prepared parton level[2] sample in the Les-Houches Event (LHE) format [216].

  HERWIG 7 supports matrix element calculation up to NLO. There are many built-in matrix elements that can be run directly [217], but another possibility is to use the MATCHBOX [218] module: a fully integrated framework for automated NLO QCD matrix element calculation and subsequent NLO matching.

  As described in the HERWIG 7 release note [215], a limited number of processes can be computed just using built-in MATCHBOX amplitudes. The rest of the Standard Model processes can be simulated by attaching to MATCHBOX one of the external amplitude plugins such as GOSAM [219], MADGRAPH [220], NJET [221], OPENLOOPS [222] or VBFNLO [223] depending on the desired process.

  The parameters of the MATCHBOX setup used for current event simulation are given in Section 6.3.1
- **Parton shower:** both angular-ordered ($\tilde{q}$) and dipole showers are implemented. The default shower is the angular-ordered one.

[2] with free coloured partons in the final state

- **ME/PS matching:** both matching schemes, MC@NLO and POWHEG, are available through the MATCHBOX framework.
- **Hadronisation:** the cluster hadronisation model is used.
- **Underlying event:** it is simulated with an eikonal model for multiple partonic interactions.

6.3 HERWIG 7 setup

In the study described in the following, inclusive $t\bar{t}$ samples at 7 TeV and 13 TeV are produced at next-to-leading order. The matrix element is either calculated internally using MATCHBOX or taken from an existing POWHEG sample.

6.3.1 MATCHBOX setup for the matrix element generation

If MATCHBOX is used, the tree level amplitudes are provided by MADGRAPH and the one-loop amplitudes are evaluated with OPENLOOPS.

The NNPDF30 PDF set at NLO is chosen with a value of α_S equal to 0.118 [182]. Several options for the matrix element renormalisation and factorisation scales (μ_R, μ_F) are implemented in HERWIG 7. According to previous studies [224], for $t\bar{t}$ production the best agreement with data is achieved with the m_T dynamical scale:

$$\mu_R^2 = \mu_F^2 = m_{T,t}^2 + m_{T,\bar{t}}^2, \tag{6.1}$$

where $m_{T,t}$ ($m_{T,\bar{t}}$) is the transverse mass of the top (antitop) quark. These values of the renormalisation/factorisation scales are used in the presented studies as well.

The central value of the factorisation scale is also used as the maximum allowed transverse momentum of shower emissions.

The calculations are performed in a *five-flavour* scheme, named after the number of active flavours of quarks (u, d, s, c, b) in the PDF, in which the b quark is treated as massless and therefore can be found in both initial and final states.

6.3.2 Using an existing parton-level POWHEG sample

Alternatively to the MATCHBOX sample an existing parton-level POWHEG sample can be used. In the following studies, the nominal ATLAS parton level $t\bar{t}$ sample (either at 7 TeV or 13 TeV) generated with POWHEG-BOX v2 [204, 205] is used in the LHE format.

In these samples, the NLO NNPDF30 PDF set with a value of α_S equal to 0.118 is chosen for the matrix element calculation at NLO. The resummation damping factor h_{damp}, which is a parameter of

the ME/PS matching and which adjusts the radiation at high p_{T} is set to the $1.5 \times m_t$. The nominal renormalisation and factorisation scales in the matrix element are set to the E_{T} dynamical scale:

$$\mu_{\mathrm{R}}^2 = \mu_{\mathrm{F}}^2 = \frac{1}{2}\sqrt{E_{\mathrm{T},t} E_{\mathrm{T},\bar{t}}}, \tag{6.2}$$

where $E_{\mathrm{T},i}$ is the transverse energy defined as $E_{\mathrm{T},i}^2 = m_{\mathrm{T},i}^2 + p_{\mathrm{T},i}^2$ in which $m_{\mathrm{T},t}$ ($m_{\mathrm{T},\bar{t}}$) is the transverse mass and $p_{\mathrm{T},t}$ ($p_{\mathrm{T},\bar{t}}$) is the transverse momentum of the top (antitop) quark.

6.3.3 Matching, showering, hadronisation and soft QCD

The obtained matrix element is then matched through a subtractive (MC@NLO) or a multiplicative (POWHEG) procedure to the angular-ordered or to the dipole parton shower.

The PDFs used in the parton shower are taken from the NNPDF30 NLO PDF set.

For the modelling of the minimum bias and underlying event the default HERWIG 7.1 tune named `H7.1-Default` is used [225]. It includes the parton shower cutoffs and hadronisation parameters which are tuned to the LEP data [226] and the parameters of the MPI model which are tuned to the minimum-bias and underlying-event data from LHC [227].

6.4 Analysis using RIVET

The 7 TeV and 13 TeV data collected by the ATLAS detector are compared with event samples simulated with HERWIG 7.1.3 in the Athena framework. All the used observables are unfolded to particle level[3] in a fiducial phase-space[4]. The data/MC comparison is performed using the RIVET 2.5.4 program [71].

6.4.1 What is RIVET?

The RIVET[5] toolkit is a C++ class library, which provides the infrastructure and calculational tool to produce distributions corresponding to input simulated samples or data samples [71, 228]. Because of its high automation and scalability the RIVET program is useful for the validation of the generator models (when data/MC comparison is performed) and the generator tuning (if several generator settings are tested and the corresponding outputs are compared to each other). For generator tuning, the generator and reference data from RIVET is normally used as an input to the PROFESSOR tuning system [229] which in turn is used to directly predict new generator tunes.

[3] with colourless hadrons in the final state

[4] A fiducial phase-space is a phase space in which the measurement is performed. The corresponding cuts at particle level replicate the detector-level cuts. A fiducial phase space is smaller than the full phase space in which the final-state particles are produced, beacuse of the limited detector coverage, efficiency and resolution.

[5] RIVET = Robust Independent Validation of Experiment and Theory

To start with, RIVET requires two inputs: the analysis code and the samples to run on. A large number of data analyses from various experiments (LEP, HERA, RHIC, KEK-B, Tevatron, LHC and more) are already implemented in RIVET and included in its library [230]. New ones are added regularly but not all of the existing analyses which eventually result in papers have a corresponding code for RIVET. Normally, all the available RIVET analyses have a reference data for all the plotted distributions. There is a number of pure Monte-Carlo analysis which are used mostly for testing and validation. If a desired analysis is not available, there is a possibility to write a new one and use it as a separate "plugin". The input Monte–Carlo samples, in order to be recognised by RIVET, are required to be produced in a HEPMC format [231, 232].

6.4.2 Analyses used in the study

- **Analysis A: Measurement of jet shapes in top-quark pair events at $\sqrt{s}$ = 7 TeV using the ATLAS detector (ATLAS_2013_I1243871) [233]**

  The jet shapes in $t\bar{t}$ events are measured at particle level in both lepton+jets and dilepton channels using 1.8 fb^{-1} of pp collision data with $\sqrt{s}$ = 7 TeV. The differential and the integrated jet shapes of the b-quark jets are compared to the light-quark jets.

  The differential jet shape $\rho(r)$ in an annulus of inner radius $r - \Delta r/2$ and outer radius $r + \Delta r/2$ from the axis of a given jet is defined as follows:

  $$\rho(r) = \frac{1}{\Delta r} \frac{p_{\mathrm{T}}(r - \Delta r/2, r + \Delta r/2)}{p_{\mathrm{T}}(0, R)} . \tag{6.3}$$

  Here, $\Delta r = 0.04$ and $p_{\mathrm{T}}(r_1, r_2)$ is the scalar sum of the p_{T} of the jet constituents with radii between r_1 and r_2.

  Electron candidates are required to have $p_{\mathrm{T}} > 25$ GeV and $|\eta| < 2.47$. The electrons in the transition region between barrel and endcap calorimeters $1.37 \leq |\eta| < 1.52$ are not considered. Muon candidates are required to satisfy $p_{\mathrm{T}} > 20$ GeV and $|\eta| < 2.5$. Besides that, the event needs to have at least two jets with $p_{\mathrm{T}} > 25$ GeV and $|\eta| < 2.5$ in the event, and at least one of the selected jets has to be tagged as a b-jet. The missing transverse momentum has to be $E_{\mathrm{T}}^{\mathrm{miss}} > 60$ GeV in the e^+e^- and $\mu^+\mu^-$ channels, whereas in the $e\mu$ channel $H_{\mathrm{T}} > 130$ GeV is required. The Drell–Yan lepton pair background is rejected in the e^+e^- and $\mu^+\mu^-$ channels by selecting the events with $m_{ll} > 15$ GeV and $|m_{ll} - m_Z| \geq 10$ GeV.

- **Analysis B: Measurement of jet activity produced in top-quark events with an electron, a muon and two b-tagged jets in the final state in pp collisions at $\sqrt{s}$ = 13 TeV with the ATLAS detector (ATLAS_2017_I1495243) [234]**

  The $t\bar{t}$ cross sections as functions of additional-jet multiplicity and transverse momentum and the gap fraction as a function of the p_{T} threshold for additional jets are measured in the $e\mu$ channel using 3.2 fb^{-1}of pp collision data with $\sqrt{s}$ = 13 TeV. The first type of gap fraction is

measured as a ratio between the number of events $n(Q_0)$ with no additional jet with $p_T > Q_0$, and the total number of selected events $N_{t\bar{t}}$:

$$f_{\text{gap}}(Q_0) = \frac{n(Q_0)}{N_{t\bar{t}}} . \tag{6.4}$$

The second type of gap fraction is defined as the fraction of events in which the scalar p_T sum of all additional jets in the given veto region does not exceed a given threshold Q_{sum} (this subset of events is denoted as $n(Q_{\text{sum}})$):

$$f_{\text{gap}}(Q_{\text{sum}}) = \frac{n(Q_{\text{sum}})}{N_{t\bar{t}}} . \tag{6.5}$$

All measurements are presented at particle level. The events are selected by requiring an opposite charge $e\mu$ pair and at least two b-tagged jets. A jet originating from b-quark is identified as a b-jet if a hadron with $p_T > 5$ GeV containing this b-quark is associated with a jet through a ghost-matching technique [124]. Jets are reconstructed with the anti-k_t algorithm with a radius parameter $R = 0.4$. Jets and leptons are required to have $p_T > 25$ GeV and $|\eta| < 2.5$.

- **Analysis C: Measurements of top-quark pair differential cross sections in the lepton+jets channel in pp collisions at $\sqrt{s}$ = 13 TeV using the ATLAS detector (ATLAS_2017_I1614149) [235]**

  The $t\bar{t}$ differential cross sections as functions of top-quark and $t\bar{t}$ system kinematic observables are measured at particle level using 3.2 fb^{-1} of pp collision data with $\sqrt{s} = 13$ TeV. The observables used are top-quark transverse momentum and rapidity and the $t\bar{t}$ transverse momentum, rapidity and invariant mass. Events are selected in the lepton+jets channel, which is characterised by the presence of a high-p_T lepton, missing transverse momentum and at least four jets, with at least two b-tagged jets, identified using the same technique as described in Analysis B. Jets are reconstructed with the anti-k_t algorithm with a radius parameter $R = 0.4$ and are required to have $p_T > 25$ GeV and $|\eta| < 2.5$.

- **Analysis D: Monte Carlo analysis for semi-leptonic $t\bar{t}$ production studies (MC_TTBAR) [236]**

  The differential $t\bar{t}$ cross sections as functions of W and top-quark masses, and jet kinematic observables are plotted at particle level. The events are selected by requiring at least one charged lepton with $|\eta| < 4.2$ and with $p_T > 30$ GeV and at least 4 jets including two b-tagged jets. Jets are reconstructed with the anti-k_t algorithm with a radius parameter $R = 0.6$ and are required to have $|\eta| < 4.2$, whereas no p_T cut is set. The threshold on missing transverse momentum is set to $E_T^{\text{miss}} > 30$ GeV.

  This is a pure Monte–Carlo analysis for $t\bar{t}$ studies, i.e. no data is associated with it. Samples with any $\sqrt{s}$ value can be processed using this analysis.

- **Analysis E: Monte Carlo validation analysis to study fragmentation of heavy flavour hadrons in jets (MC_HFJETS) [237]**

  This analysis provides the plots to study fragmentation of heavy flavour hadrons in jets. Energy fraction, transverse momentum fraction and the transverse momentum (p_{T}) of b-hadrons (or c-hadrons) in the leading b-jet (or c-jet) are plotted at particle level as well as the transverse momentum p_{T} of the leading b- and c-jet. Jets are reconstructed with the anti-k_t algorithm with a radius parameter $R = 0.6$ with no p_{T} cut. The tagging of b- and c-jets is performed only with a space matching $\Delta R < 0.3$.

  This is a pure Monte–Carlo analysis to study heavy flavour production, i.e. no data is associated with it. Samples with any $\sqrt{s}$ value can be processed using this analysis.

6.5 Parton shower variations of MATCHBOX+HERWIG7 samples

HERWIG 7 as general purpose generator, relies on both, perturbative calculations and on non-perturbative inputs from phenomenology. Following [238], we can single out several sources of uncertainties in this case:

- Numerical: limited computational precision
- Parametric: quantities, measured experimentally (masses, coupling constants, PDFs), other than the generator parameters
- Algorithmic: ambiguities in the matching schemes, parton shower algorithms, phenomenological models
- Perturbative: limitations caused by the truncation of the α_{S} expansion series and the order of logarithms in the parton shower
- Phenomenological: fit uncertainties of the parameters in the non-perturbative models

In this study we consider only the uncertainties related to the ME/PS matching and to the calculation of the parton shower, which arise from the variation of the available scales [239]. These are the **perturbative** and **algorithmic** uncertainties:

Perturbative uncertainties are coming from the choice of the following parameters:

- The *veto* scale (μ_{Q}), which is a maximum allowed transverse momentum for emissions in the parton shower. For the dipole shower it is the same as the shower starting scale.
- The value of the *hard* scale: renormalisation (μ_{R}) and factorisation (μ_{F}) scales in the hard process.
- The values of the renormalisation and factorisation scales in the parton shower.

Scale	generation step	HERWIG 7 parameter
veto scale (μ_Q)	matching	MEMATCHING:HARDSCALEFACTOR
	PS	SHOWERHANDLER:HARDSCALEFACTOR
		DIPOLESHOWERHANDLER:HARDSCALEFACTOR
hard scale (μ_R,μ_F in ME)	ME	FACTORY:RENORMALIZATIONSCALEFACTOR
		FACTORY:FACTORIZATIONSCALEFACTOR
μ_R,μ_F in the shower	matching	MEMATCHING:RENORMALIZATIONSCALEFACTOR
		MEMATCHING:FACTORIZATIONSCALEFACTOR
	PS	SHOWERHANDLER:RENORMALIZATIONSCALEFACTOR
		SHOWERHANDLER:FACTORIZATIONSCALEFACTOR
		DIPOLESHOWERHANDLER:RENORMALIZATIONSCALEFACTOR
		DIPOLESHOWERHANDLER:FACTORIZATIONSCALEFACTOR

Table 6.1: The HERWIG 7 parameters determining the various scale factors in the matrix element (ME), matching and parton shower (PS), where SHOWERHANDLER and DIPOLESHOWERHANDLER contain the settings of the angular-ordered and dipole shower, respectively.

The impact of these choices can be estimated by performing factor two up/down variations of the corresponding HERWIG 7 parameters in MATCHBOX and in the parton shower which are listed in Table 6.1.

For consistency, the parton shower scales should be varied in a correlated manner with their counterparts in the hard process as mentioned in the HERWIG 7 documentation [240].

Most of the scale variations can be done only explicitly but for PS scales the recently implemented "on-the-fly" reweighting technique[6] is available, which has been validated [243] for Higgs boson production and $e^+e^- \to t\bar{t}$ processes in the standalone version of HERWIG 7. However, for $t\bar{t}$ production in pp collisions the validation has not been done and, as it has been checked during the current study, the weights for the down variation of μ_R converge extremely slowly and do not give consistent results with the corresponding explicit variation.

It has been followed up by HERWIG 7 authors and recently they performed a new study [244] showing that the so-called *resampling algorithms*[7] when applied in the context of parton showers can significantly improve the statistical convergence of parton shower weights. These algorithms are implemented in the new version of HERWIG 7 (v.7.2).

All the distributions with varied μ_R/μ_F shown in these studies have been obtained using the explicit variations.

Algorithmic uncertainties arise due to the choice of the

[6] The event reweighting technique allows to propagate the effect of the scale variation through the parton shower by applying a weight to each event but without having to change explicitly the varied parameters in the MC generator. The original approach [241] was difficult to implement for example for the weights related to PDFs. HERWIG 7 uses the *weighted Sudakov veto algorithm* [242] which allows to compute the weights for any splitting kernel variation at the same time as default value.

[7] Resampling means selecting n events among the N weighted ones in proportion to their weights (instead of reweighing N weighted events) [244].

- prescription for the matching algorithm,
- type of the parton shower.

As it was mentioned before, two matching possibilities are available: MC@NLO-like and POWHEG-like, and two parton showers: angular-ordered and dipole shower.

For the showering of the POWHEG-generated LHE sample all the variations mentioned above are available except the variations of the matching type (since to be consistent, the POWHEG samples should be matched using only POWHEG-like matching).

In what follows, each of these variations is studied in more details.

6.5.1 Veto scale variations

We start by quantifying the impact of the variations of the veto scale μ_Q (maximum allowed transverse momentum for shower emissions) on $t\bar{t}$ and jet kinematic observables. Three values of the veto scale are considered: $\mu_Q = \xi_Q \mu_{Q,0}$, where $\xi_Q = 0.5$, 1 or 2 is a scale factor and $\mu_{Q,0}$ is the reference scale which is set to the central value of μ_F (see Section 6.3.1). The events for this study are generated at parton level using MATCHBOX and then matched using the MC@NLO-like scheme to the angular-ordered shower. The results are presented in Figs. 6.1 and 6.2.

One can see that $|y_{t,\mathrm{had}}|$, the rapidity of the *hadronic top quark*[8], is almost not dependent on the veto scale since the corresponding variation is less than 3%. The variation of the transverse momentum of the hadronic top ($p_T^{t,\mathrm{had}}$) is larger and reach about 10% for $p_T > 500$ GeV region. For $t\bar{t}$ variables such as mass ($m_{t\bar{t}}$) and transverse momentum ($p_T^{t\bar{t}}$) and also for the number of additional jets the variation goes up to 30–40% in the tail of the distribution. The jet gap fractions do not change more than 0.5–1.5% depending on the veto region.

For several variables ($p_T^{t,\mathrm{had}}$, $p_T^{t\bar{t}}$, some of the gap fractions) the distribution corresponding to the default scale lays outside the statistical uncertainty. For most of the variables, the shift of the distribution due to the change of the scale factor is larger then the statistical uncertainty. This clearly shows that in order to be able to use the veto scale variations to estimate a perturbative uncertainty one needs first to get a proper tune for the current minimal setup so that the distributions with the default scales are consistent with 13 TeV data.

6.5.2 Renormalisation and factorisation scale variations

The perturbative variations related to the choice of the renormalisation and factorisation scales (in the hard process and in the parton shower) turn out to be of the same order as the veto scale variations considered in the previous section.

[8] top quark decaying into hadrons

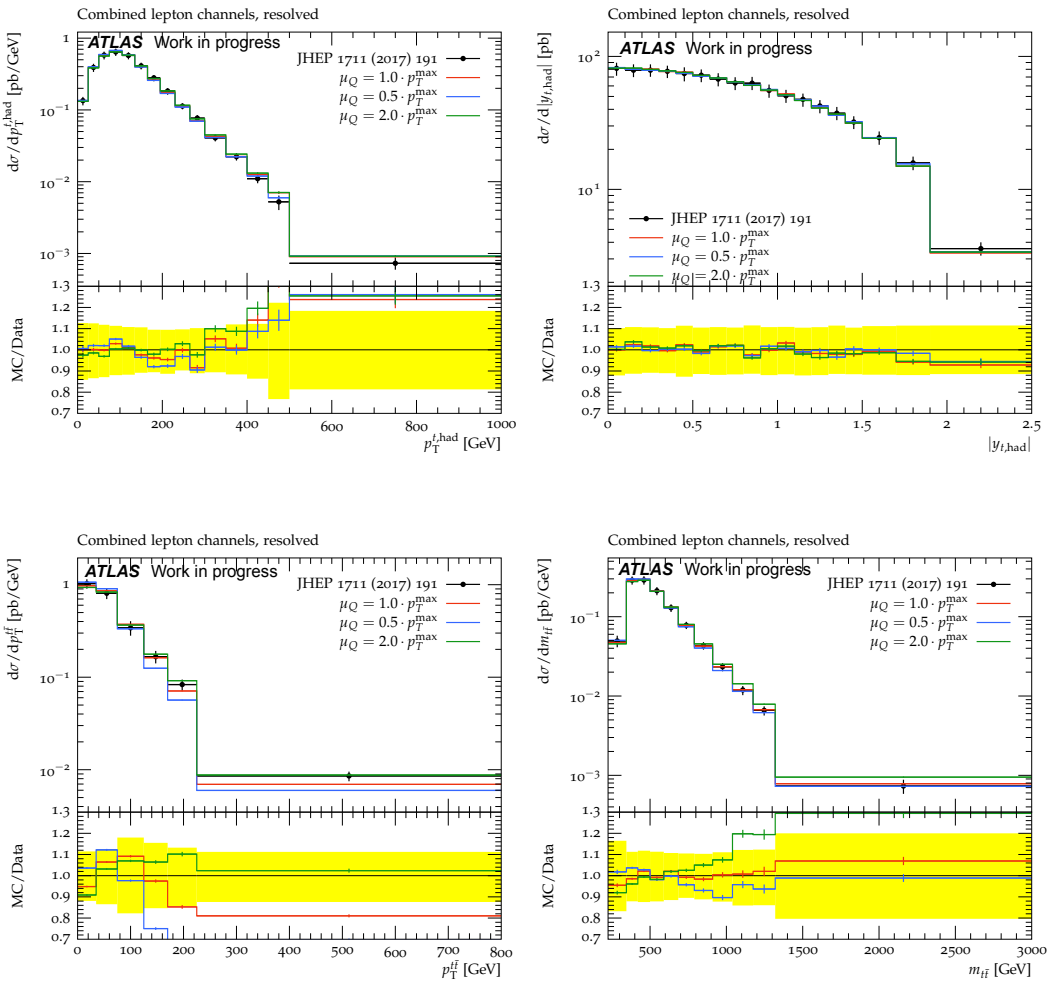

Figure 6.1: Top-quark pair differential cross sections for three values of the veto scale μ_Q. The central value of μ_F (see Section 6.3.1) is the reference scale. The comparison is performed using ATLAS data unfolded to particle level from Analysis C [235]. The yellow band represents the data statistical uncertainty.

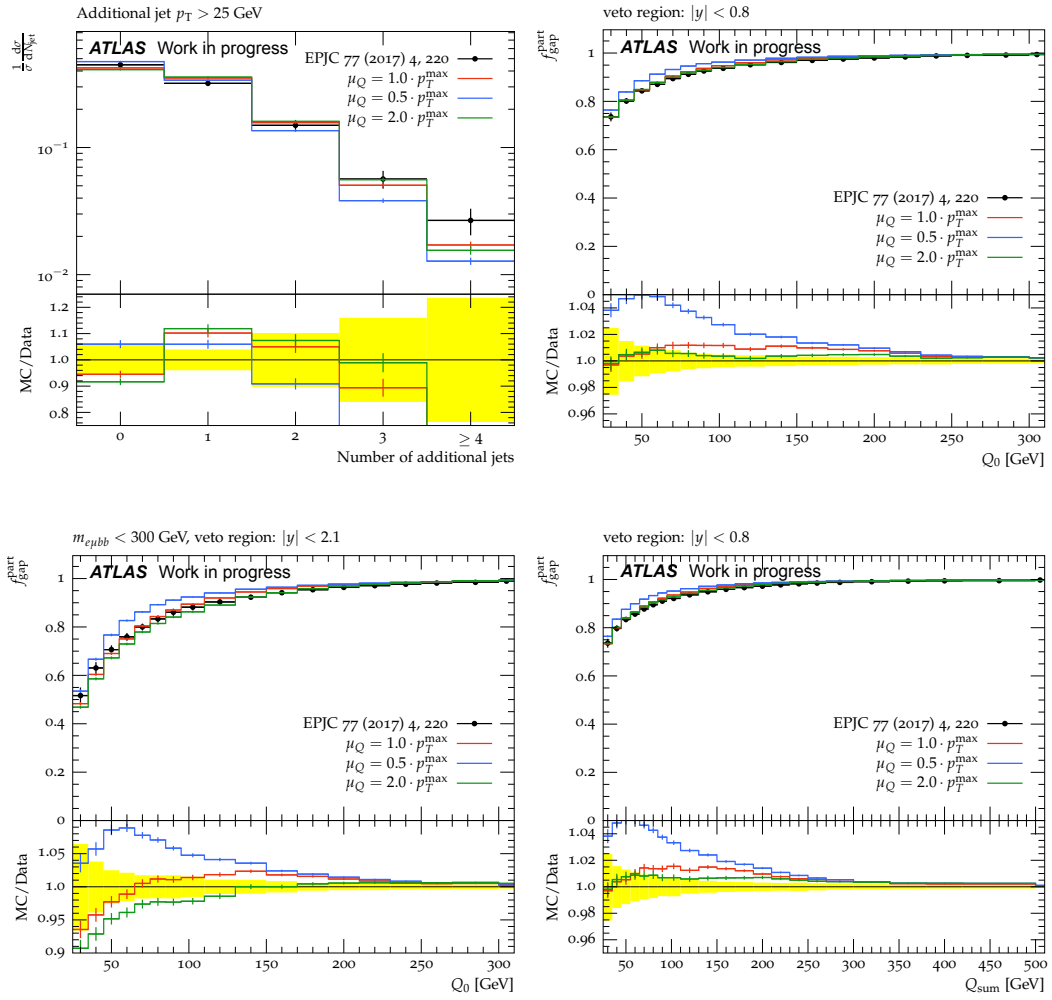

Figure 6.2: Number of additional jets and gap fractions for three values of the veto scale μ_Q. The central value of μ_F (see Section 6.3.1) is the reference scale. The comparison is performed using ATLAS data unfolded to particle level from Analysis B [234]. The yellow band represents the data statistical uncertainty.

Figs. 6.3 and 6.4 show the results corresponding to the three values of the scale factor $\xi_{R,F} = 0.5$, 1 or 2 entering the expression for the renormalisation/factorisation scale as $\mu_R = \mu_F = \xi_{R,F} m_T$, where the reference scale m_T is the one defined in Eq. (6.1).

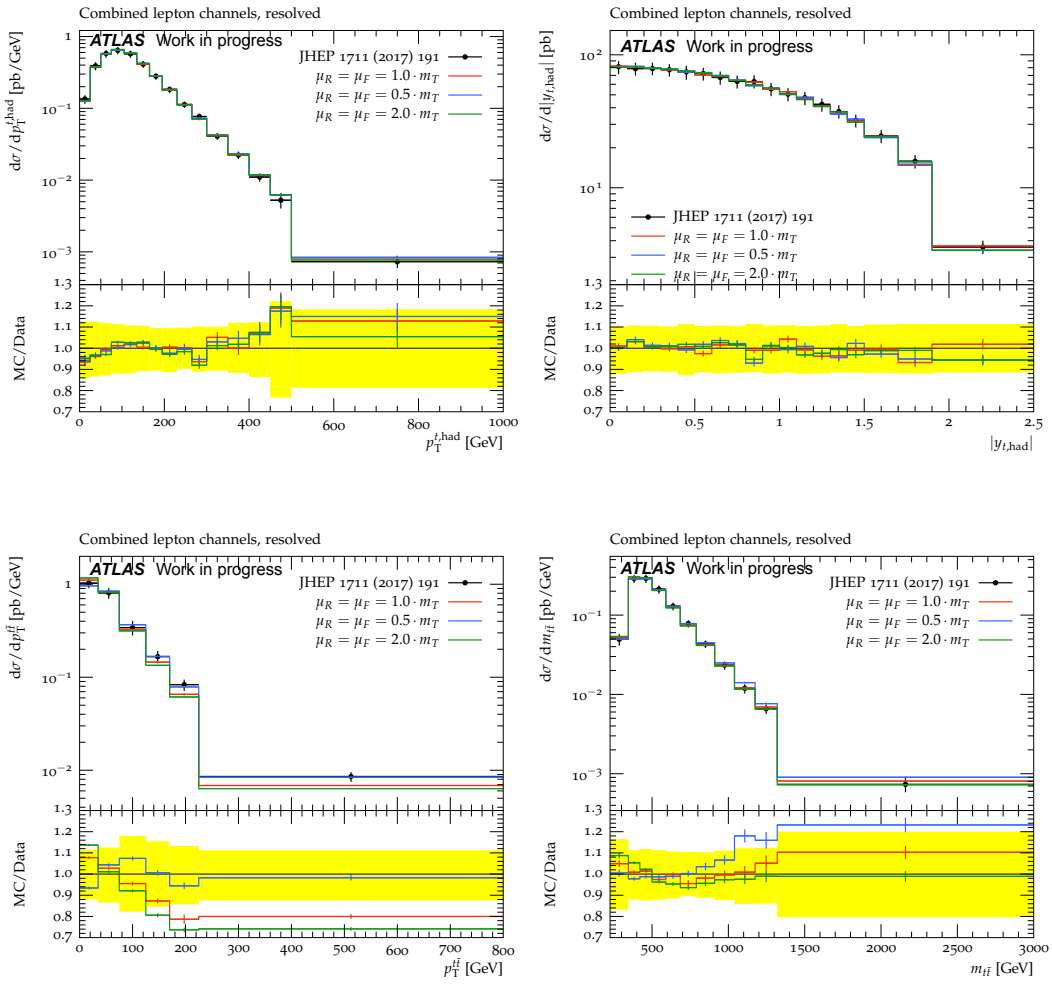

Figure 6.3: Top-quark pair differential cross sections for three values of the renormalisation (μ_R) and factorisation (μ_F) scales in the parton shower. The reference scale m_T was defined in Eq. (6.1). The hadronisation is simulated using POWHEG-like matching scheme and dipole shower. The comparison is performed using ATLAS data unfolded to particle level from Analysis C [235]. The yellow band represents the data statistical uncertainty.

The parton shower scale uncertainty varies from $\sim$ 1% for jet gap fractions and the rapidity of the hadronic top quark to 10–20% for other $t\bar{t}$ variables. The number of additional jets at large number of jets varies up to 50%.

In the event sample used here the MATCHBOX-generated matrix element is matched using a POWHEG-like scheme to the dipole shower. One can see that the $p_T^{t\bar{t}}$ distribution and the gap fractions differ from the data by more than the data statistical uncertainty for the default value of the scale factor.

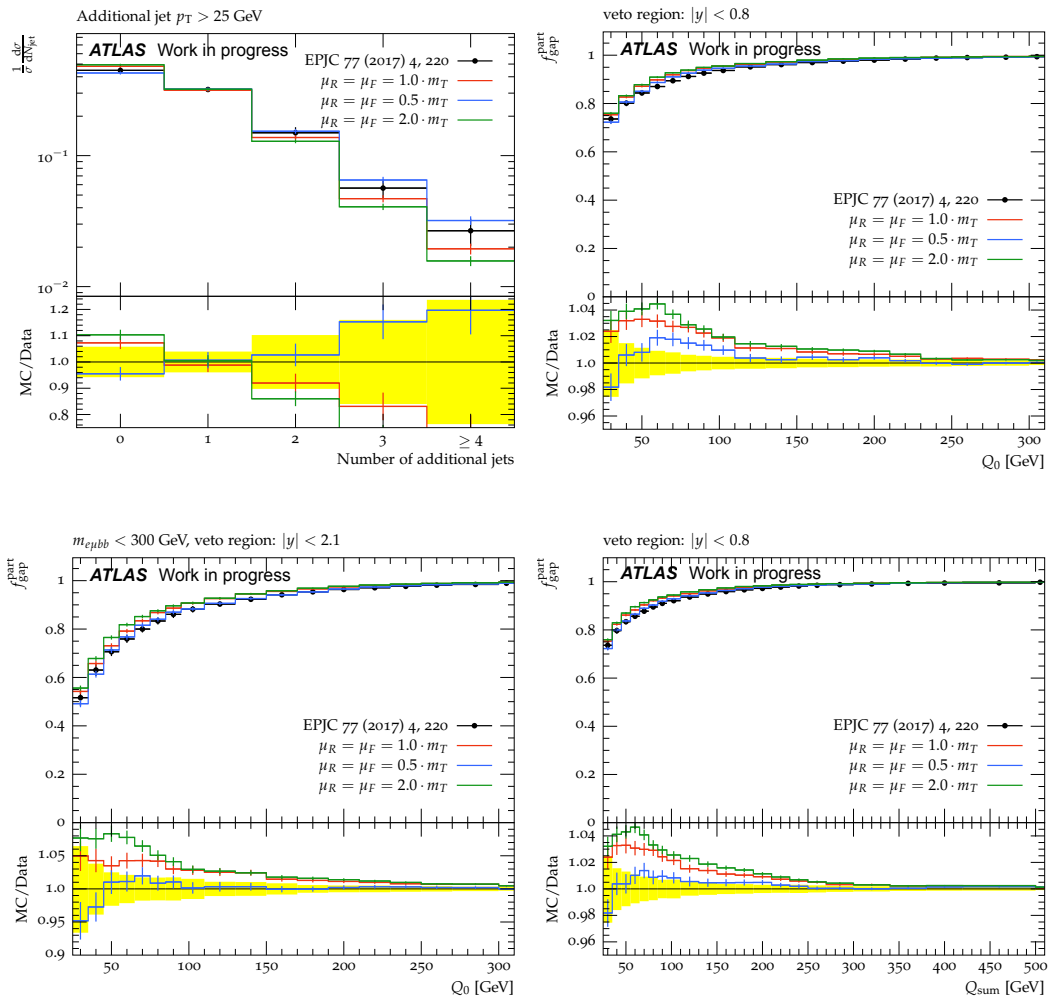

Figure 6.4: Number of additional jets and gap fractions for three values of the renormalisation (μ_R) and factorisation (μ_F) scales in the parton shower. The reference scale m_T was defined in Eq. (6.1). The hadronisation is simulated using POWHEG-like matching scheme and dipole-ordered shower. The comparison is performed using ATLAS data unfolded to particle level from Analysis B [234]. The yellow band represents the data statistical uncertainty.

Also, as for the μ_{Q} variations, for some of the variables the shifts of the distributions due to the scale variations are larger than the statistical uncertainty.

One could use these variations to build the corresponding parton shower uncertainty but it would be overestimating the effect of the $\mu_{\mathrm{R}}/\mu_{\mathrm{F}}$ choice (for certain observables, such as gap fractions, for example) for the current HERWIG 7 tune.

6.5.3 Shower type and matching variations

Looking at the jet shape distributions at 7 TeV shown in Fig. 6.5 one can see that depending on the chosen matching scheme (MC@NLO- or POWHEG-like) and shower type (angular-ordered or dipole) the jet shapes of the light jets vary by 5–10% and the ones of the b-jets— by 10–20%. Fig. 6.6 shows variations at the level of 10–20% for $t\bar{t}$ observables, mostly larger in the end of the distributions. The gap fractions do not vary more than by 0.5–1% in Fig. 6.7 and the number of additional jets varies by 20–50%.

For the 7 TeV distributions all the matching and shower combinations give results consistent with the data within the statistical uncertainty, except for the b-jet shapes at large r for the dipole shower. Consequently, the parton shower uncertainty built using the variations shown above could correctly reflect the ambiguity due to the choice of the shower type and matching algorithm in modelling 7 TeV data.

For the 13 TeV distributions the consistency with the data is much worse, especially in the tails of the distributions. At 13 TeV, distributions for the transverse momentum of the hadronic top quark ($p_{\mathrm{T}}^{t,\mathrm{had}}$) and for the number of additional jets are better described by the dipole shower whereas the gap fraction distributions are more consistent with the data when one uses the angular-ordered shower (which is normally taken as default setup).

So, unlike the case of 7 TeV data, the current HERWIG 7 tune does not allow to define a trustable shower type/matching uncertainty for many of the observables in the 13 TeV data.

6.6 Parton shower variations of POWHEG+HERWIG7 samples

In this section we repeat the same parton shower variation procedure on POWHEG samples showered with HERWIG 7. The only variation which will be unavailable is the matching type variation since only the multiplicative (POWHEG-like) matching scheme can be used for a POWHEG LHE sample. We will analyse the effect of these variations and compare it with the results of the MATCHBOX-generated samples presented in the previous section.

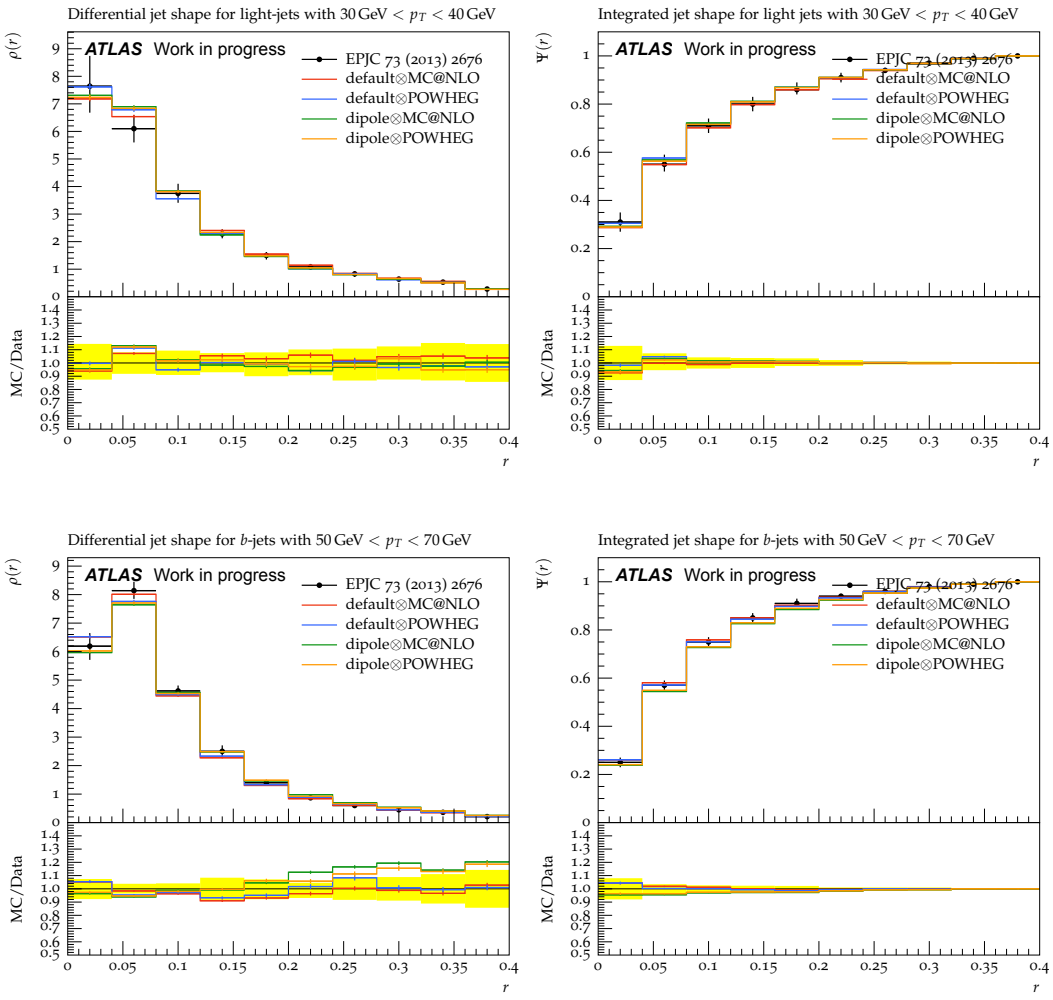

Figure 6.5: Differential and integrated jet shape distributions at 7 TeV for the MC@NLO-like and POWHEG-like matching schemes and for the angular-ordered (denoted as "default") and dipole showers. The comparison is performed using ATLAS data unfolded to particle level from Analysis A [233]. The yellow band represents the data statistical uncertainty.

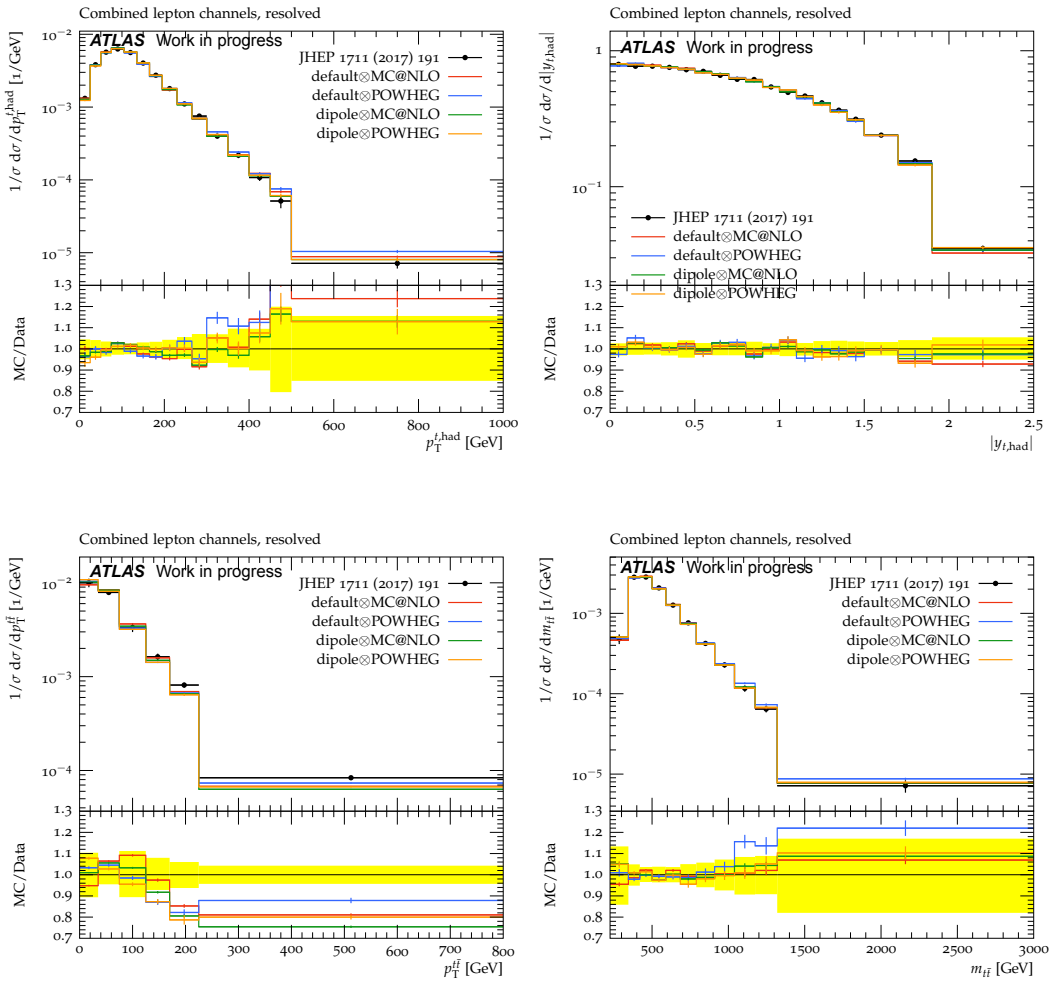

Figure 6.6: Top-quark pair differential cross sections at 13 TeV are compared for the MC@NLO-like and POWHEG-like matching schemes and for the angular-ordered (denoted as "default") and dipole showers. The comparison is performed using ATLAS data unfolded to particle level from Analysis C [235]. The yellow band represents the data statistical uncertainty.

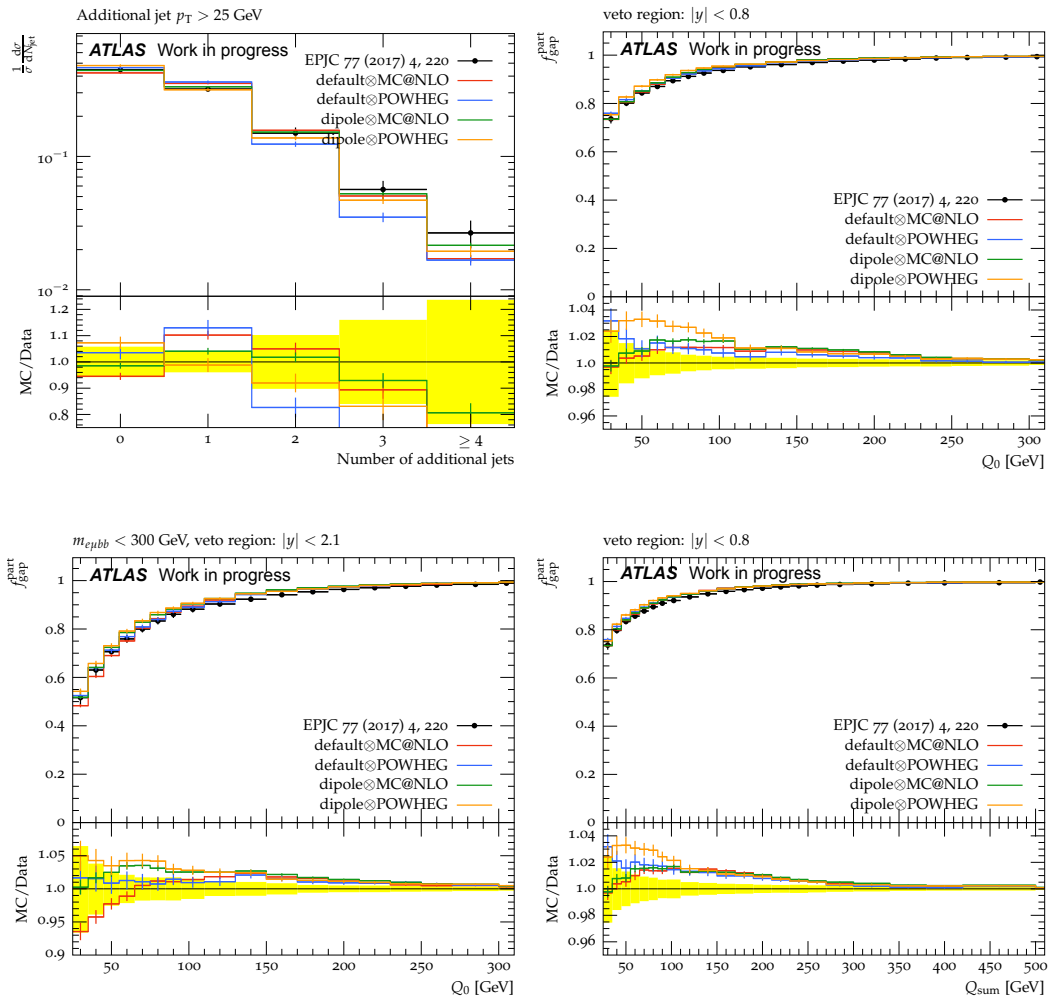

Figure 6.7: Number of additional jets and gap fractions at 13 TeV for MC@NLO-like and POWHEG-like matching schemes and for the angular-ordered (denoted as "default") and dipole showers. The comparison is performed using ATLAS data unfolded to particle level from Analysis B [234]. The yellow band represents the data statistical uncertainty.

6.6.1 Veto scale variations

As in Section 6.5. we consider three veto scale values: $\mu_{\mathrm{Q}} = \xi_{\mathrm{Q}}\mu_{\mathrm{Q},0}$, where ξ_{Q} =0.5,1 or 2 is a scale factor and $\mu_{\mathrm{Q},0}$ is the reference scale equal to the central value of μ_{F} (see Section 6.3.1). Here, the Les-Houches events generated with POWHEG are showered using the angular-ordered shower. The results for the $t\bar{t}$ and jet distributions are presented in Figs. 6.8 and 6.9.

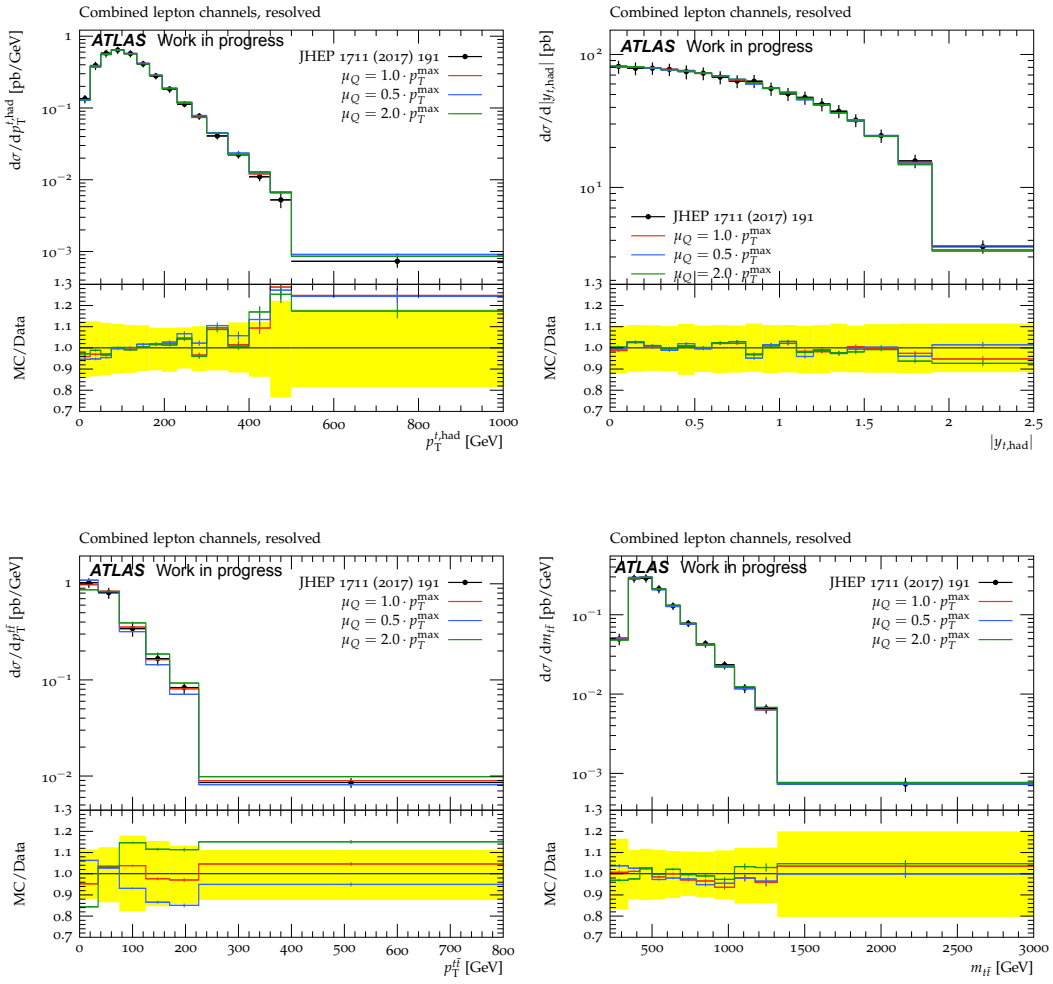

Figure 6.8: Top-quark pair differential cross sections for three values of the veto scale μ_{Q} in POWHEG+HERWIG7 samples. The maximum allowed transverse momentum for shower emissions, $p_{\mathrm{T}}^{\mathrm{max}}$, is the reference scale. The comparison is performed using ATLAS data unfolded to particle level from Analysis C [235].

Comparing the shifts caused by the veto scale variations in the showered LHE samples and MATCHBOX samples, one can make several observations:

- In the $t\bar{t}$ differential cross sections the shifts in the POWHEG+HERWIG7 samples (Fig. 6.8) are smaller than in the MATCHBOX+HERWIG7 samples (Fig. 6.1).

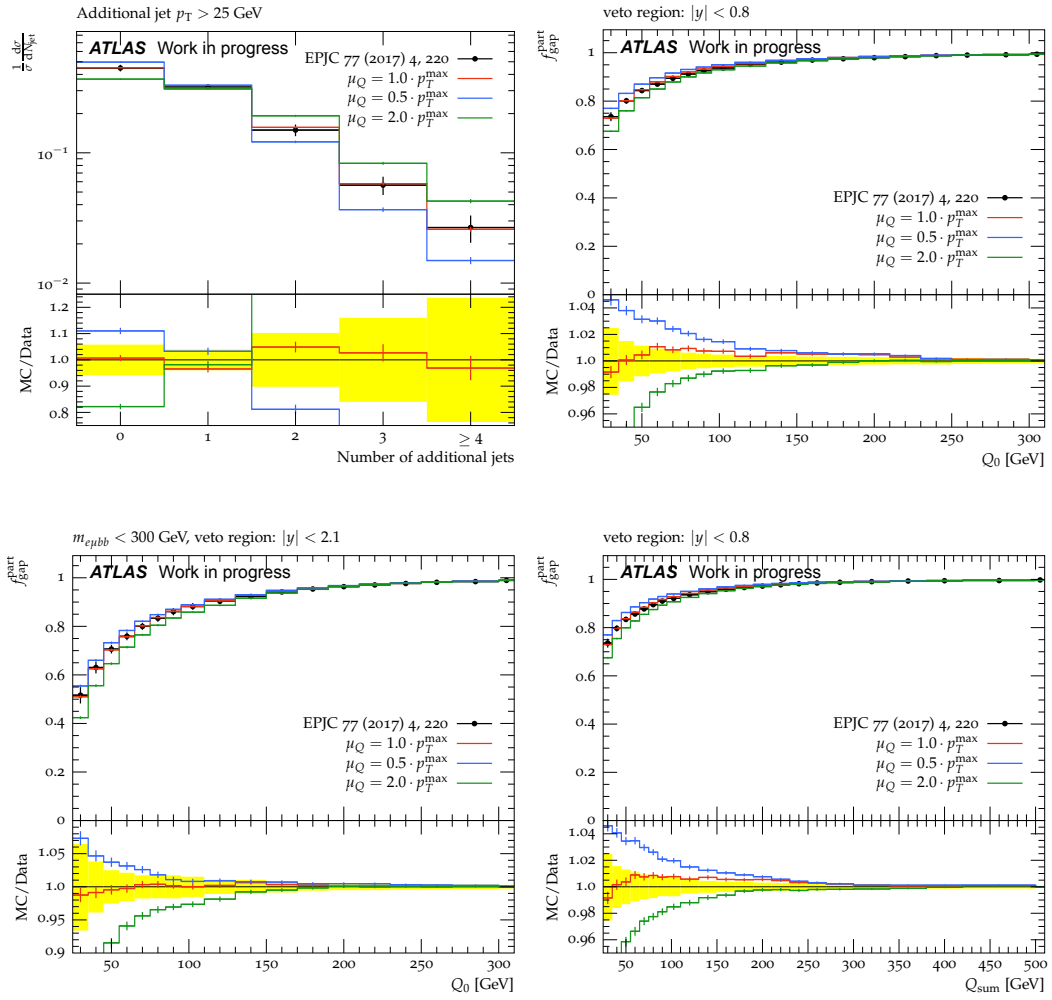

Figure 6.9: Number of additional jets and gap fractions for three values of the veto scale μ_Q in POWHEG+HERWIG7 samples. The maximum allowed transverse momentum for shower emissions, p_T^{max}, is the reference scale. The comparison is performed using ATLAS data unfolded to particle level from Analysis B [234].

- In the gap fractions and the number of additional jets the up variation results in symmetric (to the down one) and larger variation in the POWHEG+HERWIG7 samples (Fig. 6.9) than in the MATCHBOX+HERWIG7 samples (Fig. 6.2).
- The POWHEG+HERWIG7 samples with the default setup are much more consistent with the data (except for the last bin in $p_{\mathrm{T}}^{t,\mathrm{had}}$ distribution) than the MATCHBOX+HERWIG7 samples.

The differentces in the POWHEG+HERWIG7 setup (w.r.t MATCHBOX+HERWIG7 setup) which result in better description of the data is discussed in Section 6.3. More detailed comparison of the POWHEG+HERWIG7 and MATCHBOX+HERWIG7 setups and discussion on the compatibility of the corresponding results will be done in Section 6.6.4.

6.6.2 Renormalisation and factorisation scale variations

Analogously to Section 6.5 the $\mu_{\mathrm{R}}/\mu_{\mathrm{F}}$ scale variations correspond to the three values of the scale factor $\xi_{\mathrm{R,F}}$ =0.5,1 or 2 in front of the renormalisation/factorisation scale $\mu_{\mathrm{R}} = \mu_{\mathrm{F}} = \xi_{\mathrm{R,F}} m_{\mathrm{T}}$, where the reference scale m_{T} is the one defined in Eq. (6.1).

As for the veto scale variations, we observe very small changes in the differential cross section distributions (Fig. 6.10). The gap fraction distributions also negligibly change under $\mu_{\mathrm{R}}/\mu_{\mathrm{F}}$ variations (Fig. 6.11) and only the number of additional jets change by an amount comparable with that is observed in the MATCHBOX+HERWIG7 samples (Fig. 6.4).

6.6.3 Shower type variations

One can see from Figs. 6.12 and 6.13 that the choice of the shower type (angular-ordered or dipole) does not have a significant impact on the observed distributions. This may be explained by the fact that only the initial-state radiation emission is added in POWHEG but not the final-state radiation which is then not involved in the showering process. Notice also that distributions with both showers lay inside the statistical uncertainty band of the data (except for the $p_{\mathrm{T}}^{t,\mathrm{had}}$, for which the dipole shower gives in the last bins of the distribution predictions more consistent with the data).

This picture is very different from the algorithmic variations of the MATCHBOX+HERWIG7 sample: on Fig. 6.6 and especially on Fig. 6.7 it was shown that every matching/shower combination gives a unique distribution and for different variables different combinations give more consistent result relatively to the data.

6.6.4 POWHEG+HERWIG7 vs MATCHBOX+HERWIG7 comparison

Having seen how different the results are using the POWHEG+HERWIG7 and MATCHBOX+HERWIG7 samples for both, default and varied scales, one may raise a question: which parameters in these setups are responsible for the observed differences?

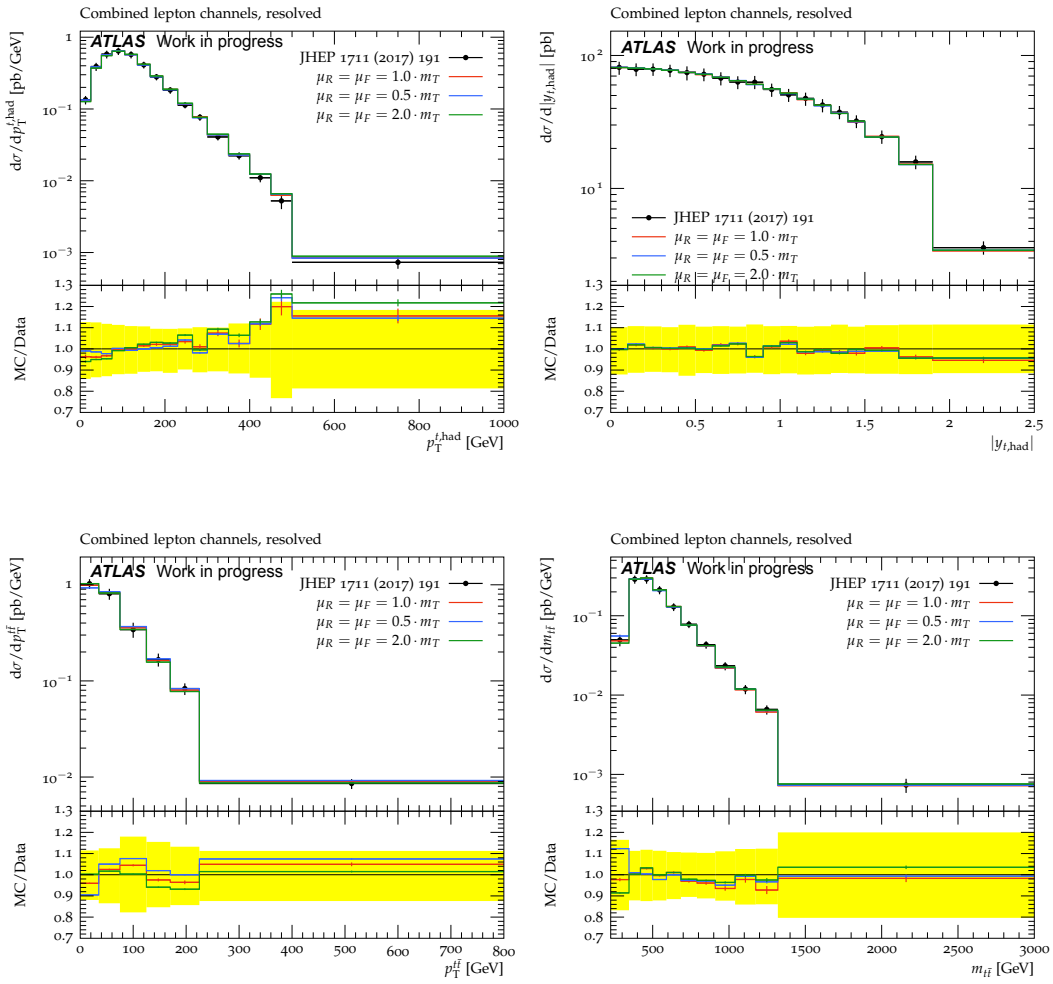

Figure 6.10: Top-quark pair differential cross sections for three values of the renormalisation (μ_R) and factorisation (μ_F) scales in the parton shower in POWHEG+HERWIG7 samples. The reference scale (TOPPAIRMTSCALE, defined in Eq. (6.1)) is denoted by m_T. The hadronisation is simulated using POWHEG-like matching scheme and dipole shower. The comparison is performed using ATLAS data unfolded to particle level from Analysis C [235].

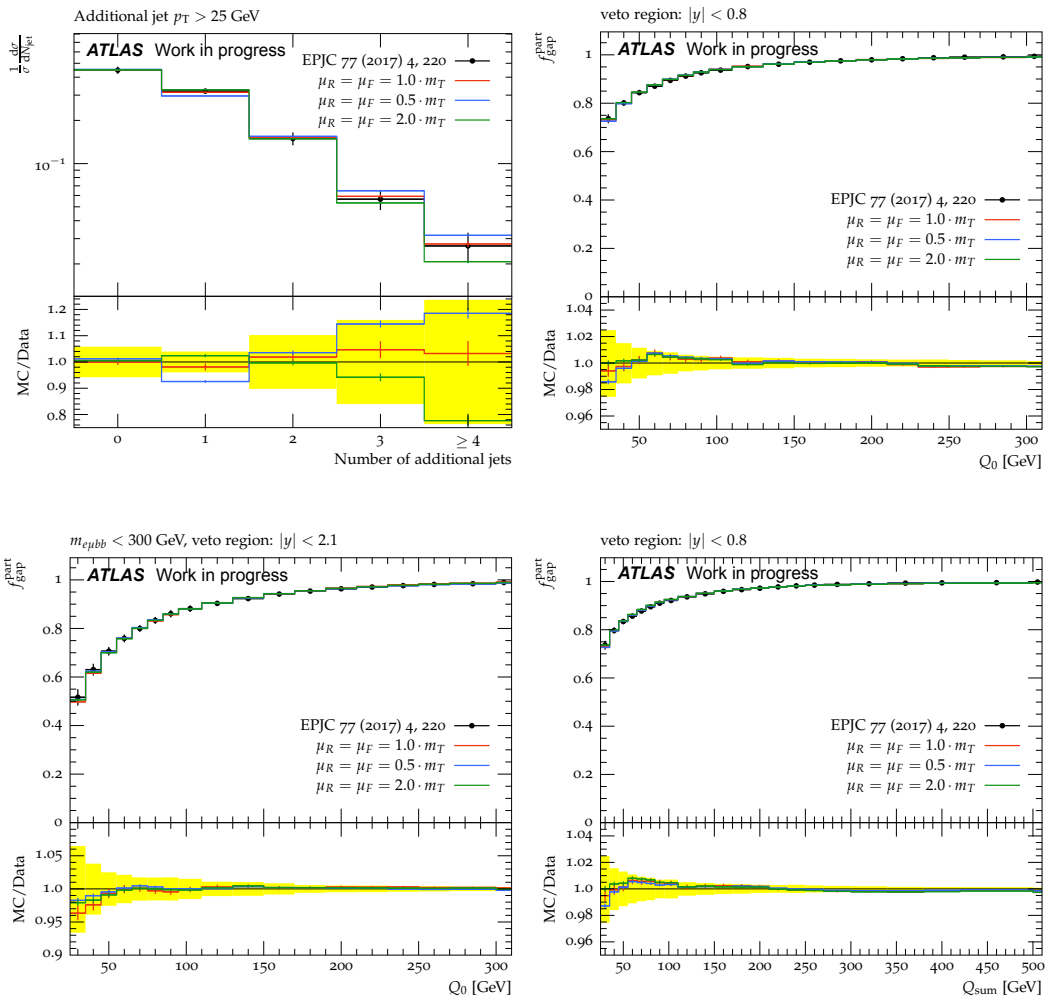

Figure 6.11: Number of additional jets and gap fractions for three values of the renormalisation (μ_R) and factorisation (μ_F) scales in the parton shower in POWHEG+HERWIG7 samples. The reference scale (TOPPAIRMTSCALE, defined in Eq. (6.1)) is denoted by m_T. The hadronisation is simulated using POWHEG-like matching scheme and dipole-ordered shower. The comparison is performed using ATLAS data unfolded to particle level from Analysis B [234].

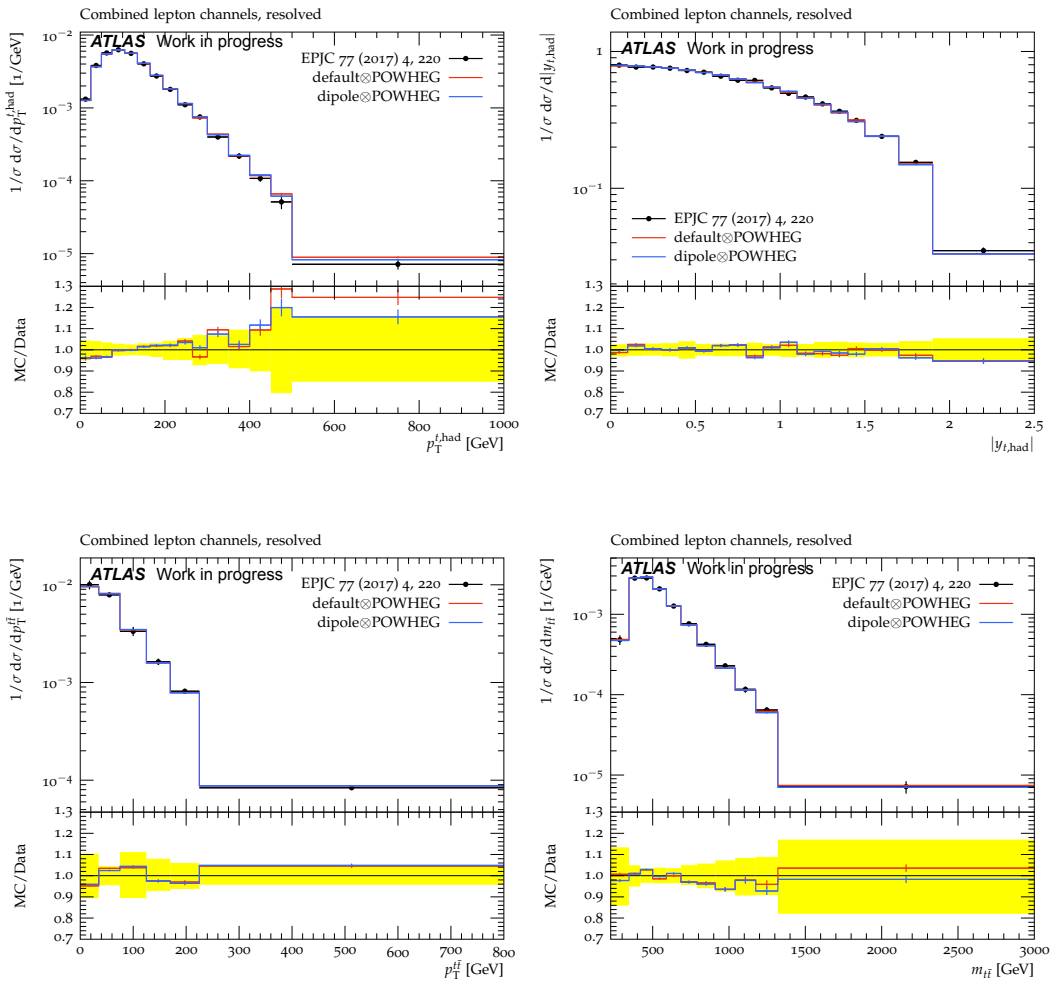

Figure 6.12: Top-quark pair differential cross sections at 13 TeV are compared for the angular-ordered (denoted as "default") and dipole showers in POWHEG+HERWIG7 samples. The comparison is performed using ATLAS data unfolded to particle level from Analysis C [235].

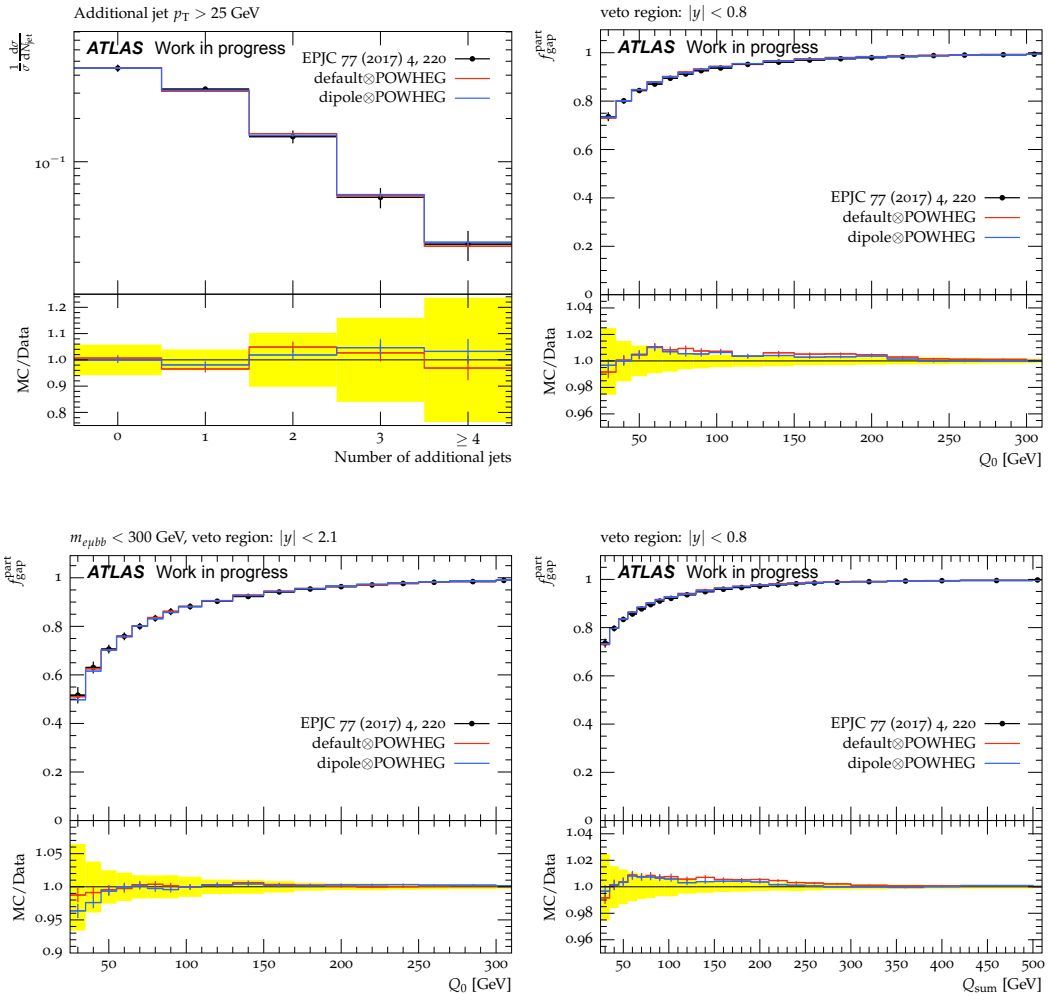

Figure 6.13: Number of additional jets and gap fractions at 13 TeV for the angular-ordered (denoted as "default") and dipole showers in POWHEG+HERWIG7 samples. The comparison is performed using ATLAS data unfolded to particle level from Analysis B [234].

It has been shown on Figs. 6.12 and 6.13 that both showers give the same distributions for POWHEG+HERWIG7 which was not the case for the corresponding matching/shower setups in MATCHBOX+HERWIG7. Therefore, one should pay attention to the differences in the matrix element settings between POWHEG standalode and POWHEG within MATCHBOX.

In MATCHBOX, the default settings include restriction in the phase space of the NLO matched emission. This is done in order to generate both $\mathbb{S}$ and $\mathbb{H}$ type POWHEG events [55, 56]. Here, $\mathbb{S}$ denotes "standard" events which contain Born-level states (see 2.4) and $\mathbb{H}$ ("hard") denotes events with one emission already occurred, due to NLO effect, before the showering. The transverse momentum of the hard emission in $\mathbb{S}$ events is limited by the veto scale.

The original POWHEG formalism used in POWHEG standalone includes $\mathbb{S}$ events only. This setup with only $\mathbb{S}$ events can be also run within MATCHBOX by switching off the phase space restriction and the hard scale profile in the matrix element ("Matchbox, POW settings" in Figs. 6.14 and 6.15, compared to "Matchbox default", corresponding to the default MATCHBOX setup with both $\mathbb{S}$ and $\mathbb{H}$ events).

Another difference is the reference renormalisation/factorisation scale in the matrix element. MATCHBOX uses m_{T} scale defined in Eq. (6.1), whereas POWHEG uses E_{T} scale (see Eq. (6.2)).

Finally, a significant role is played by the POWHEG parameter h_{damp} which regulates the high-p_{T} emission against which the $t\bar{t}$ system recoils. If the matrix element is calculated using MATCHBOX the h_{damp} limit is not set, i.e. it is equal to infinity, because the corresponding parameter is not included in the framework. On the other hand, in the POWHEG+HERWIG7 sample the h_{damp} parameter is set to $1.5m_t$ (with m_t being the top quark mass) in the matrix element generated using POWHEG, where this parameter can be changed. Consequently, already at parton level in MATCHBOX sample, comparing to POWHEG+HERWIG7 sample, harder emission is allowed by the Sudakov form factor (see Section 2.3 for the definition).

From Figs. 6.14 and 6.15 we can see the effect of having a different value of h_{damp} parameter if we compare two distributions: "Powheg" (POWHEG+HERWIG7 sample) and "Matchbox, POW settings" (a MATCHBOX sample with POWHEG matching and $\mathbb{S}$ events only, like in POWHEG). The only difference between these two samples is the value of h_{damp}: it is equal to $1.5m_t$ in POWHEG+HERWIG7 sample and it is infinite in MATCHBOX sample. From the figures one can see that by generating $\mathbb{S}$ events only within MATCHBOX with POWHEG matching one can reach consistency with the POWHEG+HERWIG7 sample for $t\bar{t}$ inclusive observables, but for the hadronisation-related jet observables a significant difference remains related to h_{damp}.

6.7 Discussion and outlook

In the studies described in this chapter, it has been presented how the parton shower and matching variations in HERWIG 7.1.3 impact various $t\bar{t}$ and jet observables. Several $t\bar{t}$ analyses have been used for running on Monte–Carlo $t\bar{t}$ samples generated using HERWIG 7.1.3.

The effects of the scale variations have been studied in order to explore the possibility of introducing a parton shower uncertainty associated to HERWIG 7.1.3 simulations used in ATLAS analyses.

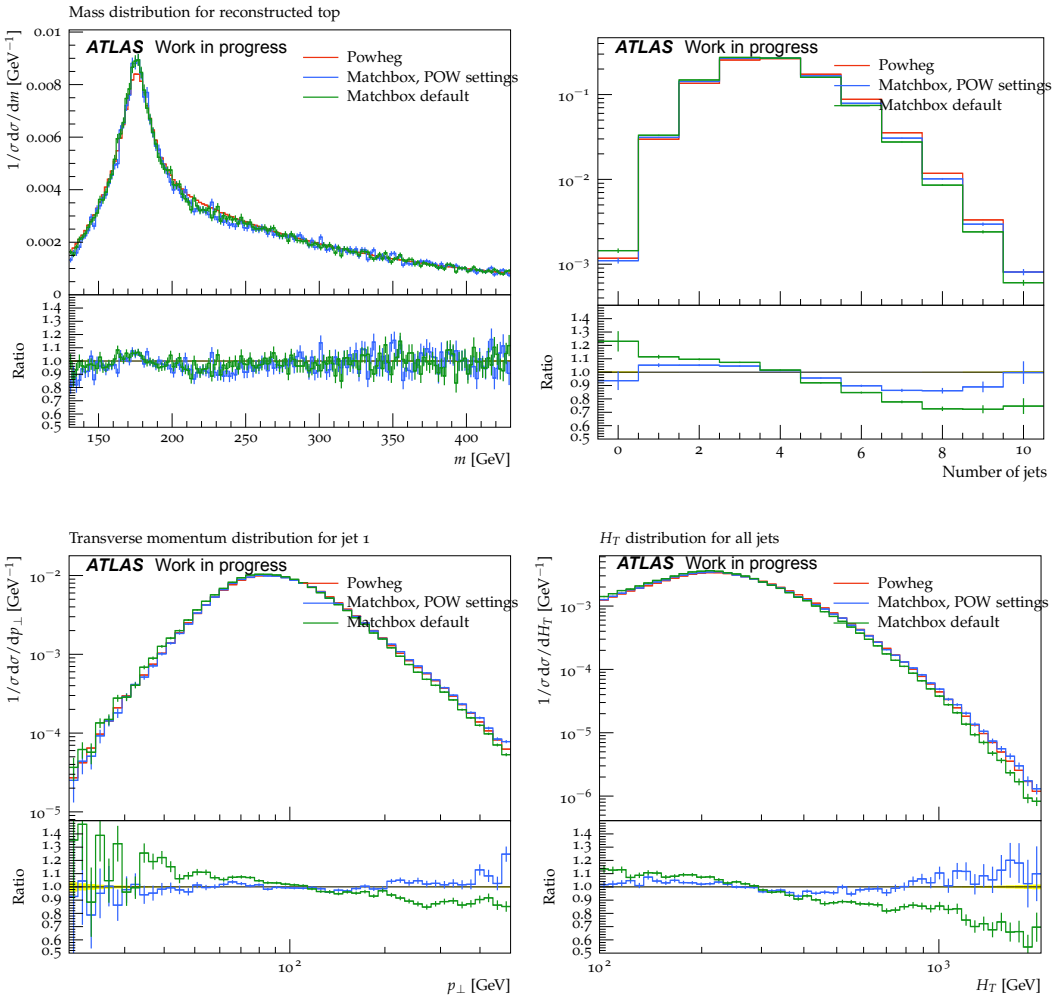

Figure 6.14: Top-quark pair differential cross-sections and jet multiplicity for POWHEG samples ($h_{\text{damp}} = 1.5m_t$) and samples generated with MATCHBOX (h_{damp} not set) with two different settings: the default ones ("Matchbox default") which lead to the generation of events of both type, $\mathbb{S}$ and $\mathbb{H}$, and POWHEG-like settings ("Matchbox, POW settings") which allow the generation of $\mathbb{S}$ events only. Both samples are showered with HERWIG 7 with the same setup. The comparison is performed using Analysis D [236].

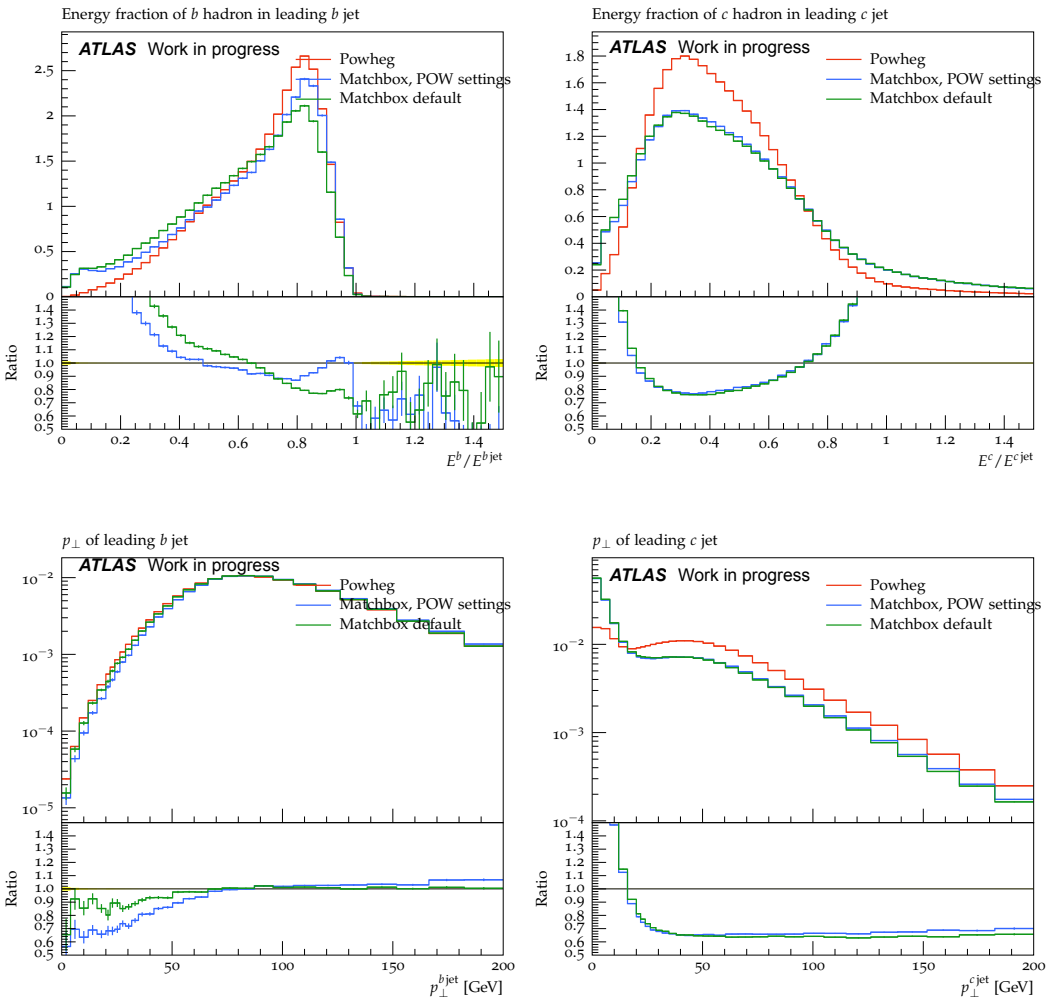

Figure 6.15: Fragmentation observables of the heavy flavour hadrons for POWHEG samples ($h_{\mathrm{damp}} = 1.5 m_t$) and samples generated with MATCHBOX (h_{damp} not set) with two different settings: default ones ("Matchbox default") which lead to the generation of events of both type, $\mathbb{S}$ and $\mathbb{H}$, and POWHEG-like settings ("Matchbox, POW settings") which allow the generation of $\mathbb{S}$ events only. Both samples are showered with HERWIG 7 with the same setup. The comparison is performed using Analysis E [237].

Looking at the studies presented here, the following recipe can be suggested to assess parton shower uncertainties using Matchbox and POWHEG+HERWIG7 samples:

- Perform factor two up/down variations of the veto scale (μ_Q)
- Perform factor two up/down variations of the parton shower μ_R/μ_F (simultaneously with the corresponding μ_R/μ_F variations in the hard process)
- Compare two matching setups: MC@NLO and POWHEG (not for the LHE showering)
- Compare two shower types: angular-ordered and dipole showers.

To summarise the effects of the variations for the different observables using POWHEG samples we can say that jet gap fractions are affected by several percent, the $t\bar{t}$ kinematic observables by a couple of tens percent and the number of additional jets up to 50% and more.

Considering the MATCHBOX+HERWIG7 samples, there are several limiting factors which prevent them to have a well-defined uncertainty and start to use it in analyses:

- The impossibility to perform all the scale variations "on-the-fly" using reweighting. For the veto scale variations the reweighting option is not yet available, for the μ_R/μ_F variations the weights corresponding to the μ_R down variation do not converge for the $pp \to t\bar{t}$ process (in HERWIG 7.1.3, solved in the new version HERWIG 7.2).
- The default hadronisation tune of HERWIG 7.1.3 (`H7.1-Default`) does not give results compatible with data (within the uncertainty) for certain distributions (for the scale variations and even for the default settings in certain cases) specifically at 13 TeV. This can be seen by comparing how differently the shower/matching variations shift the distributions at 7 TeV (Fig. 6.5) and at 13 TeV (Fig. 6.6 and Fig. 6.7) knowing that HERWIG 7.1.3 has been properly tuned for 7 TeV data.
- There is no possibility to change the h_{damp} factor. Note that the POHWEG+HERWIG7 sample where h_{damp} is set to $1.5m_t$ in POWHEG shows better consistency with data than the MATCHBOX sample where h_{damp} is not set (see e.g. Fig. 6.7 and Fig. 6.13), which suggests that h_{damp} may be an important additional handle for tuning.
- Not so much a limiting factor as an important option to keep in mind for tuning is the fact that the default MATCHBOX setup with POWHEG matching includes restriction in the phase space of the NLO matched emission, which is absent in POWHEG standalone. However, this restriction can be switched off (see the discussion in Section 6.6.4).

The distributions corresponding to the POWHEG+HERWIG7 samples are much more compatible with data, although some of the scale variations cause shifts which are much larger than the data statistical uncertainty (Fig. 6.9). One may conclude that a certain revision of the variation sizes is needed here. The reweighting for the veto scale variations is not available in the POWHEG+HERWIG7 sample, as well as in Matchbox. The issue with the convergence of the μ_R/μ_F scale variations persists for this case as well (in HERWIG 7.1.3, it may be solved in the new version HERWIG 7.2).

Despite the fact that for $pp \to t\bar{t}$ processes the parton shower HERWIG 7 uncertainty cannot be easily introduced at the moment (one would have to perform the explicit scale variations and generate multiple samples for each case, which is not a common practice in ATLAS), the performed study is

important to understand the current picture of the available variations and the status of the $t\bar{t}$ production simulation with HERWIG 7 in general. It sheds light on the present issues and has helped to plan the usage of HERWIG 7 for future ATLAS $t\bar{t}$ Monte–Carlo simulations.

7 Measurements of observables sensitive to colour reconnection in $t\bar{t}$ dilepton events at $\sqrt{s} = 13$ TeV with the ATLAS detector

As top quark mass measurements become more precise, the systematic uncertainties, in particular the colour reconnection (CR) systematic uncertainty, become more and more important. As is was mentioned in Section 4.5.1, some of the Pythia 8 CR models lead to large CR uncertainty in the m_t measurements. We hope that they can be constrained by auxiliary measurements.

The aim of the analysis presented in this chapter is to constrain/exclude Pythia 8 CR models by comparing Pythia MC distributions sensitive to CR with 13 TeV $t\bar{t}$ data distributions. The measurement is done in the dilepton $t\bar{t}$ decay channel at 13 TeV. To reduce the background, we consider only $e^{\pm}\mu^{\mp}$ events with at least two identified jets exactly two of which are b-jets.

This chapter focuses on particular studies that I have performed related to the unfolding of two-dimensional variables and the estimation of systematic uncertainties on the unfolded distributions.

Colour reconnection in $t\bar{t}$ production

The definition of the colour reconnection mechanism and a short history of its developments are given in Section 2.6. In the Pythia 8 generator, used to model the parton shower and hadronisation in the current $t\bar{t}$ analyses, several CR models are available [245, 246]. They differ in the way the reconnections are implemented and in the particles, which are involved in the CR.

There are the following three basic Pythia 8 CR models:

- The MPI-based CR model [247]: the partons in this scheme are classified according to which other partons they are connected to (forming a MPI system). Then the systems are ordered according to their p_T. Afterwards the individual MPI systems are tentatively merged. When the colour flow of two MPI systems is merged, the partons of a system with lower p_T are added to the strings of a system with higher p_T in such a way that the resulting string length is the smallest possible (see the string hadronisation model description in Section 2.5). The probability of a MPI system with a scale p_T to merge with a MPI system with a harder scale (reconnection probability) is:

$$P = \frac{(R_{\text{rec}} p_{T,0})^2}{(R_{\text{rec}} p_{T,0})^2 + (p_T)^2}, \tag{7.1}$$

  where the range R_{rec} is an effective parameter (free parameter of the model), which controls how many reconnections can occur and $p_{T,0}$ is a dampening parameter, the same for all MPI systems.

First, the colour reconnection probability of the lowest-p_{T} system and the second lowest one is calculated. If these systems are not reconnected (merged), the procedure is repeated for the lowest-p_{T} system and the third lowest one and so on. As soon as the lowest-p_{T} system is merged with some other system, the reconnection probability computation is repeated for the lowest-p_{T} system among the remaining ones. The simulation the system merging happens in the direction opposite to how the calculation of probabilities was done: from systems with the highest p_{T} to the ones with the lowest p_{T}.

- The QCD-based model [245]: it relies on the minimisation of the string length and on the properties of the $SU(3)_C$ QCD symmetry group. In this scheme, all possible pairs of dipoles are constructed and then, if some pair has a lower string length, one switches to it. This is done iteratively until no more reconnections can lower the total string length per event λ[1]. The main feature of this model is the introduction of junction structures, when three string pieces form a Y-shaped topology, which leads to additional baryon formation in this model.

  The QCD-based model includes several tuneable parameters, such as the hadronic mass scale used in the definition of the string length, the number of string "colours" (where only strings with the same "colour" are allowed to reconnect, not to be confused with the number of QCD colours) and various switches allowing the formation of junctions and different options for the string length definition.

- The gluon-move model [247]: as it follows from the name, this scheme involves only manipulations with gluons. It consists of two steps: a "move" step and an optional "flip" step, which are used to reduce the total string length λ. First, all gluons and colour-connected parton pairs are identified. Then, for each gluon and parton pair, the calculation of how λ shifts if the gluon is moved inside the parton pair is performed. The gluon move corresponding to the largest decrease of λ is carried out. The procedure is repeated as long as there are allowed gluon moves. The flip step is similar to the move step, but instead of moving gluons, one performs flips in colour chains with crossed colour lines (a flip means that a quark end becomes connected to a different antiquark end than previously).

  The free parameters of this model include a hadronic mass-square scale, a parameter which defines a probability that a given gluon will be considered for being moved, a parameter that restricts the number of gluon moves/flips and a switch for allowed flip types.

In the default Powheg+Pythia8 setup used in this analyses CR is not included. The three CR models described above define three alternative setups that could be compared with data.

7.1 Data and Monte Carlo samples

This analysis uses the full Run 2 data set collected during 2015–2018 corresponding to a total integrated luminosity of 139 fb^{-1} at the centre-of-mass energy of $\sqrt{s}$ = 13 TeV.

[1] λ, the total string length (calculated per event) is a rapidity range available for particle production, or, loosely speaking, the "free energy" of a string system, available for particle production [247].

To test different colour reconnection models, different POWHEG+PYTHIA8 Monte Carlo samples are used. These samples are processed through the GEANT4 detector simulation. The full ATLAS detector simulation is used for most of the samples, except for those used to evaluate the systematic uncertainties, for which the AtlasFast 2 simulation is used.

The MPI in the same and neighbouring bunch crossings (pile-up) is modelled by overlaying the minimum-bias events simulated using the PYTHIA 8 (v8.186) with A3 tune [248] and the NNPDF2.3 LO PDF set [180] over the hard scattering events.

7.1.1 $t\bar{t}$ signal samples

The signal $t\bar{t}$ production is simulated using the following generator. The matrix element is modelled at NLO using POWHEG-BOX v2 [204, 205], where the h_{damp} parameter is set to 1.5 m_{top} and the NNPDF3.0 NLO [182] PDF set is chosen. The renormalisation and factorisation scales are set to the default scale $\sqrt{m_t^2 + p_{\text{T}}^2}$. The parton shower and the hadronisation are simulated using PYTHIA 8 (v8.230) [246] with A14 tune [208] and the NNPDF2.3 LO PDF set. The decays of b- and c- hadrons are simulated using the EVTGEN v1.6.0 program [249].

The total $t\bar{t}$ cross section is normalised to the theoretical NNLO+NNLL calculation which is computed using the Top++2.0 program [151, 152] and yields $\sigma(t\bar{t}) = 832 \pm 51$ fb for a top quark mass of $m_t = 172.5$ GeV.

In what follows we describe how the signal modelling uncertainties are determined and which extra samples have been produced to estimate these uncertainties:

- The **ISR** uncertainty is estimated by comparing the nominal $t\bar{t}$ sample with two additional samples with higher and lower parton radiation:
  - Higher parton radiations are simulated by varying the $\mu_{\text{R,F}}$ scales by a factor of 0.5, simultaneous increasing h_{damp} to 3.0 m_{top} and setting the `Var3c up` variation of the A14 tune. The `Var3c` parameter varies α_{S} in the ISR.
  - Lower parton radiations are simulated by varying $\mu_{\text{R,F}}$ by a factor of 2.0 while keeping h_{damp} at 1.5 m_{top} and using the `Var3c down` variation of the A14 tune.
- The **FSR** uncertainty is computed by performing variation of the $\mu_{\text{R,F}}$ scales for QCD emission in the FSR by factors of 0.5 and 2.0.
- For the **PDF** uncertainty we use 100 variations of the NNPDF3.0 NLO PDF set. Furthermore, the central values are compared between the NNPDF3.0 NLO, CT14 NNLO [183] and MMHT2014 NNLO [250] PDF sets.
- To find the **parton shower and hadronisation** uncertainty we compare the nominal setup with a POWHEG+HERWIG7 sample: the NLO matrix element is generated using POWHEG-BOX v2 and NNPDF3.0 NLO PDF and the parton showering is done using HERWIG7.0.4 with the `H7UE` tune [215] and the MMHT2014 LO PDF set.

- The **NLO matching** uncertainty is assessed by comparing the nominal POWHEG+PYTHIA8 sample to the alternative aMC@NLO+PYTHIA8 sample. The matrix element of the alternative sample is generated using MADGRAPH5_aMC@NLOv2.6.0 with the NNPDF3.0 NLO PDF set and the parton shower is simulated with PYTHIA8.230 with the A14 tune and the NNPDF2.3 LO PDF set. The shower starting scale is chosen to be $\mu_{\mathrm{Q}} = H_{\mathrm{T}}/2$, where H_{T} is defined as a scalar sum of the p_{T} of all outgoing partons. The choice of $\mu_{\mathrm{R,F}}$ scales is the same as in the POWHEG setup.

To evaluate the sensitivity of the measurement to CR parameters, we use three POWHEG+PYTHIA8 $t\bar{t}$ samples generated using three different CR models: the MPI-based (ATLCR0), the QCD-based (ATLCR1) and the gluon-move model (ATLCR2).

7.1.2 Background samples

The main background processes used in this analysis that could lead to a $e\mu$ final state are the following:

- Single-top quark production in association with W-boson is modelled at NLO using POWHEG-BOX v2 in the five-flavour scheme with the NNPDF3.0 NLO PDF set. The $\mu_{\mathrm{R,F}}$ scales are set to m_t. The interference with $t\bar{t}$ events [251] is handled using the diagram removal scheme [252]. The parton shower and hadronisation is simulated using PYTHIA8.230 with A14 tune and the NNPDF2.3 LO PDF set.

- Z-boson production in association with jets is simulated using SHERPA2.2 [253]. The NLO ME of the setup with up to two jets and the LO ME with up to four jets are computed using the COMIX [254] and OPENLOOPS [222, 255] libraries. The dipole parton shower and the cluster hadronisation model are used with the default SHERPA2.2 parameters and the NNPDF3.0 NNLO PDF set. The NLO ME of a given jet multiplicity are matched using the MC@NLO matching scheme and then different jet multiplicities are merged into an inclusive sample using the CKKW matching [58, 256] extended to NLO accuracy using the MEPS@NLO prescription [257]. The merging cut $Q_{\mathrm{cut}} = 20$ GeV is used. The cross section is normalised to NNLO prediction [258]. More details are given in [259].

- Diboson production is simulated using SHERPA 2.2 using the dipole parton shower and the NNPDF3.0 NNLO PDF set. Samples with different jet multiplicity are matched and merged in the same way as the Z+jets samples.

  The uncertainties for the background samples are estimated in the same way as for the signal samples using alternative MC samples.

The pile-up background is subtracted as described in Section 7.2.3.

7.2 Data selection and event reconstruction

The same offline reconstruction is applied to both data and simulated samples.

7.2.1 Detector level reconstruction and selection

The detector objects resulting from a decay of the top quark pair are electrons, muons, jets and missing transverse momentum.

Events are selected, if they contain exactly one isolated electron and one isolated muon with opposite charges and at least two jets with $p_{\mathrm{T}} > 25$ GeV, two of which being identified as b-jets. The p_{T} and other cuts are given below in the object definitions. The single electron and single muon triggers used to select these events are presented in Table 7.1.

Electron triggers		
year	trigger name	p_{T} thresholds in L1 and HLT, and ID/isolation HLT requirements
2015	HLT_e24_lhmedium_L1EM20VH	$p_{\mathrm{T}} > 20$ GeV (L1); $p_{\mathrm{T}} > 24$ GeV, medium ID (HLT),
	HLT_e60_lhmedium	$p_{\mathrm{T}} > 60$ GeV, medium ID (HLT)
	HLT_e120_lhloose	$p_{\mathrm{T}} > 120$ GeV, loose ID (HLT)
2016, 2017, 2018,	HLT_e26_lhtight_nod0_ivarloose	$p_{\mathrm{T}} > 26$ GeV, tight ID, loose isolation (HLT),
	HLT_e60_lhmedium_nod0	$p_{\mathrm{T}} > 60$ GeV, medium ID (HLT)
	HLT_e140_lhloose_nod0	$p_{\mathrm{T}} > 140$ GeV, loose ID (HLT)
Muon triggers		
year	trigger name	p_{T} threshold and quality requirements
2015	HLT_mu20_iloose_L1MU15	$p_{\mathrm{T}} > 15$ GeV (L1); $p_{\mathrm{T}} > 20$ GeV, loose isolation (HLT),
	HLT_mu50	$p_{\mathrm{T}} > 50$ GeV (HLT)
2016, 2017, 2018	HLT_mu26_ivarmedium	$p_{\mathrm{T}} > 26$ GeV, medium isolation (HLT)
	HLT_mu50	$p_{\mathrm{T}} > 50$ GeV (HLT)

Table 7.1: Single electron and single muon triggers used in the analysis. The electron likelihood requirements (tight/medium/loose) are shown with a prefix lh. The isolation requirements (tight/medium/loose) are shown with a prefix i or ivar). The prefix ivar means that the isolation selection is computed using inner detector tracks reconstructed within a cone with a variable size which depend on p_{T}. The suffix nod0 means that there is no impact parameter requirement. For each data-taking year, a logical OR of all corresponding triggers is used.

An overview of the detector objects and their reconstruction methods is given in Section 3.3. The following detector level objects are selected in this analysis:

- **Electron** candidates have to fulfil the TightLH quality requirements and the Gradient isolation criteria, in particular these electrons should come from the primary vertex (PV). This is reflected in requirements on the electron transverse impact parameter significance d_0/σ_{d_0} and on its longitudinal impact parameter z_0, which are measured relative to the PV. Electron candidates are required to have $d_0/\sigma_{d_0} < 5$ and $|z_0 \sin(\theta)| < 0.5$ mm. These requirements allow to reduce the contamination of non-prompt electrons from heavy-flavour decays inside the jets and from photon conversions. The transverse momentum of an electron candidate should be $p_{\mathrm{T}} > 25$ GeV

and the pseudorapidity of the corresponding EM cluster should satisfy $|\eta_{\text{cluster}}| < 2.47$ excluding the transition region $1.37 < |\eta_{\text{cluster}}| < 1.52$.

- **Muon** candidates have to pass the `Medium` quality requirements and the `FCTight_FixedRad` isolation requirement. This is done in order to reduce the contamination of background muons from hadronic decays. Furthermore, muons have to originate from a PV, i.e. $d_0/\sigma_{d_0} < 3$ and $|z_0 \sin(\theta)| < 0.5$ mm, and to satisfy $p_{\text{T}} > 25$ GeV and $|\eta| < 2.5$.

- **Jets** are reconstructed from topological clusters using the anti-k_t algorithm with a radius parameter $R = 0.4$. Before the reconstruction, jet energy clusters are calibrated to the electromagnetic scale and after the reconstruction, jets are calibrated to the jet energy scale (JES) in order to correct the jet energy to its truth particle energy. The jet-vertex-tagger (JVT) discriminant is used to suppress the jets originating from pile-up interactions. A cut JVT > 0.59 is required for jets with $p_{\text{T}} < 60$ GeV and $|\eta| < 2.4$. The reconstructed jets are required to have $p_{\text{T}} > 25$ GeV and $|\eta| < 2.5$. The jets originating from b-quarks are identified using the MV2c10 tagging algorithm (see Section 3.3.5) with a 70% b-jet efficiency operating point.

- The reconstructed **tracks** are required to have $p_{\text{T}} > 500$ MeV, $|\eta| < 2.5$ and to be outside the selected jets and leptons: a track within $\Delta R < 0.4$ around a jet or within $\Delta R < 0.01$ around an electron is discarded. The good quality of tracks is ensured by the following selection requirement: the track candidates need to have 9 (11) silicon hits for $|\eta| < 1.65$ ($|\eta| > 1.65$), at least 1 hit in the IBL or in the first pixel layer, no missing hits in the pixel detector and two or fewer missing silicon hits. The candidate tracks are required to be associated with a primary vertex. The pile-up tracks (tracks originating from other pp interactions within the same bunch crossing) are partially removed by selecting tracks with $|d_0| < 1.5$ mm and $z_0 \sin|\theta| < 1.5$ mm.

The selected events are further required to have: the dilepton invariant mass $m_{ll} > 15$ GeV, the number of selected tracks $N_{\text{trk}} < 100$ and the number of interactions per bunch crossing $10 < \mu < 60$. The latest two cuts are applied in order to avoid regions with low data statistics and high contribution of pile-up tracks.

The overlapping detector objects are removed in the following order:

- An electron is removed, if its track is overlapping with a track of another electron,
- A calorimeter-tagged muon is rejected if it shares an Inner Detector track with an electron,
- An electron is rejected if it shares an Inner Detector track with a muon (not calorimeter-tagged),
- A jet is removed if it is within $\Delta R < 0.4$ of an electron,
- An electron is removed if it is within $\Delta R < 0.4$ of any of the remaining jets,
- A jet is removed if it has less than 3 tracks associated to it and is within $\Delta R < 0.2$ of a muon,
- A jet is removed if it has less than 3 tracks associated to it and has a muon Inner Detector track ghost-associated to it (see how the ghost association is done in Section 3.3.5),
- A muon is removed if it is within $\Delta R < 0.4$ of any of remaining jets.

7.2.2 Particle level reconstruction and selection

For the MC samples, in addition to the detector level objects also particle level truth objects are defined. "Particle level" refers to stable particles with a mean lifetime $\tau > 0.3 \cdot 10^{-10}$ s. The particle level selection, which defines the fiducial phase space of the analysis, follows the cuts from the detector level selection and is applied only to the $t\bar{t}$ signal events.

Particle object and reconstructed object definition follows the general recommendations of the Top Physics ATLAS group [260]. The following particle objects are defined:

- Truth **leptons** are electrons and muons originating from the W boson decay, while the leptons from hadron and τ decays are rejected. Each lepton is "dressed" with their radiated photons within a cone of $\Delta R < 0.1$, which consists of summing the lepton four-momentum with the photons four-momenta.
- Truth **jets** are reconstructed using the anti-k_t algorithm with a width parameter of $R = 0.4$ using the FastJet package. All stable particles except the truth leptons and photons associated with them are used for the jet clustering. This implies that the b-jet energy is close to the energy of the b-quark before the hadronisation and fragmentation.
- Truth ***b*-jets** are reconstructed jets which are b-tagged using ghost tagging: the energy of any b-hadron with $p_{\mathrm{T}} > 5$ GeV is renormalised to $\sim 10^{-6}$ GeV in order not to change the momentum of the jet, then the b-hadron is clustered with other particles and finally one checks if this b-hadron is inside the jet or not.
- **Charged particles** are stable charged particles with a proper lifetime $c\tau > 10$ mm, not associated to selected leptons and jets.

The event selection at particle level is done in such a way that it mimics the detector level selection. Events are required to contain one electron and one muon, both with $p_{\mathrm{T}} > 25$ GeV, $|\eta| < 2.5$ and with opposite charges, at least two jets with $p_{\mathrm{T}} > 25$ GeV and $|\eta| < 2.5$, two of which should be b-tagged. A selected event should contain $N_{\mathrm{ch}} < 100$ charged particles, which have $p_{\mathrm{T}} > 0.5$ GeV, $|\eta| < 2.5$, and are outside a cone of $\Delta R < 0.4$ around any particle level jet and outside a cone of $\Delta R < 0.01$ cone around any particle level lepton.

Instead of the object overlap removal at particle level an event veto is used: an event containing a selected lepton which is located within a cone of $\Delta R < 0.4$ around a selected jet is rejected.

7.2.3 Track background subtraction

In this section we give a brief description of how the background of pile-up, secondary and fake tracks is estimated. The pile-up tracks, which are one of the major background sources, are the tracks of particles originating from additional proton-proton collisions, which happen simultaneously with the hard scattering. The secondary tracks belong to particles coming from the interactions of primary particles with the detector material and the fake tracks do not correspond to real particles but consist of hits left by several particles. The fake tracks make a very small contribution to the background.

Because of that they are combined with the secondary tracks which contribute a bit more. So, in what follows "secondary tracks" will mean "secondary+fake" tracks combined.

To obtain a per-event estimate of the track background, a MC template method is used. For each considered 1D variable (see Section 7.3.1) we build templates, i.e. distributions of the number of pile-up or secondary tracks, for different bins of the number of reconstructed tracks using $t\bar{t}$ simulation. The template are built using the truth information available in the MC to identify pile-up tracks or secondary tracks. We observe a significant dependence of the pile-up/secondaries contribution only as a function of the number of reconstructed tracks. For example, we see no such dependence on the average number of interactions or on the sum of the transverse momenta of all tracks. More details are given in [261]. To estimate the actual number of pile-up and secondary tracks in the data, MC/data scale factors are estimated by fitting the rate of pile-up tracks using template of the longitudinal impact parameter (z_0) and the rate of secondary tracks using template of the transverse impact parameter significance (d_0/σ_{d_0}).

7.3 Unfolding to fiducial phase space

Unfolding is a procedure to correct the measured distributions for detector-related effects: acceptance, efficiency and resolution. The unfolding is done in order to be able to directly compare data from different experiments and predictions from theory, so that one does not need, for example, to process the theory predictions through the detector simulation.

There are several unfolding approaches: simple matrix inversion and bin-by-bin correction methods [262], Singular Value Decomposition method [263], fully Bayesian unfolding [264], iterative Bayesian Unfolding (IBU) by D'Agostini [191]. For this analysis, the IBU approach is used, which is implemented in the RooUnfold package [192].

Detector effects are corrected in the following way:

- The **acceptance** of the detector defines the phase space region, that the detector is able to measure. The acceptance unfolding correction is defined as the ratio between the number of events that pass both the detector-level ("reconstructed" or "reco") selection and the particle-level selection $N^i_{\text{reco}\wedge\text{part}}$ over the number of events that pass only the detector-level selection N^i_{reco} in a particular bin i of a detector-level distribution:

$$f^i_{\text{acc}} \equiv \frac{N^i_{\text{reco}\wedge\text{part}}}{N^i_{\text{reco}}}. \tag{7.2}$$

  The factor f^i_{acc} corrects for events outside the fiducial phase space which pass the detector-level selection.

- The **efficiency** is the detector ability to reconstruct a particle with a certain parameters. The efficiency unfolding correction is defined as the ratio between the number of events that pass

both the detector-level and the particle-level selection $N^j_{\text{reco}\wedge\text{part}}$ over the number of events that pass only the particle-level selection N^j_{part} in a particular bin j of a particle-level distribution:

$$\epsilon^j \equiv \frac{N^j_{\text{reco}\wedge\text{part}}}{N^j_{\text{part}}}. \tag{7.3}$$

The $1/\epsilon^j$ factor corrects for events which fall into the fiducial volume but are not reconstructed by the detector.

- The **resolution** reflects the precision to measure the particle properties given the limited detector accuracy. As a result, the reconstructed distribution becomes distorted w.r.t. the distribution at particle level: events "migrate" between bins, which means that some events fall into different bins at particle and detector levels. These bin-to-bin migrations are described by the response matrix $\mathcal{M}_{ij}$, which elements are defined by the following equation:

$$N^i_{\text{reco}\wedge\text{part}} = \sum_j \mathcal{M}_{ij} N^j_{\text{reco}\wedge\text{part}}, \tag{7.4}$$

where the indices i and j loop over the bins of the distributions at detector and particle levels, respectively. The migration matrix is obtained from the response matrix by normalising the bin contents in each row and column. It represents the fraction of the migrated events.

All the unfolding corrections are evaluated using simulated events.

The unfolding procedure is expressed by the following formula:

$$N^i_{\text{unfold}} = \frac{1}{\epsilon^i} \sum_j \mathcal{M}^{-1}_{ij} f^j_{\text{acc}} (N^j_{\text{data}} - N^j_{\text{bkg}}), \tag{7.5}$$

where N^i_{unfold} is the number of unfolded events in bin i, N^j_{data} and N^j_{bkg} are the numbers of data and background reconstructed events in bin j, f^j_{acc}, ϵ^i and $\mathcal{M}_{ij}$ are the unfolding corrections and the response matrix which have been defined above.

The main difficulty consists in calculating the inverse of the response matrix. In the iterative Bayesian unfolding method, $\mathcal{M}^{-1}_{ij}$ is calculated iteratively using the Bayes theorem:

$$P(T|D) = \frac{P(D|T)P(T)}{P(D)}, \tag{7.6}$$

where $P(D)$ is the probability of the data distribution, $P(T)$ is the probability of the truth distribution ("prior"), $P(D|T)$ is the probability of the data distribution for a given truth distribution and $P(T|D)$ is the probability of the truth distribution given the data distribution ("posterior"). In practice, $P(D|T)$ represents the migration matrix and the posterior probability $P(T|D)$ is the inverse of the migration matrix.

The iterative procedure is performed as follows:

- First of all, an initial hypothesis for the prior $P_0(T)$ needs to be made. In the IBU implementation of the RooUnfold package, the initial prior is the simulated truth distribution (we calculate it at particle level, as described in the previous section)[2].
- Then, the $P_n(D)$ distribution, where n refers to the iteration number, is found as a convolution of $P(D|T)$ and $P_n(T)$, i.e. as a product of the migration matrix and the prior, defined for the nth iteration:
$$P_n(D_i) = \sum_j P(D_i|T_j)P_n(T_j), \tag{7.7}$$
where i and j are the bin numbers of the distributions and the migration matrix.
- The next step is to find the nth estimate of the inverse of the migration matrix by substituting $P_n(T)$, $P_n(D)$ and the migration matrix into the Bayes formula Eq. (7.6). Its (k, i) element is equal to:
$$P_n(T_k|D_i) = \frac{P(D_i|T_k)P_n(T_k)}{P_n(D_i)}. \tag{7.8}$$
- Finally, the unfolding step is performed (see Eq. (7.5)) to find the unfolded distribution using the data (detector level) distribution and the nth estimate of the inverse of the migration matrix. The unfolded distribution is then used as a prior for the $(n+1)$st iteration. The iterative procedure is repeated until the unfolded distribution converges. In this analysis, the number of iterations is 4.

7.3.1 Sensitive observables

In this analysis, the following one-dimensional variables sensitive to the choice of CR model are chosen:

- The charged particles multiplicity N_{trk}: the number of selected tracks in an event after removal of the lepton and jet tracks. The bin edges are $[0, 10, 20, 30, 40, 50, 60, 70, 80]$.
- The scalar sum of the transverse momenta $\sum p_{\text{T}}$: the sum of the transverse momenta of the selected tracks. The bin edges are $[0, 10, 20, 30, 40, 50, 60, 70, 80]$ GeV.
- The mean transverse momentum of the charged particles $\langle p_{\text{T}} \rangle$: the sum of the transverse momenta of the selected tracks divided by the number of tracks. The bin edges (in GeV) are $[0.5, 0.7, 0.8.0.9, 1.1, 1.2, 1.3, 1.4, 1.5, 1.6, 1.8, 2.0]$.

The particle-level distributions of these variables with finer binning for different Pythia 8 CR models are shown in Fig. 7.1.

The binning of these variables are optimised by taking into account the resolution of the variables, the statistical uncertainty and the spread of events around the diagonal of the respective migration matrices. The minimal bin size is defined by the resolution and by the requirement, that the statistical uncertainty in each bin has to be $< 10\%$. Then, the diagonal of the migration matrix corresponding to the optimal binning should contain at least 50% of the events. The details of the binning optimisation

[2] In the original D'Agotini method, a flat distribution is taken as initial prior. Taking the truth distribution instead does not bias the final result, but allows to converge after fewer iterations [192].

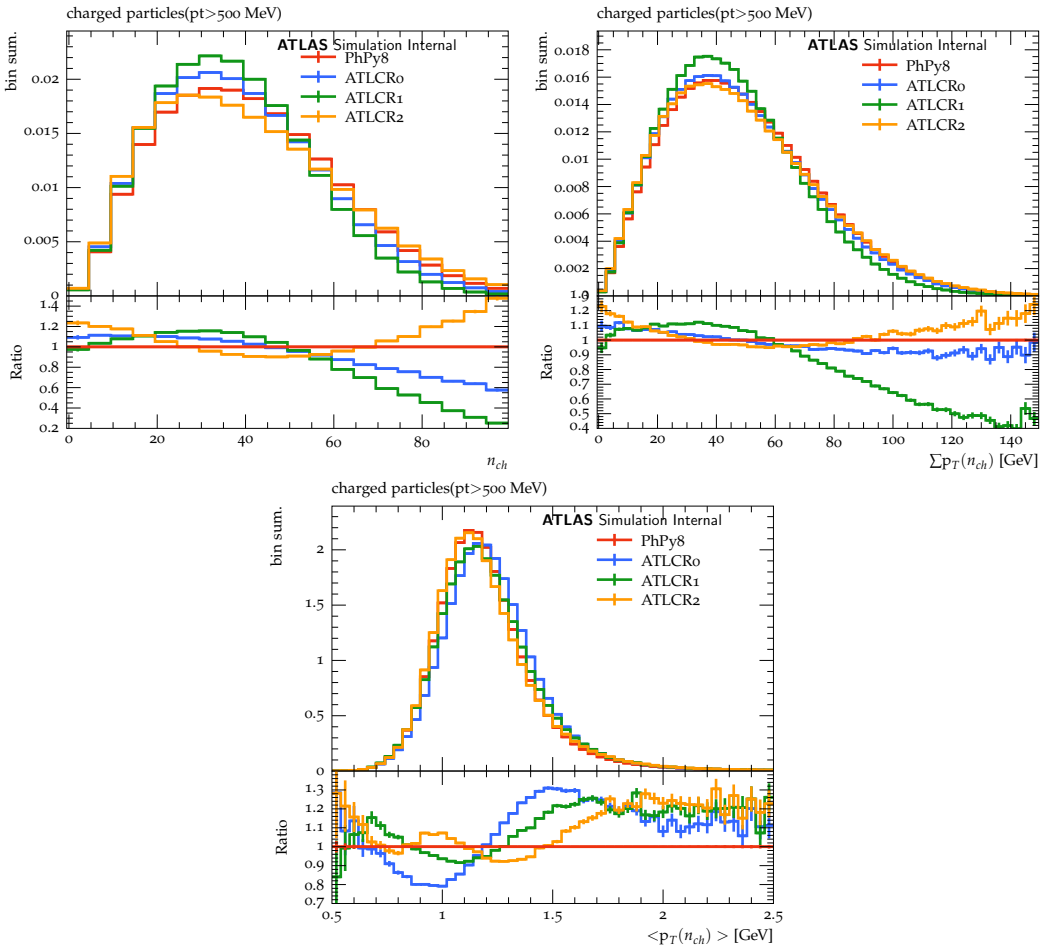

Figure 7.1: Particle-level distributions obtained from POWHEG+PYTHIA8 samples with the A14 tune ("PhPy8") without CR and with three different CR models ("ATLCR0,1,2"). The following distributions are compared: the number of charged particles (upper left), the sum of p_{T} of all charged particles (upper right)), the average p_{T} of all charged particles (bottom) [261].

study is described in [261]. The migration matrices for the one-dimensional variables are shown in Fig. 7.2.

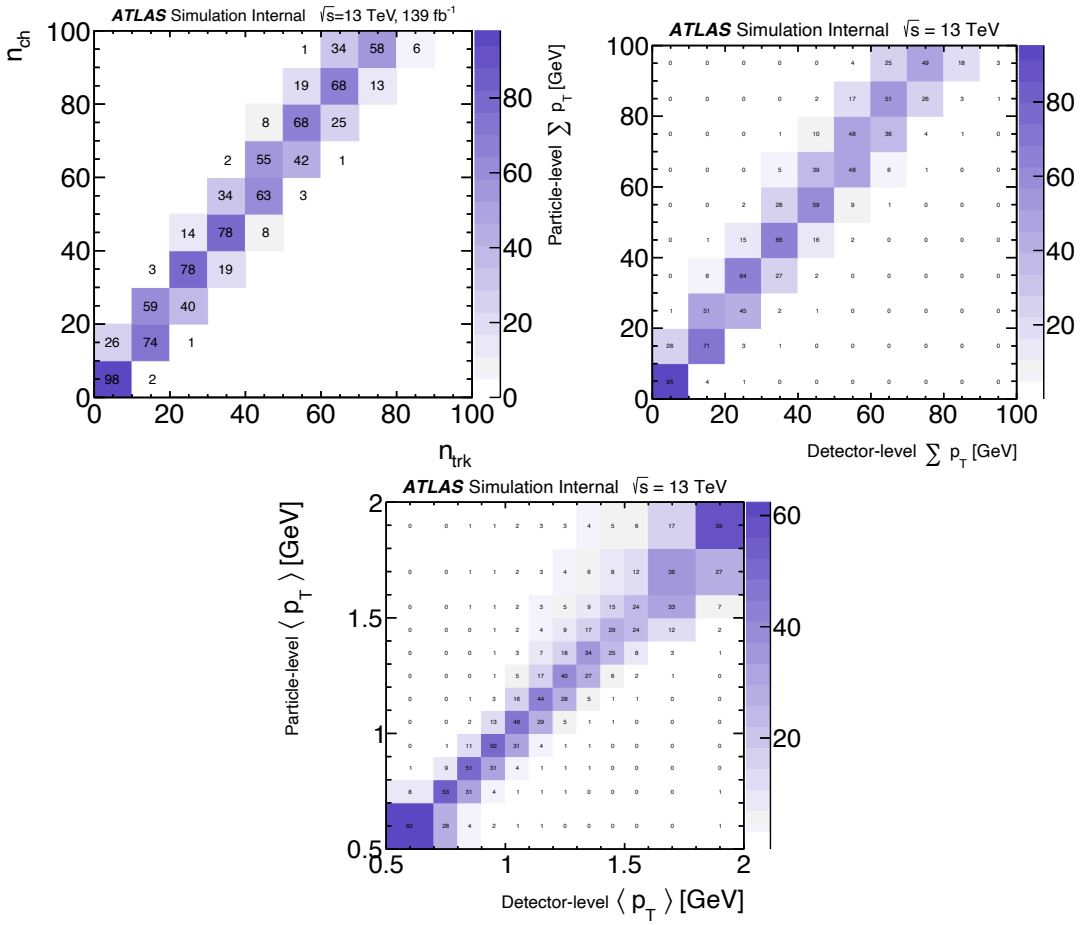

Figure 7.2: Migration matrices of N_{trk} (upper left), $\sum p_{\text{T}}$ (upper right) and $\langle p_{\text{T}} \rangle$ (bottom).

The diagonals of the migration matrices for N_{trk} and $\sum p_{\text{T}}$ variables are "inclined": the largest values of these migration matrices are not on the main diagonal and are shifted towards lower values of the number of selected tracks. This comes from the fact that the track reconstructed efficiency (ratio of the number of selected tracks to the number of charged particles) is about 76%. The obtained overall tracking efficiency is compatible with the one measured by the tracking group in [109] (see also Section 3.3.1).

We also use the two-dimensional variables, constructed by combining the 1D ones, which can result in higher sensitivity to the CR models:

- The scalar sum of the transverse momenta per charged particle multiplicity $N_{\text{trk}} \times \sum p_{\text{T}}$: the $\sum p_{\text{T}}$ distribution in bins of N_{trk}. The following binning scheme is used:
  - For $0 < N_{\text{trk}} < 20$, the $\sum p_{\text{T}}$ edges are $[0, 10, 100]$ GeV,

  - For $20 < N_{\text{trk}} < 40$, the $\sum p_{\text{T}}$ edges are $[0, 35, 100]$ GeV,
  - For $40 < N_{\text{trk}} < 60$, the $\sum p_{\text{T}}$ edges are $[0, 60, 100]$ GeV,
  - For $60 < N_{\text{trk}} < 80$, the $\sum p_{\text{T}}$ edges are $[0, 80, 100]$ GeV.

- The mean transverse momentum of the charged particles per charged particle multiplicity $N_{\text{trk}} \times \langle p_{\text{T}} \rangle$: the $\langle p_{\text{T}} \rangle$ distribution in bins of N_{trk}. The following binning scheme is used:
  - For $0 < N_{\text{trk}} < 10$, the $\langle p_{\text{T}} \rangle$ edges are $[0.5, 1.2, 2.0]$ GeV,
  - For $10 < N_{\text{trk}} < 20$, the $\langle p_{\text{T}} \rangle$ edges are $[0.5, 1.4, 2.0]$ GeV,
  - For $20 < N_{\text{trk}} < 40$, the $\langle p_{\text{T}} \rangle$ edges are $[0.5, 2.0]$ GeV,
  - For $40 < N_{\text{trk}} < 60$, the $\langle p_{\text{T}} \rangle$ edges are $[0.5, 1.2, 2.0]$ GeV,
  - For $60 < N_{\text{trk}} < 80$, the $\langle p_{\text{T}} \rangle$ edges are $[0.5, 1.2, 2.0]$ GeV.

The binning of the 2D variables has been optimised in the same way as for 1D distributions, i.e. using information on data statistical uncertainty, resolution and diagonality of the migration matrices. The distributions of data statistical uncertainty and resolution are given in Fig. 7.3 and Fig. 7.4 respectively. The "local minima" present in the resolution distributions are currently investigated.

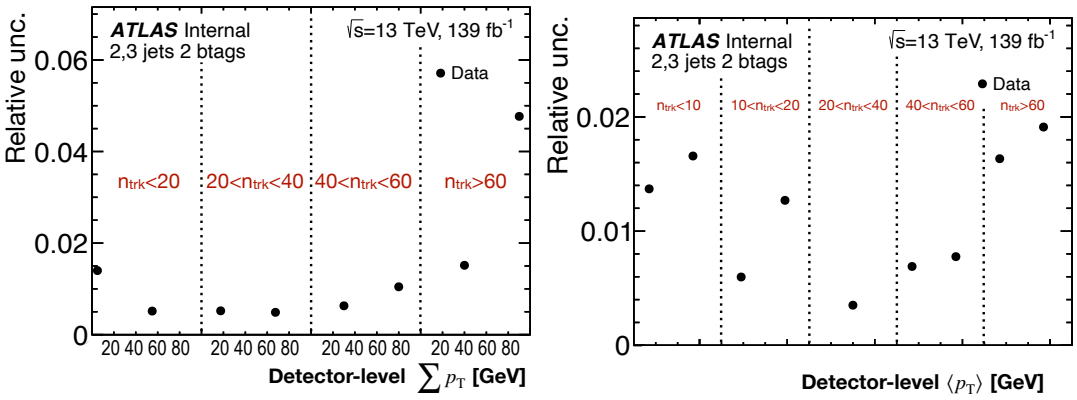

Figure 7.3: Data statistical uncertainty of $N_{\text{trk}} \times \sum p_{\text{T}}$ variable (left) and of $N_{\text{trk}} \times \langle p_{\text{T}} \rangle$ variable (right).

The migration matrices for the $N_{\text{trk}} \times \sum p_{\text{T}}$ and $N_{\text{trk}} \times \langle p_{\text{T}} \rangle$ variables are shown in Fig. 7.5. The main diagonals of the matrices are inclined, as the ones for the 1D distributions, due to the track reconstruction efficiency of 76%. Requirement of having at least 50% of the events on the main diagonal was the main reason to choose very coarse $\sum p_{\text{T}}$ and $\langle p_{\text{T}} \rangle$ bins: there are not more than 2 bins in each N_{trk} bin.

In the following, we will focus on the two-dimensional variables, mainly on $N_{\text{trk}} \times \sum p_{\text{T}}$. For the moment, we consider only normalised distributions, we plan to use also the absolute distributions later.

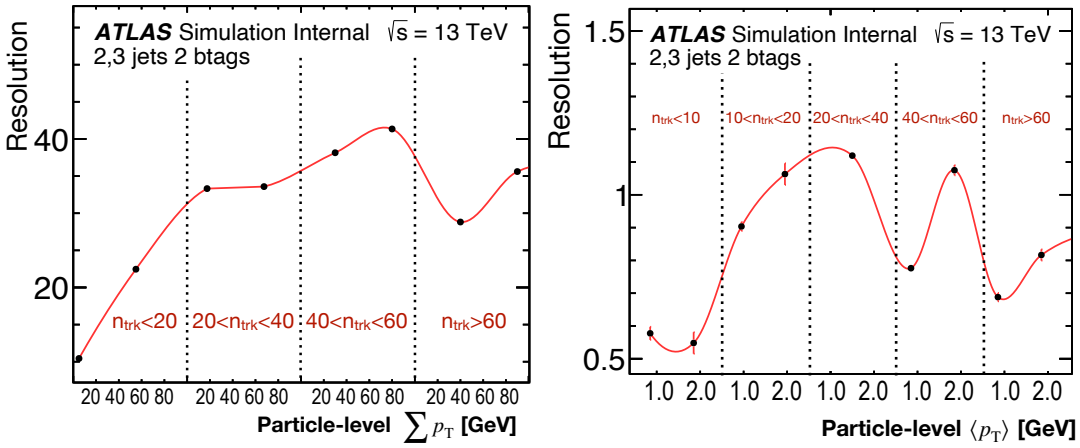

Figure 7.4: Resolution of $N_{\text{trk}} \times \sum p_{\text{T}}$ variable (left) and of $N_{\text{trk}} \times \langle p_{\text{T}} \rangle$ variable (right).

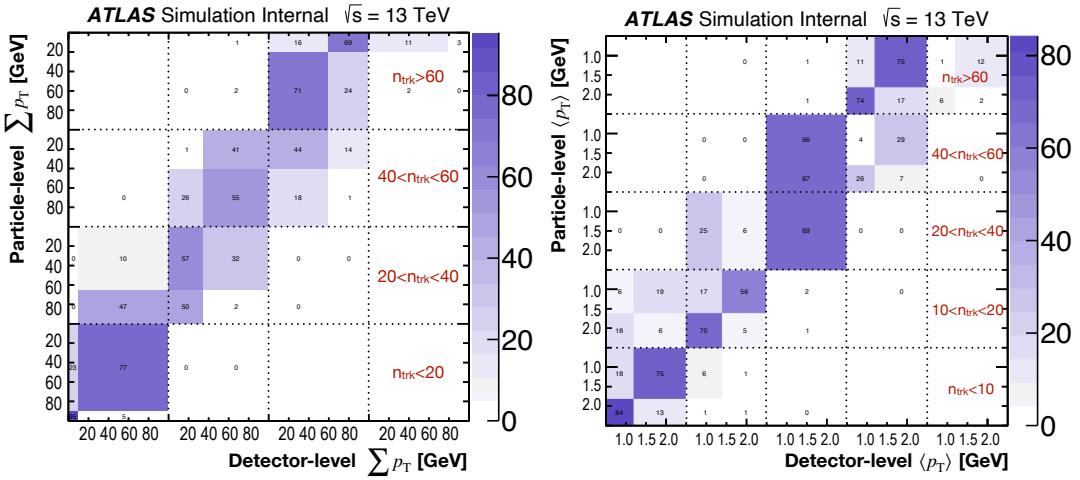

Figure 7.5: Migration matrices of $N_{\text{trk}} \times \sum p_{\text{T}}$ variable (left) and of $N_{\text{trk}} \times \langle p_{\text{T}} \rangle$ variable (right).

7.3.2 Closure tests

The consistency of the unfolding procedure has been checked in a closure test, in which the simulated $t\bar{t}$ sample is unfolded with a migration matrix constructed using the same MC events. Then, the unfolded distribution is compared to the truth distribution, which also was used to build the migration matrix. The comparison of the truth distribution and the unfolded distribution for the two 2D variables in Fig. 7.6 shows good closure for both variables.

7.3.3 Stress tests

Stress tests are performed in order to check that the unfolding procedure is not biased. For that, the simulated detector level distribution to be unfolded and the particle level distribution are reweighted using the same "stress function". Then, the stressed detector level distribution is unfolded using

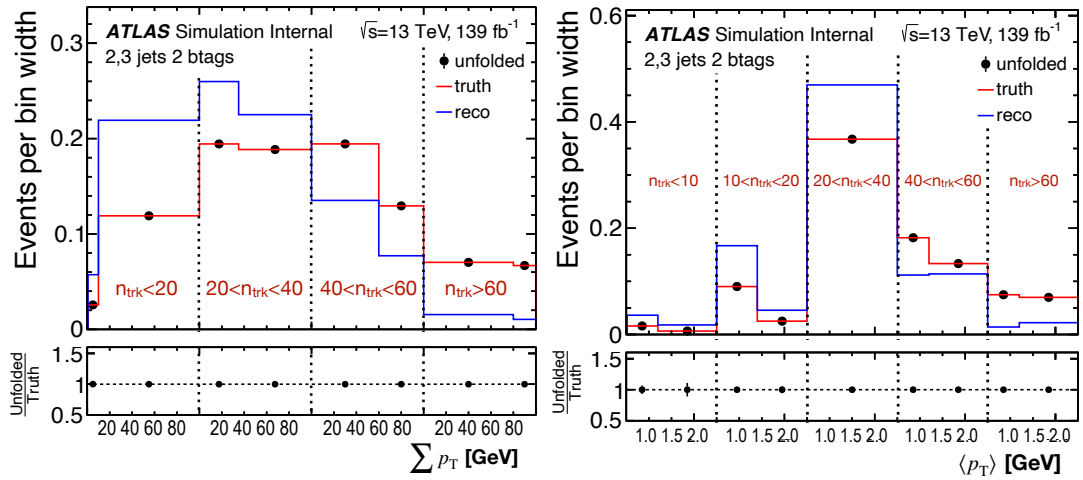

Figure 7.6: Closure test results for the unfolding to particle-level of $N_{\text{trk}} \times \sum p_{\text{T}}$ distribution (left) and of $N_{\text{trk}} \times \langle p_{\text{T}} \rangle$ distribution (right).

the unfolded corrections and the migration matrix calculated using the non-stressed samples. If the unfolding procedure is not biased, the unfolded stressed distribution should be compatible with the stressed particle level distribution.

The stress tests for the 1D spectra have been performed and they are reflected in [261]. The results of the stress test for the 2D spectra, in which the reweighting is performed using linear functions, are shown in Fig. 7.7. The slopes of linear functions are chosen in such a way that the extreme bins are weighted by 10%, 20%, 30%, and 40%. The results of the stress test show a good ability of the unfolding to recover the reweighted distributions.

7.3.4 Pull tests

Pull tests are performed to prove that the unfolding procedure is able to correctly unfold pseudo-data which are fluctuated around their nominal values. Pseudo-experiments are constructed by smearing the detector level distributions bin-by-bin by drawing a random number which follows a Poisson distribution with a mean equal to the bin content. The fluctuated distribution is unfolded using the nominal migration matrix and unfolding corrections. The difference between the unfolded and truth bin values divided by the standard deviation of the fluctuation in this bin defines the *pull* in this bin. For each bin, the distribution of pulls calculated for 1000 pseudo-experiments is fitted to a Gaussian function. The mean and the width of the Gaussian fit are expected to be consistent with zero and one, respectively.

The results of the pull test for the $N_{\text{trk}} \times \sum p_{\text{T}}$ variable in Fig. 7.8 show that indeed the mean and the width of the fitted pull distributions are compatible with zero and one for all the bins.

We are going to perform the pull test for the $N_{\text{trk}} \times \langle p_{\text{T}} \rangle$ distribution as well.

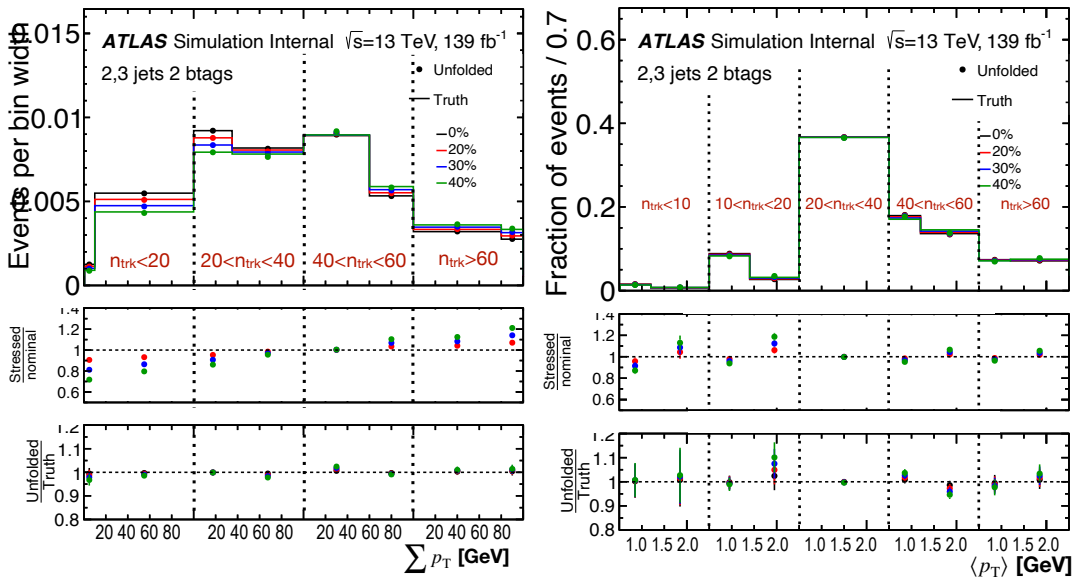

Figure 7.7: Stress test results for the unfolding to particle-level of $N_{\text{trk}} \times \sum p_{\text{T}}$ distribution (left) and of $N_{\text{trk}} \times \langle p_{\text{T}} \rangle$ distribution (right). Linear stress function is used for the reweighting. The middle pad shows the ratio of the stressed and the nominal distributions. The lower pad shows the ratio of the unfolded and the truth distributions.

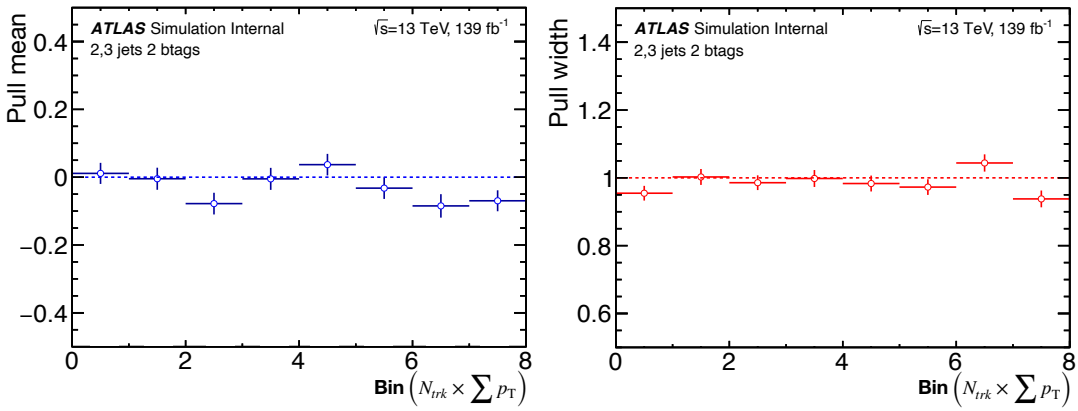

Figure 7.8: The mean (left) and the width (right) of the Gaussian fit of the pull distributions for different bins of $N_{\text{trk}} \times \sum p_{\text{T}}$.

7.4 Systematic uncertainties

Several sources of systematic uncertainties for the measured observables are considered: uncertainties from detector effects ("detector systematic" uncertainties) and uncertainties on the modelling of the signal and the background processes ("modelling systematic" uncertainties).

The detector systematic uncertainties of the unfolded distributions are computed as differences between the shifted detector level distributions unfolded using the nominal unfolding corrections and the nominal unfolded distributions. The up and down shifts in each bin of the detector level distributions are done according to the variations of the corresponding systematic component. Some of the detector systematics effects are neglected, because they result in a negligible shift of the reconstructed distribution. The qualitative criterion which determines whether the uncertainty component will be neglected or not is based on a χ^2 computation. A χ^2 is calculated as a sum of squared differences between the shifted and the original distributions in each bin, each divided by the square of the statistical uncertainty in this bin. If the p-value of the χ^2 (χ^2-*probability*) is below 50%, the corresponding systematic component is taken into account in the final uncertainty. This criteria ensures that only statistically significant variations are taken into account as systematic uncertainties.

The systematic uncertainties due to the modelling of the signal $t\bar{t}$ sample is determined by unfolding the alternative MC samples using the nominal unfolding corrections and comparing them to the truth distribution. Each modelling uncertainty component is equal to the difference between the unfolded and truth distributions.

The systematic uncertainties are currently calculated only for two 1D variables, N_{trk} and $\sum p_{\text{T}}$ and one 2D variable, $N_{\text{trk}} \times \sum p_{\text{T}}$. The uncertainties related to the tracks background rate are only estimated for N_{trk} and $\sum p_{\text{T}}$ for the moment (details in [261]). We are planning to estimate them also for other variables in the future.

7.4.1 Detector systematics

Number of pile-up events

Scale factors are applied to simulated events in order to match the MC pile-up distribution to data. An uncertainty on these scale factors is related to the residual mismatch between the instantaneous luminosity in data and in simulation. The χ^2-probability of this uncertainty is 100%, therefore, it is not considered in the unfolding.

Lepton uncertainties

Disagreements between data and simulation related to the lepton reconstruction, identification, isolation and trigger efficiencies are corrected for by applying scale factors, that are determined by the *tag-and-probe method*[3] using $Z \to ll$ ($l = e\mu$) events. The lepton uncertainties are evaluated by

[3] In the tag-and-probe method, one of the leptons in the event is reconstructed using strict selection requirements ("tag"), while the other lepton candidate provides an unbiased samples of "probes", which is used to measure the efficiency by fitting to a Z-boson mass peak.

varying the scale factors within their uncertainties. For example, the impact of the lepton energy scale and resolution is computed by scaling each lepton p_{T} up and down by one standard deviation of the corresponding scale factor and by re-applying the event selection.

For the muons, there are five sources of systematic uncertainty: the smearing of the Inner Detector track, the smearing of the Muon Spectrometer track and three components related to the muon p_{T} scale.

All the lepton uncertainties have χ^2-probabilities of 100% w.r.t. the nominal, so they are neglected.

Jet uncertainties

The **JES** uncertainty is evaluated by performing up/down jet energy variations according to the uncertainties derived from *in-situ* calibration measurements which use a model with 29 nuisance parameters (NP) (see Section 3.3.5). These NPs account for various effects: η inter-calibration, jet flavour composition and response, b-jets, detector modelling, statistics, data/MC non-closure and several pile-up properties.

The **JER** uncertainty is estimated in a similar way as the JES uncertainty using a model with 7 NPs.

The **JVT** uncertainty covers the differences in JVT efficiency between data and simulation and is calculated by varying the corresponding scale factor up and down by one standard deviation.

Only a few of the jet uncertainties described above result in a χ^2-probability$< 50\%$:

- `JET_Pileup_RhoTopology`: the uncertainty on the jet p_{T} density MC modelling,
- `JET_Flavor_Composition`: the uncertainty on the jet flavour (quark/gluon) composition,
- `JET_Flavor_Response`: the uncertainty on the jet response for gluon-initiated jets,
- `JET_EffectiveNP_Modelling1`: effective nuisance parameter (NP) of one of the jet modelling uncertainty components.
- `JET_JET_EtaIntercalibration_Modelling`: the uncertainty on the *in-situ* η inter-calibration mismodelling.
- `JET_JER_EffectiveNP3`: one of the effective NPs of the JER uncertainty,

Missing transverse momentum

The energy/momentum scale uncertainties of the leptons and jets are also propagated to the $E_{\mathrm{T}}^{\mathrm{miss}}$ calculations. Their impact is evaluated by shifting the lepton or jet energy and by redoing the event selection.

The remaining contribution to the $E_{\mathrm{T}}^{\mathrm{miss}}$ uncertainty related to the $E_{\mathrm{T}}^{\mathrm{miss}}$ soft terms is calculated by doing the energy scale variations and the resolution smearing in the parallel and perpendicular directions to the hard-p_{T} plane according to their uncertainties. Several uncertainty components are defined: the soft track p_{T} scale shift along the hard-p_{T} axis, the soft track p_{T} resolution smearing along and perpendicular to the hard-p_{T} axis.

The $E_{\mathrm{T}}^{\mathrm{miss}}$ uncertainties have χ^2-probabilities of 100% and so are neglected.

Track uncertainties

The systematic uncertainties associated to the d_0 and z_0 impact parameters resolution are estimated using the track smearing tool. Given a set of tracks, the tool replaces the impact parameter of each track with a random value drawn from a Gaussian distribution with mean at the original impact parameter and standard deviation taken from smearing maps, which are obtained in dedicated studies. Two other uncertainty components related to the simulation of the inactive silicon pixels are found by randomly disabling 5% of the pixel modules.

There are also systematic uncertainties related to the weak modes in the alignment, i.e. the modes in which the detector can be misshapen and which cannot be fully taken into account by the alignment procedure. These uncertainties can be estimated by reweighting tracks in order to simulate the impact of such weak modes.

All the track uncertainties have a χ^2-probability of 100% and so are neglected.

However, the list of the track uncertainties mentioned above is still preliminary and will be checked and possibly expanded.

7.4.2 Signal modelling systematics

The uncertainty due to the choice of the **matrix element** (ME) generator is calculated by unfolding the MC@NLO+Pythia 8 sample using the corrections and the migration matrix obtained using the Powheg+Pythia8 sample and comparing the result with the particle level distributions from the MC@NLO+Pythia 8 sample.

The **parton shower and hadronisation** (PS) uncertainty is estimated by unfolding the Powheg+Herwig 7 sample using the corrections and the migration matrix obtained using the Powheg+Pythia 8 sample and comparing the result with the particle level distributions from the Powheg+Herwig 7 sample.

The **colour reconnection** (CR) uncertainty is estimated by unfolding alternative Powheg+Pythia 8 samples simulated using different Pythia 8 tunes (ATLCR0, ATLCR1, ATLCR2, see Section 7.1) using the corrections and the migration matrix obtained using the Powheg+Pythia 8 sample and comparing the result with the particle level distributions from the alternative samples.

7.4.3 Background systematics

The background rate uncertainties are calculated by varying the background rates up and down within the following uncertainties:

- tW production: 10%,
- Fake leptons: 50%,
- $t\bar{t}$+vector boson production: 10%,

- diboson production: 20%,
- Z+jets production: 20%.

The pile-up tracks background rate is varied for N_{trk} and $\sum p_{\text{T}}$ variables and considered as another source of systematic uncertainties. The variation for the N_{trk} distribution is done according to the pile-up scale factor uncertainties and the variation for the $\sum p_{\text{T}}$ distribution is done using a reweighting function.

7.4.4 Systematic uncertainties of the unfolded distributions

The relative detector uncertainties of the unfolded two-dimensional distributions are shown in Fig. 7.9 on the left. The dominant uncertainty is coming from the jet flavour composition effects.

The modelling systematic uncertainties of the unfolded distributions are shown in Fig. 7.9 on the right. The matrix element uncertainty gives the largest contribution in most of the bins and the parton shower and hadronisation dominates in the remaining ones. In general, the modelling uncertainties are an order of magnitude larger then the detector uncertainty components.

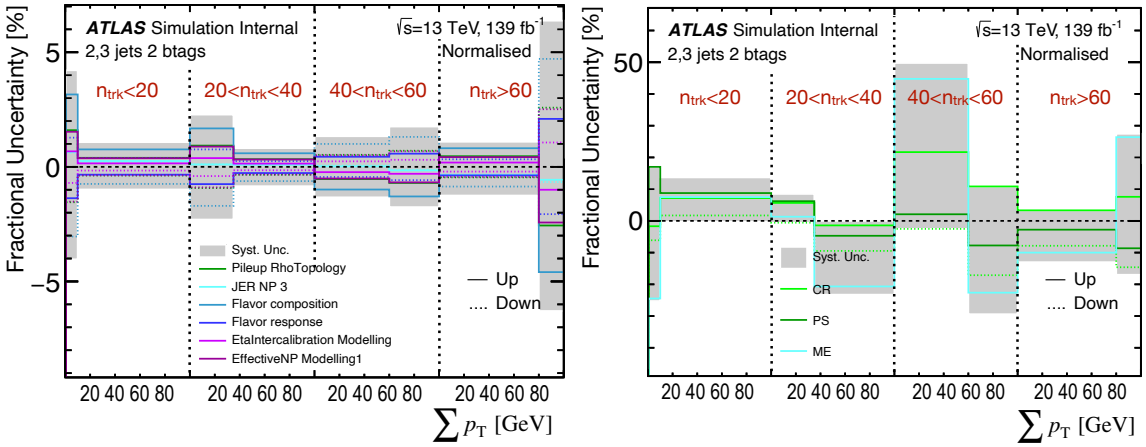

Figure 7.9: Relative detector (left) and modelling (right) systematic uncertainties for the $N_{\text{trk}} \times \sum p_{\text{T}}$ distributions.

7.4.5 Sensitivity to colour reconnection models

We did a first estimate of how the unfolded distributions vary when changing the CR model in the POWHEG+PYTHIA 8 sample. For that, we unfold the alternative POWHEG+PYTHIA 8 samples simulated using different PYTHIA 8 tunes (ATLCR0, ATLCR1, ATLCR2, see Section 7.1) using the corrections and the migration matrix obtained using the POWHEG+PYTHIA 8 sample and compare the result with the particle level distributions from the alternative samples. The relative differences between the unfolded distributions from the alternative POWHEG+PYTHIA 8 samples and from the nominal POWHEG+PYTHIA 8 sample are shown in Fig. 7.10 on the right. In order to see if the measured distributions would be sensitive enough to constrain some CR models, we compare the variations due

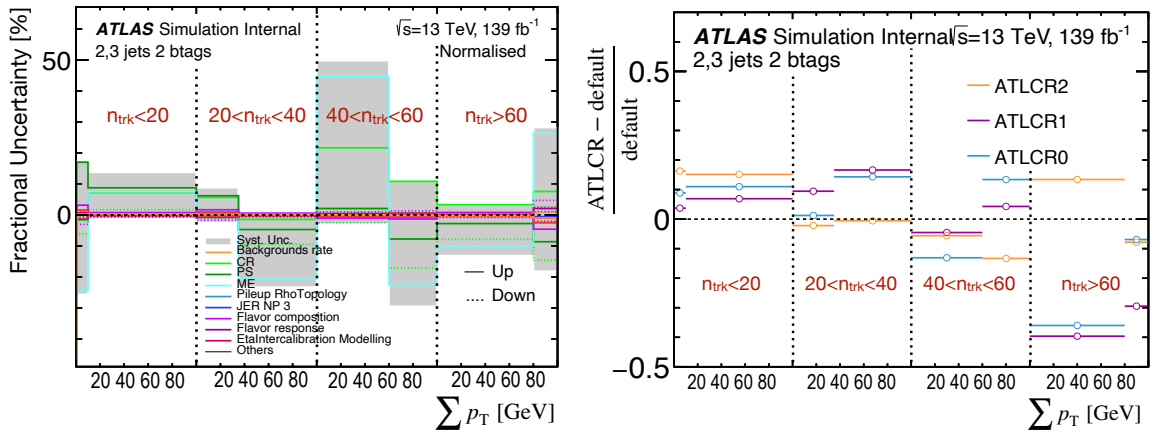

Figure 7.10: Relative total systematic uncertainty (left) and relative differences between the unfolded distributions obtained from alternative CR and nominal POWHEG+PYTHIA 8 samples (right) for $N_{\text{trk}} \times \sum p_{\text{T}}$ observable.

to the CR model choice with the total systematic uncertainty (shown in Fig. 7.10 on the left). The comparison shows that in some of the bins (for instance in the bins 4 and 7) the CR variation may exceed the total uncertainty, which could help to constrain the CR models.

7.5 Conclusion and next steps

In this chapter, a study of observables sensitive to the colour reconnection uncertainty using $t\bar{t}$ dilepton events has been presented. We unfold one- and two-dimensional observables related to the number of tracks and sum or average of p_{T} of the tracks in order to compare the data distributions unfolded to particle level with the simulated distributions corresponding to different PYTHIA 8 CR models. This would allow to constrain/reject the CR models which do not describe the data well and to improve the CR uncertainty definition for the top quark mass measurements.

At the current stage, we have tested the unfolding procedure for both 2D variables using MC simulated samples and estimated various systematic uncertainties for the unfolded $N_{\text{trk}} \times \sum p_{\text{T}}$ distribution. During the next steps we are going to estimate the systematic uncertainties for the $N_{\text{trk}} \times \langle p_{\text{T}} \rangle$ distribution and the tracks background rates for both 2D variables using the methods employed for 1D variables and construct the covariance matrices containing all the systematic uncertainty components. Among the systematic uncertainties which have already been estimated, the largest component is related to the choice of the matrix element generator. The largest detector systematic uncertainty is related to the jet flavour composition effects. Preliminary comparison of the total uncertainty with the variations due to the choice of different CR models hints at the possibility to constrain some CR models using several bins of the $N_{\text{trk}} \times \sum p_{\text{T}}$ distribution, in which the shift due to CR variation is larger than the total uncertainty.

Up to now, the analysis procedure has been tested using MC simulations. After finishing all the developments we will run the analysis on data.

8 Study of the impact of jets recalibration on the hadronisation uncertainty in top quark mass measurements at $\sqrt{s}$ = 13 TeV with the ATLAS detector

The current definition of the hadronisation uncertainty in top quark mass measurements is based on a comparison of two setups: POWHEG+PYTHIA 8 and POWHEG+HERWIG 7 (see Section 4.5.1). However, an hadronisation uncertainty defined like that potentially overlaps with the JES uncertainty since different parton shower and hadronisation models in PYTHIA and HERWIG also change the calibration of the jet energies. This issue motivates us to try to disentangle the two uncertainties and to make the hadronisation uncertainty definition more coherent.

The goal of the study presented in this chapter is to factorise out the JES effects from hadronisation uncertainty, as done in [265], by recalibrating the energy scale of the jets in POWHEG+PYTHIA 8 to match that in POWHEG+HERWIG 7.

To check whether the recalibration has an effect, we extract the top quark mass from the original POWHEG+PYTHIA 8 and POWHEG+HERWIG 7 samples and from the recalibrated POWHEG+PYTHIA 8 sample and compute, how the hadronisation uncertainty (PYTHIA–HERWIG difference in m_t) changes with the recalibration.

8.1 Monte Carlo samples

In this study, we work only with simulated samples. Several MC samples simulating $t\bar{t}$ events in the dilepton decay channel are used for this study: a POWHEG+PYTHIA 8 sample with the nominal top quark mass m_t = 172.5 GeV ("nominal" sample), POWHEG+PYTHIA 8 samples with other top quark masses ("mass-varied" samples) and a POWHEG+HERWIG 7 sample with the nominal top quark mass m_t = 172.5 but an alternative hadronisation model.

The nominal and the mass-varied samples are simulated using the POWHEG generator interfaced to PYTHIA 8. POWHEG-BOX v2 [204, 205] is used to compute the matrix element at NLO order in α_S with the NNPDF3.0 NLO [182] PDF set and the h_{damp} parameter set to 1.5 m_{top}. The renormalisation and factorisation scales are set to the default scale $\sqrt{m_{\text{top}}^2 + p_{\text{T}}^2}$. The parton shower and the hadronisation are simulated using PYTHIA v8.230 [246] with A14 tune [208] and the NNPDF2.3 LO PDF set. The decays of the b- and c- hadrons are simulated using the EVTGEN v1.6.0 program. A two lepton filter is applied during the event generation, so that only $t\bar{t}$ events in the dilepton decay channel

are produced. In total, nine POWHEG+PYTHIA8 samples are used: the nominal sample is generated with m_t = 172.5 GeV and the mass-varied samples correspond to the following top quark masses: $m_t \in [169.00, 171.00, 172.00, 172.25, 172.75, 173.00, 174.00, 176.00]$ GeV.

In the sample with an alternative hadronisation model, a NLO matrix element is calculated using POWHEG with the same settings as for the nominal POWHEG+PYTHIA8 sample, but the parton shower and hadronisation are modelled using HERWIG 7.1.3 [213] with the `H7.1-Default` tune [225]. The top quark mass is set to m_t = 172.5 GeV, as in the nominal POWHEG+PYTHIA8 sample.

The total $t\bar{t}$ cross section of the samples is normalised to the theoretical NNLO+NNLL calculation, computed with the Top++2.0 program [151, 152] and yields $\sigma(t\bar{t})$ = 832 ± 51 fb for a top quark mass m_t = 172.5 GeV.

Detector effects are simulated using ATLFASTII GEANT 4 for all the samples.

8.2 Object and event selection

8.2.1 Detector level reconstruction and selection

The selection process is divided in two parts: the first set of cuts ("preselection") is applied before the recalibration of jet energy scale (JES) is done and the rest of the cuts is applied afterwards. For the samples with default jet energy scale calibration the final selection is done immediately after the preselection step.

The preselection consists in choosing events with one isolated electron and one isolated muon with opposite charges, both with $p_{\mathrm{T}} > 20$ GeV and with a dilepton invariant mass $m_{ll} > 15$ GeV. The electron and muon triggers used are identical to the ones used in the analysis described in Chapter 7 (see Table 7.1). The electrons and muons used in this analysis are defined as in Section 7.2.1, except for different p_{T} cuts, which are mentioned above. The same `Gradient` isolation requirement is used for both, electrons and muons. The jet definition is also the same as in Section 7.2.1, but the preselection p_{T} cut is 6 GeV and no requirement on the jet number is set.

After the jet energy scale calibration, the overlap removal is done, as described in Section 7.2.1. Then, an additional selection criterion is applied: at least two jets with $p_{\mathrm{T}} > 25$ GeV[1] and $|\eta| < 2.5$ are required and at least one of them has to be b-tagged with 64% efficiency using the MV2c10 tagger.

8.2.2 Particle level reconstruction and selection

The particle level selection (see Section 7.2.2 for object definitions) is used for the HERWIG 7 and the nominal PYTHIA 8 samples to construct the recalibration curves. The particle level cuts are analogous to the detector level ones. The presence of exactly one electron and exactly one muon, both with $p_{\mathrm{T}} > 20$ GeV is required. Truth particle jets with $p_{\mathrm{T}} > 20$ GeV are selected. No cut on the jet number

[1] The $p_{\mathrm{T}} > 25$ GeV cut is a standard jet p_{T} cut for the top quark mass analyses in the dilepton channel. For the preselection step, we choose a very low jet p_{T} cut (6 GeV) in order to apply the jet recalibration to all the jets before the final selection.

is applied, since we need information on as many jets as possible to build the recalibration functions. The overlap removal at the particle level is not done is order to keep all the jets.

8.2.3 M_{lb} distribution

In Section 8.4, for the top quark mass extraction we use the distribution of the invariant mass of a b-tagged jet and a lepton (e or μ), M_{lb}. Two lepton-b-jet combinations are possible and we pick the one which leads to the lowest average invariant mass $(M_{eb_1} + M_{\mu b_2})/2$[2].

To perform the template parametrisation in Section 8.4 we use the M_{lb} distribution in the range $30 < M_{lb} < 155$ GeV. This range is found to be optimal from the point of view of the template fit quality (larger range results in higher χ^2 of the fit) and of the uncertainties on the fitting parameters (smaller range increases the uncertainties).

8.3 Jet recalibration

After jet reconstruction, the JES is calibrated to match the energy of the jet of stable particles that enter the detector. To recalibrate the jet energy provided by one MC generator to the energy generated by another MC generator one basically needs to "replace" the particle level jet response. This can be done by applying a scale factor, i.e. the ratio between the jet responses corresponding to one generator and another generator.

The calorimeter response to particle level jets is defined as the mean value of the ratio of the reconstructed jet p_{T} to the particle level (generated) jet p_{T}:

$$\mathcal{R}^{\mathrm{particle}} = \left\langle \frac{p_{\mathrm{T}}^{\mathrm{reco}}}{p_{\mathrm{T}}^{\mathrm{particle}}} \right\rangle . \tag{8.1}$$

The mean value is calculated using a Gaussian fit of the p_{T} ratio. The jet response is measured as a function of the particle level jet p_{T} in bins of jet η.

Then, to recalibrate the Powheg+Pythia 8 sample to Powheg+Herwig 7, one needs to apply a scale factor to all the jets from the Powheg+Pythia 8 sample. This scale factor is equal to the ratio of the calorimeter Powheg+Herwig 7 response to the Powheg+Pythia 8 response:

$$C = \frac{\mathcal{R}^{\mathrm{particle}}_{\mathrm{Herwig}}}{\mathcal{R}^{\mathrm{particle}}_{\mathrm{Pythia}}}. \tag{8.2}$$

The scale factor is applied to the jet four-momentum before the final jet selection (see previous section) and before the jet-lepton overlap removal.

[2] The procedure of lepton-b-jet assignment is the same as in [164]. Studies performed in [266] confirm the nearly optimal performance of the minimum M_{lb} criterion for the jet-to-lepton assignment.

The calibration functions are defined for each flavour of jet separately: for c-jets, b-jets, jets originating from light quarks and gluon jets. This is done because the response and the impact of each jet flavour can be different between the two generators.

The jet flavour (flavour of a parton from which it originates) and its particle level p_{T} are accessed in the following way:

- First, some isolation is applied to the reconstructed jets: a jet is not considered if there is another reconstructed jet with $p_{\mathrm{T}}^{\text{EM scale}} > 7$ GeV within a cone $\Delta R < 1$ around the jet.

- For each isolated jet we obtain its flavour and the particle-level p_{T}. We investigated two ways for accessing this information:

  1. Use the ghost-matching technique [124] to get the truth flavour and the particle level p_{T} of a jet,

  2. Use a custom jet matching. To match a reconstructed jet to a particle jet and find its particle level p_{T}, the closest particle jet within $\Delta R < 0.3$ around the jet is taken. To find the flavour of the jet, it is matched to the parton which is most likely its origin: the most energetic parton within a cone of $\Delta R < 0.4$.

  When comparing the calorimeter responses obtained using the two methods, we see almost no difference for jets generated using Powheg+Pythia 8 and some per cent difference for light quark jets generated using Powheg+Herwig 7. Since the first method is considered as "official" and more coherent for ATLAS analyses, we will use it for accessing the truth information in the rest of the analysis.

- Finally, the calibration curve as a function of the particle jet p_{T} is found for each jet flavour in each $|\eta|$ bin as the fitted ratio of the calorimeter responses, see Eq. (8.2).

The calorimeter responses of the jets in Powheg+Herwig 7, Powheg+Pythia 8 and Powheg+Pythia 8 recalibrated to Powheg+Herwig 7 samples are given in Fig. 8.1. Some residual difference between the Powheg+Pythia 8 recalibrated and Powheg+Herwig 7 is still left, because we are correcting only the jet energies, but the difference internal jet substructure, which comes from the different parton shower models used in Pythia 8 and Herwig 7, remains.

8.4 Top quark mass measurements using recalibrated samples

In order to check the impact of the jet recalibration on the hadronisation uncertainty of the top quark mass measurement, we perform a top quark mass extraction from Powheg+Herwig 7, Powheg+Pythia 8 and the recalibrated Powheg+Pythia 8 samples using a template method (see Section 4.3).

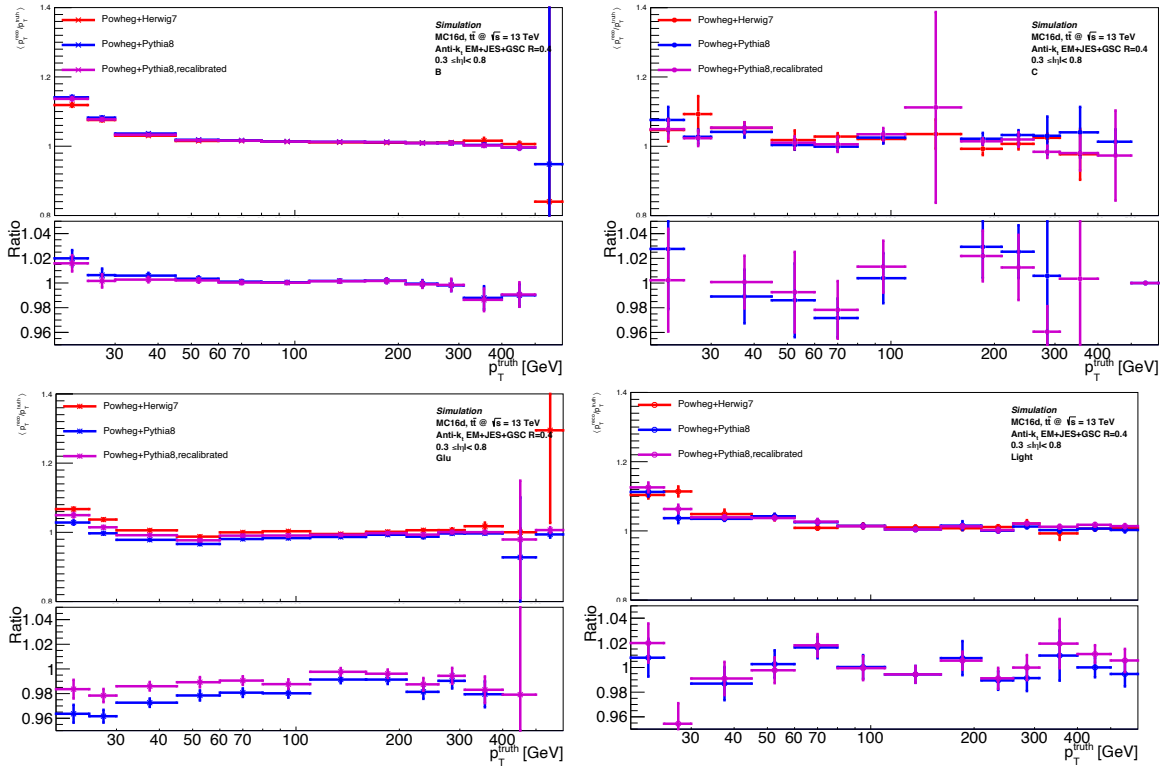

Figure 8.1: The calorimeter responses of jets in POWHEG+HERWIG 7 (red), POWHEG+PYTHIA 8 (blue) and POWHEG+PYTHIA 8 recalibrated to POWHEG+HERWIG 7 (magenta) samples. The bottom pad shows the ratios of the jet responses w.r.t. those from the POWHEG+HERWIG 7 sample.

8.4.1 Template fit

In this study, the templates are built using M_{lb} distributions using the POWHEG+PYTHIA 8 samples with a number of discrete values of m_t, which were mentioned in Section 8.1. We fit the templates using a sum of two gaussian distributions. We show in Fig. 8.2 the fitted templates for some of the m_t values. The binning of the histograms used for the templates is chosen to be 1 GeV since it gives a χ^2 value closer to unity and smaller values of the fitting parameter uncertainties than the other binning steps that were tested.

This fit function has five parameters in total: the mean values and the standard deviations of the two gaussians and the fraction of the second gaussian. The dependence of these parameters as a function of m_t, together with the corresponding linear fits versus m_t are shown in Fig. 8.3 for the electron channel (i.e. when we consider the M_{eb} distribution) and in Fig. 8.4 for the muon channel ($M_{\mu b}$). Large errors are observed for the parameters which are not sensitive to the top quark mass (i.e. all except of the mean of the first gaussian), which result in low χ^2 of the respective linear fits. This may be connected to the fact that the M_{lb} fitting range is not large enough to constrain those errors. However, when expending the fitting range, the M_{lb} distribution starts to deviate from the fitting function in the "tails" of the distribution, which results in high χ^2 values of the M_{lb} fit.

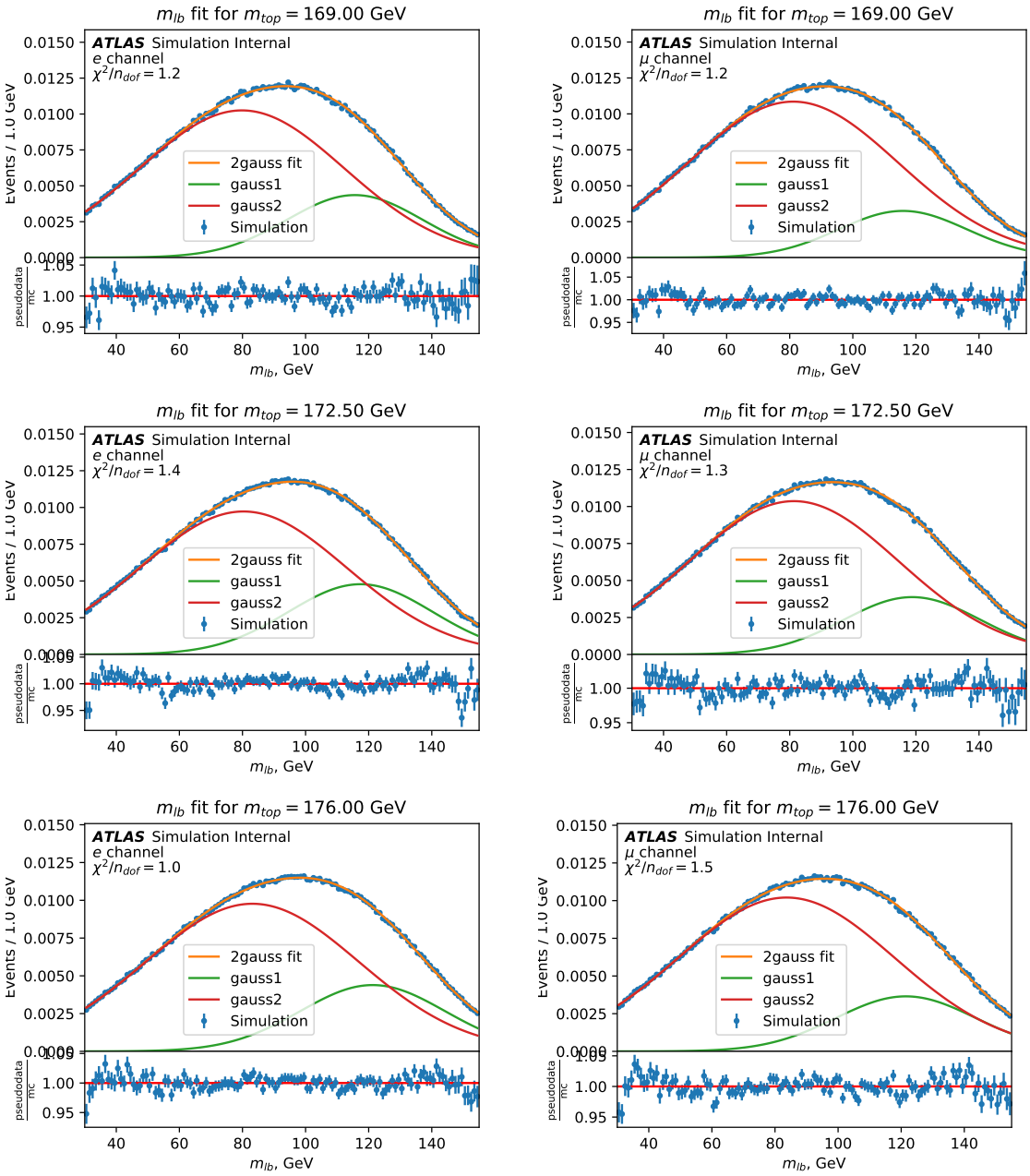

Figure 8.2: The M_{eb} (left) and $M_{\mu b}$ (right) template fits for $m_t = 169.0, 172.5$ and 175.0 GeV (from top to bottom).

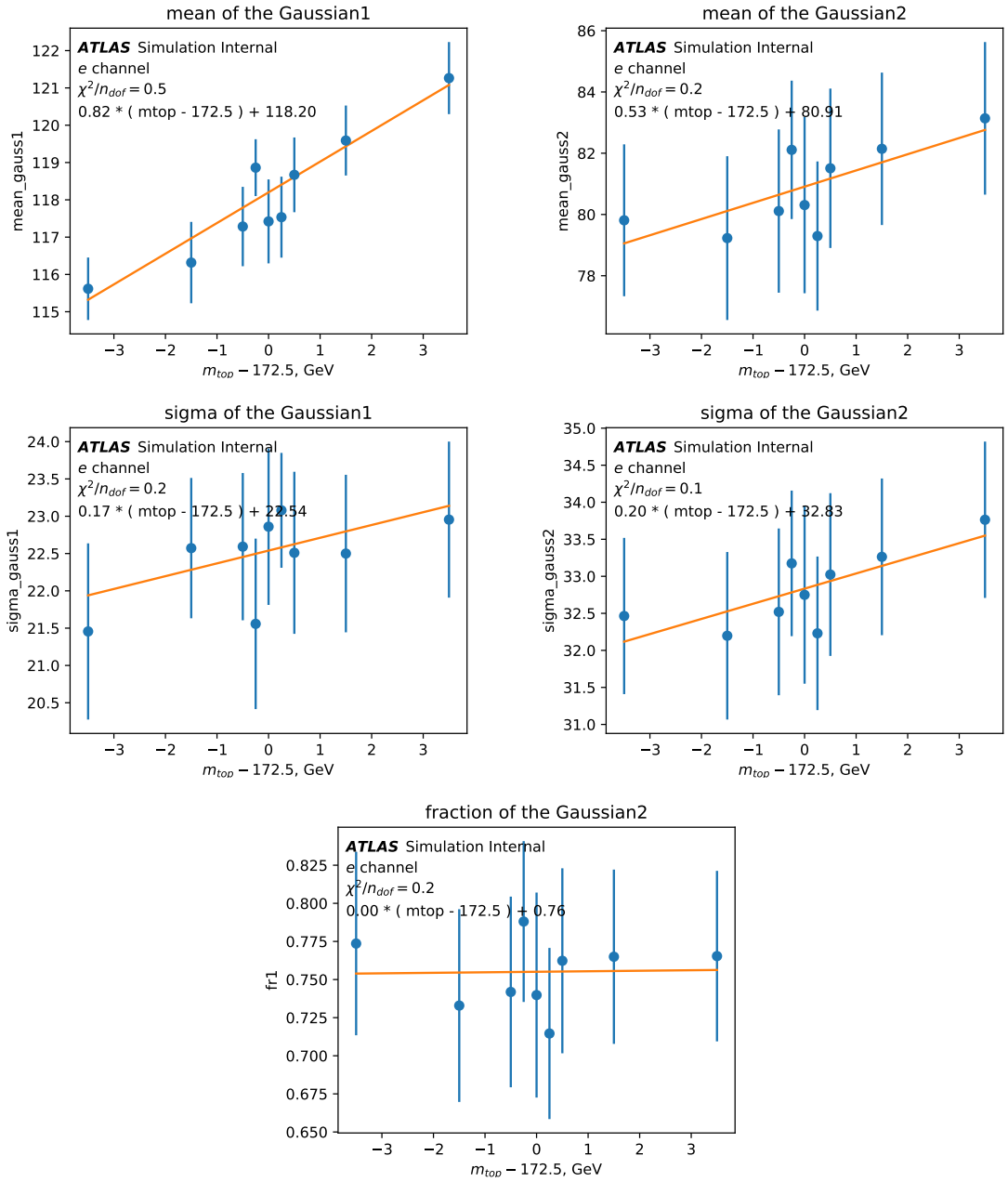

Figure 8.3: The m_t dependence of the M_{eb} template fit parameters and the linear fits of these dependencies. The formula for the fit function is written on each plot.

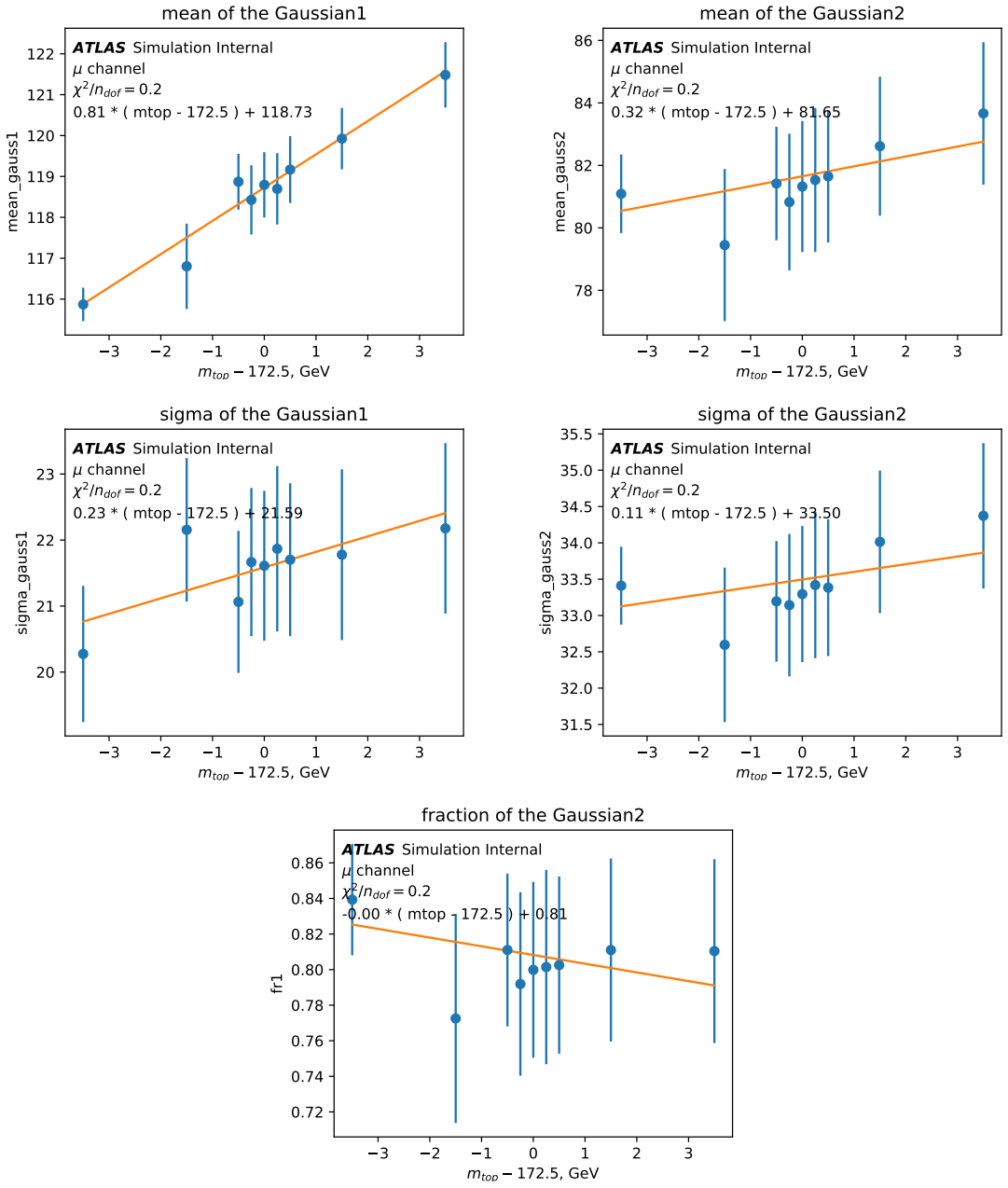

Figure 8.4: The m_t dependence of the $M_{\mu b}$ template fit parameters and the linear fits of these dependencies. The formula for the fit function is written on each plot.

It is clear from the figures that the mean of the first Gaussian is the most sensitive parameter to the m_t since the slope of its distribution is the steepest one.

Mass extraction

The top quark mass is extracted using an unbinned likelihood fit (implemented in the `RooFit` library [267]) to the MC sample for all events, $i = 1, \ldots, N$. The likelihood function maximised is:

$$\mathcal{L}(m_t) = \prod_{i=1}^{N} \left[(1 - f) \cdot P_{\text{gauss1}}(M_{lb}^{i} | m_t) + f \cdot P_{\text{gauss2}}(M_{lb}^{i}) \right], \tag{8.3}$$

where P_{gauss1} and P_{gauss2} are the probability density functions for the two gaussians used in the template fit and f is the fraction of the second gaussian in the template fit. The probability density functions are the normalised gaussian distributions used in the M_{lb} fit.

8.4.2 Closure test

In order to test the mass extraction procedure we perform a closure test: we extract the mass from all the POWHEG+PYTHIA 8 samples that we use to build the templates. In Fig. 8.5 we show the difference between the extracted m_t and the input m_t of the MC sample for different input m_t. Also, we fit the distribution of the differences with a zero-degree polynomial: for a perfect closure the fitted value has to be zero. We observe a perfect closure for the muon channel (mass extraction from the $M_{\mu b}$ distribution) and a slight non-closure ($\sim 1\sigma$) for the electron channel. The non-closure in the electron channel may be caused by some bias in the selection procedure. It needs to be further investigated. For example, we plan to compare various kinematic distributions and study if there are any MC/Data features between the electron and muon channels.

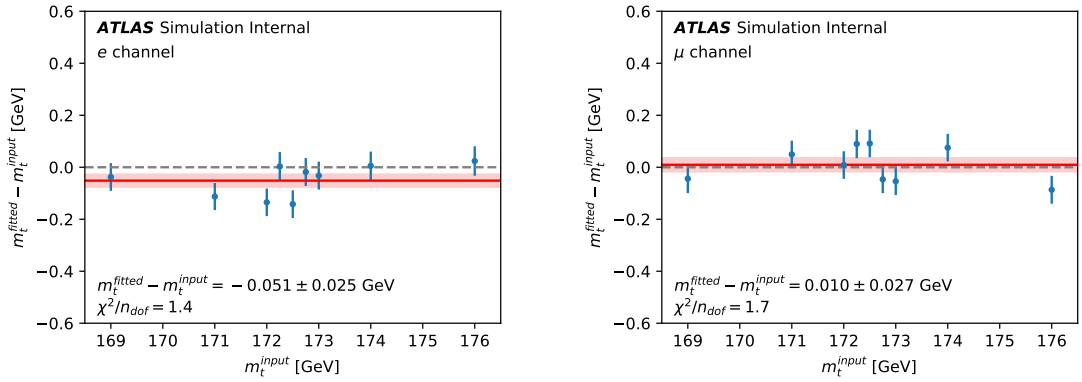

Figure 8.5: The closure test for the mass extraction from the M_{eb} (left) and the $M_{\mu b}$ (right) distributions.

8.5 Results and next steps

In Table 8.1 we present the results of the mass extraction from the POWHEG+HERWIG 7, POWHEG+PYTHIA 8 and the recalibrated POWHEG+PYTHIA 8 samples.

sample	m_t from M_{eb} (in GeV)	m_t from $M_{\mu b}$ (in GeV)
POWHEG+HERWIG 7	172.14 ± 0.05	172.29 ± 0.05
POWHEG+PYTHIA 8	172.36 ± 0.05	172.59 ± 0.05
POWHEG+PYTHIA 8 recalibrated	172.27 ± 0.05	172.51 ± 0.05

Table 8.1: m_t and its fit uncertainty (in GeV) extracted using the M_{eb} and $M_{\mu b}$ from different samples. The input top quark mass is m_t = 172.5 GeV in all samples. The m_t uncertainty in the table is the fit uncertainty.

We see that the recalibration indeed influences the extracted mass and reduces the hadronisation uncertainty, which is the difference between the masses extracted from the POWHEG+HERWIG 7 and POWHEG+PYTHIA 8 samples. The hadronisation uncertainty of the top quark mass extracted from the M_{eb} distribution decreases from 0.22 GeV to 0.13 GeV. For the mass extracted from the $M_{\mu b}$ distribution it decreases from 0.30 GeV to 0.22 GeV.

Several further steps in this analysis could be planned. First of all, the observed non-closure in the electron channel related either to the selection procedure or to some data/MC difference should be investigated. The statistical uncertainty of the calibration parameters would need to be taken into account and propagated through the mass extraction procedure. Also, the jet recalibration could be repeated using the parton level jet response instead of the particle level one and the change in the hadronisation uncertainty in this case could be compared with the particle level one. This test would show potential differences between the particle and parton level jet responses.

If the resulting effect of the recalibration on m_t is confirmed to be significant comparing to its uncertainty, it would need to be subtracted from the hadronisation uncertainty on m_t.

Conclusion

This thesis presents several analyses related to top quark mass measurements and to improvements of the systematics uncertainties in such measurements.

The first analysis is related to the top quark pole mass measurements. The top quark mass is extracted by comparing the measured single and double differential $t\bar{t}$ cross sections to the theoretical fixed order NNLO calculations. We used the results of the differential cross section measurement, which was done in the lepton+jets top quark decay channel and used the data set recorded by ATLAS in 2015–2016 at a centre-of-mass energy of $\sqrt{s}$ = 13 TeV, corresponding to an integrated luminosity of 36 fb^{-1}. The full mass extraction procedure has been developed and tested using the NLO+PS MC simulated pseudo-data samples. A preliminary estimate of the uncertainty breakdown has been performed. The total expected uncertainty of the top quark mass extracted from the double differential cross section as a function of the $t\bar{t}$ invariant mass and the p_{T} of the hadronic top quark is at the level of 600 MeV. The dominant uncertainties are related to the theoretical sources: the choice of the QCD scales, the PDF sets and the value of the strong coupling. The largest contribution to the experimental uncertainty comes from the jet-related systematic uncertainties.

The second study, described in this thesis, focuses on the variations of the parton shower parameters in Herwig 7.1.3 and their impact on the various $t\bar{t}$ and jet observables. The effect of these variations have been studied in order to explore the possibility to introduce a new definition for the parton shower uncertainty in top quark analyses, based solely on the Herwig 7 simulations. A possible recipe to assess the parton shower uncertainty is suggested for two cases, when the whole event generation is carried out by the Matchbox module of Herwig 7 and when Herwig 7 is used only to simulate the parton shower and the hadronisation effects. In the first case, the following variations need to be done: the veto scale variations, the renormalisation and factorisation scale variations, the comparison of the two NLO matching setups (MC@NLO versus Powheg) and finally, the comparison of the two shower types (angular-ordered versus dipole). In the second case, all the variations mentioned above, except the matching type variation, are relevant to the parton shower uncertainty. However, such definition of uncertainty cannot be easily introduced at the moment, mainly because many of the needed scale variations cannot be calculated using reweighting in the considered generator version Herwig 7.1.3.

The next analysis is related to the measurement of the observables sensitive to colour reconnection (CR). The aim of the analysis is to try to constrain or exclude some of the Pythia 8 CR models by comparing the distributions simulated using these models to data. The measurement is performed using $t\bar{t}$ events in dilepton top quark decay channel using 13 TeV data recorded by ATLAS in 2015-2018. We study the distributions of the two-dimensional observables built from the number of charged particle tracks and either the sum or the average of their transverse momenta. We use the Iterative Bayesian Unfolding technique to correct these distributions for detector effects and obtain the corresponding distributions at particle level. Preliminary comparison of the total uncertainty with the variations

due to the choice of different CR models hints at the possibility to constrain some CR models using several bins of the $N_{\text{trk}} \times \sum p_{\text{T}}$ distribution, in which the shift due to CR variation is larger than the total uncertainty.

The final analysis presented in this thesis concerns the possible improvement of the hadronisation uncertainty in the top quark mass measurements. We are estimating the jet energy scale (JES) effects present in the hadronisation uncertainty in its current definition, which is based on the comparison of Pythia 8 and Herwig 7 setups. This JES contribution has to be removed from the hadronisation uncertainty since it is already taken into account by the total JES uncertainty. To calculate this contribution, we perform recalibration of the jet energies using the ratio of jet responses in the Pythia 8 and Herwig 7 generators. After that, we perform a top quark mass extraction using a template method and compare, how the hadronisation uncertainty of the top quark mass changes after the recalibration. The estimated change in the uncertainty is of the order of 0.1 GeV, without taking into account the MC statistical uncertainty.

In the future, further improvements in the top quark mass measurements can be performed. Apart from removing the double counting in the hadronisation uncertainty and constraining the colour reconnection using more data, the top quark pole measurement from the double differential cross section can be improved using the full Run 2 dataset aiming at even more precision. The binning of the differential cross sections can be optimised in future analyses by using the m_t sensitivity information of different regions of $m^{t\bar{t}}$ and $p_{\text{T}}^{t,\text{had}}$, as it was suggested in the sensitivity study of the top quark pole mass measurement, described in this thesis. Together with the $m^{t\bar{t}}$ and $p_{\text{T}}^{t,\text{had}}$, other variables sensitive to m_t such as e.g. the rapidity of the $t\bar{t}$ system, can be used to build the differential cross section and then higher-dimensional differential cross section could be used for the mass extraction.

Résumé

La compréhension actuelle de la physique des particules est basée sur le modèle standard (MS), qui décrit toutes les particules élémentaires et toutes leurs interactions, à l'exception de la gravité. Les prédictions du MS ont été confirmées avec succès dans de nombreuses expériences à haute énergie. La vérification récente et la plus célèbre du MS est l'observation du boson de Higgs par les expériences ATLAS et CMS au grand collisionneur de hadrons (Large Hadron Collider, LHC) du CERN en 2012.

Les paramètres du modèle standard sont mesurés en analysant les données de collision collectées aux collisionneurs, tels que le LHC. Cette thèse présente plusieurs analyses de données effectuées dans ATLAS, l'une des deux plus grandes expériences du LHC. Les analyses presentées concernent la mesure de la masse du quark top et des études visant à réduire l'incertitude sur ces mesures. Au LHC, qui est un collisionneur proton-proton, les paires de quarks top sont principalement produites par fusion de gluons. Les diagrammes de Feynman correspondants sont montrés Fig. 8.6.

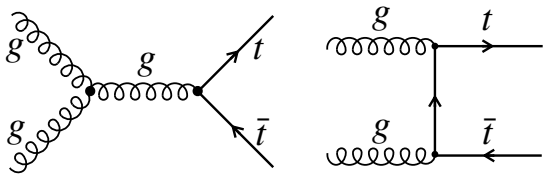

(a) gluon fusion, s-channel (b) gluon fusion, t-channel

Figure 8.6: Diagrammes de Feynman de la production $t\bar{t}$ au LHC.

Le quark top, qui est la particule élémentaire la plus lourde du MS, y occupe une place particulière. Ayant le plus grand couplage au boson de Higgs, le quark top induit l'une des principales contributions dans de nombreux calculs perturbatifs. Par exemple, le quark top contribue largement aux corrections de boucle d'autocouplage de Higgs, qui déterminent la stabilité du vide et permettent d'estimer la durée de vie de l'Univers. De plus, la masse du quark top apparaît dans les tests de cohérence de la théorie électrofaible, avec l'estimation de la masse du boson W et du boson de Higgs. Pour toutes ces raisons, une détermination précise de la masse du quark top est importante.

Les méthodes "indirectes" de mesure de la masse du quark top, qui permettent de mesurer la masse $\overline{\text{MS}}$ ou la masse au pôle du quark top théoriquement bien défini, donnaient jusqu'à récemment une incertitude beaucoup plus grande (1-1,5%) que le méthodes "directes" (0,5%), dans lesquelles la masse du quark top ou une observable sensible à celle-ci est directement reconstruite. La grande incertitude dans les mesures indirectes est généralement liée aux incertitudes sur les prédictions théoriques, qui sont comparées aux sections efficaces totales ou différentielles $t\bar{t}$ mesurées. Actuellement, des calculs

théoriques de plus en plus précis deviennent disponibles, en particulier pour les sections efficaces différentielles $t\bar{t}$, permettant d'améliorer l'incertitude sur la mesure de la masse du quark top dans les méthodes indirectes et de la rendre comparable à l'incertitude donnée par les méthodes directes.

Mesures de la masse au pôle du quark top

La première partie de cette thèse présente la détermination de la masse au pôle du quark top à partir de sections efficaces $t\bar{t}$ doublement différentielles mesurées dans le canal lepton+jets à $\sqrt{s}$ = 13 TeV avec le détecteur ATLAS. La masse du quark top est déterminée en comparant les sections efficaces $t\bar{t}$ différentielles mesurées avec les calculs théoriques au troisième ordre dominant (NNLO). Nous considérons la section efficace $t\bar{t}$ en fonction de la masse invariante du système $t\bar{t}$ et de l'impulsion transverse (p_{T}) du quark top, qui se désintègre en hadrons. Nous utilisons les résultats de la mesure de section efficaces différentielles, qui sont effectué dans le canal de désintégration du quark top lepton+jets. L'ensemble des données enregistré par ATLAS en 2015-2016 à une énergie du centre de masse de $\sqrt{s}$ = 13 TeV, est utilisée correspondant à une luminosité intégrée de 36 fb^{-1}.

La procédure d'extraction de masse complète a été développée et testée à l'aide des échantillons Monte Carlo (MC) générés au second ordre dominant (NLO). La masse du quark top est extraite comme la valeur qui minimise un χ^2 construit en utilisant les prédictions théoriques, les distributions différentielles mesurées et la matrice de covariance contenant toutes les incertitudes statistiques, systématiques et théoriques (sauf l'incertitude d'échelle). L'incertitude liée aux échelles de renormalisation et factorisation est calculée séparément en effectuant l'extraction de masse pour différentes combinaisons d'échelles différentes et en prenant ensuite une enveloppe de valeurs de masse extraites.

Nous avons réalisé plusieurs études supplémentaires visant à optimiser l'analyse. Une étude d'optimisation des intervales des distributions basée sur la sensibilité à la masse du quark top des variables considérées a été réalisée pour fournir des schémas de binning alternatifs possibles pour les sections efficaces différentielles. Une étude de la prise en compte de la largeur du quark top a été effectuée pour comparer les résultats d'extraction de masse obtenus à l'aide des prédictions NNLO, qui sont calculées dans l'approximation à largeur étroite, avec la masse du quark top extraite à l'aide des prédictions NNLO corrigées de la largeur. La correction de largeur utilisée dans le second cas est obtenue à partir de deux prédictions à l'ordre dominant, avec une largeur nominale et étroite du quark top, calculées à l'aide du générateur POWHEG-*ttdec*. Des tests de clôture et de linéarité ont été réalisés à l'aide d'échantillons MC afin de vérifier si la procédure entraîne un biais sur la masse extraite. Un biais dans la masse extraite dans le cas où la masse d'entrée de l'échantillon de pseudo-données ne coïncide pas avec la masse d'entrée de l'échantillon utilisé pour obtenir les corrections d'unfolding est observé. Deux solutions sont proposées pour prendre en compte ces effets. Une des solutions implique que la dépendance m_t est directement incluse dans l'étape de calcul du χ^2. Plus spécifiquement, pour chaque calcul de χ^2 à un certain point de masse, une hypothèse de masse du quark top cohérente est utilisée pour l'unfolding du vecteur des valeurs de section efficace différentielle mesurées.

L'estimation préliminaire des incertitudes sur la masse du quark top extraite de la section efficace doublement différentielle est résumée Table 8.2. L'incertitude totale attendue sur la masse du quark top extraite est au niveau de 600 MeV. Les incertitudes dominantes sont liées aux sources théoriques: choix des échelles QCD, incertitudes provenant des fonctions de distributions de partons et sur la

Source d'incertitude	δm_t (GeV)
Bruit de fond	+0.27 -0.21
b-tagging	+0.19 -0.10
Jets	+0.33 -0.29
Leptons	+0.09 -0.02
Impulsion transverse manquante	+0.03 -0.07
Fonctions de distribution de partons (PDF)	+0.12 -0.05
Générateur	+0.27 -0.20
Rayonnement dans l'état initial et final	+0.13 -0.13
Hadronisation	+0.01 -0.01
Incertitude systématique expérimentale totale	+0.47 -0.44
Incertitude statistique expérimentale totale	+0.04 -0.04
Incertitudes théoriques PDF et α_S	+0.30 -0.20
Incertitude théorique d'échelle	+0.12 -0.35
Incertitude totale	+0.59 -0.60

Table 8.2: Résumé des incertitudes statistiques et systématiques attendues sur la masse du quark top extraite d'un ajustement de $\frac{d^2\sigma}{dm^{t\bar{t}}\,dp_T^{t,\mathrm{had}}}$ aux prévisions NNLO. Les pseudo-données sont des événements simulés au NLO.

valeur du couplage fort. La plus grande contribution à l'incertitude expérimentale provient de l'erreur systématique liée aux jets.

La conclusion principale de cette analyse est l'estimation préliminaire de l'incertitude totale de la masse du quark top extraite, qui se traduit par une valeur < 1 GeV assez prometteuse. Comme étapes suivantes, nous prévoyons d'estimer l'incertitude sur la masse du quark top en utilisant le nouveau schéma d'extraction de la masse dans lequel la dépendance d'unfolding à m_t est prise en compte, puis de procéder à l'extraction de la masse du quark top à l'aide de données.

Etudes sur l'amélioration des incertitudes systématiques sur la masse du quark top

Comme les mesures de la masse du quark top deviennent plus précises, certaines des incertitudes systématiques en particulier liées à la modelisation du signal $t\bar{t}$, qui n'étaient pas dominantes auparavant, deviennent plus importantes. Par conséquent, des études dédiées doivent être effectuées afin d'améliorer la définition de ces incertitudes pour vérifier si les modèles de simulation actuels utilisés pour estimer ces incertitudes de modelisation décrivent assez bien les données les plus récentes ou s'ils doivent être contraints. Les trois prochains chapitres de cette thèse sont consacrés à l'amélioration de ces incertitudes systématiques.

Incertitudes sur la modélisation des gerbes partoniques dans Herwig 7 pour la production $t\bar{t}$

Une approche alternative pour définir les incertitudes sur les gerbes partoniques et l'hadronisation est discutée. Nous étudions les variations des paramètres de la gerbe partonique dans Herwig 7.1.3 et leur impact sur les différent observables reliées au système $t\bar{t}$ et aux jets. L'effet de ces variations a été

étudié afin d'explorer la possibilité d'introduire une nouvelle définition de l'incertitude sur les gerbes partoniques dans les analyses liées au quark top, basée uniquement sur les simulations HERWIG 7.

Une procedure possible pour évaluer l'incertitude sur les gerbes partoniques est suggérée pour deux cas, lorsque la génération entière de l'événement est effectuée par le module MATCHBOX de HERWIG 7 et lorsque HERWIG 7 est utilisé uniquement pour simuler les gerbes partoniques et les effets d'hadronisation. Dans le premier cas, les variations suivantes doivent être effectuées: variations d'échelle de veto, variations d'échelle de renormalisation et de factorisation, comparaison de deux configurations d'appariement ou *matching* (MC@NLO contre Powheg) et enfin, comparaison entre deux types de gerbe partonique (ordonné angulairement ou dipôle). Dans le deuxième cas, toutes les variations mentionnées ci-dessus, à l'exception de la variation de type de matching, sont pertinentes pour l'incertitude sur les gerbes partoniques. Nous avons étudié également l'impact des variations des paramètres de la gerbe partonique mentionnés ci-dessus sur la masse et autres observables du système $t\bar{t}$, ainsi que sur des variables liées aux jets.

Une telle définition de l'incertitude ne peut pas être facilement introduite pour le moment, principalement parce que bon nombre de variations d'échelle nécessaires ne peuvent pas être calculées en utilisant la repondération dans la version de générateur considérée HERWIG 7.1.3.

Mesures des observables sensibles à la reconnexion de couleur dans les événements $t\bar{t}$

Cette analyse vise à améliorer l'incertitude sur la reconnection de couleur (RC) dans les mesures de masse du quark top en contraignant certains des modèles de RC dans le générateur MC PYTHIA 8 en utilisant les événements $t\bar{t}$ dans le canal dileptonique. L'ensemble des données du Run 2 du LHC, collectées en 2015-2018 et correspondant à une luminosité totale intégrée de 139 fb^{-1} à $\sqrt{s}$ = 13 TeV, est utilisé. Nous considérons trois modèles de RC fournis dans PYTHIA 8: MPI, QCD et "gluon-move".

Les observables principales qui dépendent le plus du choix du modèle de RC sont liées au nombre de particules chargées dans l'événement et à leurs impulsions transverses. En particulier, nous avons étudé les distributions bidimensionnelles construites à partir du nombre de traces de particules chargées et soit de la somme, soit de la moyenne de leurs impulsions transverses.

Nous utilisons la technique dite d'unfolding bayésien itératif pour corriger ces distributions des effets du détecteur et obtenir les distributions corrigées au niveau particule. Plusieurs tests de la procédure d'unfolding ont été réalisés. La cohérence de l'unfolding a été vérifiée dans un test de clôture, dans lequel l'unfolding de l'échantillon simulé est fait en utilisant des corrections de dépliage obtenues à partir du même échantillon. Les résultats des "stress tests", dans lesquels la distribution est repondérée, puis l'unfolding est exécuté avec des corrections nominales, ont montré que l'unfolding n'est pas biaisé. Ensuite, les résultats de "pull test" ont prouvé que la procédure de l'unfolding est capable de mesurer correctement des données, qui fluctuent autour de leurs valeurs nominales.

Nous avons réalisé une estimation préliminaire des incertitudes systématiques. L'incertitude systématique dominante est liée à la modélisation de l'élément de matrice et elle est estimée en comparant deux configurations, dans lesquelles le générateur soit MC@NLO soit POWHEG est utilisé. L'incertitude systématique expérimentale dominante est liée à la modélisation de la composition en saveur des jets (*jet flavour composition*). Enfin, nous avons comparé les valeurs préliminaires de l'incertitude

systématique totale à la variation relative de la distribution due au changement de modèle de RC pour la distribution $N_{\text{trk}} \times \sum p_{\text{T}}$, voir Fig. 8.7. Nous observons que dans certains bins la variation de RC est plus grande que l'incertitude totale, ce qui peut aider à contraindre certains des modèles de RC.

Les prochaines étapes de cette analyse comprendront l'estimation de l'incertitude liée à l'estimation de bruit de fond des traces pour les observables 2D, puis la réexécution de l'analyse à l'aide de données.

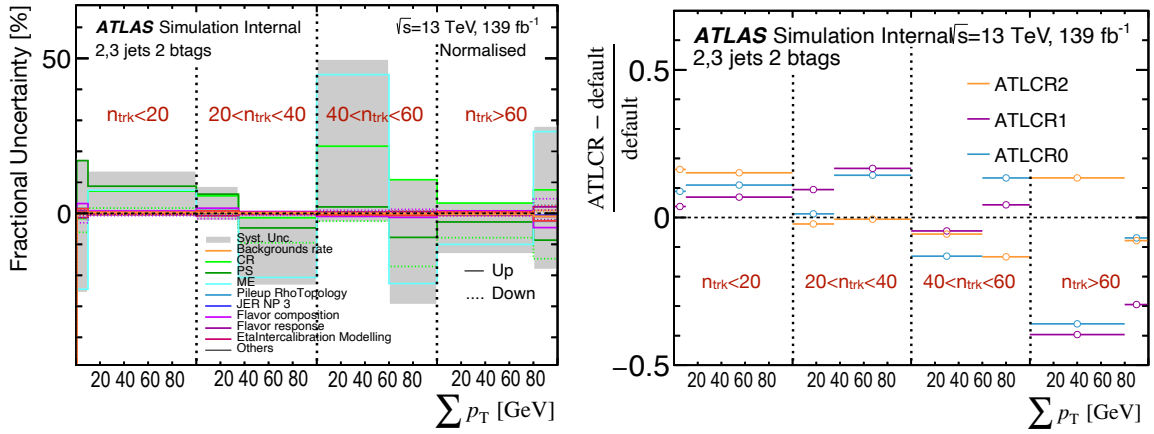

Figure 8.7: Incertitude systématique totale relative (à gauche) et différences relatives entre les distributions unfoldées obtenues à partir des échantillons avec des modèles de RC alternatifs et échantillon nominal POWHEG+PYTHIA 8 (à droite) pour $N_{\text{trk}} \times \sum p_{\text{T}}$ observable.

Incertitude sur l'hadronisation dans les mesures de masse du quark top

La dernière analyse incluse dans cette thèse vise à améliorer l'incertitude liée à l'hadronisation dans les mesures de la masse du quark top. Nous avons estimé les effets d'échelle de l'énergie des jets au sein de l'incertitude liée à l'hadronisation dans sa définition actuelle, qui est basée sur la comparaison des configurations PYTHIA 8 et HERWIG 7. Cette contribution d'échelle d'énergie des jets doit être soustraite de l'incertitude d'hadronisation car elle est déjà prise en compte dans l'incertitude sur l'échelle totale d'énergie des jets.

La méthode de base utilisée dans cette étude est le recalibrage du réponse en énergie des jets, qui est définie par rapport à un certain générateur MC, pour correspondre au réponse en énergie dans un autre générateur MC.

Nous effectuons un recalibrage de l'énergies des jets en utilisant le rapport des réponses énergétiques des jets au niveau particule dans les générateurs PYTHIA 8 et HERWIG 7. La réponse en énergie des jets au niveau des particules est la moyenne du rapport de l'impulsions transversales du jet aux niveau reconstruit et au niveau particule, qui est ajusté avec une fonction gaussienne. Les fonctions de recalibrage sont obtenues pour chaque "saveur" de jet (b-jet, c-jet, jet provenant d'un quark léger ou jet de gluon) séparément. Par exemple, la réponse calorimétrique des jets de gluon dans les échantillons POWHEG+HERWIG 7, POWHEG+PYTHIA 8 et POWHEG+PYTHIA 8 recalibré au POWHEG+HERWIG 7 sont présentés Fig. 8.8.

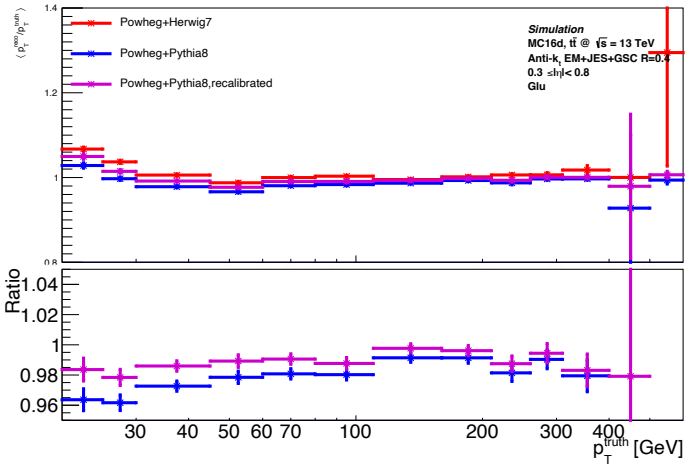

Figure 8.8: Réponses calorimétriques des jets de gluon dans les échantillons POWHEG+HERWIG 7 (rouge), POWHEG+PYTHIA 8 (bleu) et POWHEG+PYTHIA 8 recalibré au POWHEG+HERWIG 7 (magenta). Le pavé inférieur montre les rapports des réponses des jets par rapport à ceux de l'échantillon POWHEG+HERWIG 7.

Pour voir s'il y a un effet dû au recalibrage, nous extrayons la masse du quark top (m_t) des échantillons d'origine et recalibrés en utilisant une méthode des templates. Nous utilisons la distribution de la masse invariante du lepton et du jet de quark b pour construire les templates correspondant à différentes masses du quark top. Chaque template correspond à la somme des deux distributions gausssiennes. Chaque paramètre qui depend de la masse du quark top est ajusté à l'aide d'une fonction linéaire. En utilisant ce paramétrage, nous extrayons m_t avec un ajustement de vraisemblance ("unbinned likelihood fit").

Pour vérifier les performances de la méthode d'extraction de masse, nous effectuons un test de clôture dans lequel nous extrayons la valeur de m_t de tous les échantillons utilisés pour construire les templates, puis examinons la différence entre la masse d'entrée et la masse extraite. On obtient une clôture parfaite dans le canal muon et une légère bias dans le canal électron, qui est actuellement encore à l'étude.

Les résultats de la mesure de la masse du quark top dans les échantillons POWHEG+HERWIG 7, POWHEG+PYTHIA 8 et POWHEG+PYTHIA 8 recalibré sont donnés Table 8.3.

échantillon	canal électron (en GeV)	canal muon (en GeV)
POWHEG+HERWIG 7	172.14 ± 0.05	172.29 ± 0.05
POWHEG+PYTHIA 8	172.36 ± 0.05	172.59 ± 0.05
POWHEG+PYTHIA 8 recalibré	172.27 ± 0.05	172.51 ± 0.05

Table 8.3: Mesure de la masse du quark top et son incertitude liée à l'ajustement (en GeV) extraits dans les canaux électron et muon pour des échantillons différents. La masse du quark top en entrée est $m_t = 172,5$ GeV dans tous les échantillons.

Dans les deux canaux, nous observons une réduction de 0,1 GeV de l'incertitude d'hadronisation après le recalibrage.

Dans une prochaine étape, nous prévoyons de prendre en compte l'incertitude statistique Monte-Carlo des coefficients de calibrage et de répéter le recalibrage en utilisant la réponse des jets au niveau partonique. La différence entre les résultats obtenus en utilisant la réponse au niveau particule et au niveau parton nous aidera à mieux comprendre comment l'hadronisation et les effets d'événements sous-jacents diffèrent dans les modèles d'hadronisation de HERWIG et PYTHIA.

Bibliography

[1] S. L. Glashow, *Partial-symmetries of weak interactions*, Nuclear Physics **22** (1961) 579 , ISSN: 0029-5582, URL: http://www.sciencedirect.com/science/article/pii/0029558261904692.

[2] A. Salam and J. Ward, *Electromagnetic and weak interactions*, Physics Letters **13** (1964) 168 , ISSN: 0031-9163, URL: http://www.sciencedirect.com/science/article/pii/0031916364907115.

[3] G. Aad et al., *Observation of a new particle in the search for the Standard Model Higgs boson with the ATLAS detector at the LHC*, Phys. Lett. **B716** (2012) 1, arXiv: 1207.7214 [hep-ex].

[4] S. Chatrchyan et al., *Observation of a New Boson at a Mass of 125 GeV with the CMS Experiment at the LHC*, Phys. Lett. **B716** (2012) 30, arXiv: 1207.7235 [hep-ex].

[5] M. E. Peskin and D. V. Schroeder, *An Introduction to quantum field theory*, Addison-Wesley, 1995, ISBN: 9780201503975, 0201503972, URL: http://www.slac.stanford.edu/~mpeskin/QFT.html.

[6] C. P. Burgess and G. D. Moore, *The standard model: A primer*, Cambridge University Press, 2006, ISBN: 9780511254857, 9781107404267, 9780521860369.

[7] M. Tanabashi et al., *Review of Particle Physics*, Phys. Rev. **D98** (2018) 030001.

[8] D. H. Perkins, *Introduction to high energy physics*, 1982, ISBN: 9780521621960.

[9] P. W. Higgs, *Broken Symmetries and the Masses of Gauge Bosons*, Phys. Rev. Lett. **13** (16 1964) 508, URL: https://link.aps.org/doi/10.1103/PhysRevLett.13.508.

[10] F. Englert and R. Brout, *Broken Symmetry and the Mass of Gauge Vector Mesons*, Phys. Rev. Lett. **13** (9 1964) 321, URL: https://link.aps.org/doi/10.1103/PhysRevLett.13.321.

[11] G. S. Guralnik, C. R. Hagen and T. W. B. Kibble, *Global Conservation Laws and Massless Particles*, Phys. Rev. Lett. **13** (20 1964) 585, URL: https://link.aps.org/doi/10.1103/PhysRevLett.13.585.

[12] M. Gell-Mann, *A Schematic Model of Baryons and Mesons*, Phys. Lett. **8** (1964) 214.

[13] G. Zweig, *An SU_3 model for strong interaction symmetry and its breaking; Version 1*, tech. rep. CERN-TH-401, CERN, 1964, URL: https://cds.cern.ch/record/352337.

[14] G. Zweig, *An SU_3 model for strong interaction symmetry and its breaking; Version 2*, (1964) 80 p, Version 1 is CERN preprint 8182/TH.401, Jan. 17, 1964, URL: https://cds.cern.ch/record/570209.

[15] S. Glashow, J. Iliopoulos and L. Maiani, *Weak Interactions with Lepton-Hadron Symmetry*, Phys. Rev. D **2** (1970) 1285.

[16] J. Augustin et al., *Discovery of a Narrow Resonance in e^+e^- Annihilation*, Phys. Rev. Lett. **33** (1974) 1406.

[17] J. Aubert et al., *Experimental Observation of a Heavy Particle J*, Phys. Rev. Lett. **33** (1974) 1404.

[18] M. Kobayashi and T. Maskawa, *CP Violation in the Renormalizable Theory of Weak Interaction*, Prog. Theor. Phys. **49** (1973) 652.

[19] S. W. Herb et al., *Observation of a Dimuon Resonance at 9.5-GeV in 400-GeV Proton-Nucleus Collisions*, Phys. Rev. Lett. **39** (1977) 252.

[20] F. Abe et al., *Observation of top quark production in $\bar{p}p$ collisions*, Phys. Rev. Lett. **74** (1995) 2626, arXiv: hep-ex/9503002 [hep-ex].

[21] S. Abachi et al., *Observation of the top quark*, Phys. Rev. Lett. **74** (1995) 2632, arXiv: hep-ex/9503003 [hep-ex].

[22] R. Brandelik et al., *Evidence for Planar Events in e+ e- Annihilation at High-Energies*, Phys. Lett. B **86** (1979) 243.

[23] H. Fritzsch, M. Gell-Mann and H. Leutwyler, *Advantages of the Color Octet Gluon Picture*, Phys. Lett. B **47** (1973) 365.

[24] G. Arnison et al., *Experimental Observation of Isolated Large Transverse Energy Electrons with Associated Missing Energy at s**(1/2) = 540-GeV*, Phys. Lett. B **122** (1983) 103.

[25] G. Arnison et al., *Experimental Observation of Lepton Pairs of Invariant Mass Around 95-GeV/c**2 at the CERN SPS Collider*, Phys. Lett. B **126** (1983) 398.

[26] M. Banner et al., *Observation of Single Isolated Electrons of High Transverse Momentum in Events with Missing Transverse Energy at the CERN anti-p p Collider*, Phys. Lett. B **122** (1983) 476.

[27] P. Bagnaia et al., *Evidence for $Z^0 \to e^+e^-$ at the CERN $\bar{p}p$ Collider*, Phys. Lett. B **129** (1983) 130.

[28] N. Cabibbo, *Unitary Symmetry and Leptonic Decays*, Phys. Rev. Lett. **10** (1963) 531.

[29] Y. Fukuda et al., *Evidence for oscillation of atmospheric neutrinos*, Phys. Rev. Lett. **81** (1998) 1562, arXiv: hep-ex/9807003.

[30] Q. Ahmad et al., *Direct evidence for neutrino flavor transformation from neutral current interactions in the Sudbury Neutrino Observatory*, Phys. Rev. Lett. **89** (2002) 011301, arXiv: nucl-ex/0204008.

[31] K. Eguchi et al.,
First results from KamLAND: Evidence for reactor anti-neutrino disappearance,
Phys. Rev. Lett. **90** (2003) 021802, arXiv: hep-ex/0212021.

[32] B. Pontecorvo, *Neutrino Experiments and the Problem of Conservation of Leptonic Charge*,
Sov. Phys. JETP **26** (1968) 984.

[33] Z. Maki, M. Nakagawa and S. Sakata, *Remarks on the unified model of elementary particles*,
Prog. Theor. Phys. **28** (1962) 870.

[34] J. Ellis, 'Higgs Physics', *2013 European School of High-Energy Physics*, 2015 117,
arXiv: 1312.5672 [hep-ph].

[35] A. Buckley et al., *General-purpose event generators for LHC physics*,
Phys. Rept. **504** (2011) 145, arXiv: 1101.2599 [hep-ph].

[36] G. Altarelli and G. Parisi, *Asymptotic Freedom in Parton Language*,
Nucl. Phys. **B126** (1977) 298.

[37] Y. L. Dokshitzer, *Calculation of the Structure Functions for Deep Inelastic Scattering and e+ e- Annihilation by Perturbation Theory in Quantum Chromodynamics.*,
Sov. Phys. JETP **46** (1977) 641, [Zh. Eksp. Teor. Fiz.73,1216(1977)].

[38] V. N. Gribov and L. N. Lipatov, *Deep inelastic e p scattering in perturbation theory*,
Sov. J. Nucl. Phys. **15** (1972) 438, [Yad. Fiz.15,781(1972)].

[39] S. Alekhin, J. Blumlein, S. Klein and S. Moch, *The 3, 4, and 5-flavor NNLO Parton from Deep-Inelastic-Scattering Data and at Hadron Colliders*, Phys. Rev. **D81** (2010) 014032,
arXiv: 0908.2766 [hep-ph].

[40] P. M. Nadolsky et al., *Implications of CTEQ global analysis for collider observables*,
Phys. Rev. **D78** (2008) 013004, arXiv: 0802.0007 [hep-ph].

[41] M. Gluck, P. Jimenez-Delgado and E. Reya,
Dynamical parton distributions of the nucleon and very small-x physics,
Eur. Phys. J. **C53** (2008) 355, arXiv: 0709.0614 [hep-ph].

[42] F. D. Aaron et al., *Combined Measurement and QCD Analysis of the Inclusive e+- p Scattering Cross Sections at HERA*, JHEP **01** (2010) 109, arXiv: 0911.0884 [hep-ex].

[43] A. D. Martin, W. J. Stirling, R. S. Thorne and G. Watt, *Parton distributions for the LHC*,
Eur. Phys. J. **C63** (2009) 189, arXiv: 0901.0002 [hep-ph].

[44] R. D. Ball et al.,
A first unbiased global NLO determination of parton distributions and their uncertainties,
Nucl. Phys. **B838** (2010) 136, arXiv: 1002.4407 [hep-ph].

[45] M. R. Whalley, D. Bourilkov and R. C. Group,
'The Les Houches accord PDFs (LHAPDF) and LHAGLUE', *HERA and the LHC: A Workshop on the implications of HERA for LHC physics. Proceedings, Part B*, 2005 575,
arXiv: hep-ph/0508110 [hep-ph].

[46] R. K. Ellis, W. J. Stirling and B. R. Webber, *QCD and collider physics*,
Camb. Monogr. Part. Phys. Nucl. Phys. Cosmol. **8** (1996) 1.

[47] G. Marchesini and B. R. Webber, *Simulation of QCD Jets Including Soft Gluon Interference*, Nucl. Phys. **B238** (1984) 1.

[48] S. Catani, B. R. Webber and G. Marchesini, *QCD coherent branching and semiinclusive processes at large x*, Nucl. Phys. **B349** (1991) 635.

[49] S. Catani, Y. L. Dokshitzer, M. Olsson, G. Turnock and B. R. Webber, *New clustering algorithm for multi - jet cross-sections in e+ e- annihilation*, Phys. Lett. **B269** (1991) 432.

[50] S. Catani, S. Dittmaier and Z. Trocsanyi, *One loop singular behavior of QCD and SUSY QCD amplitudes with massive partons*, Phys. Lett. **B500** (2001) 149, arXiv: hep-ph/0011222 [hep-ph].

[51] M. Cacciari and S. Catani, *Soft gluon resummation for the fragmentation of light and heavy quarks at large x*, Nucl. Phys. **B617** (2001) 253, arXiv: hep-ph/0107138 [hep-ph].

[52] S. Platzer and S. Gieseke, *Coherent Parton Showers with Local Recoils*, JHEP **01** (2011) 024, arXiv: 0909.5593 [hep-ph].

[53] S. Catani and M. H. Seymour, *A General algorithm for calculating jet cross-sections in NLO QCD*, Nucl. Phys. **B485** (1997) 291, [Erratum: Nucl. Phys.B510,503(1998)], arXiv: hep-ph/9605323 [hep-ph].

[54] M. Bengtsson and T. Sjostrand, *Coherent Parton Showers Versus Matrix Elements: Implications of PETRA - PEP Data*, Phys. Lett. **B185** (1987) 435.

[55] S. Frixione and B. R. Webber, *Matching NLO QCD computations and parton shower simulations*, JHEP **06** (2002) 029, arXiv: hep-ph/0204244 [hep-ph].

[56] S. Frixione, P. Nason and B. R. Webber, *Matching NLO QCD and parton showers in heavy flavor production*, JHEP **08** (2003) 007, arXiv: hep-ph/0305252 [hep-ph].

[57] S. Frixione, P. Nason and C. Oleari, *Matching NLO QCD computations with Parton Shower simulations: the POWHEG method*, JHEP **11** (2007) 070, arXiv: 0709.2092 [hep-ph].

[58] S. Catani, F. Krauss, R. Kuhn and B. Webber, *QCD matrix elements + parton showers*, JHEP **11** (2001) 063, arXiv: hep-ph/0109231.

[59] L. Lonnblad, *Correcting the color dipole cascade model with fixed order matrix elements*, JHEP **05** (2002) 046, arXiv: hep-ph/0112284.

[60] J. Alwall et al., *Comparative study of various algorithms for the merging of parton showers and matrix elements in hadronic collisions*, Eur. Phys. J. C **53** (2008) 473, arXiv: 0706.2569 [hep-ph].

[61] B. Andersson, G. Gustafson, G. Ingelman and T. Sjostrand, *Parton Fragmentation and String Dynamics*, Phys. Rept. **97** (1983) 31.

[62] B. Andersson, *The Lund model*, Camb. Monogr. Part. Phys. Nucl. Phys. Cosmol. **7** (1997) 1.

[63] B. R. Webber, *A QCD Model for Jet Fragmentation Including Soft Gluon Interference*, Nucl. Phys. **B238** (1984) 492.

[64] G. Marchesini and B. R. Webber, *Monte Carlo Simulation of General Hard Processes with Coherent QCD Radiation*, Nucl. Phys. **B310** (1988) 461.

[65] D. Amati and G. Veneziano, *Preconfinement as a Property of Perturbative QCD*, Phys. Lett. **83B** (1979) 87.

[66] T. Gleisberg et al., *Event generation with SHERPA 1.1*, JHEP **02** (2009) 007, arXiv: 0811.4622 [hep-ph].

[67] M. Cacciari, G. P. Salam and S. Sapeta, *On the characterisation of the underlying event*, JHEP **04** (2010) 065, arXiv: 0912.4926 [hep-ph].

[68] M. Bahr, S. Gieseke and M. H. Seymour, *Simulation of multiple partonic interactions in Herwig++*, JHEP **07** (2008) 076, arXiv: 0803.3633 [hep-ph].

[69] I. Borozan and M. H. Seymour, *An Eikonal model for multiparticle production in hadron hadron interactions*, JHEP **09** (2002) 015, arXiv: hep-ph/0207283 [hep-ph].

[70] T. Sjostrand and M. van Zijl, *A Multiple Interaction Model for the Event Structure in Hadron Collisions*, Phys. Rev. **D36** (1987) 2019.

[71] A. Buckley et al., *Rivet user manual*, Comput. Phys. Commun. **184** (2013) 2803, arXiv: 1003.0694 [hep-ph].

[72] T. Sjöstrand, 'Colour reconnection and its effects on precise measurements at the LHC', *Proceedings of the XLIII International Symposium on Multiparticle Dynamics (ISMD13)*, 2013, arXiv: 1310.8073 [hep-ph].

[73] G. Gustafson, U. Pettersson and P. M. Zerwas, *Jet Final States in W W Pair Production and Color Screening in the QCD Vacuum*, Phys. Lett. **B209** (1988) 90.

[74] T. Sjostrand and V. A. Khoze, *Does the W mass reconstruction survive QCD effects?*, Phys. Rev. Lett. **72** (1994) 28, arXiv: hep-ph/9310276 [hep-ph].

[75] T. Sjostrand and V. A. Khoze, *On Color rearrangement in hadronic W+ W- events*, Z. Phys. **C62** (1994) 281, arXiv: hep-ph/9310242 [hep-ph].

[76] G. Gustafson and J. Hakkinen, *Color interference and confinement effects in W pair production*, Z. Phys. **C64** (1994) 659.

[77] B. R. Webber, *Color reconnection and Bose-Einstein effects*, J. Phys. **G24** (1998) 287, arXiv: hep-ph/9708463 [hep-ph].

[78] W. Buchmuller and A. Hebecker, *A Parton model for diffractive processes in deep inelastic scattering*, Phys. Lett. **B355** (1995) 573, arXiv: hep-ph/9504374 [hep-ph].

[79] M. Sandhoff and P. Z. Skands, 'Colour annealing - a toy model of colour reconnections', *Physics at TeV colliders. Proceedings, Workshop, Les Houches, France, May 2-20, 2005*, 2005, URL: http://lss.fnal.gov/cgi-bin/find_paper.pl?conf-05-518-t.

[80] P. Z. Skands and D. Wicke, *Non-perturbative QCD effects and the top mass at the Tevatron*, Eur. Phys. J. **C52** (2007) 133, arXiv: hep-ph/0703081 [HEP-PH].

[81] P. Z. Skands, *Tuning Monte Carlo Generators: The Perugia Tunes*, Phys. Rev. **D82** (2010) 074018, arXiv: 1005.3457 [hep-ph].

[82] P. V. Landshoff and O. Nachtmann, *Vacuum Structure and Diffraction Scattering*, Z. Phys. **C35** (1987) 405.

[83] L. Evans and P. Bryant, *LHC Machine*, JINST **3** (2008) S08001.

[84] E. Mobs, *The CERN accelerator complex. Complexe des accélérateurs du CERN*, (2016), General Photo, URL: https://cds.cern.ch/record/2197559.

[85] A. Collaboration, *Luminosity public results for Run 2*, (status for 2019 year), URL: https://twiki.cern.ch/twiki/bin/view/AtlasPublic/LuminosityPublicResultsRun2.

[86] G. Aad et al., *The ATLAS Experiment at the CERN Large Hadron Collider*, JINST **3** (2008) S08003.

[87] J. Pequenao, 'Computer generated image of the whole ATLAS detector', 2008, URL: https://cds.cern.ch/record/1095924.

[88] *ATLAS inner detector: Technical Design Report, 1*, Technical Design Report ATLAS, CERN, 1997, URL: https://cds.cern.ch/record/331063.

[89] S Haywood, L Rossi, R Nickerson and A Romaniouk, *ATLAS inner detector: Technical Design Report, 2*, Technical Design Report ATLAS, CERN, 1997, URL: https://cds.cern.ch/record/331064.

[90] K. Potamianos, *The upgraded Pixel detector and the commissioning of the Inner Detector tracking of the ATLAS experiment for Run-2 at the Large Hadron Collider*, PoS **EPS-HEP2015** (2015) 261, arXiv: 1608.07850 [physics.ins-det].

[91] M Capeans et al., *ATLAS Insertable B-Layer Technical Design Report*, tech. rep. CERN-LHCC-2010-013. ATLAS-TDR-19, 2010, URL: https://cds.cern.ch/record/1291633.

[92] J. Pequenao, 'Computer Generated image of the ATLAS calorimeter', 2008, URL: https://cds.cern.ch/record/1095927.

[93] C. Fabjan and F. Gianotti, *Calorimetry for particle physics*, Rev. Mod. Phys. **75** (2003) 1243.

[94] *ATLAS muon spectrometer: Technical Design Report*, Technical Design Report ATLAS, CERN, 1997, URL: https://cds.cern.ch/record/331068.

[95] G. Avoni et al., *The new LUCID-2 detector for luminosity measurement and monitoring in ATLAS*, JINST **13** (2018) P07017.

[96] S van der Meer, *Calibration of the effective beam height in the ISR*, tech. rep. CERN-ISR-PO-68-31. ISR-PO-68-31, CERN, 1968, URL: https://cds.cern.ch/record/296752.

[97] M. Aaboud et al., *Performance of the ATLAS Trigger System in 2015*, Eur. Phys. J. **C77** (2017) 317, arXiv: 1611.09661 [hep-ex].

[98] S. Agostinelli et al., *GEANT4: A Simulation toolkit*, Nucl. Instrum. Meth. A **506** (2003) 250.

[99] C. ATLAS et al., *The simulation principle and performance of the ATLAS fast calorimeter simulation FastCaloSim*, tech. rep. ATL-PHYS-PUB-2010-013, CERN, 2010, URL: https://cds.cern.ch/record/1300517.

[100] M. Aaboud et al., *Performance of the ATLAS Track Reconstruction Algorithms in Dense Environments in LHC Run 2*, Eur. Phys. J. C **77** (2017) 673, arXiv: 1704.07983 [hep-ex].

[101] T. Cornelissen et al., *The new ATLAS track reconstruction (NEWT)*, J. Phys. Conf. Ser. **119** (2008) 032014, ed. by R. Sobie, R. Tafirout and J. Thomson.

[102] A. Rosenfeld and J. Pfaltz, *Pfalz, J.L.: Sequential Operations in Digital Picture Processing. Journal of the ACM 13(4), 471-494*, J. ACM **13** (1966) 471.

[103] G. Aad et al., *A neural network clustering algorithm for the ATLAS silicon pixel detector*, JINST **9** (2014) P09009, arXiv: 1406.7690 [hep-ex].

[104] G. Aad et al., *Expected Performance of the ATLAS Experiment - Detector, Trigger and Physics*, (2009), arXiv: 0901.0512 [hep-ex].

[105] R. Fruhwirth, *Application of Kalman filtering to track and vertex fitting*, Nucl. Instrum. Meth. A **262** (1987) 444.

[106] J. Illingworth and J. Kittler, *A survey of the hough transform*, Computer Vision, Graphics, and Image Processing **44** (1988) 87 , ISSN: 0734-189X, URL: http://www.sciencedirect.com/science/article/pii/S0734189X88800331.

[107] M. Aaboud et al., *Reconstruction of primary vertices at the ATLAS experiment in Run 1 proton–proton collisions at the LHC*, Eur. Phys. J. C **77** (2017) 332, arXiv: 1611.10235 [physics.ins-det].

[108] T. Robertson and J. D. Cryer, *An Iterative Procedure for Estimating the Mode*, Journal of the American Statistical Association **69** (1974) 1012, ISSN: 01621459, URL: http://www.jstor.org/stable/2286181.

[109] *Early Inner Detector Tracking Performance in the 2015 data at $\sqrt{s} = 13$ TeV*, tech. rep. ATL-PHYS-PUB-2015-051, CERN, 2015, URL: https://cds.cern.ch/record/2110140.

[110] *Vertex Reconstruction Performance of the ATLAS Detector at "$\sqrt{s} = 13$ TeV"*, tech. rep. ATL-PHYS-PUB-2015-026, CERN, 2015, URL: https://cds.cern.ch/record/2037717.

[111] W Lampl et al., *Calorimeter Clustering Algorithms: Description and Performance*, tech. rep. ATL-LARG-PUB-2008-002. ATL-COM-LARG-2008-003, CERN, 2008, URL: https://cds.cern.ch/record/1099735.

[112] M. Aaboud et al., *Jet reconstruction and performance using particle flow with the ATLAS Detector*, Eur. Phys. J. C **77** (2017) 466, arXiv: 1703.10485 [hep-ex].

[113] G. Aad et al.,
Topological cell clustering in the ATLAS calorimeters and its performance in LHC Run 1,
Eur. Phys. J. C **77** (2017) 490, arXiv: 1603.02934 [hep-ex].

[114] M. Aaboud et al., *Electron reconstruction and identification in the ATLAS experiment using the 2015 and 2016 LHC proton-proton collision data at $\sqrt{s} = 13$ TeV*,
Eur. Phys. J. C **79** (2019) 639, arXiv: 1902.04655 [physics.ins-det].

[115] *Electron and photon reconstruction and performance in ATLAS using a dynamical, topological cell clustering-based approach*, tech. rep. ATL-PHYS-PUB-2017-022, CERN, 2017, URL: https://cds.cern.ch/record/2298955.

[116] T. G. Cornelissen et al., *The global chi**2 track fitter in ATLAS*,
J. Phys. Conf. Ser. **119** (2008) 032013, ed. by R. Sobie, R. Tafirout and J. Thomson.

[117] M. Aaboud et al., *Electron efficiency measurements with the ATLAS detector using 2012 LHC proton–proton collision data*, Eur. Phys. J. C **77** (2017) 195, arXiv: 1612.01456 [hep-ex].

[118] *Improved electron reconstruction in ATLAS using the Gaussian Sum Filter-based model for bremsstrahlung*, tech. rep. ATLAS-CONF-2012-047, CERN, 2012,
URL: https://cds.cern.ch/record/1449796.

[119] G. Aad et al., *Muon reconstruction performance of the ATLAS detector in proton–proton collision data at $\sqrt{s}$ =13 TeV*, Eur. Phys. J. C **76** (2016) 292, arXiv: 1603.05598 [hep-ex].

[120] P. Mukhopadhyay and B. B. Chaudhuri, *A Survey of Hough Transform*,
Pattern Recogn. **48** (2015) 993–1010, ISSN: 0031-3203,
URL: https://doi.org/10.1016/j.patcog.2014.08.027.

[121] M. Cacciari, G. P. Salam and G. Soyez, *The anti-k_t jet clustering algorithm*,
JHEP **04** (2008) 063, arXiv: 0802.1189 [hep-ph].

[122] M. Cacciari, G. P. Salam and G. Soyez, *FastJet User Manual*, Eur. Phys. J. C **72** (2012) 1896, arXiv: 1111.6097 [hep-ph].

[123] M. Aaboud et al., *Jet energy scale measurements and their systematic uncertainties in proton-proton collisions at $\sqrt{s}$ = 13 TeV with the ATLAS detector*,
Phys. Rev. D **96** (2017) 072002, arXiv: 1703.09665 [hep-ex].

[124] M. Cacciari and G. P. Salam, *Pileup subtraction using jet areas*, Phys. Lett. B **659** (2008) 119, arXiv: 0707.1378 [hep-ph].

[125] *Pile-up subtraction and suppression for jets in ATLAS*, tech. rep. ATLAS-CONF-2013-083, CERN, 2013, URL: https://cds.cern.ch/record/1570994.

[126] G. Aad et al., *Performance of pile-up mitigation techniques for jets in pp collisions at $\sqrt{s}$ = 8 TeV using the ATLAS detector*, Eur. Phys. J. C **76** (2016) 581, arXiv: 1510.03823 [hep-ex].

[127] *Jet global sequential corrections with the ATLAS detector in proton-proton collisions at sqrt(s) = 8 TeV*, tech. rep. ATLAS-CONF-2015-002, CERN, 2015,
URL: https://cds.cern.ch/record/2001682.

[128] G. Aad et al.,
Jet energy measurement with the ATLAS detector in proton-proton collisions at $\sqrt{s}$ = 7 TeV,
Eur. Phys. J. C **73** (2013) 2304, arXiv: 1112.6426 [hep-ex].

[129] *Monte Carlo Calibration and Combination of In-situ Measurements of Jet Energy Scale, Jet Energy Resolution and Jet Mass in ATLAS*, tech. rep. ATLAS-CONF-2015-037, CERN, 2015, URL: https://cds.cern.ch/record/2044941.

[130] *Expected performance of the ATLAS b-tagging algorithms in Run-2*, tech. rep. ATL-PHYS-PUB-2015-022, CERN, 2015, URL: http://cds.cern.ch/record/2037697.

[131] *Commissioning of the ATLAS high-performance b-tagging algorithms in the 7 TeV collision data*, tech. rep. ATLAS-CONF-2011-102, CERN, 2011, URL: https://cds.cern.ch/record/1369219.

[132] M. Aaboud et al., *Measurements of b-jet tagging efficiency with the ATLAS detector using $t\bar{t}$ events at $\sqrt{s}$ = 13 TeV*, JHEP **08** (2018) 089, arXiv: 1805.01845 [hep-ex].

[133] *Optimisation of the ATLAS b-tagging performance for the 2016 LHC Run*, tech. rep. ATL-PHYS-PUB-2016-012, CERN, 2016, URL: https://cds.cern.ch/record/2160731.

[134] M. Aaboud et al., *Performance of missing transverse momentum reconstruction with the ATLAS detector using proton-proton collisions at $\sqrt{s}$ = 13 TeV*, Eur. Phys. J. C **78** (2018) 903, arXiv: 1802.08168 [hep-ex].

[135] M. Jezabek and J. H. Kuhn, *QCD Corrections to Semileptonic Decays of Heavy Quarks*, Nucl. Phys. B **314** (1989) 1.

[136] J. Erler and M. Schott, *Electroweak Precision Tests of the Standard Model after the Discovery of the Higgs Boson*, Prog. Part. Nucl. Phys. **106** (2019) 68, arXiv: 1902.05142 [hep-ph].

[137] A. Quadt, *Top quark physics at hadron colliders*, Eur. Phys. J. C **48** (2006) 835.

[138] J. Haller et al., *Update of the global electroweak fit and constraints on two-Higgs-doublet models*, Eur. Phys. J. C **78** (2018) 675, arXiv: 1803.01853 [hep-ph].

[139] G. Degrassi et al., *Higgs mass and vacuum stability in the Standard Model at NNLO*, JHEP **08** (2012) 098, arXiv: 1205.6497 [hep-ph].

[140] A. Andreassen, W. Frost and M. D. Schwartz, *Scale Invariant Instantons and the Complete Lifetime of the Standard Model*, Phys. Rev. D **97** (2018) 056006, arXiv: 1707.08124 [hep-ph].

[141] U. Husemann, *Top-Quark Physics: Status and Prospects*, Prog. Part. Nucl. Phys. **95** (2017) 48, arXiv: 1704.01356 [hep-ex].

[142] P. Nason, 'The Top Mass in Hadronic Collisions', *From My Vast Repertoire ...: Guido Altarelli's Legacy*, ed. by A. Levy, S. Forte and G. Ridolfi, 2019 123, arXiv: 1712.02796 [hep-ph].

[143] M. Beneke, *Renormalons*, Phys. Rept. **317** (1999) 1, arXiv: hep-ph/9807443.

[144] M. Beneke, P. Marquard, P. Nason and M. Steinhauser, *On the ultimate uncertainty of the top quark pole mass*, Phys. Lett. B **775** (2017) 63, arXiv: 1605.03609 [hep-ph].

[145] A. H. Hoang, C. Lepenik and M. Preisser, *On the Light Massive Flavor Dependence of the Large Order Asymptotic Behavior and the Ambiguity of the Pole Mass*, JHEP **09** (2017) 099, arXiv: 1706.08526 [hep-ph].

[146] K. Chetyrkin, *Corrections of order alpha-s**3 to R(had) in pQCD with light gluinos*, Phys. Lett. B **391** (1997) 402, arXiv: hep-ph/9608480.

[147] A. H. Hoang and I. W. Stewart, *Top Mass Measurements from Jets and the Tevatron Top-Quark Mass*, Nucl. Phys. B Proc. Suppl. **185** (2008) 220, ed. by G. Bellettini, G. Chiarelli and R. Tenchini, arXiv: 0808.0222 [hep-ph].

[148] P. Marquard, A. V. Smirnov, V. A. Smirnov and M. Steinhauser, *Quark Mass Relations to Four-Loop Order in Perturbative QCD*, Phys. Rev. Lett. **114** (2015) 142002, arXiv: 1502.01030 [hep-ph].

[149] M. Butenschoen et al., *Top Quark Mass Calibration for Monte Carlo Event Generators*, Phys. Rev. Lett. **117** (2016) 232001, arXiv: 1608.01318 [hep-ph].

[150] LHCTopWG, *LHCTopWG Summary Plots*, 2019, URL: https://twiki.cern.ch/twiki/bin/view/LHCPhysics/LHCTopWGSummaryPlots.

[151] M. Czakon, P. Fiedler and A. Mitov, *Total Top-Quark Pair-Production Cross Section at Hadron Colliders Through $O(\alpha_S^4)$*, Phys. Rev. Lett. **110** (2013) 252004, arXiv: 1303.6254 [hep-ph].

[152] M. Czakon and A. Mitov, *NNLO corrections to top pair production at hadron colliders: the quark-gluon reaction*, JHEP **01** (2013) 080, arXiv: 1210.6832 [hep-ph].

[153] T. S. DØ's Top/Higgs Group, *Feynman diagrams for talks*, 2011, URL: https://www-d0.fnal.gov/Run2Physics/top/top_public_web_pages/top_feynman_diagrams.html.

[154] F. Fiedler, A. Grohsjean, P. Haefner and P. Schieferdecker, *The Matrix Element Method and its Application in Measurements of the Top Quark Mass*, Nucl. Instrum. Meth. A **624** (2010) 203, arXiv: 1003.1316 [hep-ex].

[155] V. M. Abazov et al., *Precision measurement of the top-quark mass in lepton+jets final states*, Phys. Rev. D **91** (2015) 112003, arXiv: 1501.07912 [hep-ex].

[156] T. Aaltonen et al., *Top quark mass measurement using the template method at CDF*, Phys. Rev. D **83** (2011) 111101, arXiv: 1105.0192 [hep-ex].

[157] L. Lyons, D. Gibaut and P. Clifford, *How to Combine Correlated Estimates of a Single Physical Quantity*, Nucl. Instrum. Meth. A **270** (1988) 110.

[158] D. c. CDF collaboration, *Combination of CDF and D0 results on the mass of the top quark using up 9.7 fb^{-1} at the Tevatron*, (2016), arXiv: 1608.01881 [hep-ex].

[159] M. Aaboud et al., *Top-quark mass measurement in the all-hadronic $t\bar{t}$ decay channel at $\sqrt{s}$ = 8 TeV with the ATLAS detector*, JHEP **09** (2017) 118, arXiv: 1702.07546 [hep-ex].

[160] *Measurement of the top quark mass in the all-jets final state at* $\sqrt{s} = 13$ TeV, tech. rep. CMS-PAS-TOP-17-008, CERN, 2018, URL: https://cds.cern.ch/record/2628540.

[161] M. Aaboud et al., *Measurement of the top quark mass in the* $t\bar{t} \to$ *lepton+jets channel from* $\sqrt{s} = 8$ *TeV ATLAS data and combination with previous results*, Eur. Phys. J. C **79** (2019) 290, arXiv: 1810.01772 [hep-ex].

[162] V. Khachatryan et al., *Measurement of the top quark mass using proton-proton data at* $\sqrt{(s)} = 7$ *and 8 TeV*, Phys. Rev. D **93** (2016) 072004, arXiv: 1509.04044 [hep-ex].

[163] A. M. Sirunyan et al., *Measurement of the top quark mass with lepton+jets final states using* p p *collisions at* $\sqrt{s} = 13$ *TeV*, Eur. Phys. J. C **78** (2018) 891, arXiv: 1805.01428 [hep-ex].

[164] M. Aaboud et al., *Measurement of the top quark mass in the* $t\bar{t} \to$ *dilepton channel from* $\sqrt{s} = 8$ *TeV ATLAS data*, Phys. Lett. B **761** (2016) 350, arXiv: 1606.02179 [hep-ex].

[165] A. M. Sirunyan et al., *Measurement of the top quark mass in the dileptonic* $t\bar{t}$ *decay channel using the mass observables* $M_{b\ell}$, M_{T2}, *and* $M_{b\ell\nu}$ *in pp collisions at* $\sqrt{s} = 8$ *TeV*, Phys. Rev. D **96** (2017) 032002, arXiv: 1704.06142 [hep-ex].

[166] W. S. Cho, K. Choi, Y. G. Kim and C. B. Park, *M(T2)-assisted on-shell reconstruction of missing momenta and its application to spin measurement at the LHC*, Phys. Rev. D **79** (2009) 031701, arXiv: 0810.4853 [hep-ph].

[167] A. J. Barr and C. G. Lester, *A Review of the Mass Measurement Techniques proposed for the Large Hadron Collider*, J. Phys. G **37** (2010) 123001, arXiv: 1004.2732 [hep-ph].

[168] V. M. Abazov et al., *Determination of the pole and* $\overline{MS}$ *masses of the top quark from the* $t\bar{t}$ *cross section*, Phys. Lett. B **703** (2011) 422, arXiv: 1104.2887 [hep-ex].

[169] V. M. Abazov et al., *Measurement of the Inclusive* $t\bar{t}$ *Production Cross Section in* $p\bar{p}$ *Collisions at* $\sqrt{s} = 1.96$ *TeV and Determination of the Top Quark Pole Mass*, Phys. Rev. D **94** (2016) 092004, arXiv: 1605.06168 [hep-ex].

[170] G. Aad et al., *Measurement of the* $t\bar{t}$ *production cross-section and lepton differential distributions in* $e\mu$ *dilepton events from* pp *collisions at* $\sqrt{s} = 13$ *TeV with the ATLAS detector*, (2019), arXiv: 1910.08819 [hep-ex].

[171] *Measurement of the* $\mathrm{t\bar{t}}$ *production cross section, the top quark mass, and the strong coupling constant using events in the dilepton final state in pp collisions at* $\sqrt{s} = 13$ TeV, tech. rep. CMS-PAS-TOP-17-001, CERN, 2018, URL: https://cds.cern.ch/record/2639182.

[172] M. Aaboud et al., *Measurement of lepton differential distributions and the top quark mass in* $t\bar{t}$ *production in* pp *collisions at* $\sqrt{s} = 8$ *TeV with the ATLAS detector*, Eur. Phys. J. C **77** (2017) 804, arXiv: 1709.09407 [hep-ex].

[173] G. Aad et al., *Measurement of the top-quark mass in $t\bar{t}$ + 1-jet events collected with the ATLAS detector in pp collisions at $\sqrt{s}$ = 8 TeV*, JHEP **11** (2019) 150, arXiv: 1905.02302 [hep-ex].

[174] *Determination of the normalised invariant mass distribution of* $\mathrm{t\bar{t}}$*+jet and extraction of the top quark mass*, tech. rep. CMS-PAS-TOP-13-006, CERN, 2016, URL: https://cds.cern.ch/record/2153653.

[175] A. M. Sirunyan et al., *Running of the top quark mass from proton-proton collisions at $\sqrt{s}$ = 13TeV*, Phys. Lett. B **803** (2020) 135263, arXiv: 1909.09193 [hep-ex].

[176] A. M. Sirunyan et al., *Measurement of the jet mass distribution and top quark mass in hadronic decays of boosted top quarks in pp collisions at $\sqrt{s}$ = 13 TeV*, Phys. Rev. Lett. **124** (2020) 202001, arXiv: 1911.03800 [hep-ex].

[177] A. M. Sirunyan et al., *Measurement of* $\mathrm{t\bar{t}}$ *normalised multi-differential cross sections in pp collisions at $\sqrt{s}$ = 13 TeV, and simultaneous determination of the strong coupling strength, top quark pole mass, and parton distribution functions*, (2019), arXiv: 1904.05237 [hep-ex].

[178] H.-L. Lai et al., *New parton distributions for collider physics*, Phys. Rev. D **82** (2010) 074024, arXiv: 1007.2241 [hep-ph].

[179] G. Watt and R. Thorne, *Study of Monte Carlo approach to experimental uncertainty propagation with MSTW 2008 PDFs*, JHEP **08** (2012) 052, arXiv: 1205.4024 [hep-ph].

[180] R. D. Ball et al., *Parton distributions with LHC data*, Nucl. Phys. B **867** (2013) 244, arXiv: 1207.1303 [hep-ph].

[181] M. Botje et al., *The PDF4LHC Working Group Interim Recommendations*, (2011), arXiv: 1101.0538 [hep-ph].

[182] R. D. Ball et al., *Parton distributions for the LHC Run II*, JHEP **04** (2015) 040, arXiv: 1410.8849 [hep-ph].

[183] S. Dulat et al., *New parton distribution functions from a global analysis of quantum chromodynamics*, Phys. Rev. D **93** (2016) 033006, arXiv: 1506.07443 [hep-ph].

[184] G. Aad et al., *Jet energy measurement and its systematic uncertainty in proton-proton collisions at $\sqrt{s}$ = 7 TeV with the ATLAS detector*, Eur. Phys. J. C **75** (2015) 17, arXiv: 1406.0076 [hep-ex].

[185] *Data-driven determination of the energy scale and resolution of jets reconstructed in the ATLAS calorimeters using dijet and multijet events at $\sqrt{s}$ = 8 TeV*, tech. rep. ATLAS-CONF-2015-017, CERN, 2015, URL: https://cds.cern.ch/record/2008678.

[186] G. Aad et al., *Performance of b-Jet Identification in the ATLAS Experiment*, JINST **11** (2016) P04008, arXiv: 1512.01094 [hep-ex].

[187] G. Aad et al., *Electron reconstruction and identification efficiency measurements with the ATLAS detector using the 2011 LHC proton-proton collision data*, Eur. Phys. J. C **74** (2014) 2941, arXiv: 1404.2240 [hep-ex].

[188] G. Aad et al., *Measurement of the muon reconstruction performance of the ATLAS detector using 2011 and 2012 LHC proton–proton collision data*, Eur. Phys. J. C **74** (2014) 3130, arXiv: 1407.3935 [hep-ex].

[189] G. Aad et al., *Measurements of top-quark pair differential and double-differential cross-sections in the ℓ+jets channel with pp collisions at $\sqrt{s}$ = 13 TeV using the ATLAS detector*, Eur. Phys. J. C **79** (2019) 1028, arXiv: 1908.07305 [hep-ex].

[190] G. Aad et al., *Measurement of the top quark pair production cross-section with ATLAS in the single lepton channel*, Phys. Lett. B **711** (2012) 244, arXiv: 1201.1889 [hep-ex].

[191] G. D'Agostini, *A Multidimensional unfolding method based on Bayes' theorem*, Nucl. Instrum. Meth. A **362** (1995) 487.

[192] T. Adye, 'Unfolding algorithms and tests using RooUnfold', *PHYSTAT 2011*, CERN, 2011 313, arXiv: 1105.1160 [physics.data-an].

[193] G. Aad et al., *Measurement of the differential cross-section of highly boosted top quarks as a function of their transverse momentum in $\sqrt{s}$ = 8 TeV proton-proton collisions using the ATLAS detector*, Phys. Rev. D **93** (2016) 032009, arXiv: 1510.03818 [hep-ex].

[194] J.-F. Arguin et al., *Measurement of the top-antitop pair differential fiducial cross-section as a function of the top quark p_T in the boosted topology*, tech. rep. ATL-COM-PHYS-2013-1093, CERN, 2013, URL: https://cds.cern.ch/record/1570997.

[195] L. Bellagamba et al., *Top quark pole mass determination from top-quark pair differential cross-sections in the lepton+jets channel in $\sqrt{s}$ = 13 proton–proton collisions using the ATLAS detector*, tech. rep. ATL-COM-PHYS-2018-1447, CERN, 2018, URL: https://cds.cern.ch/record/2643398.

[196] M. Czakon, D. Heymes and A. Mitov, *High-precision differential predictions for top-quark pairs at the LHC*, Phys. Rev. Lett. **116** (2016) 082003, arXiv: 1511.00549 [hep-ph].

[197] M. Czakon, D. Heymes and A. Mitov, *Dynamical scales for multi-TeV top-pair production at the LHC*, JHEP **04** (2017) 071, arXiv: 1606.03350 [hep-ph].

[198] T. Kluge, K. Rabbertz and M. Wobisch, 'FastNLO: Fast pQCD calculations for PDF fits', *14th International Workshop on Deep Inelastic Scattering*, 2006 483, arXiv: hep-ph/0609285.

[199] M. Wobisch, D. Britzger, T. Kluge, K. Rabbertz and F. Stober, *Theory-Data Comparisons for Jet Measurements in Hadron-Induced Processes*, (2011), arXiv: 1109.1310 [hep-ph].

[200] D. Britzger, K. Rabbertz, F. Stober and M. Wobisch, 'New features in version 2 of the fastNLO project', *20th International Workshop on Deep-Inelastic Scattering and Related Subjects*, 2012 217, arXiv: 1208.3641 [hep-ph].

[201] M. Czakon, D. Heymes and A. Mitov,
fastNLO tables for NNLO top-quark pair differential distributions, (2017),
arXiv: 1704.08551 [hep-ph].

[202] J. Butterworth et al., *PDF4LHC recommendations for LHC Run II*,
J. Phys. G **43** (2016) 023001, arXiv: 1510.03865 [hep-ph].

[203] J. M. Campbell, R. K. Ellis, P. Nason and E. Re,
Top-Pair Production and Decay at NLO Matched with Parton Showers, JHEP **04** (2015) 114,
arXiv: 1412.1828 [hep-ph].

[204] P. Nason, *A New method for combining NLO QCD with shower Monte Carlo algorithms*,
JHEP **11** (2004) 040, arXiv: hep-ph/0409146 [hep-ph].

[205] S. Frixione, P. Nason and G. Ridolfi,
A Positive-weight next-to-leading-order Monte Carlo for heavy flavour hadroproduction,
JHEP **09** (2007) 126, arXiv: 0707.3088 [hep-ph].

[206] P. Artoisenet, R. Frederix, O. Mattelaer and R. Rietkerk,
Automatic spin-entangled decays of heavy resonances in Monte Carlo simulations,
JHEP **03** (2013) 015, arXiv: 1212.3460 [hep-ph].

[207] T. Sjostrand, S. Mrenna and P. Z. Skands, *A Brief Introduction to PYTHIA 8.1*,
Comput. Phys. Commun. **178** (2008) 852, arXiv: 0710.3820 [hep-ph].

[208] *ATLAS Pythia 8 tunes to 7 TeV datas*, tech. rep. ATL-PHYS-PUB-2014-021, CERN, 2014,
URL: https://cds.cern.ch/record/1966419.

[209] *Summary of ATLAS Pythia 8 tunes*, tech. rep. ATL-PHYS-PUB-2012-003, CERN, 2012,
URL: https://cds.cern.ch/record/1474107.

[210] R. Barlow, 'Asymmetric Errors',
Statistical Problems in Particle Physics, Astrophysics, and Cosmology,
ed. by L. Lyons, R. Mount and R. Reitmeyer, 2003 250,
arXiv: physics/0401042 [physics.data-an].

[211] T. Sjostrand, S. Mrenna and P. Z. Skands, *PYTHIA 6.4 Physics and Manual*,
JHEP **05** (2006) 026, arXiv: hep-ph/0603175 [hep-ph].

[212] M. Bahr et al., *Herwig++ Physics and Manual*, Eur. Phys. J. **C58** (2008) 639,
arXiv: 0803.0883 [hep-ph].

[213] J. Bellm et al., *Herwig 7.1 Release Note*, (2017), arXiv: 1705.06919 [hep-ph].

[214] J. Bellm et al., *Herwig++ 2.7 Release Note*, (2013), arXiv: 1310.6877 [hep-ph].

[215] J. Bellm et al., *Herwig 7.0/Herwig++ 3.0 release note*, Eur. Phys. J. **C76** (2016) 196,
arXiv: 1512.01178 [hep-ph].

[216] J. Alwall et al., *A Standard format for Les Houches event files*,
Comput. Phys. Commun. **176** (2007) 300, arXiv: hep-ph/0609017 [hep-ph].

[217] Herwig 7 Collaboration, *Using built-in matrix elements in Herwig 7*,
URL: https://herwig.hepforge.org/tutorials/hardprocess/builtin.html.

[218] S. Platzer and S. Gieseke, *Dipole Showers and Automated NLO Matching in Herwig++*,
Eur. Phys. J. **C72** (2012) 2187, arXiv: 1109.6256 [hep-ph].

[219] G. Cullen et al., *GoSam-2.0: a tool for automated one-loop calculations within the Standard Model and beyond*, Eur. Phys. J. **C74** (2014) 3001, arXiv: 1404.7096 [hep-ph].

[220] J. Alwall et al., *The automated computation of tree-level and next-to-leading order differential cross sections, and their matching to parton shower simulations*, JHEP **07** (2014) 079, arXiv: 1405.0301 [hep-ph].

[221] S. Badger, B. Biedermann, P. Uwer and V. Yundin, *Numerical evaluation of virtual corrections to multi-jet production in massless QCD*, Comput. Phys. Commun. **184** (2013) 1981, arXiv: 1209.0100 [hep-ph].

[222] F. Cascioli, P. Maierhofer and S. Pozzorini, *Scattering Amplitudes with Open Loops*, Phys. Rev. Lett. **108** (2012) 111601, arXiv: 1111.5206 [hep-ph].

[223] K. Arnold et al., *VBFNLO: A Parton level Monte Carlo for processes with electroweak bosons*, Comput. Phys. Commun. **180** (2009) 1661, arXiv: 0811.4559 [hep-ph].

[224] L. M. Scyboz, A. Knue and S. Kluth, *A study of the sensitivity to the Herwig 7 parameters of $t\bar{t}$ production measurements in pp collisions with the ATLAS experiment at the LHC*, tech. rep. ATL-COM-PHYS-2017-1244, CERN, 2017, URL: https://cds.cern.ch/record/2280482.

[225] D. Reichelt, P. Richardson and A. Siodmok, *Improving the Simulation of Quark and Gluon Jets with Herwig 7*, Eur. Phys. J. C **77** (2017) 876, arXiv: 1708.01491 [hep-ph].

[226] A. Kupco, 'Cluster hadronization in HERWIG 5.9', *Monte Carlo generators for HERA physics. Proceedings, Workshop, Hamburg, Germany, 1998-1999*, 1998 292, arXiv: hep-ph/9906412 [hep-ph].

[227] S. Gieseke, C. Rohr and A. Siodmok, *Colour reconnections in Herwig++*, Eur. Phys. J. **C72** (2012) 2225, arXiv: 1206.0041 [hep-ph].

[228] A. Buckley et al., *Rivet toolkit*, URL: https://rivet.hepforge.org/.

[229] A. Buckley and H. Schulz, *Professor tuning system*, URL: https://professor.hepforge.org.

[230] A. Buckley et al., *Rivet analyses reference*, URL: https://rivet.hepforge.org/analyses.html.

[231] M. Dobbs, J. B. Hansen, L. Garren and L. Sonnenschein, *HepMC3 event record library*, URL: http://hepmc.web.cern.ch/hepmc/.

[232] M. Dobbs, J. B. Hansen, L. Garren and L. Sonnenschein, *HepMC 2.06 user manual*, URL: http://lcgapp.cern.ch/project/simu/HepMC/206/HepMC2_user_manual.pdf.

[233] G. Aad et al., *Measurement of jet shapes in top-quark pair events at $\sqrt{s} = 7$ TeV using the ATLAS detector*, Eur. Phys. J. **C73** (2013) 2676, arXiv: 1307.5749 [hep-ex].

[234] M. Aaboud et al., *Measurement of jet activity produced in top-quark events with an electron, a muon and two b-tagged jets in the final state in pp collisions at $\sqrt{s} = 13$ TeV with the ATLAS detector*, Eur. Phys. J. **C77** (2017) 220, arXiv: 1610.09978 [hep-ex].

[235] M. Aaboud et al., *Measurements of top-quark pair differential cross-sections in the lepton+jets channel in pp collisions at $\sqrt{s}$ = 13 TeV using the ATLAS detector*, JHEP **11** (2017) 191, arXiv: 1708.00727 [hep-ex].

[236] Hoeth, Hendrik and Buckley, Andy and Mallows, Dave and Kawalec, Michal, *Rivet analyses reference: MC analysis for ttbar studies*, URL: https://rivet.hepforge.org/analyses/MC_TTBAR.html.

[237] A. Buckley, *Rivet analyses reference: Monte Carlo validation analysis to study heavy flavour productions*, URL: https://rivet.hepforge.org/analyses/MC_HFJETS.html.

[238] J. Bellm, G. Nail, S. Plätzer, P. Schichtel and A. Siódmok, *Parton Shower Uncertainties with Herwig 7: Benchmarks at Leading Order*, Eur. Phys. J. **C76** (2016) 665, arXiv: 1605.01338 [hep-ph].

[239] K. Cormier, S. Plätzer, C. Reuschle, P. Richardson and S. Webster, *Parton Shower and Matching Uncertainties in Top Quark Pair Production with Herwig 7*, (2018), arXiv: 1810.06493 [hep-ph].

[240] Herwig 7 Collaboration, *Herwig 7 tutorials*, URL: https://herwig.hepforge.org/tutorials/.

[241] P. Stephens and A. van Hameren, *Propagation of uncertainty in a parton shower*, (2007), arXiv: hep-ph/0703240 [HEP-PH].

[242] S. Platzer and M. Sjodahl, *The Sudakov Veto Algorithm Reloaded*, Eur. Phys. J. Plus **127** (2012) 26, arXiv: 1108.6180 [hep-ph].

[243] J. Bellm, S. Plätzer, P. Richardson, A. Siódmok and S. Webster, *Reweighting Parton Showers*, Phys. Rev. **D94** (2016) 034028, arXiv: 1605.08256 [hep-ph].

[244] J. Olsson, S. Plätzer and M. Sjödahl, *Resampling Algorithms for High Energy Physics Simulations*, (2019), arXiv: 1912.02436 [hep-ph].

[245] J. R. Christiansen and P. Z. Skands, *String Formation Beyond Leading Colour*, JHEP **08** (2015) 003, arXiv: 1505.01681 [hep-ph].

[246] T. Sjöstrand et al., *An introduction to PYTHIA 8.2*, Comput. Phys. Commun. **191** (2015) 159, arXiv: 1410.3012 [hep-ph].

[247] S. Argyropoulos and T. Sjöstrand, *Effects of color reconnection on $t\bar{t}$ final states at the LHC*, JHEP **11** (2014) 043, arXiv: 1407.6653 [hep-ph].

[248] *The Pythia 8 A3 tune description of ATLAS minimum bias and inelastic measurements incorporating the Donnachie-Landshoff diffractive model*, tech. rep. ATL-PHYS-PUB-2016-017, CERN, 2016, URL: https://cds.cern.ch/record/2206965.

[249] D. Lange, *The EvtGen particle decay simulation package*, Nucl. Instrum. Meth. A **462** (2001) 152, ed. by S. Erhan, P. Schlein and Y. Rozen.

[250] L. Harland-Lang, A. Martin, P. Motylinski and R. Thorne, *Parton distributions in the LHC era: MMHT 2014 PDFs*, Eur. Phys. J. C **75** (2015) 204, arXiv: 1412.3989 [hep-ph].

[251] *Studies on top-quark Monte Carlo modelling for Top2016*, tech. rep. ATL-PHYS-PUB-2016-020, CERN, 2016, URL: https://cds.cern.ch/record/2216168.

[252] S. Frixione, E. Laenen, P. Motylinski, B. R. Webber and C. D. White, *Single-top hadroproduction in association with a W boson*, JHEP **07** (2008) 029, arXiv: 0805.3067 [hep-ph].

[253] E. Bothmann et al., *Event Generation with Sherpa 2.2*, SciPost Phys. **7** (2019) 034, arXiv: 1905.09127 [hep-ph].

[254] T. Gleisberg and S. Hoeche, *Comix, a new matrix element generator*, JHEP **12** (2008) 039, arXiv: 0808.3674 [hep-ph].

[255] A. Denner, S. Dittmaier and L. Hofer, *Collier: a fortran-based Complex One-Loop LIbrary in Extended Regularizations*, Comput. Phys. Commun. **212** (2017) 220, arXiv: 1604.06792 [hep-ph].

[256] S. Hoeche, F. Krauss, S. Schumann and F. Siegert, *QCD matrix elements and truncated showers*, JHEP **05** (2009) 053, arXiv: 0903.1219 [hep-ph].

[257] S. Hoeche, F. Krauss, M. Schonherr and F. Siegert, *QCD matrix elements + parton showers: The NLO case*, JHEP **04** (2013) 027, arXiv: 1207.5030 [hep-ph].

[258] C. Anastasiou, L. J. Dixon, K. Melnikov and F. Petriello, *High precision QCD at hadron colliders: Electroweak gauge boson rapidity distributions at NNLO*, Phys. Rev. D **69** (2004) 094008, arXiv: hep-ph/0312266.

[259] *ATLAS simulation of boson plus jets processes in Run 2*, tech. rep. ATL-PHYS-PUB-2017-006, CERN, 2017, URL: https://cds.cern.ch/record/2261937.

[260] *Fiducial Top-quark measurements*, URL: https://twiki.cern.ch/twiki/bin/view/AtlasProtected/TopFiducial.

[261] D. Hirschbuehl et al., *Measurements of observables sensitive to colour reconnection in $t\bar{t}$ dilepton events with the ATLAS detector at $\sqrt{s}$ = 13 TeV*, tech. rep. ATL-COM-PHYS-2019-888, CERN, 2019, URL: https://cds.cern.ch/record/2682602.

[262] A Armbruster, K Kroeninger, B Malaescu and F Spano, *Practical considerations for unfolding*, tech. rep. ATL-COM-PHYS-2014-277, CERN, 2014, URL: https://cds.cern.ch/record/1694351.

[263] A. Hocker and V. Kartvelishvili, *SVD approach to data unfolding*, Nucl. Instrum. Meth. A **372** (1996) 469, arXiv: hep-ph/9509307.

[264] G. Choudalakis, *Fully Bayesian Unfolding*, (2012), arXiv: 1201.4612 [physics.data-an].

[265] *Impact of fragmentation modelling on the top quark mass measurement using the ATLAS detector*, tech. rep. ATL-PHYS-PUB-2015-042, CERN, 2015, URL: https://cds.cern.ch/record/2054420.

[266] R. Nisius, A. A. Maier and G. Cortiana, *Measurement of the Top Quark Mass in the $t\bar{t} \to$ dilepton Channel from $\sqrt{s} = 8$ TeV ATLAS Data*, tech. rep. ATL-COM-PHYS-2016-031, Note: The draft Version 1.0 contains the unblinded result (in Tables and Figures) although the text in some places, by mistake, still refers to the blinding.: CERN, 2016, URL: https://cds.cern.ch/record/2124214.

[267] W. Verkerke and D. P. Kirkby, *The RooFit toolkit for data modeling*, eConf **C0303241** (2003) MOLT007, ed. by L. Lyons and M. Karagoz, arXiv: physics/0306116.

université PARIS-SACLAY

ÉCOLE DOCTORALE
Particules, hadrons, énergie et noyau : instrumentation, imagerie, cosmos et simulation (PHENIICS)

Titre : Mesure de la masse au pôle du quark top à l'aide de sections efficaces $t\bar{t}$ différentielles dans l'expérience ATLAS au LHC et amélioration des incertitudes de modélisation dans les analyses de masse du quark top

Mots clés : LHC, ATLAS, quark top, masse

Résumé : Le quark top se demarque du reste des particules élémentaires du modèle standard (MS). Étant la particule élémentaire la plus lourde, le quark top ne s'hadronise pas, ce qui permet de mesurer sa masse directement. Le quark top est également la source principale de corrections radiatives dans de nombreux calculs perturbatifs. La détermination précise de la masse du quark top est importante dans les tests de la cohérence du MS.
Actuellement, les mesures de la masse du quark top les plus précises utilisent des méthodes "standard", dans lesquelles la distribution de la masse est directement reconstruite. Un point faible principal de ces méthodes est qu'elles sont basées largement sur les simulations Monte Carlo (MC) et permettent d'extraire uniquement une "masse MC du quark top", i.e. liée à un paramètre d'un générateur MC. Les méthodes "alternatives" sont capables de déterminer une masse du quark top théoriquement bien définie car elles mesurent des observables qui peuvent être obtenues à partir de calculs théoriques.
Cette thèse de doctorat décrit l'une des alternatives pour la mesure de la masse du quark top, dans laquelle pour la première fois la masse au pôle du quark top est déterminée en ajustant les sections efficaces $t\bar{t}$ doublement différentielles mesurées à 13 TeV avec le détecteur ATLAS aux calculs théoriques au troisième ordre dominant. L'étude se concentre sur les tests de la cohérence de la procédure d'analyse.
Un chapitre de cette thèse est également consacré aux études liées aux variations des gerbes partoniques dans le générateur MC Herwig7 pour la production $t\bar{t}$. Cette étude est motivée par l'importance croissante de l'incertitude sur la modélisation des gerbes partoniques dans les mesures liées au quark top dans ATLAS et par la nécessité de définir cette incertitude de manière plus cohérente.
De plus, cette thèse décrit deux analyses visant à mieux comprendre et à améliorer deux composantes importantes de l'incertitude des mesures de masse du quark top: l'incertitude sur la reconnection de couleur et l'incertitude sur l'hadronisation. L'analyse sur la reconnection de couleur se concentre sur l'étude d'observables bidimensionelles sensibles aux modèles de reconnection de couleur dans le générateur MC Pythia8. L'analyse sur l'hadronisation étudie comment le recalibrage des jets influence l'incertitude de l'hadronisation de la masse du quark top à l'aide des simulations MC.

Title : Measurement of the top quark pole mass using double differential $t\bar{t}$ cross sections in the ATLAS experiment at the LHC and improvement of the modelling uncertainties in top quark mass analyses

Keywords : LHC, ATLAS, top quark, mass

Abstract : The top quark is unique among the elementary particles of the Standard Model (SM). Being the heaviest elementary particle, the top quark does not hadronise, which allows to measure directly its mass. The top quark is also the main source of radiative corrections in many perturbative calculations. Precise determination of the top quark mass is important in consistency tests of the SM.
Currently, the most precise top quark mass measurements employ "standard" methods, in which the top quark mass distribution is directly reconstructed. The main weakness of these methods is that they largely rely on the Monte Carlo (MC) simulations and allow to extract only a "MC top quark mass", which is a parameter of a MC generator. However, the "alternative" methods are able to determine a theoretically well-defined top quark mass because they measure observables which can be obtained from theory.
This doctoral thesis describes one of the top quark mass alternative measurements, in which for the first time the top quark pole mass is determined by fitting the double differential $t\bar{t}$ cross sections measured at 13 TeV with the ATLAS detector to the next-to-next-to-leading order theoretical calculations. The study is in particular focusing on the consistency tests of the analysis procedure.
One chapter of this thesis is also devoted to studies related to parton shower variations in the Herwig7 MC generator in the context of $t\bar{t}$ production. This study is motivated by the increasing importance of the parton shower uncertainty in top quark analyses in ATLAS and a need for its more consistent definition.
Also, this thesis describes two analyses aiming at better understanding and improving two important uncertainty components of the top quark mass measurements: the colour reconnection uncertainty and the hadronisation uncertainty. The colour reconnection analysis concentrates on the bayesian unfolding of two-dimensional observables, which are sensitive to the colour reconnection models of the Pythia8 MC generator. On the other hand, the hadronisation uncertainty analysis studies how jet recalibration influences the top quark mass hadronisation uncertainty using MC simulated samples.

Université Paris-Saclay
Espace Technologique / Immeuble Discovery
Route de l'Orme aux Merisiers RD 128 / 91190 Saint-Aubin, France